ON THE PHYSICS AND CONTROL OF STREAKS INDUCED BY AN ISOLATED ROUGHNESS ELEMENT

By

Kyle McHugh Bade

A DISSERTATION

Submitted to
Michigan State University
in partial fulfillment of the requirements
for the degree of

Mechanical Engineering - Doctor of Philosophy

ABSTRACT

ON THE PHYSICS AND CONTROL OF STREAKS INDUCED BY AN ISOLATED ROUGHNESS ELEMENT

By

Kyle McHugh Bade

This study is motivated by understanding the physics and controlling transient growth, and subsequent bypass transition of the laminar boundary layer to turbulence. Toward this end, an active isolated roughness element placed at the wall in a Blasius boundary layer is used to introduce steady and unsteady streak disturbances (known to be the precursor to the formation of turbulent spots in bypass transition) in a controlled way; enabling systematic investigation of the evolution of the disturbances and of potential methods to control them in real time. In the first part of this work, a parametric investigation using hot-wire measurements throughout discrete y-z planes (normal to the freestream velocity) examines the streamwise development of the streak disturbance and how it is influenced by key parameters; namely, the freestream velocity, U_{∞} , as well as the cylindrical roughness element height, k, and diameter, D. The hot-wire data are complemented with flow visualizations; correlations are drawn between these data, distinguishing non-transitioning, intermittent, and continuously transitioning flows. An increase in U_{∞} , k, or D causes the total disturbance energy, E, to increase, without evidence of transient growth for non-transitional cases. However, examination of the energy of individual disturbance features reveals that the highspeed disturbance experiences a streamwise region of transient growth for all cases, and that the eventual decay or continued growth of this disturbance correlates well with the onset of transition. The Disturbance Energy Density, e, is introduced to provide a more appropriate measure (than E) of isolated disturbance amplitude growth or decay. The normalized disturbance energy density is found to scale with k^6 and U^6_{∞} leading to a collective scaling term represented by $Re^6_{k\infty}$, when the streamwise coordinate is normalized as $(x^*-x^*_k)=(x-x_k)\frac{U_{\infty}}{\nu}\frac{k}{D}$ (where x_k is the streamwise location of the roughness element and ν is the kinematic viscosity). The scaling is successful over a large domain, where $(x^*-x^*_k) \gtrsim 5$.

In the second part of this study, a series of control experiments is carried out with the goal of cancelling, or reducing the strength of the roughness element induced streaks in real time, and hence prevent, or delay, the onset of bypass transition. The control strategy utilizes two wall-mounted hot-wire shear stress sensors, one upstream and one downstream of a plasma actuator to provide inputs to a feedforward-feedback control model. The control model is constructed by collecting disturbance-input to shear-stress-output (I/O) data to empirically determine the parameters of zeroth- and first-order boundary layer response models, which capture the boundary layer dynamics. The model parameters are subsequently used to tune the feedforward and PI-feedback controllers. The control is examined over a range of k, U_{∞} , feedback sensor positions (x_{fb}) , unsteady disturbance frequencies (f_k) , and control strategies; and is found to nearly completely cancel the steady state disturbance at the downstream sensor location. However, due to a mismatch in the spatial distribution of the disturbances generated by the roughness element and the actuator, the control is not as effective over a y-zplane, reducing the planar disturbance energy by up to 66.2%. Near-complete cancellation is expected with proper actuator design to match the spatial characteristics of the roughness element and plasma actuator induced disturbances. The control of unsteady disturbances demonstrates a limited frequency response, with a maximum controllable frequency of $f_k \lesssim 1.3$ Hz; although substantially higher frequencies can be controlled by improving the feedforward controller model and/or moving the feedback sensor closer to the actuator, to reduce the convective time delay in the control loop.

Copyright by KYLE MCHUGH BADE 2014 To my son, Callum.

ACKNOWLEDGMENTS

I would like to give my deepest thanks and appreciation to my advisor, Prof. Ahmed Naguib. His guidance and support throughout my PhD experience have helped me to learn and grow immensely. He has provided a unique experience toward exploring many aspects of fluid mechanics research while maintaining the constant objectives set forth by the primary research project. Our many conversations have allowed me to absorb his careful and focused approach to research and I will forever benefit from the time I have spent working with him and in his lab. Thank you very much for this opportunity.

I have been fortunate to work on a project that has often been a collaborative effort, and I would like to thank Dr. Ronnie Hanson and Prof. Philippe Lavoie, of the University of Toronto, Institute for Aerospace Studies for their help and friendship. Dr. Brandt Belson and Prof. Clancy Rowley, of Princeton University, have been extremely helpful through this work as well and I am grateful to have had the opportunity to collaborate with them.

Thank you to my wife Lisa, who has been incredibly supportive and understanding throughout this exhaustive, but exciting endeavor. I love you very much and I am so thankful for our many blessings. Thank you for your constant support while pursuing this degree.

Finally, thank you to my parents, family, and friends for their support, without whom I would not be able to achieve the many goals I pursue; as well as my current and former coworkers who have challenged and helped me to develop my engineering career.

This material is based upon work supported by the National Science Foundation under Grant No. CMMI-0932546. Any opinions, findings, and conclusions or recommendations expressed in this material are those of the author(s) and do not necessarily reflect the views of the National Science Foundation.

TABLE OF CONTENTS

LIST (OF TABLES	ix
LIST (OF FIGURES	X
KEY T	ΓΟ SYMBOLS AND ABBREVIATIONS	xxii
Chapte	er 1 Introduction	1
1.1	Boundary Layer Instability	2
1.2	Transient Growth	4
1.3	Secondary Instability	6
1.4	Streak Disturbance Generation in Experiments	7
1.5	Control of Transient Growth	9
Chapte	er 2 Experimental Setup	12
2.1	Wind Tunnel Setup	12
2.2	Flat Plate Setup	13
2.3	Roughness Element Setup	13
2.4	Hot Wire Setup	17
2.5	Flow Visualization Setup	22
2.6	Control Hardware Setup	24
	2.6.1 Plasma Actuator Setup	28
	2.6.2 Shear Stress Sensor Setup	32
Chapte	er 3 Steady-State Disturbance Results	36
3.1	Undisturbed (Basic) Flow	36
3.2	Disturbance Character	40
	3.2.1 Disturbance Description	40
	3.2.2 Flow Visualization Results	42
	3.2.3 Hot Wire Results	50
3.3	Disturbance Energy	58
3.4	Disturbance Energy Density	64
	3.4.1 Wall-Normal Characteristic Length Scale	68
	3.4.2 Spanwise Characteristic Length Scale	71
2 -	3.4.3 Disturbance Energy Density Results	74
3.5	Disturbance Energy Density Scaling	75
Chapte	er 4 Unsteady Disturbance Results	82
4.1	Kinematics of the Unsteady Roughness Element	82
4.2	Unsteady Disturbance Evolution	86

Chapte	er 5 Control Model Development	93
5.1	Control Model	93
5.2	Boundary Layer Response Models	98
	5.2.1 Roughness Element Response Model	98
	5.2.2 Plasma Actuator Model	103
5.3	Controller Design	109
	5.3.1 Feedforward Controller	111
	5.3.2 Feedback Controller	113
	5.3.2.1 Feedback Controller Windup Correction	115
5.4	Steady State Analysis of I/O Models	116
Chapte	er 6 Control Experiment Results	120
6.1	Steady Disturbance Control	120
6.2	Unsteady Disturbance Control	130
0.2	6.2.1 Effect of Roughness Element Height	131
	6.2.2 Effect of Freestream Velocity	140
	6.2.3 Feedforward vs. Feedback vs. Combined Control	144
	6.2.4 Effect of the Streamwise Location of the Feedback Sensor	150
	6.2.5 Effect of the Unsteady Disturbance Frequency	155
Chapte	er 7 Conclusions	168
7.1	Physical Aspects of the Roughness Element Induced Disturbance	168
7.2	Control of the Roughness Element Induced Disturbance	172
7.3	Comments for Future Physics Experiments	176
7.4	Comments for Future Control Experiments	177
APPE	NDIX	181
BIBLI	OCR APHV	187

LIST OF TABLES

Table 2.1	Summary of test case parameters. Note that the symbol shape represents the freestream velocity: 4 m/s (\neg , downward triangle) 5 m/s (\neg , circle) and 6 m/s (\neg , upward triangle), the symbol/line color represents the roughness height, and the line style (solid/dashed) is used for representing the roughness element diameter	16
Table 5.1	Parameters used in the upstream disturbance shear stress to down-stream disturbance shear stress boundary layer response model, with the downstream (feedback) shear stress sensor positioned at various streamwise locations. Note that the model development process was repeated with an independent dataset at the x_{fb} - x_k =300 mm location, and these results are also provided, although they were never used for control experiments	103
Table 5.2	Parameters used in the plasma actuator voltage to downstream disturbance shear stress boundary layer response model, with the downstream (feedback) shear stress sensor positioned at various streamwise locations. Note that the model development process was repeated with an independent dataset at the x_{fb} - x_k =300 mm location, and these results are also provided, although they were never used for control experiments	109
Table 5.3	Parameters used in the feedforward and anti-windup feedback controllers, with the downstream (feedback) shear stress sensor positioned at various streamwise locations. Note that the model development process was repeated with an independent dataset at the x_{fb} - x_k =300 mm location, and these results are also provided, although they were never used for control experiments	111
Table 6.1	Summary of test parameters for the control experiments. Subsets of experiments (separated by a line) investigate the effect of each parameter (highlighted in darker gray)	121

LIST OF FIGURES

Figure 2.1	Flat plate geometry, with 4-single-wire hot wire assembly, seven y - z measurement planes, and a representative y - z measurement grid. The seven hot wire measurement planes, covering the range of $25 \leqslant x$ - $x_k \leqslant 300$, are shown to-scale to give perspective of the data collection domain, but these planes are non-physical and do not represent any physical structure	14
Figure 2.2	Schematic of the Squiggle motor and laser sensor arrangement in the (left) x - y plane (laser not shown, for clarity) and the (right) y - z plane, with relevant mechanical pieces used to ensure accurate and repeatable roughness element actuation	16
Figure 2.3	The hot wire velocity signal and laser roughness element height signal during two actuation cycles of the roughness element with the hot wire located at $(x-x_k, y, z) = (150, 2, -3)$ mm with the following conditions: $(k, D, U_{\infty})=(1.29 \text{ mm}, 5.0 \text{ m/s})$	19
Figure 2.4	Schematic of the flow visualization setup components and geometry	22
Figure 2.5	The arrangement of the control components relative to the flat plate; demonstrated are: i) the isolated roughness element, ii) the upstream wall-mounted shear stress sensor, iii) the plasma actuator assembly, iv) the downstream shear stress sensor (mounted to the 3D overhead traverse), and v) the freestream velocity hot wire probe (mounted to the 3D traverse). The relative location and scale of all control elements is shown to-scale to give proper perspective of the control domain	25
Figure 2.6	A block diagram of the control equipment and associated cabling/wiring of the many hardware components and I/O signals. The description of the PC (NI) and NI-DAQ Board components is provide in §2.4	28
Figure 2.7	Diagram of the SDBD plasma actuator geometry used here demonstrating the positive electrode, ground electrode, and dielectric layer, plasma formation region, and induced flow. The insulting material acts as a base for the plasma actuator components and prevents plasma from forming on the grounding electrode side of the dielectric.	29

Figure 2.8	Plan- and Cross-section views $(A-A \text{ and } B-B)$ of the SDBD plasma actuator geometry demonstrating the positive electrode, ground electrode, and dielectric layer, and plasma formation region. Section $B-B$ also shows a drawing of the flow disturbance produced by the actuator. A low-speed streak forms where a wall-normal disturbance velocity away form the plate is produced, and vice versa. This is due to low speed fluid moving away and towards the wall, respectively.	30
Figure 2.9	Schematic of the counter rotating vortex pair produced in the boundary layer by the plasma actuator and the associated streamwise-velocity disturbance. Red: positive disturbance, Blue: negative disturbance	31
Figure 2.10	Boundary layer profiles at a) x_{ff} - x_k =65 mm and b) x_{fb} - x_k =300 mm demonstrating the wall-normal location of the upstream and downstream shear stress sensors, respectively, within the linear region of the undisturbed Blasius boundary layer	33
Figure 2.11	The upstream shear stress sensor assembly, demonstrating the method used to allow variable wall-normal positioning of the sensor using a stationary plug with two small holes for the hotwire broaches; the hot wire body is mounted on a small manual y -axis stage	35
Figure 3.1	(a) The measured, self-similar, Blasius boundary layer profiles at x - x_k =25, 50, 100, 150, 200, 250, and 300 mm for the three freestream velocities of interest (\triangle, \circ, \neg) and according to theory ($-$) with the inset figure demonstrating the shape factor for velocity profiles measured at the three velocities and all streamwise locations. The error bars indicate the range of shape factors calculated across all test cases at each location, and (b) the measured boundary layer thickness (\triangle, \circ, \neg) and theoretical Blasius boundary layer thickness ($-$) with the inset figure highlighting the boundary layer thickness at the roughness element location. Note that all values are spanwise average results, denoted with $\langle \ \rangle_z$	38
Figure 3.2	Distribution of shape factor H_{12} across the spanwise direction at all streamwise locations for $U_{\infty}=5.0$ m/s. Note that each of the seven vertical subplots on the left represent the spanwise data at the streamwise location as noted immediately to the right, which then provides the spanwise-average result, $\langle H_{12} \rangle_z$	39

Figure 3.3	Schematic of the counter rotating vortex pair produced in the boundary layer by an isolated roughness element and the associated streamwise-velocity disturbance. Red: positive disturbance, Blue: negative disturbance	41
Figure 3.4	Instantaneous flow visualizations of the streak disturbance in the x - z plane with $D=5.0$ mm and $U_{\infty}=5.0$ m/s, at a) k =1.40 mm, b) k =1.51 mm, c) k =1.60 mm, and d) k =2.00 mm; with the smoke-wire at $(x$ - x_k , y)=(-25, 2) mm and laser sheet at y \approx 3 \pm 1 mm from the wall.	44
Figure 3.5	Diagram illustrating the characteristic shape, by streamlines of the disturbance velocity field, of the fundamental mode of the a) symmetric (varicose) and b) antisymmetric (sinuous) disturbance patterns for a spanwise periodic disturbance. The gray section represents a singe spanwise cycle. (These diagrams are reproduced from Vaughan & Zaki [49])	46
Figure 3.6	Smoke-wire image of the successive hairpin vortex structure generated downstream of the roughness element for $k=2.0$ mm, $D=5.0$ mm, and $U_{\infty}=5.0$ m/s; with the smoke-wire at $(x-x_k,y)=(-25,1)$ mm and laser sheet at $y\approx 2\pm 1$ mm from the wall	47
Figure 3.7	Mark-up of the results in Figure 3.4d demonstrating the half-angle assessments of the turbulent wedge two-stage spanwise growth	49
Figure 3.8	Spatial development of the y-z planar disturbance with variable k and constant D =5.0 mm and U_{∞} =5.0 m/s for a) k =0.5, b) k =1.0, c) k =1.29, d) k =1.4 mm, e) k =1.51, f) k =1.6, and g) k =2.0 mm	51
Figure 3.9	Spatial development of the y-z planar disturbance with variable U_{∞} and constant $k=1.0$ mm and $D=5.0$ mm for a) $U_{\infty}=4.0$, b) $U_{\infty}=5.0$, and c) $U_{\infty}=6.0$ mm	53
Figure 3.10	Spatial development of the y - z planar disturbance with variable D and constant k =1.51 mm and U_{∞} =5.0 m/s for a) D =5.0 and b) D =3.175 mm	54
Figure 3.11	Disturbance and Blasius velocity profiles at $(x-x_k, z)=(300, 0)$ mm, for $k=2.0$ mm, $D=5.0$ mm, and $U_{\infty}=5.0$ m/s. The difference between the two profiles gives the disturbance intensity $()$	55
Figure 3.12	E for various k , U_{∞} , and D combinations for an isolated roughness element. See Table 2.1 for the complete parameter definitions for each case	59

Figure 3.13	Definition of three identifiable velocity disturbance regions: The low speed wake disturbance (E_{wake}) , the vortex induced high-speed disturbance (E_+) , and the vortex induced low-speed disturbance (E) ; same data as Figure 3.21, case 3, x - $x_k = 100$ mm. Note that the feature outlines are drawn at $u'/U_{\infty} = \pm 0.003$	61
Figure 3.14	Streamwise evolution of the total disturbance energy, E , as well as the contribution from the low-speed wake (E_{wake}) , positive vortexinduced (E_+) , and negative vortex-induced (E) streaks for D =5.0mm and U_{∞} =5.0 m/s with a) k =0.5, b) k =1.0, c) k =1.29, d) k =1.4, e) k =1.51, f) k =1.6, and g) k =2.0 mm	63
Figure 3.15	An example of disturbance a) energy, E , normalized by the energy at $x=0.3$, E_0 and b) amplitude, A , for a streak to demonstrate that the total disturbance energy and the disturbance amplitude may not follow the same streamwise trend of growth and decay. (This figure is borrowed from Andersson $et\ al.\ [2])$	66
Figure 3.16	A for various k , U_{∞} , and D combinations for an isolated roughness element. The marginal stability amplitude, $A(x)=0.26$, is noted with a black dash line with no symbols. See Table 2.1 for the complete parameter definitions for each case.	66
Figure 3.17	Schematic representation of an idealized spatially growing streak disturbance without amplification.	67
Figure 3.18	Demonstration of the characteristic wall-normal and spanwise length scales (η_c and z_c , respectively) for $k=1.29$ mm, $D=5.0$ mm, and $U_{\infty}=5.0$ m/s, located at x - $x_k=300$ mm. In the top-left plot is the contour plot of the disturbance velocity. The top-right plot demonstrates the root of the sum-in- z of the square of the disturbance velocity, the peak of which gives the characteristic wall-normal length, η_c . The bottom plot demonstrates the sum-in- y of the disturbance velocity with the zero-crossings distance representative of the spanwise characteristic length scale, z_c	69
Figure 3.19	Determination of η_c for various k with $D{=}5.0$ mm and $U_{\infty}{=}5.0$ m/s, at a) $x{-}x_k{=}25$ mm and b) at $x{-}x_k{=}100$ mm	70
Figure 3.20	Streamwise evolution of η_c for various values of k , D , and U_{∞} . See Table 2.1 for the complete parameter definitions for each case	70

Figure 3.21	Demonstration of the characteristic wall-normal and spanwise length scales (η_c and z_c , respectively) for $k=1.29$ mm, $D=5.0$ mm, and $U_{\infty}=5.0$ m/s, located at x - $x_k=100$ mm. In the top-left plot is the contour plot of the disturbance velocity. The top-right plot demonstrates the root of the sum-in- z of the square of the disturbance velocity, the peak of which give the characteristics wall-normal length, η_c . The bottom plot demonstrates the sum-in- y of the disturbance velocity with the zero-crossings distance representative of the spanwise characteristic length scale, z_c	73
Figure 3.22	Streamwise evolution of z_c for various k , D , and U_{∞} combinations for an isolated roughness element; note, the transitional cases are removed because the z_c characteristic length scale is not appropriate for these cases given the fundamental change in the shape of the spanwise distribution of the disturbance velocity	73
Figure 3.23	The disturbance energy density, e , for various k , U_{∞} , and D combinations for an isolated roughness element. See Table 2.1 for the complete parameter definitions for each case	74
Figure 3.24	The disturbance energy density, e , versus the scaled streamwise coordinate $(x^* - x_k^*)$, for various k , U_{∞} , and D combinations for an isolated roughness element. See Table 2.1 for the complete parameter definitions for each case.	79
Figure 3.25	$e/(U_{\infty}^2 k^6)$ for various k, D , and U_{∞} combinations	79
Figure 3.26	e/U_{∞}^{8} for various k , D , and U_{∞} combinations	80
Figure 3.27	$e/(U_{\infty}^2 Re_{k\infty}^6)$ for various $k,D,$ and U_{∞} combinations; semi log plot .	80
Figure 3.28	$e/(U_{\infty}^2 R e_{k\infty}^6)$ for various k , D , and U_{∞} combinations; linear plot, zoomed in, with no lines	81
Figure 4.1	Roughness element actuation kinematics, during upward motion, experienced when using the electromagnetic solenoid with a fully deployed roughness element height of a) k =0.50 mm and b) k =1.29 mm	84
Figure 4.2	Roughness element actuation kinematics during upward motion, experienced when using the piezoelectric Squiggle motor, with a fully deployed roughness element height of a) $k=1.29$ mm and b) $k=2.00$ mm	85

Figure 4.3	Unsteady streamwise velocity disturbance contours with a fully deployed roughness element height of $k=0.50$ mm, using a solenoid to actuate the roughness element. The roughness element height versus time is provided in the top-left plot; five time instants (t_1-t_5) corresponding to the disturbance contour results are labeled	87
Figure 4.4	Unsteady streamwise velocity disturbance contours with a fully deployed roughness element height of $k=1.29$ mm, using a solenoid to actuate the roughness element. The roughness element height versus time is provided in the top-left plot; five time instants (t_1-t_5) corresponding to the disturbance contour results are labeled	88
Figure 4.5	Unsteady streamwise velocity disturbance contours with a fully deployed roughness element height of $k=1.29$ mm, using the Squiggle motor to actuate the roughness element with prescribed motion parameters: $v_k = 7.5$ mm/s and $a_k = 1000$ mm/s ² . The roughness element height versus time is provided in the top-left plot; five time instants (t_1-t_5) corresponding to the disturbance contour results are labeled	89
Figure 4.6	Unsteady streamwise velocity disturbance contours with a fully deployed roughness element height of $k=2.00$ mm, using the Squiggle motor to actuate the roughness element with prescribed motion parameters: $v_k = 7.5$ mm/s and $a_k = 1000$ mm/s ² . The roughness element height versus time is provided in the top-left plot; five time instants (t_1-t_5) corresponding to the disturbance contour results are labeled	90
Figure 5.1	Block diagram of the primary control system components and a demonstration of the feedforward-feedback control model implementation of this study.	95
Figure 5.2	Block diagram of the feedforward-feedback control model form used in this study including the boundary layer response models and controllers.	96
Figure 5.3	Example unsteady I/O data collected for determination of the boundary layer response model to roughness disturbance input. Sata shown are obtained for "sudden" deployment of the roughness element from $k{=}0$ to 1.2 mm with the feedback sensor located at x_{fb} - x_k =300 mm.	100
Figure 5.4	Example phase-averaged I/O data for the boundary layer response model parameter determination for $k=1.2$ mm with the feedback sensor located at x_{fb} - x_k =300 mm	101

Figure 5.5	Phase averaged I/O data results for various k values with the feedback sensor at x_{fb} - x_k =300 mm. Provided are the a) roughness element motion, b) the upstream shear stress disturbance, and c) the downstream shear stress disturbance developments in time	102
Figure 5.6	Plant model, $P_{\tau'_u,\tau'_d}$, parameters for the a) gain and b) time delay with the feedback sensor at x_{fb} - x_k =300 mm	103
Figure 5.7	Example I/O data for determination of the boundary layer response model parameters for V =2.4 kV and the feedback sensor located at x_{fb} - x_k =300 mm	105
Figure 5.8	Example phase averaged I/O data for determination of the boundary layer response model parameters for a step change in input voltage from V =0 to 2.4 kV with the feedback sensor located at x_{fb} - x_k =300 mm	105
Figure 5.9	Phase averaged I/O data results for various values of the input voltage step size, V , with the feedback sensor at x_{fb} - x_k =300 mm. Provided are the a) voltage input, b) the upstream shear stress disturbance, and c) the downstream shear stress disturbance developments in time.	106
Figure 5.10	Parameters for the transfer function characterizing the dynamic response of the boundary layer to the plasma actuation: a) gain, b) time delay, and c) time constant with the feedback sensor at x_{fb} - x_k =300 mm. Note that the \circ -symbols represent the subset of useful voltages, while the \times -symbols represent non-useful plasma actuator voltages.	107
Figure 5.11	Feedback controller gain at various plasma actuator voltages, with the feedback sensor at x_{fb} - x_k =300 mm. The \circ -symbols represent the range of useful voltages, while the \times -symbols represent non-useful plasma actuator voltages. For the purposes of model development, all data points were used to determine the proper gain, because the time delay and time constant are independent of plasma voltage	114
Figure 5.12	Upstream and downstream wall shear stress disturbance for different roughness element heights, and downstream wall shear stress disturbance for different plasma actuator voltage amplitudes with the feedback sensor at x_{fb} - x_k =300 mm (noted by symbols). The broken cyan line shows the steady state downstream shear stress disturbance predicted based on multiplying the upstream shear stress disturbance with K_{τ} (see Equation 5.1). The magenta line is a least-squares straight line fit to the square symbols (see Equation 5.3)	117

Figure 6.1	Steady-state control results for the upstream (blue) and downstream (red) shear stress sensors at various roughness element heights, k , with U_{∞} =5.0 m/s and the feedback sensor located at x - x_k =300 mm.	123
Figure 6.2	Steady-state control results for the upstream (blue) and downstream (red) shear stress sensors at various freestream velocities, U_{∞} , with the feedback sensor located at x - x_k =300 mm. The roughness element height is varied from k =0 to a) k =1.0 mm and b) k =1.4 mm	123
Figure 6.3	Steady-state control results for the upstream (blue) and downstream (red) shear stress sensors at various roughness element heights and downstream shear stress sensor locations, with U_{∞} =5.0 m/s	125
Figure 6.4	Steady-state streamwise velocity disturbance contours for the a) upstream plane with $k=1.2$ mm, b) downstream plane with $k=1.2$ mm, c) downstream plane with $V=2.4$ kV, d) downstream plane with a superposition of the $k=1.2$ mm and $V=2.4$ kV disturbances, and e) downstream plane with control active with $k=1.2$ mm	126
Figure 6.5	Steady-state streamwise velocity disturbance contours for the down-stream plane with a superposition of the $k=1.2$ mm and $V=2.4$ kV disturbances with the plasma actuator plane shifted by -1 mm and multiplied by a gain of 0.52	129
Figure 6.6	Dynamic (unsteady) roughness element motion from $k=0$ to various deployment heights, k . Note that the gray bands demonstrate time periods when the roughness element is in motion, either upward or downward, for $k=1.4$ mm, and are provided on all subsequent unsteady control results plots for the appropriate k	132
Figure 6.7	Unsteady control results for the downstream shear stress at various roughness element heights with the feedback sensor located at x_{fb} - x_k =300 mm and U_{∞} =5.0 m/s. The settling time for each signal is noted with a \circ -marker	133
Figure 6.8	Unsteady control results for the downstream shear stress at various roughness element heights highlighting the transient effects during the upward motion of the roughness element; a zoomed in view of Figure 6.7. The settling time for each signal is noted with a \circ -marker.	135
Figure 6.9	Settling time for the controlled disturbance to reach 10% of the uncontrolled steady-state disturbance level, for various roughness element heights, with the feedback sensor located at x_{fb} - x_k =300 mm and U_{∞} =5.0 m/s	136

Figure 6.10	Uncontrolled unsteady disturbance development in time at x - x_k =305 mm, with a disturbance induced by a roughness element deployed from k =0 to 1.2 mm, with the feedback sensor located at x_{fb} - x_k =300 mm and drawn in the contours with a red line at (y, z) =(1.5, 2.5) mm. The top-plot provides the normalized velocity disturbance level versus time; five time instants are marked corresponding to the five disturbance contour results provided below	138
Figure 6.11	Controlled unsteady disturbance development in time at x - x_k =305 mm, with a disturbance induced by a roughness element deployed from k =0 to 1.2 mm, with the feedback sensor located at x_{fb} - x_k =300 mm and drawn in the contours with a red line at (y, z) =(1.5, 2.5) mm. The top-plot provides the normalized velocity disturbance level versus time; five time instants are marked corresponding to the five disturbance contour results provided below	139
Figure 6.12	Energy contained in the y - z planar disturbance for the uncontrolled, E , and controlled, $E_{\mathcal{C}}$, unsteady disturbance as it develops in time at x - x_k =305 mm in a) the entire y - z plane and b) in the $+z$ half plane only; with a disturbance induced by a roughness element deployed from k =0 to 1.2 mm, and the feedback sensor located at x_{fb} - x_k =300 mm	141
Figure 6.13	Unsteady control results for the downstream shear stress at various freestream velocities with the feedback sensor located at x_{fb} - x_k =300 mm and a fully deployed roughness element height of k =1.0 mm. The settling time for each signal is noted with a \circ -marker	143
Figure 6.14	Unsteady control results for the downstream shear stress at various freestream velocities with the feedback sensor located at x_{fb} - x_k =300 mm and a fully deployed roughness element height of k =1.4 mm. The settling time for each signal is noted with a \circ -marker	144
Figure 6.15	Unsteady control results for the downstream shear stress under feedforw only control (ff) , feedback-only control (fb) , and feedforward+feedback control $(ff+fb)$; with the feedback sensor located at x_{fb} - x_k =300 mm and a roughness element height of k =1.0 mm. The settling time for each signal is noted with a \circ -marker	ard-
Figure 6.16	Unsteady control results for the downstream shear stress under feedforw only control (ff) , feedback-only control (fb) , and feedforward+feedback control $(ff+fb)$; with the feedback sensor located at x_{fb} - x_k =300 mm and a roughness element height of k =1.2 mm. The settling time for each signal is noted with a \circ -marker	ard- 148

Figure 6.17	Unsteady control results for the downstream shear stress under feedforw only control (ff) , feedback-only control (fb) , and feedforward+feedback control $(ff+fb)$; with the feedback sensor located at x_{fb} - x_k =300 mm and a roughness element height of k =1.4 mm. The settling time for each signal is noted with a \circ -marker	ard- 149
Figure 6.18	Settling time for the controlled disturbance to reach 10% of the uncontrolled steady-state disturbance level, for various roughness element heights, under purely feedforward control (ff) , purely feedback control (fb) , and combined control $(ff+fb)$	150
Figure 6.19	Unsteady control results for the downstream shear stress with the feedback sensor at multiple downstream locations with a fully deployed roughness element height of $k=1.0$ mm. The settling time for each signal is noted with a \circ -marker	152
Figure 6.20	Unsteady control results for the downstream shear stress with the feedback sensor at multiple downstream locations with a fully deployed roughness element height of $k=1.2$ mm. The settling time for each signal is noted with a \circ -marker	153
Figure 6.21	Unsteady control results for the downstream shear stress with the feedback sensor at multiple downstream locations with a fully deployed roughness element height of $k=1.4$ mm. The settling time for each signal is noted with a \circ -marker	154
Figure 6.22	Settling time for the controlled disturbance to reach 10% of the uncontrolled steady-state disturbance level, for various roughness element heights, with the feedback sensor located at x_{fb} - x_k =200, 250, and 300 mm	155
Figure 6.23	Unsteady roughness element motion from $k=1.0$ to 1.2 mm with a) various steady-state hold times, t_h , resulting in b) a range of equivalent unsteady disturbance frequencies, $f_k=1/T_k$. Note that the gray bands demonstrate time periods when the roughness element is moving either up or down, with $t_h=2.0$ s ($f_k=0.25$ Hz), and are provided on all subsequent unsteady control results plots, for the applicable t_h or f_k	157

Figure 6.24	Unsteady roughness element motion from $k=1.0$ to 1.4 mm with a) various steady-state hold times, t_h , resulting in b) a range of equivalent unsteady disturbance frequencies, f_k . Note that the gray bands demonstrate time periods when the roughness element is moving either up or down, with $t_h=2.0$ s ($f_k=0.25$ Hz), and are provided on all subsequent unsteady control results plots, for the applicable t_h or f_k	159
Figure 6.25	Control results with the unsteady roughness element motion from $k=1.0$ to 1.2 mm with various steady-state hold times, t_h . The uncontrolled results are represented with thin lines, while the controlled disturbance are represented with thicker lines of the same color	160
Figure 6.26	Control results with the unsteady roughness element motion from $k{=}1.0$ to 1.4 mm with various steady-state hold times, t_h . The uncontrolled results are represented with thin lines, while the controlled disturbance are represented with thicker lines of the same color	161
Figure 6.27	Unsteady roughness element motion from $k=1.0$ to 1.2 mm with various frequencies, f_k : phase-average uncontrolled and controlled signals (left) and the corresponding FFT (right)	163
Figure 6.28	Unsteady roughness element motion from $k=1.0$ to 1.4 mm with various frequencies, f_k : phase-average uncontrolled and controlled signals (left) and the corresponding FFT (right)	164
Figure 6.29	Maximum, Mean, and RMS of the uncontrolled and controlled disturbance periods at various roughness-disturabnce frequencies for a,c,e) $k=1.0$ to 1.2 mm and b,d,f) $k=1.0$ to 1.4 mm. The maximum of the disturbance signal is noted with a hat , $\hat{\tau'}_d$, the mean is noted with an $overbar$, $\overline{\tau'}_d$, and the RMS is noted with a $tilde$, $\tilde{\tau'}_d$	166
Figure 6.30	The ratio of the controlled to the uncontrolled disturbance peak FFT values at various roughness element disturbance frequencies for a) $k=1.0$ to 1.2 mm and b) $k=1.0$ to 1.4 mm	167
Figure A.1	An example Simulink control model used in this study (note: all sub-blocks are provided below)	182
Figure A.2	Submodel: DSpace A/D (Input) and D/A (output) blocks to provide the input and output model voltage signals	183
Figure A.3	Submodel: Upstream shear stress sensor calibration, voltage to streamwise shear stress.	183

rigure A.4	streamwise shear stress	184
Figure A.5	Submodel: Conversion of the controller output, f , to voltage \dots	184
Figure A.6	Submodel: Limiting block to prevent plasma actuator voltage outside the <i>useable</i> range	184
Figure A.7	Submodel: Conversion of the limited plasma actuator voltage to downstream shear stress	185
Figure A.8	Submodel: Conversion of the integral controller output error to a voltage error for monitoring purposes	185
Figure A.9	Submodel: Freestream velocity hot wire calibration: voltage to streamwise velocity	185
Figure A.10	Submodel: Blasius shear stress correction, based on the streamwise location of the shear stress sensors and the difference between the measured freestream velocity during the I/O data collection, and measured freestream velocity at the time of the active control	186
Figure A.11	Submodel: Laser sensor calibration, voltage to roughness element height, k .	186

KEY TO SYMBOLS AND ABBREVIATIONS

Roman

- A Average of the peak positive and peak negative disturbance in a y-z plane, see Equation 3.7
- \mathcal{A} Fit coefficient, offset, for the linear fit between the plasma actuator voltage and measured feedback sensor disturbance shear stress, see Table 5.2, with the associated slope coefficient, \mathcal{B}
- a_k Roughness element actuation acceleration in the wall-normal direction
- \mathcal{B} Fit coefficient, slope, for the linear fit between the plasma actuator voltage and measured feedback sensor disturbance shear stress, see Table 5.2, with the associated offset coefficient, \mathcal{A}
- C_{V,f_w} Anti-windup controller relating the plasma actuator voltage, V, to the anti-windup control function contribution, f_w
- $C_{\tau'_d,f_{fb}}$ Feedback controller relating the downstream shear stress disturbance, τ'_d , to the feedback control contribution, f_{fb}
- $C_{\tau'_u,f_{ff}}$ Feedforward controller relating the upstream shear stress disturbance, τ'_u , to the feedforward control contribution, f_{ff}
- c Disturbance frequency
- D Roughness element diameter
- D_w Smoke-wire wire diameter
- E Disturbance energy per unit streamwise length, see Equation 3.5
- E_{-} Disturbance energy per unit streamwise length of the vortex-induced negative disturbance region, see Figure 3.13
- E_{+} Disturbance energy per unit streamwise length of the vortex-induced positive disturbance region, see Figure 3.13
- E_{rms} Disturbance energy per unit streamwise length calculated using $u'_{rms,z}$, see Equation 3.6
- E_w Disturbance energy per unit streamwise length of the negative wake disturbance region, see Figure 3.13

Disturbance energy density per unit streamwise length, see Equation 3.8 efController output parameter f_{fb} Feedback controller output parameter Feedforward controller output parameter f_{ff} f_k Frequency of the disturbance fluctuation, see §6.2.5 Anti-Windup controller output parameter f_w K_{fb} Feedback controller gain, see Table 5.3 K_{ff} Feedforward controller gain, see Table 5.3 K_t Anti-windup controller gain, see Table 5.3 K_V Plant model gain relating the plasma actuator voltage to the downstream shear stress disturbance, see Table 5.2 K_{τ} Plant model gain relating the upstream to downstream shear stress disturbance, see Table 5.1 kRoughness element height k_t Anti-windup tuning parameter Linear converter relating the controller output, f, to the plasma actuator voltage, V $L_{f,V}$ H_{12} Boundary layer shape factor NThe number of cycles used in phase averaging calculations Static pressure pPlant model relating the controller output, f, to the downstream shear stress disturbance, τ'_d Plant model relating the plasma actuator voltage, V, to the downstream shear stress disturbance, τ'_d Plant model relating the upstream shear stress disturbance, τ'_u , to the downstream shear stress disturbance, τ_d'

Reynolds number based on the roughness element height, see Equation 3.9

 Re_k

- $Re_{k,cr}$ Critical Reynolds number for roughness element transition, see Equation 3.4
- $Re_{k,\infty}$ Reynolds number based on k and U_{∞} , see Equation 3.10
- Re_x Reynolds number based on the streamwise location from the leading edge of the plate
- Re_{xv} Reynolds number based on the streamwise location from the virtual origin, see Equation 3.3
- Time, referenced to a point when the roughness element is flush with the flat plate; thus, t=0 indicates a point when k=0 and a Blasius boundary layer exists throughout the entire measurement domain. (The exception are the results of §6.2.5 where k=1.0 mm at t=0, and the disturbance is fluctuating quickly.)
- $t_{c,V}$ Time constant for the boundary layer response model relating V to τ'_d in the control experiments, see Table 5.2
- $t_{d,V}$ Time delay for the boundary layer response model relating V to τ'_d in the control experiments, see Table 5.2
- $t_{d,\tau}$ Time delay for the boundary layer response model relating τ'_u to τ'_d in the control experiments, see Table 5.1
- $t_{I,fb}$ Integral time constant for the feedback PI-controller, see Equation 5.14 and Table 5.3
- t_s Settling time, the time required for a controlled disturbance amplitude to reach, and maintain, an amplitude which is 10% or below the uncontrolled steady-sate disturbance amplitude; relative to the when the uncontrolled disturbance amplitude first reaches 10% of the uncontrolled disturbance amplitude.
- T_k Cycle period of the disturbance fluctuation, see §6.2.5
- U Basic flow streamwise velocity at steady state
- U_{∞} Streamwise freestream velocity
- u Streamwise velocity
- u' Streamwise disturbance velocity
- u_k Streamwise velocity at $x=x_k$ and y=k (in the absence of a roughness element)
- V Voltage supplied to the plasma actuator during the control experiments, in kilovolts

- \mathcal{V} Laplace form of the plasma actuator voltage, where the time-domain form is V(t)Wall-normal velocity vRoughness element actuation velocity in the wall-normal direction v_k Spanwise velocity wStreamwise coordinate \boldsymbol{x} x^* Streamwise coordinate scaled according to Equation 3.14 Streamwise location of the feedback shear stress sensor used in the control experi x_{fb} ments Streamwise location of the feedforward shear stress sensor used in the control exper x_{ff} iments Streamwise distance from the leading edge of the flat plate to the center of the x_k roughness element Virtual origin streamwise location, see Equation 3.1 x_v Wall-normal coordinate yWall-normal coordinate, characteristic length, see §3.4.1 y_c Spanwise coordinate zSpanwise coordinate, characteristic length, see §3.4.2 z_c GreekStreamwise wavenumber α β Wall-normal wavenumber
- Wall-normal wavenumber $\gamma \qquad \text{Spanwise wavenumber}$ Spanwise wavenumber $\delta \qquad \text{Blasius similarity length scale, see Equation 3.1}$ Blasius similarity length scale at $x{=}x_k$ (in the absence of a roughness element) $\delta^* \qquad \text{Displacement thickness}$ Boundary layer thickness (wall-normal distance from the wall to $u/U_\infty{=}0.99$)

- η Blasius wall-normal similarity coordinate, see Equation 3.1
- μ Dynamic viscosity of the air during measurement
- ν Kinematic viscosity of the air during measurement
- ρ Density of the air during measurement
- θ Boundary Layer momentum thickness
- τ_d' Disturbance shear stress measured by the downstream sensor in the control experiments without control
- $\tau'_{d,\mathcal{C}}$ Disturbance shear stress measured by the downstream sensor in the control experiments while the control is active
- τ'_u Disturbance shear stress measured by the upstream sensor in the control experiments without control
- $\tau'_{u,\mathcal{C}}$ Disturbance shear stress measured by the upstream sensor in the control experiments while the control is active
- τ_w Shear stress at the wall, see Equation 2.1
- $\mathcal{T}_d'(s)$ Laplace form of the downstream shear stress disturbance, where the time-domain form is $\tau_d'(t)$
- $\mathcal{T}'_u(s)$ Laplace form of the upstream shear stress disturbance, where the time-domain form is $\tau'_d(t)$

Chapter 1

Introduction

The effect of perturbation to a Blasius boundary layer and the resulting disturbed flow state has been the focus of many investigations related to boundary layer stability. By investigating the instability of the steady basic state flow to small perturbations, insight is gained regarding the physical parameters characterizing the flow (Reynolds number) and environmental disturbances influencing the boundary layer instability, with their critical values. Prevention, or delay, of flow instability and subsequent transition to turbulence offers a tractable target for drag reduction and consequent increase in the efficiency of moving fluid through engineering devices. The current study aims to provide high-resolution characterization of the steady, and unsteady, three-dimensional flow disturbance induced in a laminar boundary layer by an isolated roughness element, and to assess the effectiveness of controlling this disturbance in real time using reactive flow control.

The detailed characterization data allow examination of the spatial development of the disturbed flow field and the associated disturbance energy, with and without flow instabilities. The characterization of the roughness element induced disturbance is a precursor study toward a larger effort to actively sense and control 3D boundary layer disturbances in real-time, in the laboratory environment, which may then be applied to various real world applications where boundary layer transition reduces performance. Gaining a detailed understanding of the induced disturbance, and instability governing parameters, provides the groundwork for the subsequent control efforts.

The remainder of this Introduction will be provided in subsections to outline the background and direction of the current experimental efforts. In order to develop the governing equations for the current experimental analysis, the instability of the boundary layer to small disturbances is discussed in §1.1 with a brief explanation of linear stability theory and the classical path to turbulence. An alternative, the so called *bypass* transition, through transient growth is examined in §1.2 followed by an explanation of secondary instability, in §1.3, wherein the amplification of disturbances is considered relative to a base flow which includes the quasi three-dimensional distortion produced from transiently growing disturbances (known as *streaks*). Next, natural and artificial methods used to induce streak disturbances into the boundary layer are examined §1.4. Finally, §1.5 provides an overview of previous bypass transition control studies and presents the control objective of the present work.

1.1 Boundary Layer Instability

The governing equations for an incompressible, viscous flow of a Newtonian fluid; namely, the Navier-Stokes equations,

$$\nabla \cdot \mathbf{u} = 0, \tag{1.1a}$$

$$\left(\frac{\partial}{\partial t} + \mathbf{u} \cdot \nabla\right) \mathbf{u} = -\frac{1}{\rho} \nabla \mathbf{p} + \frac{\mu}{\rho} \nabla^2 \mathbf{u}, \tag{1.1b}$$

provide a framework by which to investigate the instability of boundary layer flow to initial disturbances; where $\mathbf{u}(x, y, z, t)$ represents the flow velocity vector, $\mathbf{p}(x, y, z, t)$ is the pressure, ρ is the density, and μ is the dynamic viscosity. According to linear stability theory, laminar boundary layer flow is unstable to exponentially growing disturbance waves, over a range of

Reynolds numbers and disturbance frequencies; as derived in the text by Drazin and Reid [17], among others. In this formulation, with the approximation of a parallel mean flow in the streamwise (x) direction, basic-state velocity variations in the wall-normal (y) direction only, represented by (U(y), V=W=0), the linearized, dimensionless governing equations become,

$$\frac{\partial u'}{\partial x} + \frac{\partial v'}{\partial y} + \frac{\partial w'}{\partial z} = 0, \tag{1.2a}$$

$$\left(\frac{\partial}{\partial t} + U \frac{\partial}{\partial x}\right) u' + \frac{\partial U}{\partial y} v' = -\frac{\partial p'}{\partial x} + \left[R^{-1} \left(\frac{\partial^2 u'}{\partial x^2} + \frac{\partial^2 (U + u')}{\partial y^2} + \frac{\partial^2 u'}{\partial z^2} \right) \right],$$
(1.2b)

$$\left(\frac{\partial}{\partial t} + U \frac{\partial}{\partial x}\right) v' = -\frac{\partial p'}{\partial y} + \left[R^{-1} \left(\frac{\partial^2 v'}{\partial x^2} + \frac{\partial^2 v'}{\partial y^2} + \frac{\partial^2 v'}{\partial z^2} \right) \right], \tag{1.2c}$$

$$\left(\frac{\partial}{\partial t} + U \frac{\partial}{\partial x}\right) w' = -\frac{\partial p'}{\partial z} + \left[R^{-1} \left(\frac{\partial^2 w'}{\partial x^2} + \frac{\partial^2 w'}{\partial y^2} + \frac{\partial^2 w'}{\partial z^2} \right) \right], \tag{1.2d}$$

and may be investigated; where $\mathbf{u}=(U(y)+u'(x,y,z,t),v'(x,y,z,t),w'(x,y,z,t))$, i.e. the basic flow with disturbance components, $R=UL/\nu$ is the Reynolds number, and L is a relevant length scale. Note that the bracketed, [], portions of Equations 1.2b-1.2d contain the viscous terms that may be neglected in the inviscid approximation. Also note that while the disturbance components are represented as unsteady terms, the basic flow is a steady, purely spatially varying flow [44]. In typical linear stability analysis, solutions for the disturbance quantities, (u',v',w',p'), are represented by Fourier, or normal, modes $(q'=\hat{q}(y)\exp[i((\alpha x+\gamma z)+\omega t)]$, where q' may be any velocity component or pressure disturbance, $\hat{q}(y)$ is the disturbance amplitude, γ and ω are real, and $\alpha=\alpha_r+i\alpha_i$) in Equations 1.2a-1.2d which allow analysis of the growth rate of the disturbance amplitudes for different frequencies and wavenumbers [17]. The flow is considered stable if solutions to the Navier-Stokes equations, q', which grow in space are not found. This growth is therefore indicated by the real portion of the solution(s); which take the form $q'=\hat{q}(y)\exp[-\alpha_i x]$, where $\alpha_i>0$

indicates a decaying disturbance mode, and α_i <0 indicates an amplifying (unstable) mode. The least stable exponentially growing mode, called the Tollmien-Schlichting (T-S) wave, can experience secondary instability which leads to transition to turbulence; this is the classical path to instability.

1.2 Transient Growth

Transient growth, also known as algebraic growth, is an inviscid mechanism that offers a path to turbulence alternative to the classical T-S wave amplification, and thus may lead to what is known as *bypass* transition; which could result in transition occurring at subcritical Reynolds number. The fundamental mechanism leading to transient growth is the interaction of the disturbance velocity with the basic flow velocity gradient, which is captured in Equations 1.2b-1.2d. Notably, the inviscid form of Equation 1.2b,

$$\left(\frac{\partial}{\partial t} + U \frac{\partial}{\partial x}\right) u' + \frac{\partial U}{\partial y} v' = -\frac{\partial p'}{\partial x},\tag{1.3}$$

highlights how the streamwise-velocity gradient in the wall normal direction, $\partial U/\partial y$, coupled with the wall-normal disturbance velocity, v', can influence the development of u' in x and t. Through this term, it is possible for v' to influence the base flow in a process Landahl [33] identified as the *lift-up* effect, which can lead to spanwise u' inhomogeneities of high-and low-speed fluid in the boundary layer. These streamwise elongated, alternating high-and low-speed regions within the boundary layer are referred to as "Klebanoff modes" by Kendall [31], wherein they were produced with grid-generated freestream turbulence, and are what is now commonly referred to as *streaks*. Streak disturbances are generally believed to be associated with streamwise vorticity, which transfers high speed fluid toward the wall

and low speed fluid away from the wall. The instability of the resulting streaky structures (referred to as *secondary instability* to differentiate it from the instability of the boundary layer without streaks) may dictate transition to turbulence if sufficient disturbance amplitude is achieved through transient growth before viscous decay becomes dominant.

A more concise representation of Equations 1.2a-1.2d, as found for example in Butler and Farrell [13], may be obtained by taking the linearized, relative to a parallel basic flow (U = U(y), V=W=0), Navier-Stokes equations, and applying the ∇^2 operator to the y-momentum, $\nabla \times ($) to the full set of Navier-Stokes equations, and manipulating the result. This leads to the wall normal disturbance velocity and vorticity formulation, or the Orr-Sommerfeld/Squire equations, for 3D disturbances in a parallel base flow,

$$\left(\frac{\partial}{\partial t} + U \frac{\partial}{\partial x}\right) \Delta v' - \frac{\partial^2 U}{\partial y^2} \frac{\partial v'}{\partial x} - \frac{1}{R} \Delta \Delta v' = 0,$$
(1.4a)

$$\left(\frac{\partial}{\partial t} + U \frac{\partial}{\partial x}\right) \omega_y' - \frac{1}{R} \Delta \omega_y' = \frac{\partial U}{\partial y} \frac{\partial v'}{\partial z}, \tag{1.4b}$$

which demonstrate a "forcing term", v', to the wall-normal vorticity, ω'_y as described by Naguib et~al.~ [40]. In Equation 1.4b, the wall-normal disturbance, v', moves fluid across the mean velocity gradient, $\partial U/\partial y$, and high-speed fluid is moved toward the wall while low speed fluid is moved away from the wall. This 3D fluid motion creates spanwise variation, $\partial u'/\partial z$ at a given y, which gives rise to wall-normal vorticity (since $\omega'_y = \partial u'/\partial z - \partial w'/\partial x$); as is described by Naguib et~al.~ [40], and more clearly demonstrates the mechanism that generates spanwise disturbance non-uniformities (streaks).

Mathematically speaking, transient growth occurs due to non-orthogonality of the eigenfunctions of the non-self-adjoint Orr-Sommerfeld/Squire operator governing the linear growth of 3D disturbances in a laminar boundary layer (with parallel basic-flow approximation), as

described by Butler and Farrell [13]. The implication of the non-orthogonal solutions to the non-self-adjoint Orr-Sommerfeld/Squire equations is that the disturbance modes may initially destructively interfere, resulting in potentially large (transient) growth, even though individually each of the modes is decaying.

1.3 Secondary Instability

The imposition of spanwise variations (streaks) on the initial Blasius boundary layer establishes a new basic flow, U = U(y, z), modifying the inviscid relationship of Equation 1.3,

$$\left(\frac{\partial}{\partial t} + U \frac{\partial}{\partial x}\right) u' + \frac{\partial U}{\partial y} v' + \frac{\partial U}{\partial z} w' = -\frac{\partial p'}{\partial x},\tag{1.5}$$

as demonstrated by Andersson et al. [2]; which includes an additional term relative to Equation 1.3, specifically, $\partial U/\partial z$. When evaluating the instability of this modified basic state (the secondary instability of the Blasius basis state), normal-mode, linear stability theory analysis allows examination of the disturbance amplification or decay. Andersson et al. [2] conducted those analyses and found that streak amplitudes >26% may excite an inviscid inflectional-type instability whereas disturbance amplitudes <26% are stable to this instability. Andersson used streak disturbances with maximum transient growth rate (i.e. optimal), in order to evaluate the influence of the disturbance growth on secondary instability. This is a significant distinction of the 2D basic state boundary layer flow, U(y, z), from the 1D basic state, U(y), in that the disturbance (streak) size and shape are of importance to inflectional instability analysis.

1.4 Streak Disturbance Generation in Experiments

Studies in which spanwise non-uniformity of the boundary layer thickness is observed, an indication of streak formation, see for example Matsubara and Alfredsson [39] or Mandal et al. [38], may involve heightened levels of freestream turbulence intensity, which constitutes the natural generation of transient growth within the boundary layer. Investigations by Bertolotti [8] and Zaki and Durbin [55] have investigated the processes that allow freestream turbulence to penetrate the boundary layer and form streamwise elongated disturbance regions, i.e. receptivity. Wall-normal rms velocity profiles of these random disturbances exhibit a similar peak location as that found in analytical investigations of optimal streamwise vortices introduced into the boundary layer [2]; thus, bypass transition, generated though natural mechanisms (i.e. freestream turbulence) is related to optimal steady streak analysis, and the linear inviscid stability analysis of Andersson et al. [2] is applicable to naturally occurring boundary layer streaks. These analyses have aided the understanding of randomly distributed streaks in the boundary layer, generated by freestream turbulence and a comprehensive review of these mechanics is provided by Zaki [56].

In the laboratory, it is advantageous to induce streak distances within the boundary layer in a controlled manner, with known strength and shape characteristics, as well as at prescribed locations. There are several explored methods for artificially introducing these disturbances, such as, suction/blowing [36], wall imbedded speakers [4], wing tip vortices, [10], discrete wall-bumps [21], and discrete wall-mounted roughness elements [6], [18], [54], [43]; among others. In the case of the roughness element, streamwise elongated regions of positive or negative flow disturbance are introduced to the boundary layer flow using an array of cylindrical roughness elements deployed along the span at a given streamwise

location, as described by, for example, Bakchinov et al. [6] or Ergin and White [18]. Also described in these, and other investigations is that these types of streak disturbances have been associated with transient growth, and thus, bypass transition. In the work of von Doenhoff and Braslow [51] the roughness element array is considered as isolated roughness elements when the spanwise spacing of the roughness elements relative to their diameter, $\Delta z/D \geqslant 3$; thus the roughness element array analyses of Ergin and White [18] should be directly applicable to the isolated roughness scenario.

Roughness element arrays have been the focus of substantial research efforts, for example, Klebanoff et al. [30], Ergin and White [18], White et al. [54], and Rizzetta and Visbal [43], which have investigated the disturbance strength, shape, and location in addition to the disturbance energy and associated scaling of the disturbance energy of individual Fourier spanwise modes. Investigations of the truly isolated roughness element induced disturbance are carried out in the present study. The isolated roughness element arrangement requires special considerations due to the lack of a spanwise length scale which are explained and developed in detail. This is in contrast to a roughness element array configuration, which provides a built-in spanwise length scale; specifically, the roughness spacing. Furthermore, downstream interaction of adjacent streak disturbances is avoided in the isolated roughness element configuration and provides new information about the disturbance amplitude, size, shape, and energy growth/decay. The review of vonDoenhoff and Braslow [51] found that roughness element geometries such as cylinders, spheres, etc. demonstrate similar critical transition criteria and thus the induced disturbance is the focus of the present investigation, rather than the specific importance of the roughness element geometry. It is important to note here that the interest in studying the isolated-streak disturbance is significant as a simplified canonical problem of the initiation of bypass transition beneath a turbulent freestream. The isolated-roughness problem is a technically significant problem in its own right as otherwise hydrodynamically smooth surfaces may have intentional local protrusions (e.g. a fastener head), or unintentional ones due to localized debris accumulation. Furthermore, the current study investigates the development of these isolated roughness element induced streaks as the roughness element is raised and lowered under a range of motion parameters. This *unsteady* streak disturbance generation and spatio-temporal disturbance development investigation is, to the author's knowledge, the first of its kind.

1.5 Control of Transient Growth

As described above, bypass transition is initiated by transient growth, which is associated with a region of streamwise development of the disturbances (streaks) before secondary instability occurs. Thus, active sensing and control within this growth region could allow the delay or prevention of bypass transition and turbulence. Experimental demonstrations of streak disturbance control are rare. Jacobson and Reynolds [27] conducted an experimental demonstration of steady-state streak disturbance control in a laminar boundary layer using oscillating cantilever-beam synthetic jets, which introduced a pair of counter-rotating vortices, opposite in sign to that generated by an upstream cylindrical element (that protruded outside the boundary layer), which generated a pair of counter-rotating vortices upstream to be targeted for amplitude reduction. In addition, an ad-hoc linear controller was used to target dynamic disturbances that were introduced using suction and the results demonstrated these disturbances could be reduced in magnitude. In one of the more successful studies, Lundell [36] used suction/blowing at the wall, coupled with wall-shear-stress sensing and feedforward control, to delay flow instability of streaks induced by heightened levels

of freestream turbulence. While an instructive demonstration of successful bypass boundary layer transition delay, Lundell tuned the level of flow control manually. This leads to the focus of the current control efforts which aim to prevent, or delay, streak disturbance instability and boundary layer breakdown to turbulence, through the development and implementation of a model-based feedforward and feedback control system to actively sense streaks and apply appropriate flow forcing, to weaken or eliminate these streaks.

Belson et al. [7] numerically investigated the optimal placement of sensors, relative to an actuator, when used for feedforward or feedback control of T-S wave disturbances. Belson found that feedforward sensors are most effective; and are fairly independent of their placement relative to the actuator. However, Belson also shows that feedforward sensors are insufficient to account for un-modeled variations (i.e. disturbances other than those of the form which are specifically targeted, or those originating downstream of the feedforward sensor), a reality in experimental implementations. Furthermore, Belson found that feedback sensors achieve better response when placed closer to the actuator, and outperform feedforward sensors in the presence of un-modeled disturbances. The present study will show that a similar sensor placement investigation for bypass transition would be beneficial. Naguib et al. [40] investigated the use of coarsely spaced sensors and demonstrated that in the streamwise elongated disturbance environment (streaky boundary layer), the streamwise wall-shear disturbance allows for the coarsest required sampling, reaching one sensor per twice the mean-spanwise-streak-width.

Following the work of Jacobson and Reynolds [27] and Lundell [36], Lundell, Monokrousos, and Brandt [37] numerically demonstrated the benefit of system identification in improved controller implementation over the *ad-hoc* methods previously implemented. Furthermore, Lundell, Monokrousos, and Brandt [37] highlighted the difficulty associated with current

actuators (e.g. suction) and suggested that available actuator technology is a significant limitation in boundary layer control efforts. (A comprehensive review of actuators for flow control is provided by Cattafesta and Sheplak [14].) Toward resolving this limitation and the implementation of streak control, Hanson et al. [23] and Hanson [25], demonstrated that plasma actuator arrays could be used to effectively reduce the energy contained within targeted modes of spanwise periodic streak disturbances generated using a static array of roughness elements. Furthermore, Hanson [25] and Hanson et al. [26]¹ provide an experimental demonstration of feedback control using a proportional-integral (PI) controller which actively senses and controls steady and slowly-varying streak disturbances; targeting the fundamental mode (having a spanwise wavenumber based on the roughness element spacing) disturbance for reduction. The targeted mode disturbance energy is shown to be reduced by 94% at the feedback sensor location in [26].

The current control efforts build upon the steady/slowly varying disturbance control of Hanson et al. [26]¹, by inducing the streak disturbances with an unsteady (and isolated) roughness element. Specifically, in the present work, the control effort targets disturbances that vary over a time scale comparable to the convective time scale over the extent of the control domain. In addition, feedforward and feedback, rather than feedback only, controllers are employed and disturbance input/shear stress disturbance output (I/O) data are used; the resulting (simple) boundary layer model parameters (gains, time delays, and time constants) are used to tune the controller parameters. The resulting control model is used to control streak disturbances, and is the first demonstration of real-time, feedforward-feedback control of streak disturbances.

¹Kyle Bade is a co-author on this study; the work was performed as part of the broader effort toward the completion of this dissertation; however, the details are not presented or discussed in detail herein, making way for the unsteady control results.

Chapter 2

Experimental Setup

2.1 Wind Tunnel Setup

The experiments were carried out in a suction-type wind tunnel with a detached blower section, eliminating any vibration from the blower. The coordinate system, as seen in Figure 2.1, is oriented such that x is the streamwise direction, y is the wall-normal direction, and z is the spanwise direction. The test section was 3.00 m long with a 0.355 m square crosssection. The test section was outfitted with three, 0.90 m long plexiglass walls at z=-0.18 m, which were hinged to allow access inside the tunnel as well as to provide optical access during testing. The roof of the tunnel had a 1 m by 10 mm slot which allowed probes connected to a traverse, mounted outside of the tunnel, to travel in the x and y directions; z-axis movement was achieved with a traverse stage located inside the tunnel and encased in an airfoil. The slotted top-side opening used compressible foam to seal the gap as the traverse moved in x. Upstream of the test section was a series of flow conditioning screens and flow straightening elements followed by an 10.8:1 contraction. The tunnel was capable of achieving flow speeds greater than 35 m/s; for the current experiments, the velocities varied from 4-6 m/s with an associated turbulence intensity level (based on the streamwise velocity fluctuation) less than 0.05% which is typical of low turbulence wind tunnels.

2.2 Flat Plate Setup

A flat plate positioned in the test section, with the leading edge 1.6 m downstream of the tunnel contraction exit, was used to generate a Blasius boundary layer, identified here as the basic state flow. The plate was made from 12.7 mm thick, 0.635 m long plexiglass which was fitted with a 63 mm long aluminum sharp leading edge and a 150 mm long aluminum trailing edge flap. The sharp leading edge, machined at 15°, provided a well defined and uniform streamwise boundary layer initiation location. A trailing edge flap was used to control the stagnation location of the incoming flow on the plate, ensuring a top-side stagnation line [44]. The plate was located between 1/3 and 1/4 of the test section height in order to minimize effects from contraction induced secondary flows, as recommended in [44]. The plate was mounted to the wind tunnel floor and given a slight angle to achieve a zero-pressure gradient boundary layer over -25 $\leq x$ - $x_k \leq$ 350 mm; where x_k is the streamwise distance from the leading edge to the roughness element, $x_k=150$ mm in the current setup. Figure 2.1 provides a schematic of the flat plate orientation with important features, components, and dimensions including the four hot wire probes used for data acquisition (described in detail in $\S 2.4$).

2.3 Roughness Element Setup

The roughness element used for the majority of this study was a Teflon cylinder of diameter, D=5mm. The roughness element was attached to a feedback controlled piezo-electric Squiggle[®] motor located below the plate that was used to control the roughness element deployment height above the plate surface, k. More importantly, the motor enabled retraction or deployment of the roughness element during measurements, which was necessary for

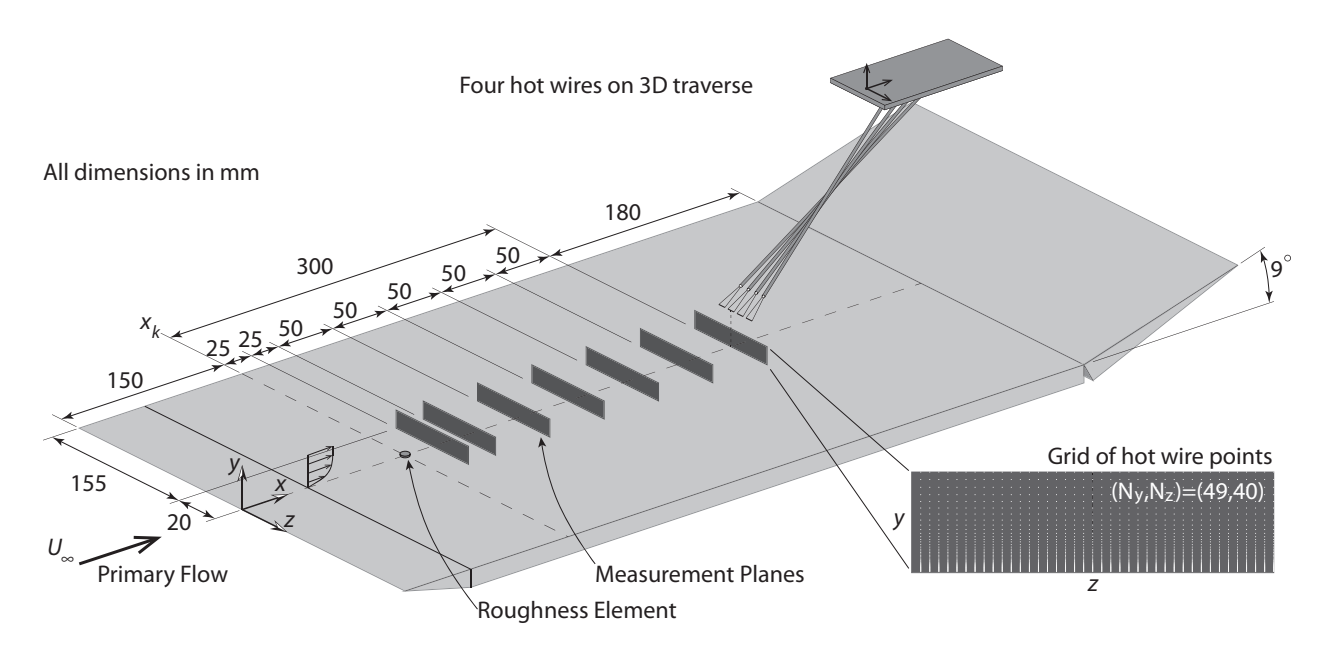


Figure 2.1: Flat plate geometry, with 4-single-wire hot wire assembly, seven y-z measurement planes, and a representative y-z measurement grid. The seven hot wire measurement planes, covering the range of $25 \leqslant x$ - $x_k \leqslant 300$, are shown to-scale to give perspective of the data collection domain, but these planes are non-physical and do not represent any physical structure.

accurate determination of the location of the hot wire probes above the wall, see §2.4. The roughness element height range was $0 \le k \le 6$ mm, to within ± 0.002 mm which was made possible with the use of a magnetic strip for position feedback. Due to the small output force from the piezoelectric motor, a teflon roughness element was used to minimize friction along the inside wall of the plate. Seven roughness element heights were used, ranging from 0.5 to 2.0 mm; specifically, k=0.5, 1.0, 1.29, 1.4, 1.51, 1.6, and 2.0 mm, in addition to k=0 mm, which was used to establish and verify the basic flow. The k=1.29 mm height was selected in order to directly compare the results with previous experiments by Lavoie et al. [34] using a spanwise periodic roughness array. The k=1.51 mm height was selected after preliminary measurements indicated that the boundary layer experienced intermittent turbulent bursts¹ at this value of k with $U_{\infty} = 5.0$ m/s and D=5.0 mm. A limited set of

¹as determined from a hot wire signal observed on an oscilloscope, with the hot wire positioned down-stream of the roughness element and within the boundary layer

tests were also conducted with a teflon cylinder of a smaller diameter, D=3.175 mm, to investigate the roughness element diameter effect on the flow disturbance characteristics. Table 2.1 provides a summary list of the test case conditions investigated in this experimental effort. The U_{∞} values were measured with a variability of $\leq 2.0\%$, which corresponds to freestream velocity variations of ± 0.3 m/s. This variation was primarily due to day-to-day blower operating condition, and very small pre/post hot wire calibration drift; note that for the majority of tests this variation from the nominal setting (i.e. 4.0, 5.0, or 6.0 m/s) was $\leq 1.0\%$. The error in the roughness element height position, k, was $\leq 0.4\%$ according to manufacturer specifications, which was verified with a laser sensor (see next paragraph). Thus, the variability/error in $Re_k = U_k k/\nu$ & $Re_{k\infty} = U_{\infty} k/\nu$ values is less than $\pm 2.4\%$. Finally, case 9 provides a repeat of case 2 for checking measurement repeatability.

The Squiggle motor, used to actuate the roughness element, is capable of using a prescribed velocity and acceleration to reach the desired position. This was checked using a laser position sensor (model: Baumer OADM 12U6450/S35A) with a measuring distance of 16-26 mm from the laser head and resolution of 0.002-0.005 mm. The sensor's output is 0-10 V which is linear over the 16-26 mm measurement range. This output was also acquired during all hot wire testing in order to verify the roughness element motion. Figure 2.2 provides a schematic of the implementation of the Squiggle motor and laser sensor setup in the vicinity of the roughness element.

Preliminary testing was conducted in order to ensure that the roughness element actuation dynamics did not excite instabilities in the flow, while allowing for the roughness element to be deployed as quickly as possible to reduce the actuation time to reach a steady state. All tests were run under the conditions: $v_k = 7.5 \text{ mm/s}$ and $a_k = 1000 \text{ mm/s}^2$, where v_k and a_k are the roughness element maximum velocity and acceleration in the wall-normal

Case	Symbol	D	k	U_{∞}	Re_k	$Re_{k\infty}$	$\delta(x_k)$
(TC)		(mm)	(mm)	(m/s)			(mm)
1		5.0	0.5	5.0	35	159	0.76
2		5.0	1.0	5.0	142	325	0.74
3		5.0	1.29	5.0	242	417	0.74
4		5.0	1.4	5.0	276	454	0.77
5		5.0	1.51	5.0	340	499	0.74
6		5.0	1.6	5.0	382	522	0.73
7		5.0	2.0	5.0	575	649	0.75
8		5.0	1.0	4.0	104	260	0.84
9(2)		5.0	1.0	5.0	149	324	0.75
10		5.0	1.0	6.0	187	379	0.67
11		5.0	1.29	4.0	175	337	0.82
12		5.0	1.6	4.0	272	420	0.82
13		5.0	0.5	6.0	59	209	0.65
14	-0	3.175	1.0	5.0	133	328	0.82
15	-0	3.175	1.29	5.0	219	425	0.83
16	-0	3.175	1.51	5.0	310	496	0.81
17	-∆	3.175	1.0	6.0	182	373	0.68

Table 2.1: Summary of test case parameters. Note that the symbol shape represents the freestream velocity: 4 m/s (\neg , downward triangle) 5 m/s (\neg , circle) and 6 m/s (\triangle , upward triangle), the symbol/line color represents the roughness height, and the line style (solid/dashed) is used for representing the roughness element diameter.

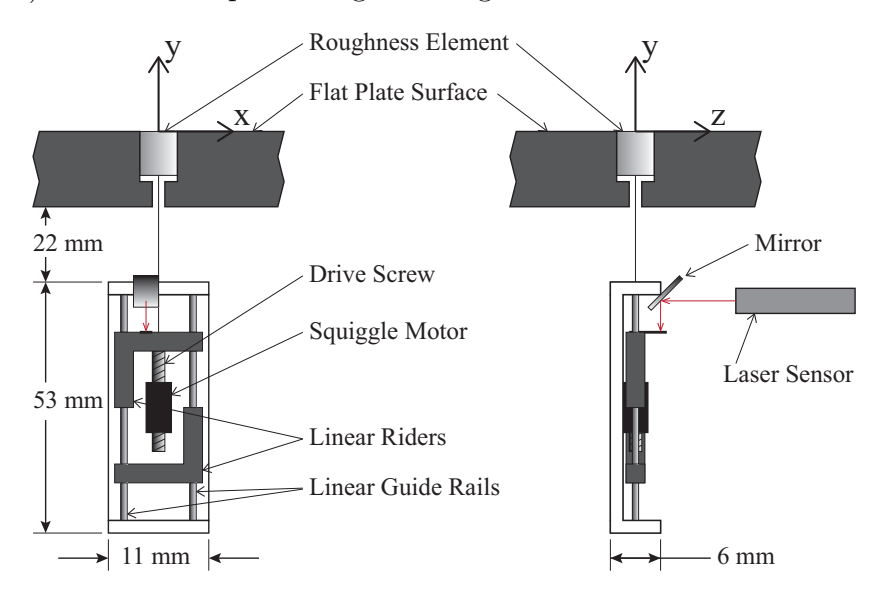


Figure 2.2: Schematic of the Squiggle motor and laser sensor arrangement in the (left) x-y plane (laser not shown, for clarity) and the (right) y-z plane, with relevant mechanical pieces used to ensure accurate and repeatable roughness element actuation.

direction, respectively.

2.4 Hot Wire Setup

The primary method of data acquisition was an array of four single-wire hot wire probes that were used to measure the streamwise velocity². The hot wire probes and sensors were manufactured in-house. The probe bodies were constructed from 3.175 mm outer diameter stainless steel tube of various lengths (0.18, 0.21, 0.24, and 0.27 m) to allow the probes to be oriented over a range of angles relative to the flat plate; as demonstrated in Figure 2.1. This arrangement was devised to avoid a major blockage at any streamwise location and to mitigate any collective "ramp" effect while using four hot wire probes in close proximity; thus, each probe was supported at a slightly different streamwise location and set to a different angle. The Blasius nature of the base flow was measured with a single probe installed, and checked after all four probes were installed, there was no change in the base flow at the probe sensor location. Additionally, each probe body was mounted to a small high-precision z-axis stage to allow for manual adjustment of the probe-to-probe spacing, or sensor-tosensor centers, which was set to 5 mm along z while keeping all sensors at the same x and y location. An overhead 3-axis traverse was used to position the four-hot-wire-probe array within the wind tunnel, as described in §2.1. Jewelers broaches were used as sensor supports (tapered diameter 0.015-0.005") and positioned the hot wire sensors approximately 25 mm upstream from the probe body. The probe supports were set to diverge from 1 mm spacing at the probe body, to fit inside the probe tube, to 3 mm spacing at the sensor location, allowing for a 1mm copper plated tungsten non-active length on either side of the 1 mm

²Strictly speaking, the measured velocity is representative of the magnitude of the streamwise and wall-normal velocity, $\sqrt{u^2 + v^2}$.

exposed tungsten sensor.

Figure 2.1 demonstrates the seven streamwise planes covering $25 \leqslant x \cdot x_k \leqslant 300$ mm, where $x_k = 150$ mm. The wall-normal spacing between measurement points was non-uniform, with smaller increments occurring in the near wall region to better resolve the larger velocity gradient in this region, and extending well outside the boundary layer region. Measurements were acquired at $-19 \leqslant z \leqslant 20$ mm from the center of the roughness element spanwise location, which is used to define the origin of the spanwise coordinate, z=0. This resulted in each of the seven y-z measurement planes including 1960 points/plane (49 in y and 40 in z) and required 8 hours to complete a single y-z measurement plane; the measurement time was the primary motivating factor to use four simultaneous hot wires.

The hot wire data acquisition setup utilized a Texas Instruments BNC-2012 board and DAQ-6061 analog-to-digital card (12-bit resolution and maximum sampling frequency of 500/8 kHz/differential channel) connected to a Windows PC. Custom matlab code was used to acquire the DAQ-board signals as well as to automate the point-to-point test matrix acquisition procedure. TSI 1054 A/B constant temperature anemometers were used to operate the four 5 μm diameter hot wires with an overheat ratio of 1.5; all hot wires had a cold resistance between 3-4 Ω . A thermocouple temperature sensor was placed within the wind tunnel, just downstream of the flat plate, in order to monitor and compensate for laboratory (reference) temperature changes over the data acquisition period (8 hours). Typical procedures, as outlined by Lemonis and Dracos [35], were used for this compensation; note that the lab temperature during all tests was $21\pm3^{\circ}$ C. The hot wire calibrations were performed in the freestream of the wind tunnel flow, above the plate. A pitot tube was also positioned in the freestream at approximately (x, y, z)=(260, 60, 130) mm, to provide a known freestream velocity in the zero-pressure gradient flow over the flat plate. Time-series acquisitions were

used to collect the output voltage from each of the four hot wires at twelve freestream velocities ranging from $1.0 \le U_{\infty} \le 6.0$ m/s. King's Law was used to fit the calibration data and find the fit coefficients for each wire; calibration curves matched with the calibration data points to within $\pm 1\%$ for all tests. Pre- and post-calibration curves agreed well and the data were discarded if the disagreement was greater than 2% at any velocity within the targeted measurement range; disagreements of much less than 2% were typical.

At each discrete measurement location, a 50 s time series was acquired at 10 kHz, which allowed for 25 cycles of undisturbed/disturbed flow states with a 2 s roughness element actuation cycle period (at 50% duty cycle). The use of an actuating roughness element allowed for steady-state undisturbed (roughness element withdrawn) and disturbed (roughness element deployed) flows to be measured in a single time series. In post-processing, the 25 cycles were phase-averaged relative to the position sensor (laser) signal to arrive at mean steady state disturbed and undisturbed results. Figure 2.3 provides a representative time series showing two cycles from the laser position sensor and a hot wire located within the positive disturbance region; the portions of the time series which were used as the *steady-state* undisturbed and disturbed velocities are highlighted.

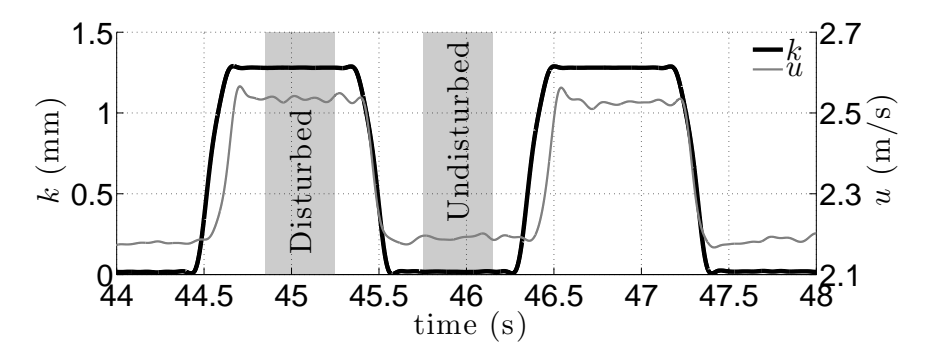


Figure 2.3: The hot wire velocity signal and laser roughness element height signal during two actuation cycles of the roughness element with the hot wire located at $(x-x_k, y, z) = (150, 2, -3)$ mm with the following conditions: $(k, D, U_{\infty})=(1.29 \text{ mm}, 5.0 \text{ mm}, 5.0 \text{ m/s})$

The process used to determine the wall-normal location of each hot wire was implemented

in post-processing of the data. The hot wire array was manually positioned "very near" the flat plate wall before acquisition began. The data acquisition was started and a 50 s time series was recorded at each of 1960 measurement locations as demonstrated by the hot wire grid shown in Figure 2.1. The probes were first traversed in the y direction, acquiring data at all 49 wall-normal grid points. After the completion of each y-profile acquisition, the probes were moved to the next z grid point and brought to the same y-location near the wall where the previous y-profile acquisition started. The result was a well-defined rectangular grid of measurement points on top of the flat plate. In post-processing, the dynamic time series were phase averaged relative to the measured position of the roughness element (voltage signal from the laser position sensor), removing any truncated actuation cycles at the beginning or end of each time series. The undisturbed-flow velocity profiles were generated by taking an average of the steady-state velocity after roughness element retraction at each wall-normal location. In a similar manner, the disturbed-flow velocity profiles were generated from steady-state data after deployment of the roughness element.

To determine the y location of the measurements relative to the wall, a least-squares linear fit of the y-profile data was performed over the range of the undisturbed (Blasius) velocity profile that is a linear function of y. Specifically, the range used to for the linear fit was $0.25 \le u/U_{\infty} \le 0.35$, which provides a linear approximation to within 0.025% on average, and a maximum point-wise error of 0.066% with the Blasius profile solution; these error estimates were determined using a least-squares fit of a linear profile to the points following the Blasius solution over this range, with the Blasius profile point-resolution equal to the measurement point spacing. The resulting fit is extrapolated to find the y location at which the velocity is zero (i.e. the no-slip condition), which is then used to define the origin for y. Because the measurement grid is known to be rectangular, a linear fit is performed on the

wall-find locations for each of the 40 z-location profiles and any non-linear deviation is error in the wall-find calculation; any misalignment of the z-axis traverse and flat plate will result in a constant slope offset. This process serves to smooth any small errors in the wall-find results.

Using the dynamic (actuated) roughness element setup, the difference between disturbed and undisturbed flows is calculated, and provides a direct velocity disturbance measurement which is not subject to deficiencies found in other methods. One common practice is to use the Blasius profile as the undisturbed state [30] which is a reasonable method once this basic state is verified, but small deviations or alterations are not captured or taken into account. Furthermore, investigations that use a direct subtraction of the Blasius profile to find the disturbed flow state are subject to errors generated by inaccurate wall-find calculations performed using the disturbed profile. Alternatively, using a spanwise average of the disturbed flow [53] results in a profile that can be checked versus the undisturbed basic state. However, the profiles rely upon the wall-find procedure of fitting the linear region of the velocity profile to determine the wall-normal location of the hot wire at each spanwise location. This process is subject to wall-find errors, which can become amplified in strong wall-normal velocity gradients as well as regions with strong disturbances that no longer guarantee a linear velocity profile. In either case these errors can present themselves randomly or as systematically in the magnitude and shape of the disturbance strength distribution. Inaccurate wall-finds using disturbed flow profiles downstream of a roughness element have been observed during the present measurements and have been documented by White and Ergin [53]. Thus, by using the dynamic roughness element, the current results contain the undisturbed and disturbed flow state at the exact same location with no dependency on wall-find accuracy resulting in an accurate flow disturbance calculation. The wall-find calculations are performed on the undisturbed velocity profile, and any errors will manifest in a wall-normal shift of the disturbance location rather than a disturbance intensity error.

2.5 Flow Visualization Setup

Smoke-wire flow visualization of the roughness element induced disturbances was conducted using a LaVision PIV system. The flat plate surface was covered with a 0.1 mm thick flat-black smooth, nylon layer. The nylon was chosen due to the light absorbent flat black color, very small thickness, and ability to be removed easily after the flow visualization experiments were completed, without any alteration or damage to the overall setup. Figure 2.4 provides a schematic of the flow visualization setup over the flat plate, depicting the laser, camera, and mirror.

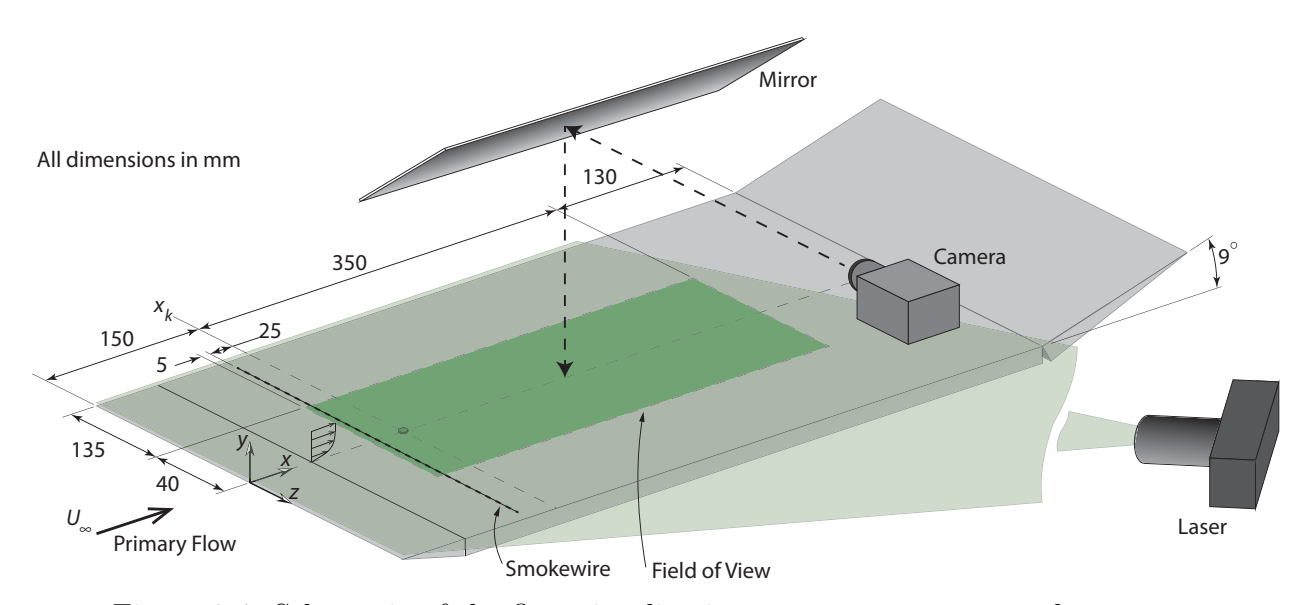


Figure 2.4: Schematic of the flow visualization setup components and geometry

The smoke-wire was stretched along the z axis and placed near the plate by attaching it to an aluminum U-shaped holder with the open end pointing towards the plate. The ends of the "U" included threaded standoffs to adjust the plate-to-smoke-wire wall-normal distance. The smoke-wire consisted of a twisted pair of 304 stainless steel wires with diameter D_w =0.1 mm. The twisted wires provided preferential oil (Bachmann Model Train Smoke Fluid) collection locations that, when subjected to a cross flow, resulted in longer (in time) smoke initiation points; furthermore, the point-to-point spacing was achieved at a regular interval. In this twisted arrangement, smoke is generated for approximately 1-3 seconds rather than less than 1 second with a single wire. In preliminary tests, twisting three wires resulted in a noticeable difference in the downstream flow character; no noticeable difference was observed with one or two wires³. The smoke-wire was isolated from the support with teflon spacers and was heated using a DC voltage of 15-25 V; the exact voltage was iteratively determined so that the smoke-wire would burn the oil consistently but as slowly as possible. The location of the smoke-wire in x and y was determined from tests at various locations including up and downstream of the roughness element and various wall-normal locations. The location that appeared to capture the induced disturbance most clearly was found to be 25 mm upstream of the roughness element and 2 mm from the wall, or $(x-x_k, y) = (-25, 2)$ mm, these results are provided in Figure 3.4. Note that Figure 3.6 provides a smoke-wire result where the wire and laser were positioned 1 mm closer to the wall which better captured some of the more complex flow structures, as detailed in §3.2.2.

In preliminary experiments, it was found that a very short exposure time was required to *freeze* the smoke for non-blurred, instantaneous visualization. The use of a standard PIV system accomplished this by providing a very short, 5 ns, laser pulse during which the camera shutter was open; while still providing adequate light intensity to the CCD camera.

³With the smoke-wire at a location within the boundary layer with $U(y) \approx 2$ m/s, the Reynolds numbers based on the smoke-wire diameter is 13.4, 26.8, and 40.2 for one, two, and three diameters, respectively; where the critical Reynolds number based on a cylinder diameter is 40. Although the twisted wires are not strictly cylinders of $2D_w$ and $3D_w$, the three twisted wires arrangement does reach this critical value and the induced flow disturbances from this arrangement is likely nearly unstable.

The camera, a 12-bit resolution, Flowmaster 2S with $2k \times 2k$ pixels was located outside the wind tunnel. A mirror located 125 mm from the plate surface, and 45° from parallel with the plate, allowed for x-z planar images to be acquired, despite no top-down access for viewing in the wind tunnel. The portion of the camera images which were used covered the range: $-30 \leqslant x$ - $x_k \leqslant 350$ mm and $-40 \leqslant z \leqslant +40$ mm. The laser, a New Wave Research MiniLase-III, Nd-YAG 50 mJ energy output per pulse, was located sufficiently far from the test plate such that the diverging laser sheet covered the desired field of view. The laser sheet was approximately 2 mm thick and was centered 3 mm from the plate surface. With the smoke-wire located at y=2 mm for the majority of tests, the smoke particles immediately downstream of the wire were only slightly illuminated by the laser, but as the boundary layer grew in x, the smoke was advected by the flow into the $y \approx 3\pm 1$ mm region.

The PIV software, DaVis, was used to set the synchronization of the laser and camera for image acquisition, with 2-6 images per second. With a flow speed in the boundary layer, at the laser sheet height, of approximately 2 m/s, flow particles travel a minimum distance of (velocity / sampling rate) = (2 m/s / 6 Hz) = 0.333 m between images; i.e. each image can be regarded as independent. The short laser pulse (5 ns), results in an *instantaneous* flow image; with 2 m/s * 5 ns = 0.01 μ m fluid particle motion during the acquisition.

2.6 Control Hardware Setup

The control experiments were performed using the same flow setup as described §2.1 and §2.2, but included additional hardware and software which are described in this section. The target disturbance was introduced using the dynamic isolated roughness element as described in §2.3. The control objective was accomplished by forcing the boundary layer by outputting

a voltage to a plasma actuator, described in §2.6.1. Input to the control model was provided by two shear stress sensors, which were placed downstream of the roughness element within the boundary layer, one sensor was located *upstream* of the plasma actuator, while the other was located *downstream* of the plasma actuator (see Figure 2.5). The placement of the shear stress sensors allowed for feedforward (via the upstream sensor) as well as feedback (via the downstream sensor) control information to be sent to the control model; these sensors are described in detail in §2.6.2. The final component of the control setup was a freestream hot wire, placed well within the freestream, in order to compute the Blasius boundary layer wall-shear-stress for a given freestream velocity. This Blasius boundary layer information was required for calibration of the near-wall shear stress sensors, as well as to provide a real-time Blasius boundary layer shear stress control target (i.e set point). The overall setup of these control components is demonstrated in Figure 2.5.

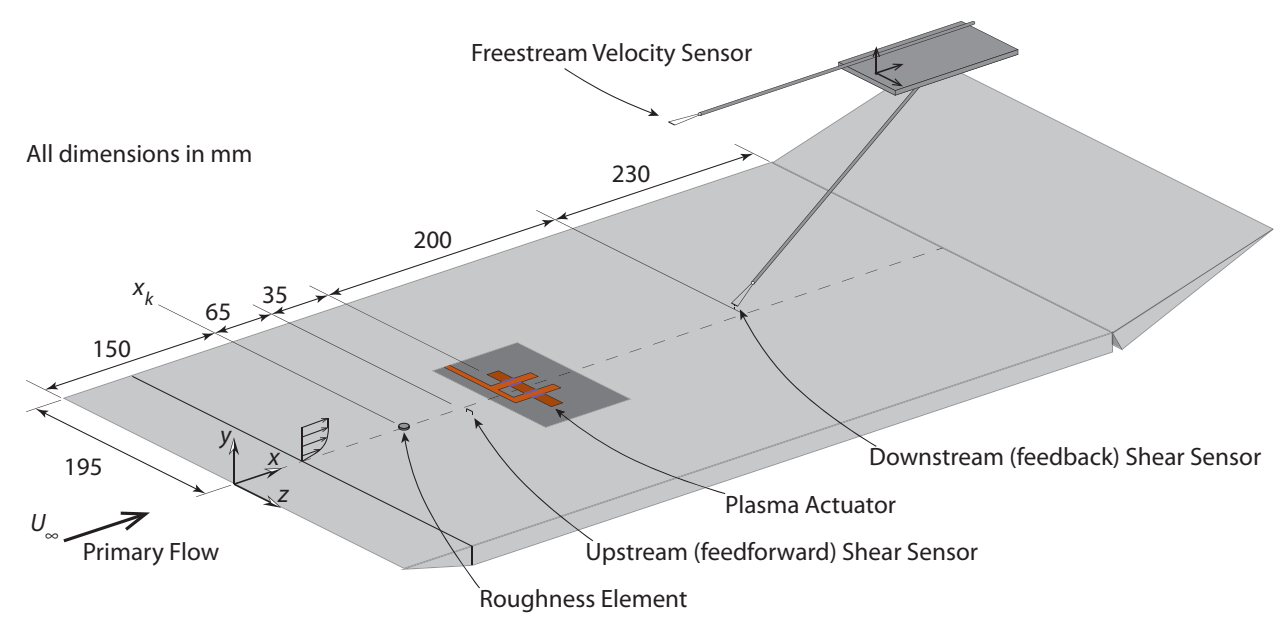


Figure 2.5: The arrangement of the control components relative to the flat plate; demonstrated are: i) the isolated roughness element, ii) the upstream wall-mounted shear stress sensor, iii) the plasma actuator assembly, iv) the downstream shear stress sensor (mounted to the 3D overhead traverse), and v) the freestream velocity hot wire probe (mounted to the 3D traverse). The relative location and scale of all control elements is shown to-scale to give proper perspective of the control domain.

The control model was implemented using digital rapid prototyping hardware having the ability to accommodate multiple input sensors (A/D channels), along with at least one control model output channel (D/A channel), in order to interface with the laboratory equipment and conduct an actual control demonstration. The input (shear stress) information was provided to the control model in near real-time, which was used by the control model to determine the proper control output (based on the control model parameters: gains, time delays, and time constants) that was passed to the output hardware for active real time control. To accomplish this, a dSpace DS1103 PPC Controller Board (with BNC connections) and expansion box were used, which was linked to the PC with a dSpace DS819 PCI Express Link Interface card. The dSpace ControlDesk 4.2 software was run using a 64-bit PC⁴ running Windows 7. The dSpace system may accommodate up to 20 channels of differential A/D input, 6 of which were used here⁵, and up to 8 channels of differential D/A output, only 1 of which was used here⁶. All channels provide 16-bit resolution which adequately resolved the low-voltage signals provided by the shear stress signals⁷. The dSpace acquisition system was used for data acquisition for Input/Output (I/O) model development (for modeling the boundary layer dynamics in response to the disturbance and actuation) as well as for the control experiments. Throughout all control effort procedures (i.e. calibrations, I/O model data acquisition, and control experiments) all cabling remained in-place and connected to prevent any ground reference variation from one procedure to the next. The only exception

⁴Intel Core2 Duo CPU E8400 3.00GHz, 8GB RAM

⁵dSpace Input Channels: 1. Upstream shear stress sensor, 2. Downstream shear stress sensor, 3. Freestream velocity sensor, 4. Laser sensor to monitor the roughness element height, 5. Voltage signal sent to the plasma actuator, and 6. On/Off signal used for plasma actuator I/O data generation

⁶dSpace Output Channels: 1. Voltage amplitude output, which was multiplied by the high-frequency drive signal generated by a function generator and passed to the high voltage amplifier; and ultimately to the plasma actuator

 $^{^{7}}$ Due to very small amplitude roughness element induced disturbances, the voltage change from the Blasius state to the disturbed state was very small. These considerations are discussed in more detail in $\S 2.6.2$

was the plasma supply voltage connection, which was switched between a function generator source (for I/O model data acquisition) and the output of the dSpace connection board (for actual control experiments). It was verified that this one connection change did not alter any of the signal voltages (shear stress sensor signals, etc.).

In order to supply the plasma actuator with a high-frequency sine wave with an amplitude dictated by the control model output, an Analog Devices AD633JNZ IC analog multiplier 8-dip chip was used. The multiplier chip provided a simple hardware solution by multiplying a 4kHz sine wave from a function generator (of unity amplitude) by the dSpace output voltage⁸. During the I/O model data acquisition, the multiplier chip was used to multiply the high-frequency sine wave signal by an on/off step-function signal (i.e. square wave) in order to provide the desired step-response forcing to the flow at various voltage amplitudes. During the control experiments, the step function signal was switched with the dSpace output signal. Figure 2.6 depicts a block diagram demonstrating the wiring of the many hardware components and analog signals used during the control efforts.

Lastly, a hot wire sensor was placed in the freestream, well above the control domain, to monitor any small fluctuations in the freestream velocity during the control experiments; this is demonstrated in Figure 2.5. The hot wire was run with a TSI 1750 anemometer using a 1.5 overheat ratio. The hot wire was calibrated and operated according to the procedures outlined in §2.4 using 10 points over the range of free stream velocities tested.

 $^{^{8}}$ In practice, the multiplier chip imposed an inherent 1/5 gain on the signal, and the function generator signal amplitude was set to 3V; therefore, the control model output was multiplied by 5/3 (in the control model) before being sent to the multiplier chip to counteract these artificial gains.

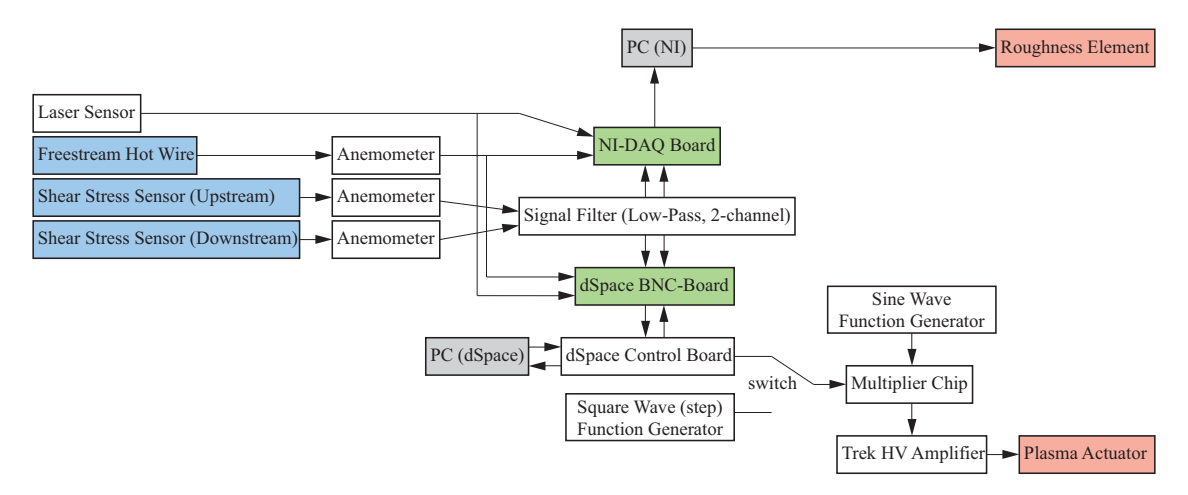


Figure 2.6: A block diagram of the control equipment and associated cabling/wiring of the many hardware components and I/O signals. The description of the PC (NI) and NI-DAQ Board components is provide in §2.4.

2.6.1 Plasma Actuator Setup

Plasma actuators were used in the control experiments to provide a counter-disturbance to the roughness element induced disturbance. Single-Dielectric-Barrier-Discharge (SDBD) plasma actuators (here on simply referred to as *plasma actuators*), provide a uniquely deployable, robust, and adjustable intensity flow forcing which is appropriate for the target control experiments. SDBD plasma actuators have been used successfully in many flow studies and control efforts, and more recently in streak disturbance cancellation efforts, [23] [24] [26] to name a few. Figure 2.7 provides a basic schematic of the geometry of a plasma actuator, noting the critical components and nominal induced flow.

A plasma actuator creates fluid momentum from electrical energy through a mechanism known as a Lorentz force. The electric field forces and accelerates ions in the neutral air by collisions with charged particles. Nearby fluid is entrained with the forced particles and a fluid jet is created. The collisions are initiated by generating a high electrical potential region, originating at the high-voltage electrode (typically 1-50 kV), and ejecting positive ions towards the lowest potential region (the dielectric surface, near the ground electrode), result-

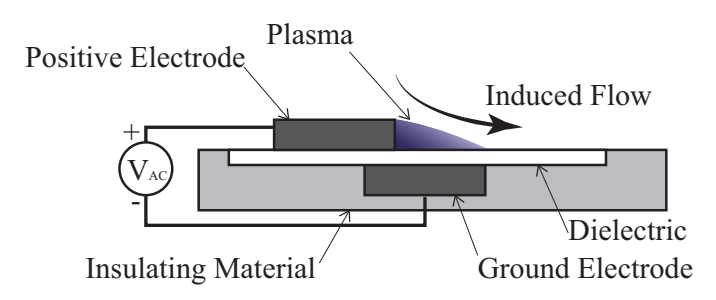


Figure 2.7: Diagram of the SDBD plasma actuator geometry used here demonstrating the positive electrode, ground electrode, and dielectric layer, plasma formation region, and induced flow. The insulting material acts as a base for the plasma actuator components and prevents plasma from forming on the grounding electrode side of the dielectric.

ing in a highly charged dielectric surface. The polarity of the electrodes is alternated using an AC voltage source (frequencies are typically from 1-10 kHz), and the transfer/collison process continues. The spatial distribution of the plasma and the induced flow forcing is highly dependent on the supply voltage and frequency as well as the geometry and arrangement of the electrodes and dielectric. The Geometry used here has proven effective and was used in the recent streak disturbance control study by Hanson et al.[26]. A comprehensive description of the forcing and mechanisms involved in inducing a flow with this type of a plasma actuator arrangement may be found in Corke et al. [15].

In order to introduce the desired flow disturbance to counteract the disturbance induced by the upstream isolated roughness element, a single pair of spanwise forcing plasma actuators was used. This is different than the efforts of [23], [24], and [26] where multiple pairs of spanwise forcing actuators were used to control spanwise-periodic streak disturbances. Figure 2.8 demonstrates the arrangement of the plasma actuator pair, indicating that the forcing from each actuator is nominally toward the other. This arrangement results in a pair of counter-rotating streamwise vortices, as demonstrated in detail by Jukes and Choi [28],[29], with a low-speed streak between the actuators shouldered by high speed streaks; as demonstrated schematically in Figure 2.9, and supported by the with hotwire measurements

presented in Figure 6.4c. This is qualitatively opposite in sign to the streaks generated by the isolated roughness element over the disturbed spatial region of the flow; as demonstrated schematically in Figure 3.3, and supported by the with hotwire measurements presented in Figure 6.4b.

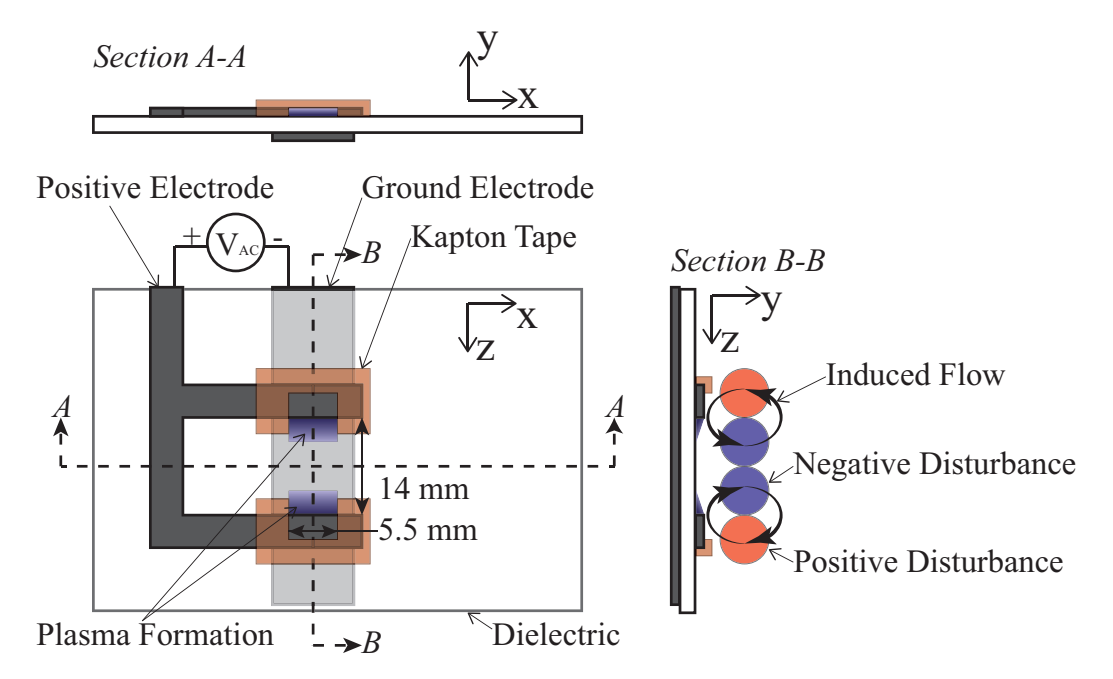


Figure 2.8: Plan- and Cross-section views (A-A and B-B) of the SDBD plasma actuator geometry demonstrating the positive electrode, ground electrode, and dielectric layer, and plasma formation region. Section B-B also shows a drawing of the flow disturbance produced by the actuator. A low-speed streak forms where a wall-normal disturbance velocity away form the plate is produced, and vice versa. This is due to low speed fluid moving away and towards the wall, respectively.

The specific geometry of the actuator was chosen based on preliminary measurements, in which various high-voltage electrode widths and streamwise lengths were tested. The width of the HV-electrode is critical in order to properly set the spanwise spacing of the counter-rotating disturbance vortices to match that of the disturbance introduced by the roughness element. A narrower spacing will generate the counter-rotating disturbances closer together, while a larger spacing will allow the counter-rotating disturbance to be more spread apart. The length of the HV-electrode is critical for setting the appropriate level of disturbance

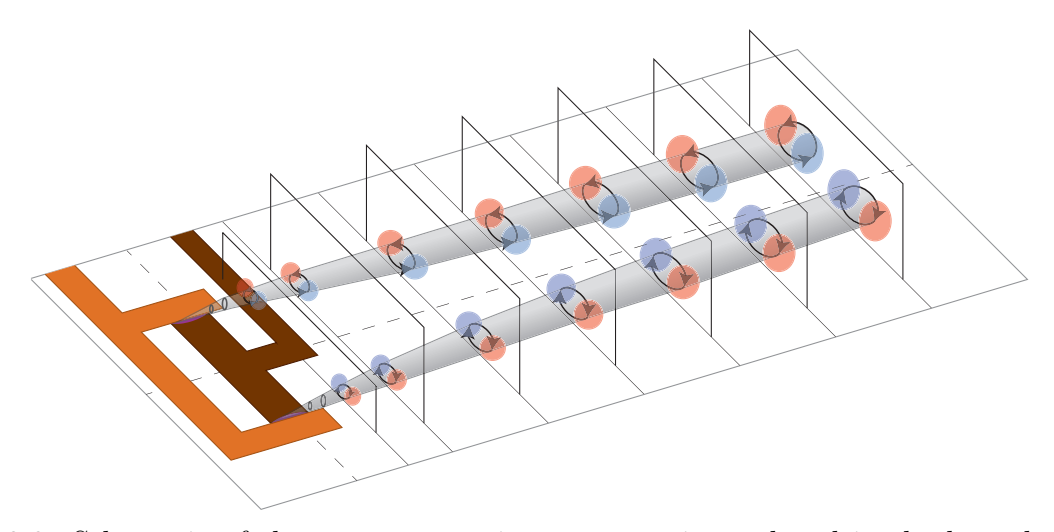


Figure 2.9: Schematic of the counter rotating vortex pair produced in the boundary layer by the plasma actuator and the associated streamwise-velocity disturbance. Red: positive disturbance, Blue: negative disturbance.

intensity during the control efforts. A long HV-electrode will require less power (voltage) to create a notable flow modification due to the increased time that the passing flow spends within the plasma forcing region; however, the minimum plasma turn-on voltage (which is essentially independent of small actuator length changes) will create a forcing that may be too large to be useful for small-disturbance-strength flow control, which is important when trying to control the weak disturbances encountered in boundary layer transition. In contrast, a short electrode will turn-on with minimal flow forcing, but larger flow disturbances may require a large voltage to achieve sufficient forcing over the shorter convection time; this forcing may be too strong and cause transition, limiting the useful range of actuator voltages and available forcing. The final geometry used in the control efforts can be seen in Figure 2.8 where the streamwise length and spanwise spacing of the high-voltage electrodes were 5.5 mm and 14.0 mm, respectively. Note that the spanwise width of the positive electrodes was not important because the outer side of each electrode was covered with Kapton tape to prevent plasma formation, this can be seen in the x-z view of Figure 2.8 (this was done to generate a disturbance that matches the isolated roughness element disturbance shape as much as possible while having an opposite sign). This geometry allowed for: i) a very low intensity of forcing at the minimum plasma turn-on voltage and ii) a disturbance intensity on the order of that generated by the roughness element at higher plasma voltages, while matching the disturbance spacing from the roughness element.

The plasma actuator is operated with a high-frequency/high-voltage supply signal, which was generated using an Agilent 33120A function generator (high-frequency sine wave), multiplied by the output of the control model (to supply the sine wave amplitude); which was then passed to a Trek model 609C-6 high-voltage DC amplifier, and sent to the plasma actuator. During the I/O model data acquisition, the output amplitude of the function generator was modulated with a second step-function signal. In each setup, a multiplier chip (Analog Devices, AD633JNZ) was used to multiply the two signals, as described in §2.6.

2.6.2 Shear Stress Sensor Setup

Two shear stress sensors were used to provide feedforward and feedback information to the control model during the control experiments; both sensors were single-wire hot-wire sensors operated using constant temperature anemometers. Both sensors were operated with Dantec MiniCTA 54T30 anemometers with the circuit gains and offsets adjusted to optimize the sensor output resolution over the range of shear stress to be expected during the control experiments, as well as to provide an output voltage within the measurable range (± 0.5 V) of both the National Instruments DAQ board (model DAQ-6061 + BNC-2012, used for calibration) and dSpace DAQ board (model CP1103, used for control experiments). Finally, the output of each anemometer was passed through a 20 Hz low-pass analog filter, Krohn-

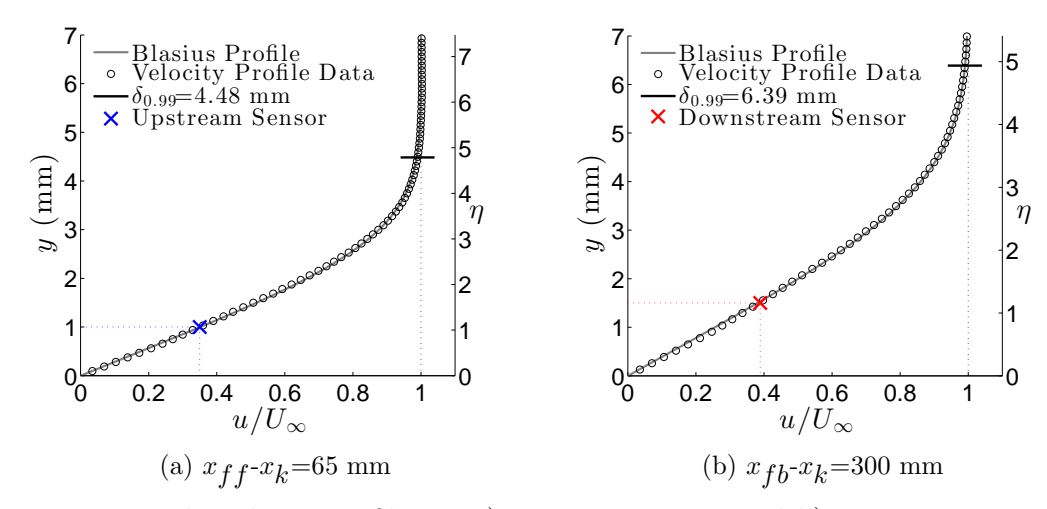


Figure 2.10: Boundary layer profiles at a) x_{ff} - x_k =65 mm and b) x_{fb} - x_k =300 mm demonstrating the wall-normal location of the upstream and downstream shear stress sensors, respectively, within the linear region of the undisturbed Blasius boundary layer.

Hite model 3202R, to remove high-frequency noise generated by external sources⁹. Each sensor was placed within the linear region of the Blasius boundary layer streamwise-velocity profile of the undisturbed flow, for calibration purposes, as demonstrated in Figure 2.10. Furthermore, each sensor was positioned along the span to be within the expected high-speed disturbance region generated by the roughness element, according to the results presented in §3.2.3. The final wall-normal location of each sensor was chosen in order to remain within the linear region of the undisturbed boundary layer, but as far from the wall as possible in order to maximize signal amplitude change in the disturbed flow, which increased with wall normal distance, until $\eta \approx 2$ (see, for example, Figure 3.19).

One of the four hot wire sensors attached to the 3D overhead traverse was used for the downstream (feedback) sensor, which allowed the feedback sensor to be positioned anywhere overtop of the plate. Note that this downstream sensor was always positioned downstream of the plasma actuator assembly in order to accomplish the feedback objective. During the

⁹Possible sources of high-frequency noise on the analog hot wire signals were: the traverse motors, plasma actuator, large blower motor driver, etc.

control experiments, the feedback sensor was placed at x_{fb} - x_k =200, 250, or 300 mm as noted in the control model development and control experiment sections (Chapter 5 and §6.2.4, respectively); resulting in a downstream shear stress sensor position of (x- x_k , y, z)= $(x_{fb}$ - x_k , 1.5, 2.5) mm depending on the feedback sensor streamwise location. Note, in order to collect the y-z planar results of the uncontrolled/controlled disturbance (such as those provided in Figure 6.4e) a hot wire sensor was fabricated and mounted through the wall of the plate, similar to that described for the upstream shear stress sensor (see next paragraph), and located at $(x_{fb}$ - x_k , y, z)=(300, 1.5, 2.5) mm.

The upstream (feedforward) sensor was constructed from a single hot-wire probe, with a plug that fit flush with the flat plate top-surface. The plug prevented any non-negligible flow from passing through the hot wire probe broach holes. The hot wire probe body was mounted to a manually-adjustable fine-resolution traverse which was used to set the wall-normal location of the sensor. The upstream sensor required this under-the-plate assembly (see Figure 2.11) in order to avoid altering the boundary layer flow within the domain of interest; the downstream sensor did not have this restriction as it was the most downstream component of the control setup. The upstream sensor was located at $(x_{ff}-x_k, y, z)=(65, 1.0, -1.5)$ mm for all tests. Note that the upstream and downstream shear stress sensors were each positioned within the high speed disturbance region, downstream of the roughness element, but on opposite sides of z=0. This was done to ensure that the presence of the upstream sensor would not effect the downstream sensor reading; however, in preliminary testing, no noticeable effect was seen.

The shear stress sensor calibrations were performed with 10 discrete shear stress values, which were achieved in the wind tunnel using a range of freestream velocities, spanning the targeted range of shear stress with and without flow disturbances. The shear stress for

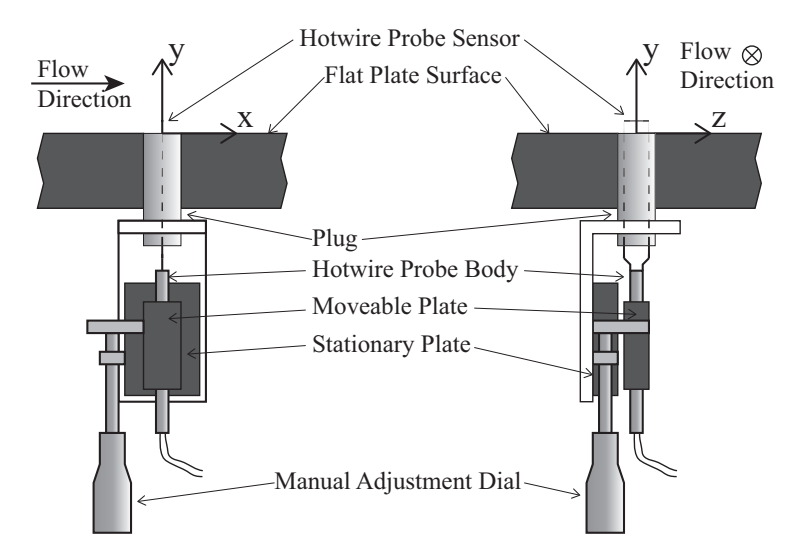


Figure 2.11: The upstream shear stress sensor assembly, demonstrating the method used to allow variable wall-normal positioning of the sensor using a stationary plug with two small holes for the hotwire broaches; the hot wire body is mounted on a small manual y-axis stage.

calibration was taken as the expected shear stress for a Blasius boundary layer at the plate wall,

$$\tau_w = \mu \left. \frac{\partial u}{\partial y} \right|_{y=0} = (0.332) \mu U_{\infty} \sqrt{\frac{U_{\infty}}{x\nu}}, \tag{2.1}$$

computed from knowledge of the freestream velocity and streamwise sensor location(s), relative to the virtual origin. A 2nd-order polynomial was fit to the hot-wire-voltage to shear-stress calibration data for both the upstream and downstream sensors to generate a calibration curve for each hot wire sensor. These calibrations were entered into the control model, allowing the control model to sample the sensor voltage, calculate the shear stress, and perform the control objectives in real-time.

Chapter 3

Steady-State Disturbance Results

The results of investigations into the physical characteristics of the disturbed flow field are organized into subsections. The discussion in the first subsection, $\S 3.1$, demonstrates the undisturbed (basic) state, a Blasius boundary layer. Next, a physical description of the disturbed boundary layer character is presented and supported with flow visualizations in $\S 3.2$. Analysis of the steady state disturbance is provided from the flow visualizations in $\S 3.2.2$. The steady state disturbance is further analyzed using detailed hot wire results in $\S 3.2.3$. In $\S 3.3$, the y-z planar disturbance energy development in the streamwise direction is examined. This is followed by the definition and investigation of the Disturbance Energy Density in $\S 3.4$. Lastly, in $\S 3.5$, a scaling argument for the disturbance energy density is empirically identified.

3.1 Undisturbed (Basic) Flow

A Blasius boundary layer is established as the basic state at three freestream velocities which were nominally: $U_{\infty} \approx 4.0$, 5.0, and 6.0 m/s; the freestream turbulence intensity at these velocities was approximately 0.02%. Figure 3.1a demonstrates the self-similar profiles of the measured boundary layer at the three freestream velocities of interest for all seven streamwise measuremen locations covering x- x_k =25 to 300 mm. In Figure 3.1a, the profiles are provided using the Blasius wall-normal similarity coordinate, η ,

$$\eta = \frac{y}{\delta}, \text{ where } \delta = \sqrt{\frac{\nu(x - x_v)}{U_{\infty}}}, \text{ and } x_v = \left(\frac{\delta^*}{1.721}\right)^2 \frac{U_{\infty}}{\nu},$$
(3.1)

as the ordinate; where the Blasius similarity length scale, δ , virtual leading edge location, x_v , and displacement thickness, δ^* , are calculated independently for each wall-normal profile and the spanwise average is used at each streamwise location. The virtual origin, x_v , as described in [44] (pp.888), accounts for the inherent non-zero pressure gradient at the plate leading edge which requires a short recovery (to a zero-pressure gradient) streamwise length. Thus, the physical streamwise distance from the leading edge, x, with the virtual origin subtracted, $x - x_v$, provides the effective downstream distance to be used in comparison with boundary layer theory, as described in the classic text by Schlichting or Schlichting and Gersten [45]. By casting the disturbance analyses in terms of η , changes in the disturbance wall-normal location with streamwise location are due to altered disturbance characteristics, rather than natural laminar boundary layer growth.

In order to quantitatively assess the accuracy of the undisturbed boundary layer profile in representing the Blasius solution, the shape factor, $H_{12} = \delta^*/\theta$, is typically employed in literature; where δ^* and θ are the displacement and momentum thickness, respectively. According to [44] the recommended Blasius shape factor is 2.59 ± 0.005 , while in practice ±0.05 is common ([36], [52]). The inset of Figure 3.1a provides the spanwise-average shape factor, $\langle H_{12}\rangle_z$, result for a representative test at each velocity (symbols) along with error bars representing the total range of spanwise-average shape factors measured during the complete matrix of test cases; the shape factor is in good agreement with a Blasius boundary layer.

In Figure 3.2, the undisturbed boundary layer shape factor for case 9, which is representative of all cases because the roughness element is not deployed, is provided to demonstrate

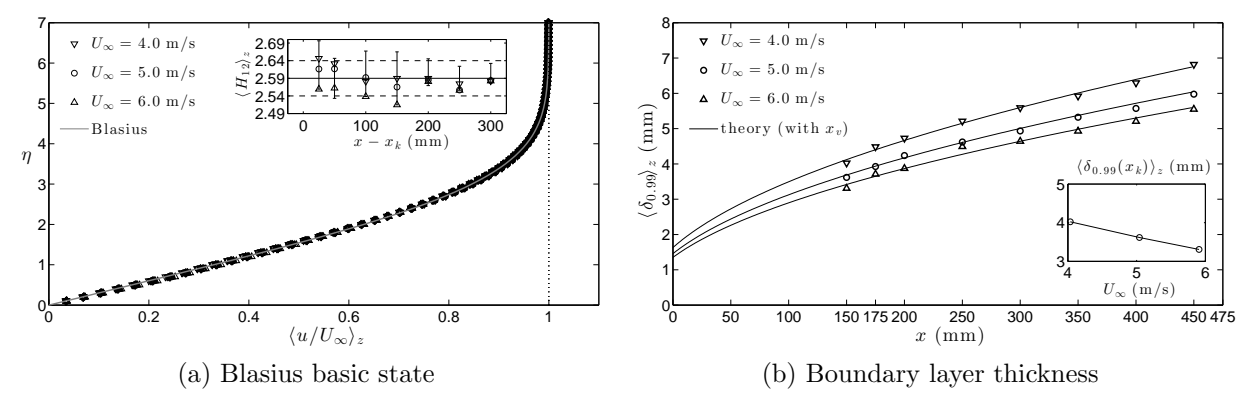


Figure 3.1: (a) The measured, self-similar, Blasius boundary layer profiles at x- x_k =25, 50, 100, 150, 200, 250, and 300 mm for the three freestream velocities of interest $(\triangle, \bigcirc, \neg)$ and according to theory (—) with the inset figure demonstrating the shape factor for velocity profiles measured at the three velocities and all streamwise locations. The error bars indicate the range of shape factors calculated across all test cases at each location, and (b) the measured boundary layer thickness $(\triangle, \bigcirc, \neg)$ and theoretical Blasius boundary layer thickness (—) with the inset figure highlighting the boundary layer thickness at the roughness element location. Note that all values are spanwise average results, denoted with $\langle \ \rangle_z$.

the spanwise variation of H_{12} over a length covering the measurement domain (-19 $\leq z \leq$ 20 mm) at each streamwise location (left), along with the spanwise-average values (right). The shape factors nearly all fall within the range typically reported in Blasius boundary layer studies (dashed lines). The spanwise variation of H_{12} demonstrates good spanwise uniformity, without systematic deviation, indicating the the variability is likely the result of random errors. Great care was taken to ensure adequate spanwise uniformity and these results demonstrated that this has been accomplished.

Figure 3.1b provides the measured boundary layer thickness, which ranged from $3.3 \le \delta_{0.99}(x) \le 7.0$ mm over the streamwise domain of the measurements, along with the theoretical boundary layer thickness according to the Blasius solution. The latter was obtained from,

$$\delta_{0.99,theory} \approx 5.0 \sqrt{\frac{(x - x_v)\nu}{U_{\infty}}} = 5\delta,$$
(3.2)

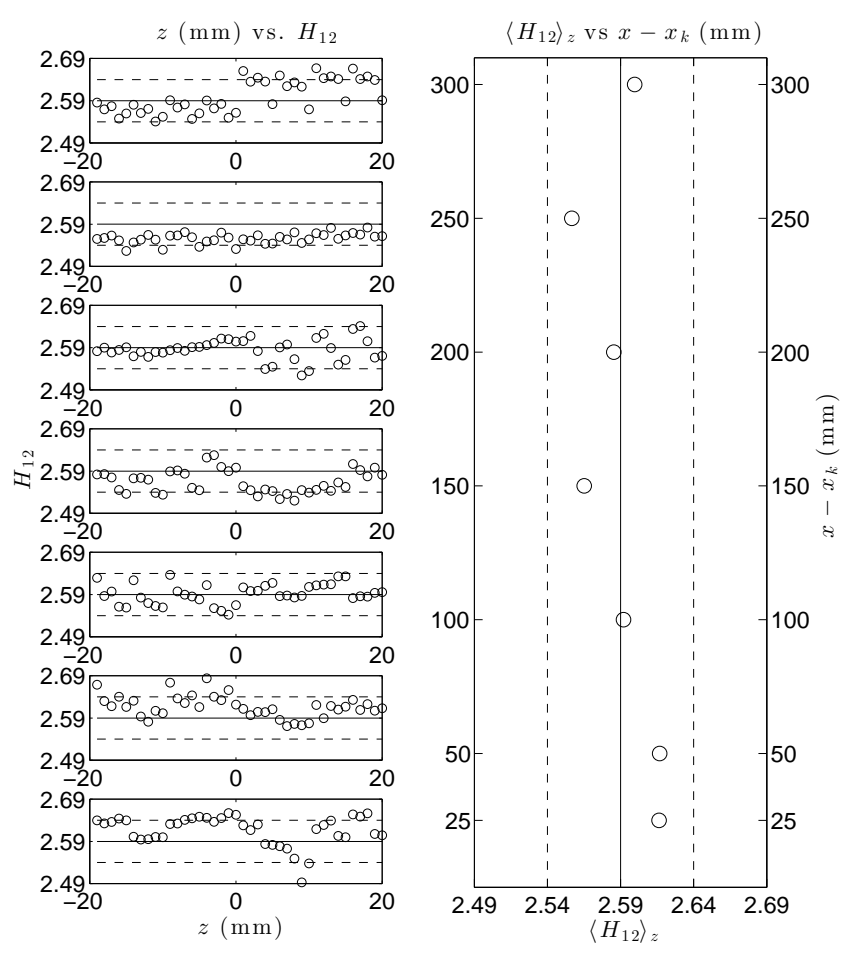


Figure 3.2: Distribution of shape factor H_{12} across the spanwise direction at all streamwise locations for U_{∞} =5.0 m/s. Note that each of the seven vertical subplots on the left represent the spanwise data at the streamwise location as noted immediately to the right, which then provides the spanwise-average result, $\langle H_{12} \rangle_z$.

which is directly calculated from zero pressure gradient boundary layer theory [45]. As expected, the boundary layer thins with increasing freestream velocity and grows in the streamwise direction with \sqrt{x} . At the roughness element location, x_k , the boundary layer thickness varied from $3.3 \le \delta_{0.99}(x_k) \le 4.0$ mm, which is highlighted in the inset of Figure 3.1b. Notably, the roughness element height range investigated here, $0 \le k \le 2.0$ mm, never exceeded the boundary layer thickness and was typically within the nominally linear range of the undisturbed (Blasius) profile; see §3.5 for an explanation of the linear boundary layer range and the cases where the roughness element was within this region.

3.2 Disturbance Character

3.2.1 Disturbance Description

It is useful to examine the character , i.e. the spatial distribution, size, and strength, of the disturbance generated by an isolated roughness element deployed from the wall. Before doing so, a physical description of the disturbance is discussed to provide a perspective for interpretation of the observed disturbance characteristics. As the undisturbed upstream boundary layer flow approaches a wall-mounted roughness element, in this case a cylinder with k < D and $k < \delta_{0.99}(x_k)$, a counter rotating pair of vortices is generated downstream of the roughness element; as demonstrated experimentally by Pattenden *et al.* [41] and computationally by Visbal [50] and Rizzetta and Visbal [43]. The two vortices are primarily aligned in the streamwise (x) direction such that they *induce* flow toward the wall on the *inside* (smaller |z| region) and away from the wall on the *outside* (larger |z| region), this arrangement is clearly investigated and described by Acarlar and Smith [1]. Figure 3.3 demonstrates this counter-rotating vortex pair arrangement schematically.

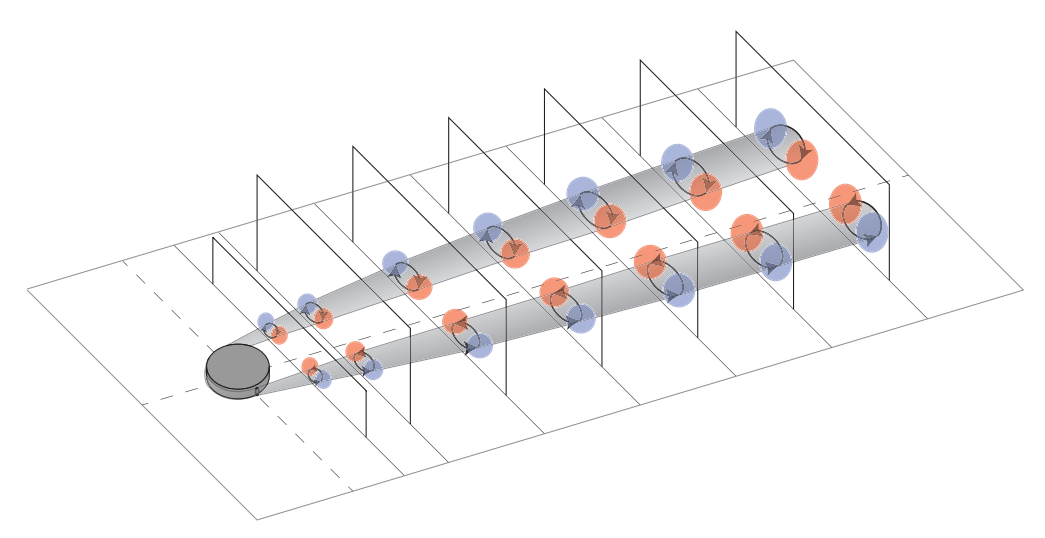


Figure 3.3: Schematic of the counter rotating vortex pair produced in the boundary layer by an isolated roughness element and the associated streamwise-velocity disturbance. Red: positive disturbance, Blue: negative disturbance.

In Figure 3.3 the streamwise-velocity sign of the disturbance (positive or negative, relative to the basic flow state) induced by the counter-rotating vortex pair is demonstrated qualitatively as lighter or darker regions. As high-speed fluid is drawn toward the wall, from larger y locations in the boundary layer, a positive disturbance is generated. The high-speed inner regions of the vortex pair may, or may not, merge in the downstream domain; if merging does occur, a single positive disturbance would result, as has been seen in some studies. Outboard of the positive regions, low speed fluid is drawn away from the wall by the vortex pair resulting in negative disturbance regions; i.e. the lift-up mechanism first identified by Landhal [33]. These streamwise elongated regions of positive and negative disturbance velocity are the streak disturbances to be characterized in this study. It is noted here that the details of the flow disturbance in the immediate vicinity (roughly $-5 \le x - x_k \le 10$ mm) of the roughness element is (likely) quite complex. However, the hot wire results show that any such disturbances quickly decay and are no longer present; thus, no special attention is given to these disturbances here. For the interested reader, there are few previous investigations

that provide detailed information in the near roughness element region. The simulations by Rizzetta & Visbal [43], specifically their Figure 14, provides good insight into the disturbance development both near the roughness element and in the downstream region. Furthermore, in an earlier study by Visbal [50], discussion is provided regarding the many detailed flow arrangements that may exist upstream of a roughness element depending on the specific flow conditions and element geometry. The experimental results of Pattenden et al. [41] provide demonstrations of surface streaking on and around a roughness element showing, experimentally, the complex disturbances that may exist in the near roughness element region. However, k=D and $k > \delta_{0.99}(x_k)$ in the Pattenden et al. [41] investigations, and while instructive, are not necessarily representative of the k < D and $k < \delta_{0.99}(x_k)$ arrangement investigated here.

In addition to the high and low speed streak disturbances generated by the counterrotating vortices, a wall-normal shear layer is established downstream of the roughness element, as described by Ergin and White [18]. This is associated with the low speed, negative
disturbance, wake region directly downstream of the roughness element; note that this disturbance feature is not included in Figure 3.3. As will be demonstrated in §3.2.3, in cases
where no boundary layer "transition" occurs, this low speed disturbance region decays and
disappears downstream. The role of this disturbance in transitional cases is also addressed
in §3.2.3.

3.2.2 Flow Visualization Results

Instantaneous images in the x-z plane were acquired to investigate the evolution of the induced disturbances and to provide information on the downstream flow transition. It should be noted that in this work the term transition does not refer to the boundary layer attaining

a fully-developed turbulent state but rather to the development of localized turbulent regions within the flow. In Figure 3.4, smoke traces are imaged after being introduced upstream of the roughness element for a range of roughness element heights. Note that in Figure 3.4 the freestream velocity and roughness element diameter remain constant. The results of Figure 3.4a at k=1.4 mm are representative of similar images acquired with k=0.5, 1.0, and 1.29 mm, where the flow does not experience transition.

Figures 3.4(a-c) demonstrate three qualitatively different flow responses to the roughness element, namely: (i)non-transitional, (ii) intermittent turbulence, and (iii) continuous turbulence. In Figure 3.4a, where k=1.40 mm, the disturbance evolves in the streamwise direction without transitioning. Directly downstream of the roughness element ($-5 \le z \le 5$ mm and $50 \le x - x_k \le 350$ mm), smoke is drawn toward the plate and away from the laser sheet, resulting in a reduction in the smoke illumination, i.e. darker smoke. This implies the presence of negative wall-normal velocity behind the element, and the associated establishment of a high-speed region as described in §3.2.1.

In Figure 3.4b, where k=1.51 mm, turbulent bursts are observed, separated by non-transitional regions. Specifically, in the streamwise range of $50 \leqslant x - x_k \leqslant 125$ mm, the flow exhibits non-transitional "darkening of the smoke"; however, from $125 \leqslant x - x_k \leqslant 225$ mm, a turbulent spot forms. The turbulent spot has spanwise size larger than the roughness element. Farther downstream, this turbulent region is followed by another, shorter, non-transitional section and another turbulent burst which demonstrates the sporadic nature of this intermittent condition. This image is representative of the many instantaneous images acquired at this intermittent condition, where the instantaneous location of the turbulent bursts is observed to exist over all streamwise locations, but never upstream of $x-x_k=60$ mm. Note that this farthest upstream location observation is the best assessment based on the limited

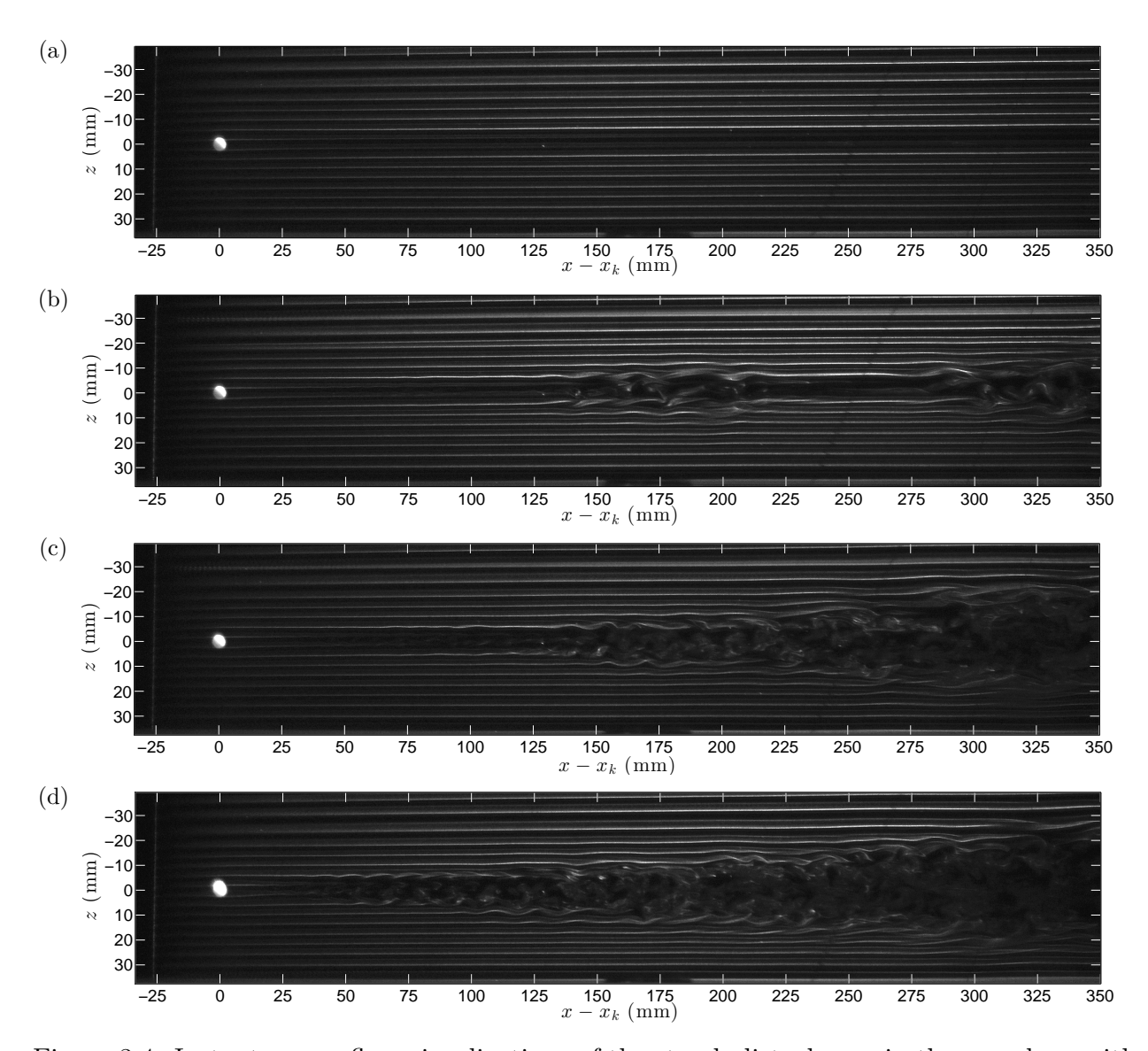


Figure 3.4: Instantaneous flow visualizations of the streak disturbance in the x-z plane with D=5.0 mm and $U_{\infty}=5.0$ m/s, at a) k=1.40 mm, b) k=1.51 mm, c) k=1.60 mm, and d) k=2.00 mm; with the smoke-wire at (x- x_k , y)=(-25, 2) mm and laser sheet at y \approx 3 \pm 1 mm from the wall.

number of independent, instantaneous images (54) captured.

In Figures 3.4c and 3.4d, where k=1.60 and 2.00 mm, respectively, unstable conditions result in continuous transition downstream of the roughness element. It is observed that the transition to a turbulent flow does not occur immediately at the roughness element streamwise location, but at some distance downstream of the roughness element. The most upstream location of observed instability when k=1.6 mm is within the region $50 \leqslant x-x_k \leqslant 80$ mm, while with k=2.0 mm instability is first observed in the region $30 \leqslant x-x_k \leqslant 50$ mm. These assessments are not rigorous, but are drawn qualitatively by noting the most upstream x location at which the smoke streak lines develop sinusoidal-like shape. The actual laminar/turbulent transition streamwise location is investigated further by hot wire measurement in §3.2.3.

In a previous study, Asai et al. [4] demonstrated symmetric and anti-symmetric (fundamental varicose and sinuous modes, respectively) disturbances experimentally which were generated downstream of an isolated element by modulating the streak downstream of the element with symmetric or asymmetric forcing using suction. Descriptions of these varicose and sinuous disturbances are also provided in Andersson et al. [2] and Vaughan & Zaki [49], both of which provide diagrams of the fundamental (and sub-harmonic) varicose and sinuous disturbance patterns (modes); these diagrams are recreated in Figure 3.5 for the fundamental modes and represent the qualitative streamline pattern of the disturbance velocity field. Noteworthy are the spanwise symmetric patterns of the varicose diagram, while the sinuous pattern provides a spanwise repeating pattern that is antisymmetric about z=0. It is not immediately clear if the disturbance patterns seen in the current investigation fall into the varicose or sinuous regimes. Andersson et al. [2] as well as Brandt et al. [11] show that the sinuous mode becomes unstable with much smaller disturbance amplitudes than the varicose

mode (26% versus 37% of the freestream velocity), and thus only the sinuous mode would be expected in experiments; although these computation studies did not consider a streak produced by an artificial obstruction, such as a roughness element. Brandt [12] considered such a streak and showed that, in fact, the spatial growth rate of the varicose mode is much larger than that of the sinuous mode in the near wake of the roughness element. Of note, is that the first sub-harmonic mode shape of the sinuous mode does provide a symmetric pattern, and Andersson notes that there is no underlying flow preference toward the fundamental or first sub-harmonic modes shapes, besides upstream flow conditions. Therefore, the disturbance patterns will be simply referred to as symmetric and antisymmetric here; although, it may be possible to distinguish the actual mode shapes.

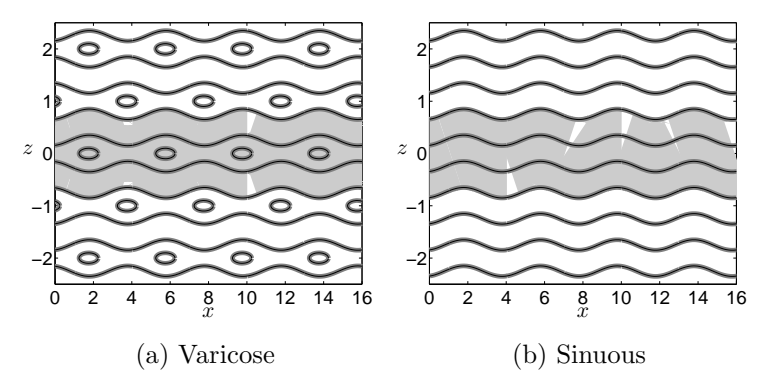


Figure 3.5: Diagram illustrating the characteristic shape, by streamlines of the disturbance velocity field, of the fundamental mode of the a) symmetric (varicose) and b) antisymmetric (sinuous) disturbance patterns for a spanwise periodic disturbance. The gray section represents a singe spanwise cycle. (These diagrams are reproduced from Vaughan & Zaki [49])

In Figure 3.4b, the turbulent spots do not appear to be symmetric, but are perhaps also not solely antisymmetric and are simply irregular in this intermittent condition. However, in Figures 3.4c and 3.4d, the disturbance appears to offer a symmetric and systematically spanwise growing turbulent pattern when in continuous transition. Asai *et al.* [4] observe that the spreading of such a turbulent wedge is indicative of successive hairpin vortex for-

mation within the boundary layer; this conclusion is supported by the investigations by Asai et al. [3] and comes from the extensive investigations and identification of successive hairpin vortices by Acarlar and Smith [1] and Haidari and Smith [22]. Figure 3.6 provides a smoke-wire visualization with the smoke-wire and laser located closer to the wall by ≈ 1 mm, at the same conditions $(x, k, D, \text{ and } U_{\infty})$ as Figure 3.4d, which demonstrates more clearly the coherent hairpin vortex structure in the region: $12 \lesssim x - x_k \lesssim 62$ mm, followed by a breakdown of the coherent hairpin structure at further downstream locations (as evident by the characteristic turbulent mixing of smoke particles).

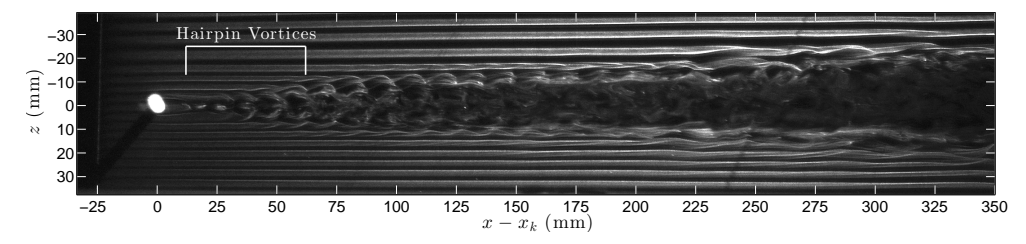


Figure 3.6: Smoke-wire image of the successive hairpin vortex structure generated down-stream of the roughness element for k=2.0 mm, D=5.0 mm, and $U_{\infty}=5.0$ m/s; with the smoke-wire at $(x-x_k, y)=(-25, 1)$ mm and laser sheet at $y\approx 2\pm 1$ mm from the wall.

Note that due to the instantaneous nature of the the images in Figures 3.4d and 3.6, the streamwise location where the streak becomes unstable and where hairpin structure heads are located will be slightly different, as these images were acquired at different times. Also, a greater spanwise extent of the disturbance is seen at the lower y location of Figure 3.6, which will be supported in the hot wire results in §3.2.3 and consistent with the observations of Asai $et\ al.\ [4]$.

Asai et al. [3] investigated the spreading of a turbulent wedge similar to that captured in the image in Figure 3.4d. Asai found spreading half-angles, dependent on the local streamwise Reynolds number, of 2° where $Re_x \leq 1.0*10^5$, 4° at $Re_x=1.1*10^5-1.7*10^5$, and 6.5° at $Re_x=2.0*10^5-2.8*10^5$ which are smaller than the typical spreading half-angle

for a turbulent spot generated without a roughness element of approximately 10° [46]. This difference was also noted in the work by Gad-el-Hak et al. [20] where the spreading half-angle of the wake disturbance emanating from a cylindrical roughness element was observed to be 2° at $Re_x \ge 0.9*10^5$. Furthermore, Gad-el-Hak distinguished between the disturbed fluid originating on the element versus that passing near the element (by means of two differently colored dyes, one of which was disseminated from the element surface, and the other was introduced to the flow upstream of the element) and found that the overall turbulent wedge region was always larger than the wake disturbance produced by the fluid originating on (or vey near) the element. The consequence of this observation is that the turbulent wedge, solely observed using flow tracers (i.e. smoke or dye) upstream of the roughness element, will be representative of the total turbulent wedge which continually entrains additional spanwise fluid into the turbulent wedge. The inner-wake region, generated from fluid originating on the element, will not be distinguished here but it is notable that Gad-el-Hak observed a 2° inner-wake; the 2° wake assessment is increased to $6\pm0.5^{\circ}$ for the larger overall turbulent wedge in the near vicinity of the roughness element. The outer turbulent region, noted by Schubauer and Klebanoff [46] as the intermittent turbulent region, is described to grow at $10\pm0.5^{\circ}$ in Gad-el-Hak's study. The results of Figures 3.4c and 3.4d appear to show a two stage spreading rate with an increase in the spread angle occurring at approximately $x-x_k \leq 225$ and 175 mm, respectively. Examining Figure 3.4d in more detail, a half-angle of $\approx 2.1^{\circ}$ is found in the region of $112 \le x - x_k \le 225$ mm, where $Re_x = 0.88 \times 10^5 - 1.26 \times 10^5$ $(Re_x=xU_\infty/\nu)$; and a half angle of $\approx 6.8^\circ$ is found in the region $225 \leqslant x-x_k \leqslant 350$ mm, where $Re_x=1.26*10^5-1.68*10^5$; these half-angle approximations are expected to be within $\pm 0.5^{\circ}$. Figure 3.7 demonstrates these results.

Quite notably, if these half-angle assessments are superposed onto the apparently tur-

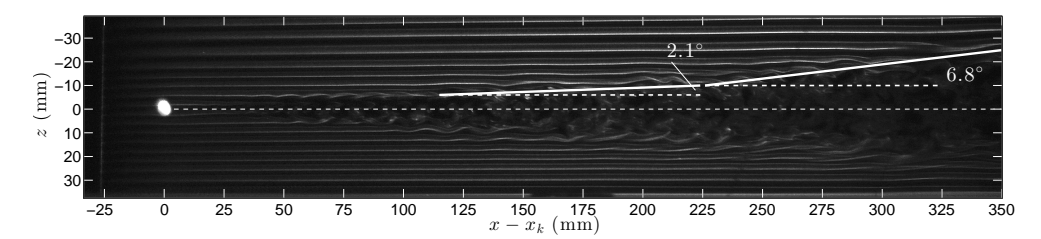


Figure 3.7: Mark-up of the results in Figure 3.4d demonstrating the half-angle assessments of the turbulent wedge two-stage spanwise growth.

bulent wedge edges of Figure 3.6, the spread rates are very similar, over the demonstrated range; albeit at a different absolute width. These results of spreading rate agree well with the Asai et al. [3] and Gad-el-Hak et al. [20] results with the rate of spreading being slightly higher in the present results than Asai, leading to potentially better agreement with the total turbulent region described by Gad-el-Hak. Asai also observes a slightly nonlinear increase in the rate of spreading of the turbulent wedge, which could be consistent with what is described here as a two-stage spreading region, and described by Gad-el-Hak as the difference between fluid originating on versus near the roughness element. Finally, the results of Asai et al. [3] and Gad-el-Hak et al. [20] did not consider the effects of the virtual origin, thus, complete agreement would not be expected. In order to provide robust turbulent wedge half-angle assessment, the Reynolds number based on streamwise location from the virtual leading edge,

$$Re_{xv} = \frac{U_{\infty}(x - x_v)}{v},\tag{3.3}$$

is determined. Thus, the two stage half-angles for the present investigations are noted as $\approx 2.1^{\circ}$ where $Re_{xy} = 0.68*10^5 - 1.06*10^5$ and $\approx 6.8^{\circ}$ where $Re_{xy} = 1.06*10^5 - 1.48*10^5$.

3.2.3 Hot Wire Results

Hot wire results of the steady-state disturbance velocity at different y-z planes over the streamwise region of interest provide detailed measurements of the disturbance size, strength, and spatial profile. Results are acquired at seven streamwise planes: x- $x_k = 25$, 50, 100, 150, 200, 250, and 300 mm where $x_k = 150$ mm, as demonstrated in Figure 2.1. The flow state is investigated at various combinations of: roughness element heights: k = 0.5, 1.0, 1.29, 1.4, 1.51, 1.6, and 2.0 mm, roughness element diameter: D = 3.175 and 5.0 mm, and freestream velocities: U_{∞} =4.0, 5.0, and 6.0 m/s; as identified in Table 2.1. Figures 3.8(a-g) provide the disturbance velocity (u' = u - U), normalized with the freestream velocity, with constant D=5.0 mm and U_{∞} =5.0 m/s for all seven k values. Figures 3.9(a-c) provide the disturbance velocity results with constant k=1.0 mm and D=5.0 mm at each of the three U_{∞} values. Finally, Figures 3.10(a-b) provide the disturbance development with constant k=1.51 mm and U_{∞} =5.0 mm for both D values. Disturbance velocity contour results at other parameter combinations demonstrate similar development as those provided in Figures 3.8-3.9.

Note that the contour levels for Figures 3.8(b-f), 3.10, and 3.9 cover $\pm 10\%$ of U_{∞} . However, where k=0.5 mm (Figure 3.8a) the levels cover $\pm 1.0\%$ of U_{∞} , and where k=2.0 mm (Figure 3.8g) the levels cover $\pm 15\%$ of U_{∞} in order to better visualize the disturbance distribution. Examining the details of the disturbances, in the most upstream plane, x- x_k =25 mm, the disturbance shape appears qualitatively similar for all k values but the intensity (u'/U_{∞}) increases with k; the same is true with increasing U_{∞} and D. The existence of a low speed region, centered downstream of the roughness element, and elevated from the wall, is apparent in all cases. This region falls in the middle between two high/low speed disturbance pairs that are presumed to be generated by the counter-rotating vortices de-

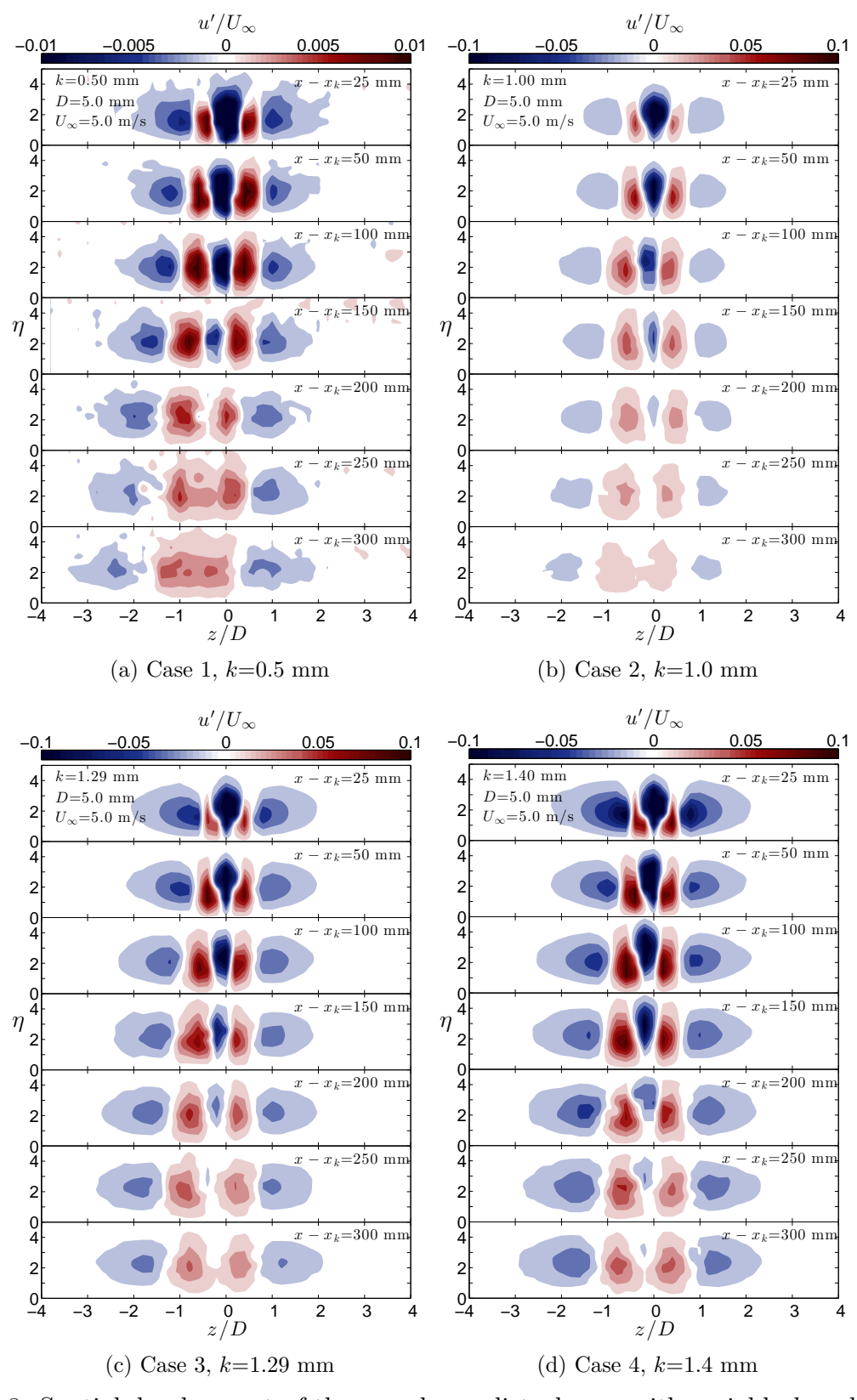
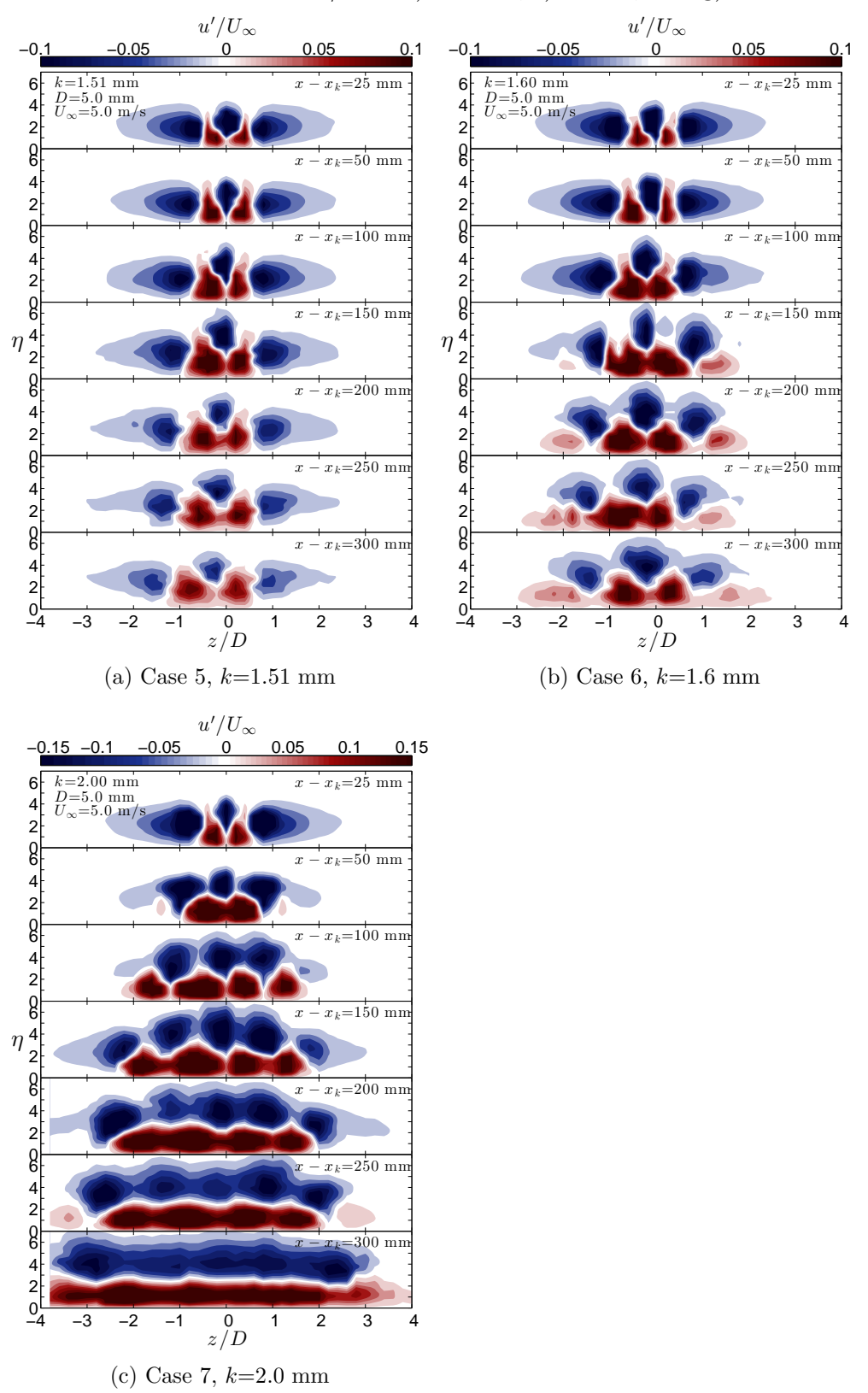


Figure 3.8: Spatial development of the y-z planar disturbance with variable k and constant D=5.0 mm and $U_{\infty}=5.0$ m/s for a) k=0.5, b) k=1.0, c) k=1.29, d) k=1.4 mm, e) k=1.51, f) k=1.6, and g) k=2.0 mm

Figure 3.8 (cont'd) Spatial development of the y-z planar disturbance with variable k and constant D=5.0 mm and $U_{\infty}=5.0$ m/s for e) k=1.51, f) k=1.6, and g) k=2.0 mm



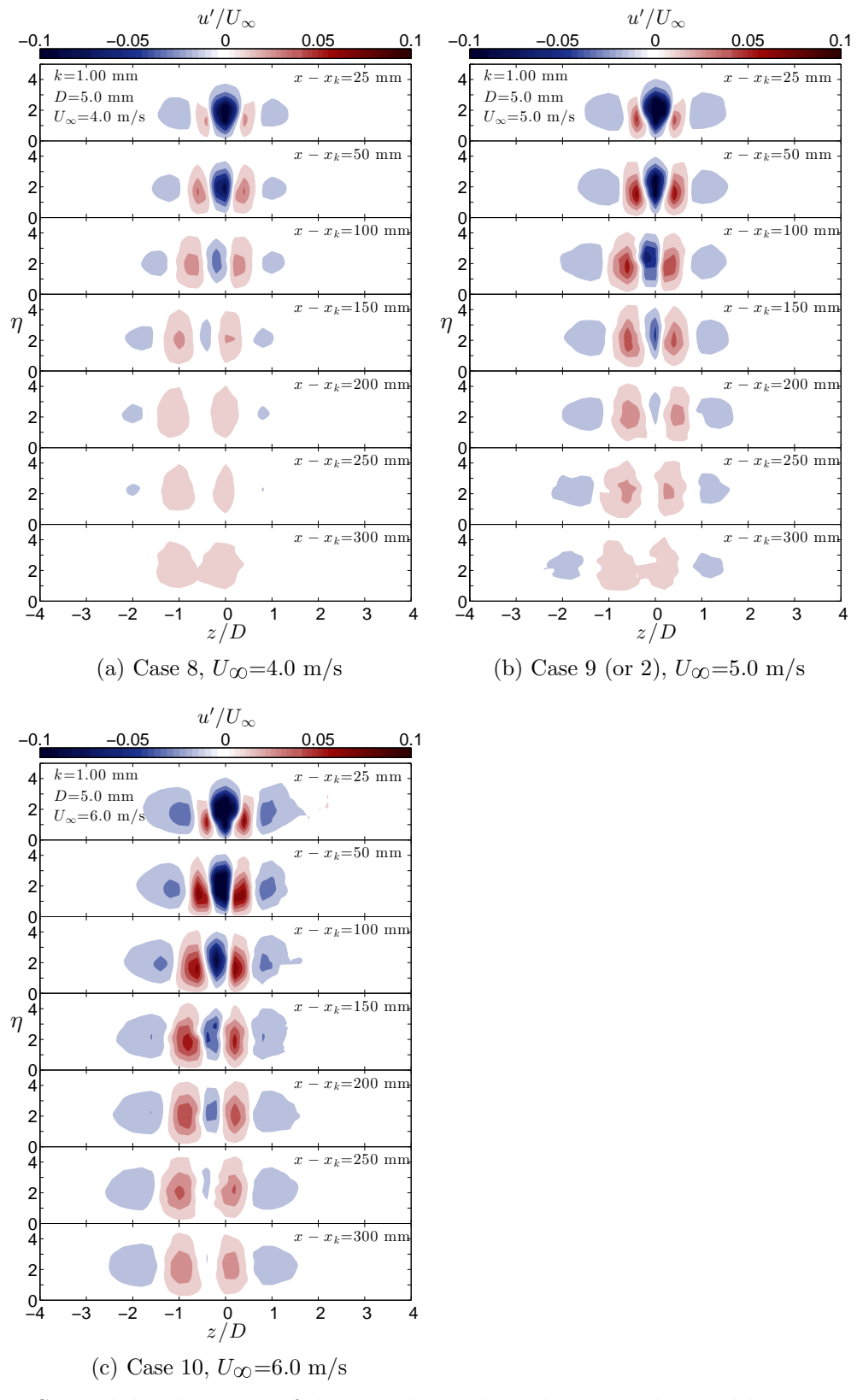


Figure 3.9: Spatial development of the y-z planar disturbance with variable U_{∞} and constant k=1.0 mm and D=5.0 mm for a) U_{∞} =4.0, b) U_{∞} =5.0, and c) U_{∞} =6.0 mm

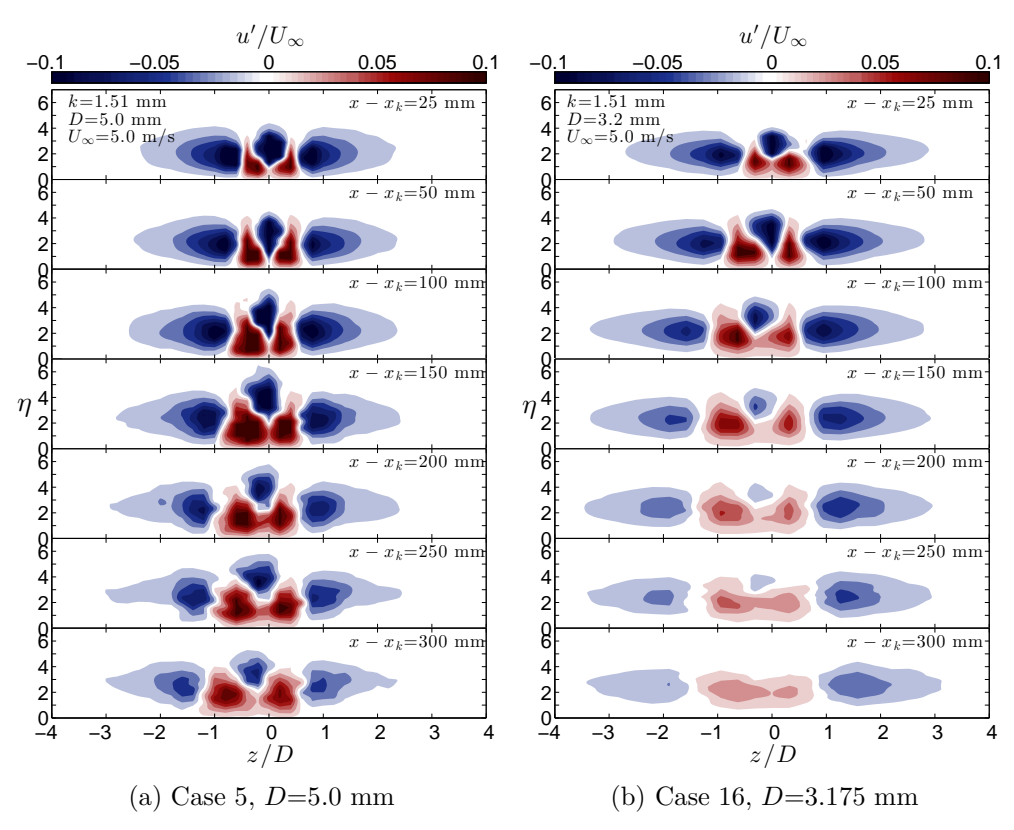


Figure 3.10: Spatial development of the y-z planar disturbance with variable D and constant k=1.51 mm and U_{∞} =5.0 m/s for a) D=5.0 and b) D=3.175 mm

picted in Figure 3.3. For all cases, the disturbance spreads in the spanwise as well as the wall-normal direction with increasing x. Notice that the wall-normal coordinate is plotted as η and therefore a disturbance that appears to not spread in the wall-normal direction with x is therefore growing with \sqrt{x} with the boundary layer growth (i.e. via viscous diffusion). There is wall-normal growth in the region $25 \leqslant x - x_k \leqslant 100$ mm, but this growth rate slows within $100 \leqslant x - x_k \leqslant 300$ mm.

For the transitioning cases, k=1.6 and 2.0 mm with D=5.0 mm and $U_{\infty}=5.0$ m/s, the disturbance re-organizes to a "quasi-spanwise uniform" distribution with the negative disturbance farther from the wall and the positive disturbance near the wall. This representation of the data is indicative of the establishment of a more full velocity profile, and hence transition to turbulence. This is demonstrated in Figure 3.11 where the undisturbed boundary layer profile (i.e. Blasius) is subtracted from the disturbed profile, at z=0, to find the disturbance intensity.

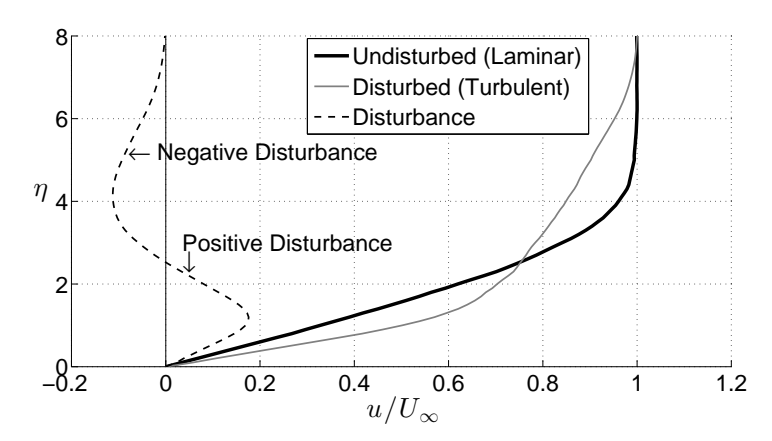


Figure 3.11: Disturbance and Blasius velocity profiles at $(x-x_k, z)=(300,0)$ mm, for k=2.0 mm, D=5.0 mm, and $U_{\infty}=5.0$ m/s. The difference between the two profiles gives the disturbance intensity (- - -)

The analysis of Figure 3.11 demonstrates the transitional character of the boundary layer at large values of x with a sufficiently large k, D, and U_{∞} combination. These results fit well with what was demonstrated via the flow visualization results showing transition for

the same cases. As determined using a hot wire in the boundary layer, and confirmed with the flow visualization results, it is found that with $D{=}5.0$ mm and $U_{\infty}{=}5.0$ m/s, the critical roughness element height for (intermittent) transition is approximately $k{=}1.51$ mm. By examining the disturbance velocity contours for $x{-}x_k{\geqslant}100$ mm in Figure 3.8e, where $k{=}1.51$ mm, the peak of the positive disturbance shifts closer to the wall and the peak of the negative disturbance shifts away from the wall, in comparison to the disturbance in the non-transitional cases. This appearance of the negative disturbance moving away from the wall, or more accurately, being replaced with positive disturbance from turbulent contributions to the phase averaged results, does not appear in Figures 3.8(a-d) where $k{<}1.51$ mm. The change in the arrangement of the high and low speed disturbances, in comparison to the non-transitional cases, appears to begin in the $x{-}x_k{=}100$ mm plane in Figure 3.8f and at the $x{-}x_k{=}50$ mm plane in Figure 3.8g. These first indications of turbulence are in good agreement with the flow visualization assessments of transition which appear to initiate around $50{\leqslant}x{-}x_k{\leqslant}80$ mm and $30{\leqslant}x{-}x_k{\leqslant}50$ mm for $k{=}1.6$ and 2.0 mm, respectively.

For the cases where no transition occurs, $k \le 1.4$ mm, the low-speed wake disturbance experiences a slow decay as x increases, nearly disappearing by x- x_k =300 mm. Conversely, for $k \ge 1.6$ mm, this low speed disturbance does not appear to undergo equally strong decay; although, by examining the intensity of this low speed region, the disturbance reduces from a peak disturbance of $u'/U_{\infty} = 0.226$ at x- x_k =50 mm to $u'/U_{\infty} = 0.113$ at x- x_k =300 mm.

Following Figure 3.8 where the disturbance streamwise development is demonstrated for various roughness element heights with a fixed freestream velocity, Figure 3.9 provides the disturbance for a fixed k and D with varying U_{∞} . The disturbance in this case does not experience transition at any of the investigated freestream velocities and a smooth streamwise development is observed with greater intensity as U_{∞} increases. Figure 3.10b provides the

disturbance induced by a smaller diameter roughness element, D=3.175 mm, with k=1.51 mm and $U_{\infty}=5.0$ m/s. In this case, no transition is observed unlike the intermittent transition which is found with the larger diameter case shown in Figure 3.10a. Also, with the spanwise coordinate normalized by D, the disturbance spanwise extent is similar to that of the larger D non-transitional cases, $-3 \lesssim z/D \lesssim 3$.

The flow visualization results demonstrate non-transitional, intermittent transition, and continuous transition of the boundary layer flow to a turbulent state at various roughness element heights with constant $U_{\infty}=5.0$ m/s and D=5.0 mm. From the hot wire results, it is found that under these conditions, intermittent transition occurs at approximately k=1.51 mm, resulting in $Re_{k\infty}=499$ or $Re_k=340$. In the review by Tani [48] reference is made to [51] in which the critical Reynolds number for transition, $Re_{k,cr}$, is said to vary as follows:

$$Re_{k,cr} = 600 \left(\frac{k}{D}\right)^{2/5}. (3.4)$$

This agrees fairly well with the flow transition characteristics observed for k=1.51 mm, where $Re_k=340$, and the corresponding critical Reynolds number based on Equation 3.4 is $Re_{k,cr}=372$. Thus, intermittent transition is first observed just below this critical Reynolds number. Note that at k=1.4 mm where $Re_k=276$, the critical Reynolds number would be $Re_{k,cr}=360$, thus, transition would not be expected based on Equation 3.4, and it was not observed. Furthermore, at k=1.6 mm where $Re_k=382$, the critical Reynolds number would be $Re_{k,cr}=380$, thus, transition would be expected based on Equation 3.4, as observed. If this same analysis is applied for the smaller diameter roughness element cases, the highest Re_k case, where $U_\infty=5.0$ m/s, k=1.51 mm, and D=3.175 mm, $Re_{k,cr}=446$, while the measured Re_k is 310; thus, transition would not be expected, and is not observed. Extending

the analysis to assess at what k value transition would be expected with the smaller D=3.175 mm, reveals k=1.76 mm as the critical roughness element height. In practice, intermittent transition is first observed at $k \approx 1.70$. Performing the same assessment with D=5.0 mm, results in a critical roughness element heights of k=1.57 mm. Thus, for both roughness element diameters, the critical roughness element height is over predicted by approximately 0.06 mm ($\leq 4.0\%$) for intermittent transition, and by an even smaller amount for continuous transition.

3.3 Disturbance Energy

In oder to quantitatively analyze the streamwise development and evolution of the disturbance induced by the isolated roughness element, the disturbance energy integrated over the y-z plane, E(x), is investigated. The calculation of the total planar disturbance energy,

$$E(x) = \frac{\rho}{2} \int_{z} \int_{y} u'(x, y, z)^{2} dy dz$$
(3.5)

provides an equivalent parameter to the kinetic energy (K.E. = $\frac{1}{2}mv^2$, where m is mass and v is velocity) of the flow disturbance per unit streamwise length.

The use of Equation 3.5 to account for the disturbance energy is appropriate for the isolated roughness element situation where the disturbance velocity goes to zero $(u' \to 0)$ as y and $z \to \infty$. Thus, the result of the integral is finite. Alternatively, there have been extensive investigations of roughness element arrays, wherein the wall-normal sum of $u'^2_{rms,z}$ provides an appropriate indication of the energy, for a spanwise-periodic disturbance, which does not decay to zero at large z locations, but repeats with a wavelength equal to the roughness element spacing. In this case, the disturbance energy per unit spanwise wavelength (Δz) ,

 $E_{rms}(x)$, is obtained:

$$E_{rms}(x) = \frac{\rho}{2} \int_{y} \left(\frac{1}{\Delta z} \int_{z} u'(x, y, z)^{2} dz \right) dy = \frac{\rho}{2} \int_{y} u'_{rms, z}(x, y)^{2} dy.$$
 (3.6)

In either case, the motivation is to assess the disturbance energy growth or decay with increasing downstream distance. Figure 3.12 provides the total y-z planar disturbance energy induced by an isolated roughness element with various heights and diameters and under a range of freestream velocities.

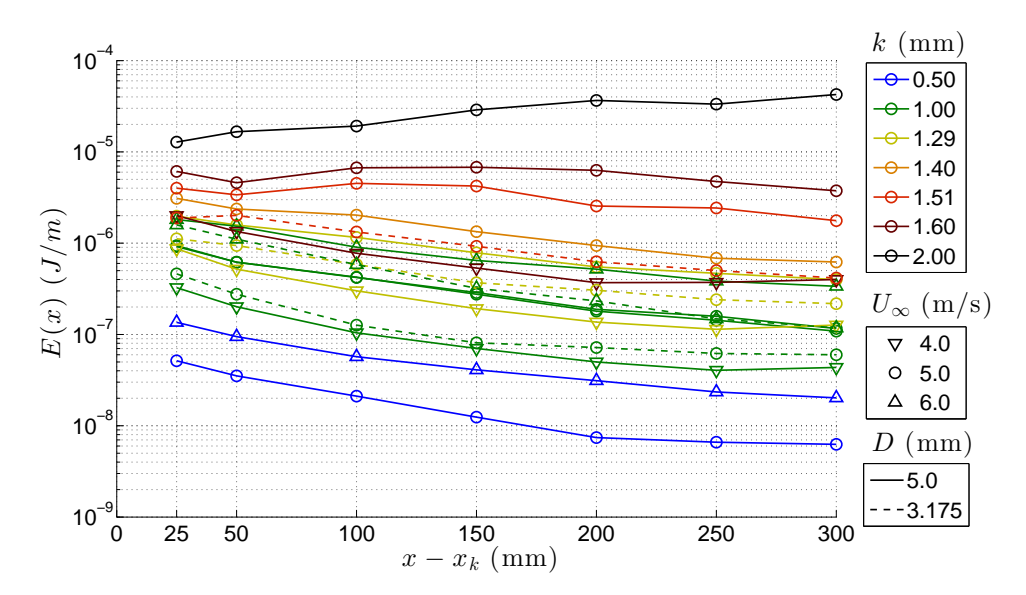


Figure 3.12: E for various k, U_{∞} , and D combinations for an isolated roughness element. See Table 2.1 for the complete parameter definitions for each case.

Note that the colors of the markers and lines in Figure 3.12 are representative of the roughness element height, k, the symbols are representative of the freestream velocity, U_{∞} , and the solid/dashed lines differentiate between the roughness element diameters, D; see Table 2.1 for the complete set of parameter definitions and symbols for each case. Also, the disturbance energy is presented here on a logarithmic scale in order to more easily visualize the wide range of energy magnitudes.

As would be expected, the total planar disturbance energy increases with an increase

in roughness element height, diameter, or freestream velocity. For all cases, except those identified as transitional, a continuous decay in total disturbance energy is observed. Any slight increase at the most downstream locations is within the measurement uncertainty and, hence is indicative of an essentially unchanging disturbance energy, rather than an indication of systematic disturbance growth. For the transitional cases, $k \ge 1.51$ mm with D=5.0 mm and $U_{\infty}=5.0$ m/s, an increase in disturbance energy with x is observed starting at locations consistent with the values identified in §3.2.2 to coincide with the first observations of instability; specifically, $50 \le x - x_k \le 100$ mm for k=1.51 and 1.6 mm, and $25 \le x - x_k \le 50$ mm for k=2.0 mm.

In order to assess the repeatability of the results shown in Figure 3.12, ten repeated measurements were acquired at x- $x_k = 25$ and 300 mm, for the case of k = 1.0 mm, $U_{\infty} = 5.0$ m/s, and D = 5.0 mm (case 2 or 9). For the most upstream location, x- $x_k = 25$ mm, the variability in the total disturbance energy of the repeated measurements was $\pm <3.75\%$; while for x- $x_k = 300$ mm, the variability was $\pm <7.0\%$. Additionally, for the same flow and geometrical parameters, measurements were repeated once at all streamwise locations; these results are provided in Figure 3.12 as cases 2 and 9 (both depicted using green circles and solid line). These cases show very good agreement at all locations with the most variability occurring at x- $x_k = 25$ and 300 mm, which is why these locations were selected for the repeatability checks with 10 samples and should represent the maximum variation.

Interestingly, there is no indication of transient growth in these results, which would be discernible by an energy amplification with x, with an eventual decay or transition event. Previous studies involving roughness element arrays ([52], [19], [54]), have provided clear observations of transient growth in the near roughness element region, which may or may not lead to transition. The transient growth mechanisms are explained in more detail, for

example, by Reshotko [42] and White et~al.~ [54], or in §1.2. In short, three-dimensional disturbances in the boundary layer can exhibit brief inviscid amplification with x, before exhibiting exponential viscous decay at sub-critical Reynolds numbers, resulting in transient growth (sometimes referred to as algebraic growth, to distinguish it from the exponential growth exhibited by amplified modal disturbances). During this short-lived growth, the disturbance may become strong enough to excite secondary instabilities that ultimately lead to turbulent flow. Examples of transient growth leading to transition and transient growth followed by viscous decay without transition, are demonstrated in Ergin and White [18].

The total disturbance energy, E, is an integral representation over the y-z plane, and hence it may not give accurate representation of the energy of the individual coherent flow features within the boundary layer: low-speed wake, and low- and high-speed vortex induced streaks. Figure 3.13 identifies these disturbance structures in a representative contour plot of the y-z planar disturbance velocity.

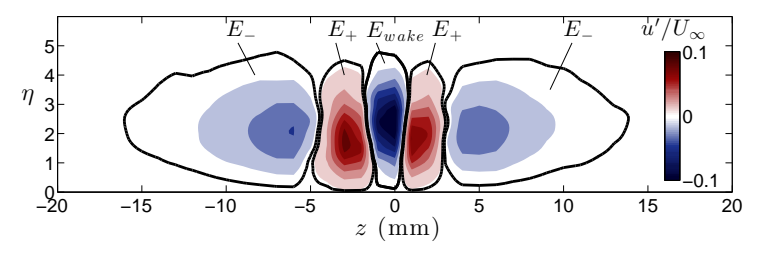


Figure 3.13: Definition of three identifiable velocity disturbance regions: The low speed wake disturbance (E_{wake}) , the vortex induced high-speed disturbance (E_{+}) , and the vortex induced low-speed disturbance (E_{-}) ; same data as Figure 3.21, case 3, x- $x_k = 100$ mm. Note that the feature outlines are drawn at $u'/U_{\infty} = \pm 0.003$.

In practice, the summation of all positive planar disturbance energy is used to calculate the y-z plane energy, E_+ (if the energy is summed only in the near vicinity of the positive streak, versus the entire measurement plane, a 0.1% reduction is found, i.e. a negligible difference). The energy from the negative disturbance induced by the vortex-pair, E_- is

found by summing all negative disturbance energy located at greater |z| locations than the maximum positive disturbance at each wall-normal distance. Similarly, the negative wake energy, E_{wake} is extracted as the negative disturbance located at smaller |z| locations than the maximum positive disturbance at each wall-normal distance. Thus, an investigation into the contribution to the total planar disturbance energy from these individual features is conducted and the streamwise development of the energy of each disturbance feature is investigated in detail. Figure 3.14 provides the streamwise development of the total disturbance energy for cases corresponding to all seven roughness element heights, with D=5.0 mm and U_{∞} =5.0 m/s (cases 1-7) along with the contribution to the total disturbance energy by the low-speed wake disturbance, and the high- and low-speed vortex-induced streak disturbances.

For the non-transitional cases, Figures 3.14(a-d), a monotonic decay of the total disturbance as well as the wake and low-speed disturbance is observed. However, the positive disturbance, E_+ , experiences various levels of growth over $25 \leqslant x \cdot x_k \leqslant 100$ mm before decaying at larger downstream locations, as would be expected from a disturbance experiencing transient growth without exciting secondary instabilities. Notably, the streamwise growth rate of E_+ , over the range $50 \leqslant x \cdot x_k \leqslant 100$ mm becomes stronger as k increases. Also, in Figure 3.14d, the negative vortex-induced disturbance is seen to grow in strength over $50 \leqslant x \cdot x_k \leqslant 100$ mm for the first time. These trends for E_+ and E_- continue for the intermittently-transitional case, Figure 3.14e, although the increase in energy from $50 \leqslant x \cdot x_k \leqslant 100$ mm is larger and sufficient to cause the total energy, E_+ , to exhibit growth over this streamwise region. For the continuously transitional case with lower E_+ , figure 3.14f, the high-speed vortex-induced energy, E_+ , demonstrates a prolonged region of disturbance growth over the region: $25 \leqslant x \cdot x_k \leqslant 150$ mm. Notably, both E_- and E_w do not exhibit any sustained, appreciable energy growth in

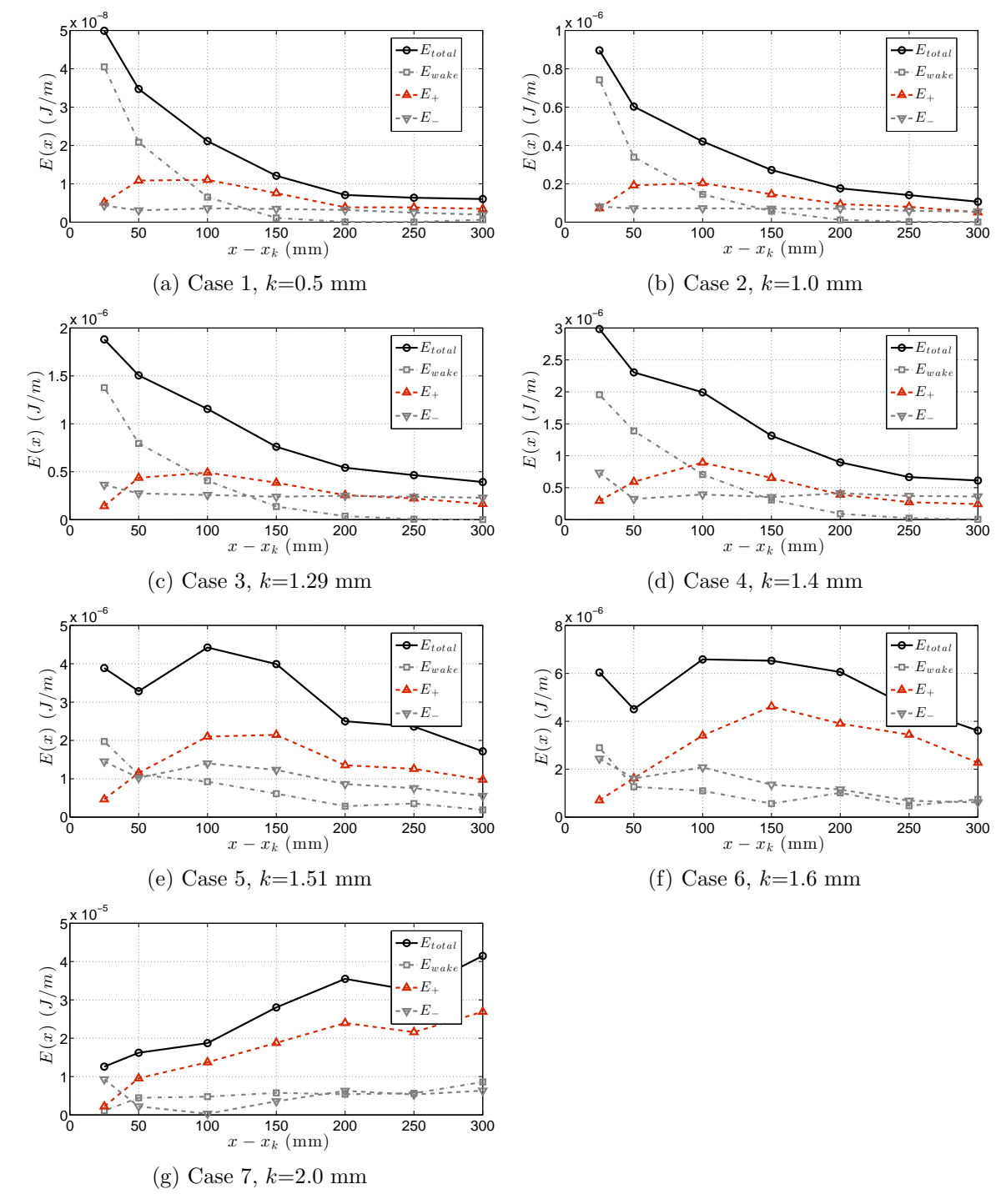


Figure 3.14: Streamwise evolution of the total disturbance energy, E, as well as the contribution from the low-speed wake (E_{wake}) , positive vortex-induced (E_+) , and negative vortex-induced (E_-) streaks for D=5.0mm and $U_{\infty}=5.0$ m/s with a) k=0.5, b) k=1.0, c) k=1.29, d) k=1.4, e) k=1.51, f) k=1.6, and g) k=2.0 mm

the transient growth region or in the downstream regions. Finally, the larger-k continuously-transitional case is provided, Figure 3.14g, and exhibits a continuously growing total disturbance which is dominated by the contribution from E_+ . A very important note, the calculation methodology to find the energy contribution for each disturbance feature was not altered for the transitional cases. Thus, where the boundary layer profile has become turbulent, and exhibits a top/bottom wall-normal split in positive/negative disturbance velocity (as described in Figure 3.11), E_+ is then representative of the total disturbance energy and no longer simply the contribution from a coherent vortex-induced streak. A similar consequence exists for the negative disturbance energy, which results in the total negative disturbance energy being arbitrarily split between E_- and E_w .

Collectively, these results suggest that the onset of transition is caused by the transient growth of the high-speed streak becoming sufficiently amplified to trigger secondary instabilities.

3.4 Disturbance Energy Density

The analysis of total planar disturbance energy is instructive regarding the overall disturbance development; however, it does not provide an appropriate metric for assessment of disturbance amplitude growth or decay, which is required for linear stability theory analysis. Linear stability theory provides an attractive method for analyzing the onset of secondary instabilities (instabilities relative to a basic state which includes the streak disturbances). Toward this end, the measurement of disturbance energy, which incorporates an integrated disturbance contribution over the entire disturbance plane, provides a more robust metric for growth/decay analysis than a simple amplitude measure, A(x), based on the peak-to-peak

disturbance velocity over a given y-z plane,

$$A(x) = (u'_{max,yz} - u'_{min,yz})/2U_{\infty}, \tag{3.7}$$

which has been used commonly in analytical [2] and experimental [4] analyses (other examples of disturbance amplitude analysis: [6], [19]). As demonstrated by Andersson et al. [2], the total disturbance energy and the disturbance amplitude may not follow the same streamwise trend of growth and decay, Figure 3.15 provides a reproduction of the results which Andersson et al. developed in order to demonstrate this point. Clearly, the normalized total disturbance energy, E/E_0 , monotonically increases in Figure 3.15a, whereas the disturbance amplitude, A, experiences a region of transient growth followed by decay. For comparison between these analytical result, and the current experimental results, Figure 3.16 provides the disturbance peak-to-peak amplitude results for those cases for which the energy was provided in Figure 3.12. In contrast to the Andersson results, but not contradictory, a systematic decay of the the overall peak-to-peak disturbance amplitude is observed. In the further analysis by Andersson et al. [2], it is found that the marginal stability for secondary instability falls with an amplitude of approximately 26% of the freestream. Figure 3.16 includes a dashed line at the $u'/U_{\infty}=0.26$ level and it is immediately clear that the continuously transitional cases are the only cases with a disturbance amplitude which exceeds 26%.

Following this motivation to focus on disturbance amplitude, for investigation with linear stability theory consideration, it is recognized that a peak-to-peak based definition of the amplitude is prone to spurious disturbance peaks as can be found in experimental data. Thus, the development of a disturbance amplitude, based on a integral rather than a point quantity

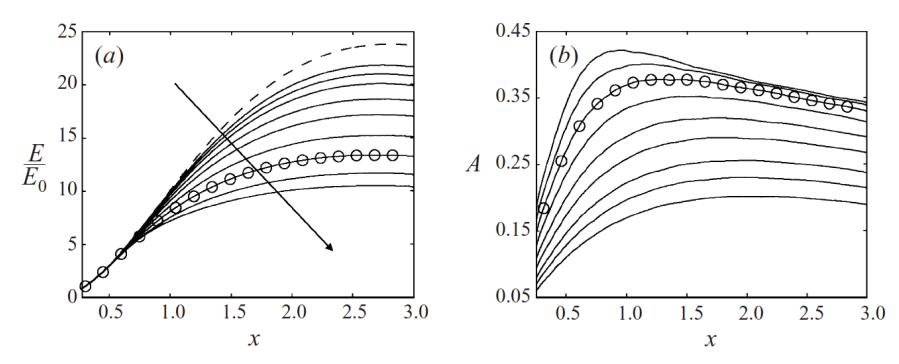


Figure 3.15: An example of disturbance a) energy, E, normalized by the energy at x=0.3, E_0 and b) amplitude, A, for a streak to demonstrate that the total disturbance energy and the disturbance amplitude may not follow the same streamwise trend of growth and decay. (This figure is borrowed from Andersson $et\ al.\ [2]$)

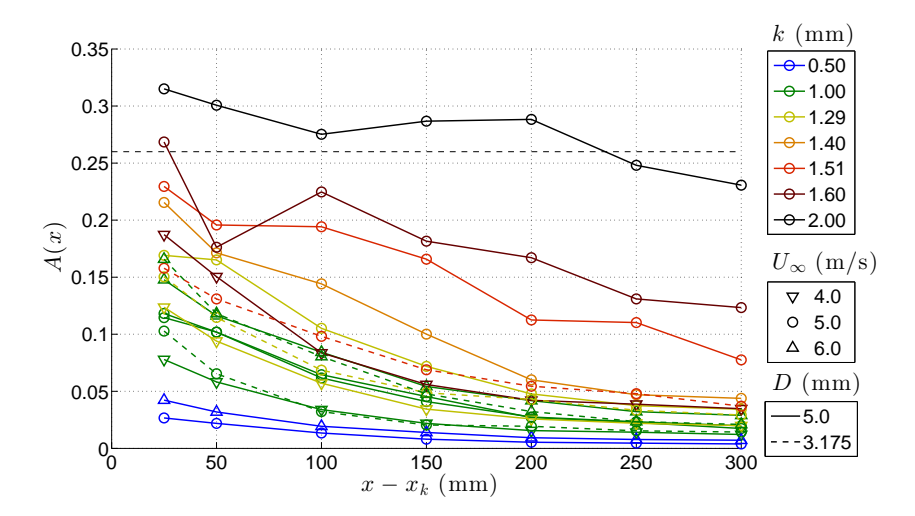


Figure 3.16: A for various k, U_{∞} , and D combinations for an isolated roughness element. The marginal stability amplitude, A(x)=0.26, is noted with a black dash line with no symbols. See Table 2.1 for the complete parameter definitions for each case.

is attractive with the intention of better capturing the growth or decay of disturbances that may initiate secondary instabilities. This development will be done for the total disturbance, with the intention that future work will focus on a measure of the amplitude of the individual disturbance features.

To facilitate the development of a representative disturbance amplitude, an example signal is considered. If the maximum amplitude of the disturbance remains constant, below the threshold to become unstable, but the spanwise extent grows, then the total disturbance energy will indicate a growing energy in x. However, because the amplitude does not increase, this growing total disturbance is no more likely to initiate secondary instability. Figure 3.17 demonstrates this schematically for an idealized (sine wave) disturbance signal. For this example, an artificial disturbance magnitude is plotted versus the spanwise coordinate, representative of a typical streak signature at some wall-normal location. The disturbance amplitude remains constant, but the spanwise extent of the disturbance grows from the top-to-bottom plots. Clearly, the integrated total energy contribution would be larger for the wider disturbance of Figure 3.17(bottom); however, because the amplitude has not increased, the streak is not expected to be any less stable.

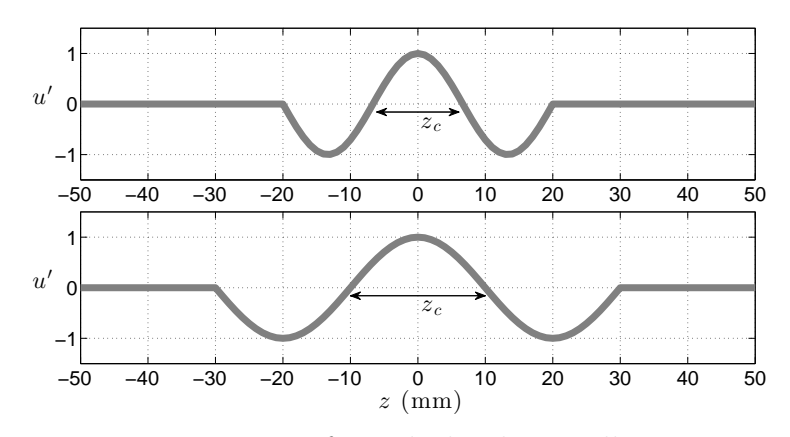


Figure 3.17: Schematic representation of an idealized spatially growing streak disturbance without amplification.

A logical method to account for this spanwise spreading is to develop spanwise length scale for normalization of the energy. In the example discussed in Figure 3.17, the spanwise extent of the positive region, z_c , could be used for normalization, which results in an equal integrated normalized energy for the top and bottom disturbance profiles.

From this example it is shown that spatial normalization of the disturbance is a necessary step in order to assess the disturbance energy in a meaningful regard, in the context of linear stability theory. This section is dedicated to developing spatial normalization for the y-z planar energy. The normalized total planar disturbance energy will be defined as the Energy Density, e. Extending the above ideas to two-dimensions to characterize the boundary layer disturbance over individual y-z planes, characteristic length scales in the wall normal, y_c (or alternatively η_c , where η_c = y_c / δ), and spanwise, z_c , directions are defined in §3.4.1 and §3.4.2, respectively. The calculation of the energy density term, e, is then given by:

$$e(x) = \frac{\rho}{2} \frac{1}{y_c(x)z_c(x)} \int_z \int_y u'(x, y, z)^2 dy dz = \frac{E(x)}{y_c(x)z_c(x)}.$$
 (3.8)

Figure 3.18 provides an example of the determination of η_c and z_c which will be fully described in §3.4.1 and §3.4.2, respectively.

3.4.1 Wall-Normal Characteristic Length Scale

Determination of a wall-normal length scale that captures disturbance spreading is a necessary step in obtaining the disturbance energy density, as defined in Equation 3.8. For the isolated roughness element, a good measure of this spreading may be found by inspection of the wall-normal distribution of the disturbance energy. To arrive at this distribution, the integral for E (Equation 3.5), is only carried along the z direction, to yield a y-dependent

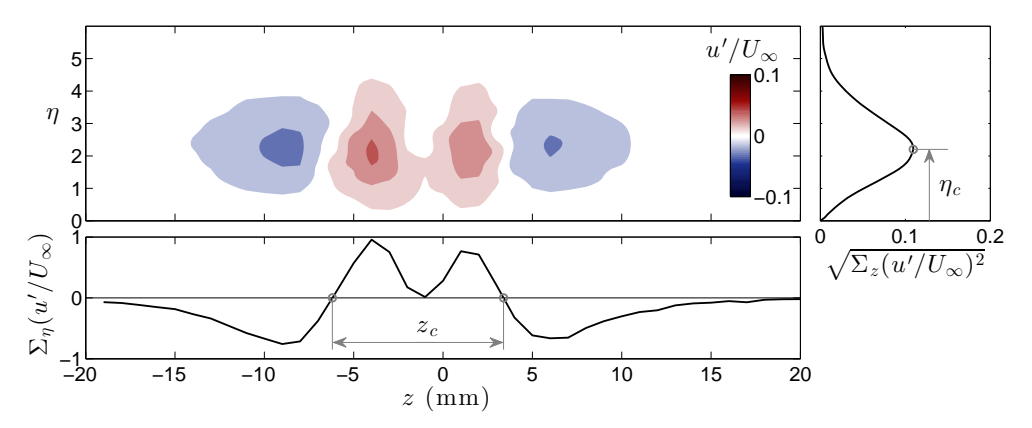


Figure 3.18: Demonstration of the characteristic wall-normal and spanwise length scales (η_c and z_c , respectively) for k=1.29 mm, D=5.0 mm, and $U_{\infty}=5.0$ m/s, located at x- $x_k=300$ mm. In the top-left plot is the contour plot of the disturbance velocity. The top-right plot demonstrates the root of the sum-in-z of the square of the disturbance velocity, the peak of which gives the characteristic wall-normal length, η_c . The bottom plot demonstrates the sum-in-y of the disturbance velocity with the zero-crossings distance representative of the spanwise characteristic length scale, z_c .

measure of the disturbance energy, which is effectively the sum of u'^2 over all z values at a given height. Examples of the resulting η -distribution (after taking the square root of the summation to express in terms of velocity) are shown in Figure 3.19 for various k values, D=5.0 mm and $U_{\infty}=5.0$ m/s at two streamwise locations: x- $x_k=25$ and 100 mm.

As seen from Figure 3.19, the wall-normal location of the profile's peak is taken as a measure of the disturbance wall-normal characteristics scale (η_c). To highlight this feature, in Figure 3.19, the peak value for each profile is identified with a circular marker; the η value at these markers indicates η_c .

In Figure 3.19a, a slight increase in η_c occurs with increasing k. At this plane, which is nearest to the roughness element, the location of peak disturbance is very close to the typical value of 2.2 found in periodic-roughness studies (see [30], [19]). In Figure 3.19b, the η_c location of the non-transitional cases ($k \leq 1.4$ mm) is approximately $\eta=2$. For the transitional cases ($k \geq 1.51$ mm), η_c drops significantly with its value appearing to reduce

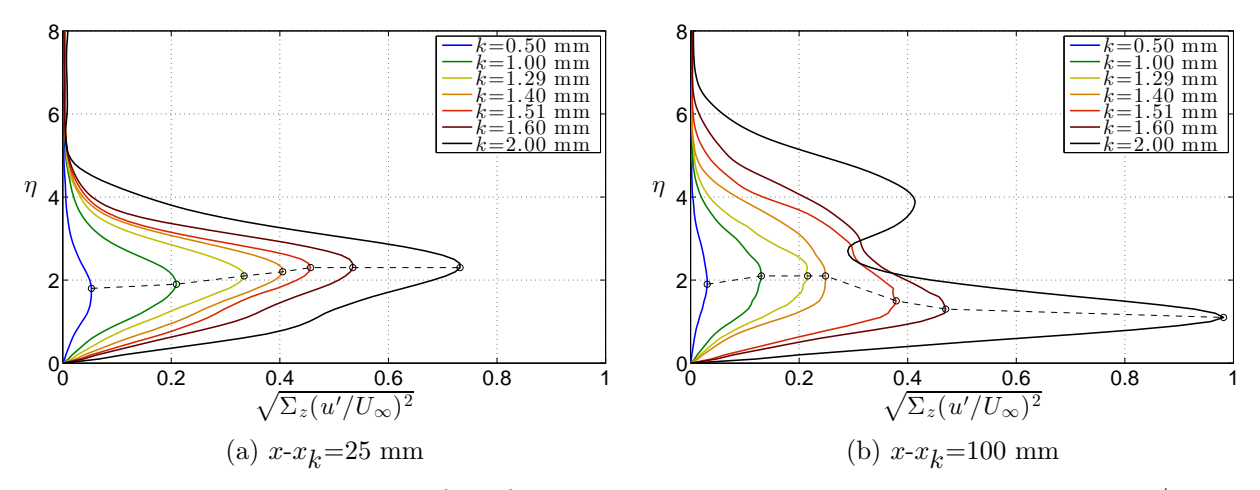


Figure 3.19: Determination of η_c for various k with $D{=}5.0$ mm and $U_{\infty}{=}5.0$ m/s, at a) $x{-}x_k{=}25$ mm and b) at $x{-}x_k{=}100$ mm

with increasing k. Figure 3.20 provides the streamwise evolution of η_c for all investigated cases.

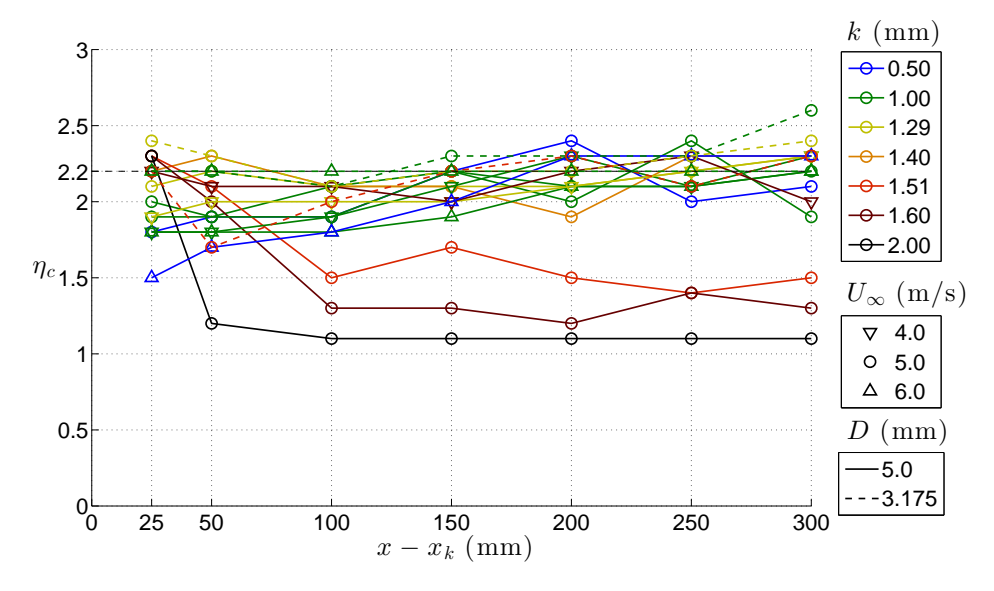


Figure 3.20: Streamwise evolution of η_c for various values of k, D, and U_{∞} . See Table 2.1 for the complete parameter definitions for each case.

For the continuously transitional cases of k=1.6 and 2.0 mm, η_c reduces in value to 1.3 and 1.1, respectively, and essentially remains at these levels through $100 \leqslant x-x_k \leqslant 300$ mm. This decrease in the wall-normal location of the peak disturbance energy arises due to the mean

velocity profile for the case of continuous transition becoming fuller and having the greatest difference from the undisturbed Blasius profile close to the wall, as described in §3.2.3, and depicted in Figure 3.11. Furthermore, the cases with transition $(k \ge 1.51 \text{ mm}, D=5.0 \text{ mm},$ and $U_{\infty}=5.0$ m/s) undergo this sharp decrease in η_c in the range previously designated as the region of first observed transition (§3.2.2). The non-transitional cases reach a nominal value of η_c = 2.2, similar to published periodic roughness results, at the streamwise distance of approximately $x-x_k=200$ mm from the roughness element. The variability in the η_c values in the $200 \le x - x_k \le 300$ mm region demonstrates no systematic change with k, D, or U_{∞} and is therefore due to experimental error and corresponds to variation of $\eta_c=2.2\pm0.2$. In the near element plane, $x-x_k=25$ mm, the η_c values are organized according to k and U_{∞} with larger η_c corresponding to larger k or smaller U_{∞} . This systematic variation of η_c may be a reflection of the time required for the peak disturbance to evolve towards an asymptotic value of η_c =2.2. A larger k results in the disturbance initiating at larger wall-normal location within the boundary layer, while a smaller U_{∞} results in a greater time for the disturbance to reach the measurement locations, which allows for shorter streamwise fetch before η_c reaches a value of 2.2.

3.4.2 Spanwise Characteristic Length Scale

An appropriate spanwise length scale for the isolated-roughness disturbance does not have an equivalent in the roughness element array situation, where the spanwise length scale is set by the roughness element spacing, Δz . Thus, the introduction of a new characteristic spanwise length scale, z_c , is required for computation of the energy density. The scale employed is based on the spanwise distribution of the disturbance velocity. A wall-normal-averaged representation of this distribution is arrived at by summing the wall-normal disturbance

spanwise velocity profiles obtained at all y locations. The summation reveals a length scale that is representative of the spanwise spacing of the vortex-pair illustrated in Figure 3.3. To clarify, consider Figure 3.18 (bottom plot) which demonstrates the outcome of the disturbance velocity summation $(\Sigma_{\eta}(u'/U_{\infty}))$ for k = 1.29 mm, D=5.0 mm, and $U_{\infty}=5.0$ m/s, at $x-x_k=100$ mm. The outboard zero-crossing points of the resulting disturbance profile are well-defined points that are chosen to characterize the disturbance spanwise length scale. It is suspected that these locations correspond to the vortex centers with the positive and negative disturbance regions existing on opposites of the zero-crossing (though this inference is not central to the objectives of this study). In practice, to find the zero crossings, a center point is manually selected and the processing algorithm searches to the left and right of the center location for zero-crossing points with positive (left of center) and negative (right of center) slope. The need for the slope-sign consideration arises where the center-point is in the low-speed (negative disturbance) wake region. In this situation, the first zero-crossings outward-from-center do not correspond to a vortex center but rather to the wake/high-speedstreak interface. The example shown in Figure 3.21 is representative of this situation. The figure also depicts the scale z_c for the case shown, in the lower plot.

Figure 3.22 provides the streamwise evolution of z_c . In the near roughness element region of $25 \leqslant x - x_k \leqslant 200$ mm, there appears to be a systematic dependence on roughness element height and diameter, as well as freestream velocity. These dependencies appear to diminish farther downstream, where there does not seem to be a correlation between k or U_{∞} with z_c .

Unlike the wall-normal characteristic length scale, there is no meaningful spanwise characteristic length scale, as defined here, for cases where secondary instabilities (i.e. transition) has occurred and therefore these cases are omitted from Figure 3.22. Examining the spread-

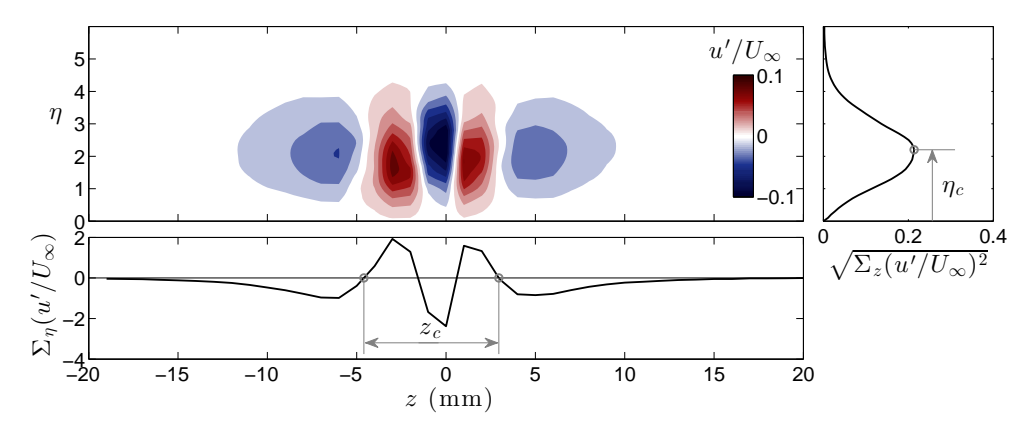


Figure 3.21: Demonstration of the characteristic wall-normal and spanwise length scales (η_c and z_c , respectively) for k=1.29 mm, D=5.0 mm, and $U_{\infty}=5.0$ m/s, located at x- $x_k=100$ mm. In the top-left plot is the contour plot of the disturbance velocity. The top-right plot demonstrates the root of the sum-in-z of the square of the disturbance velocity, the peak of which give the characteristics wall-normal length, η_c . The bottom plot demonstrates the sum-in-y of the disturbance velocity with the zero-crossings distance representative of the spanwise characteristic length scale, z_c .

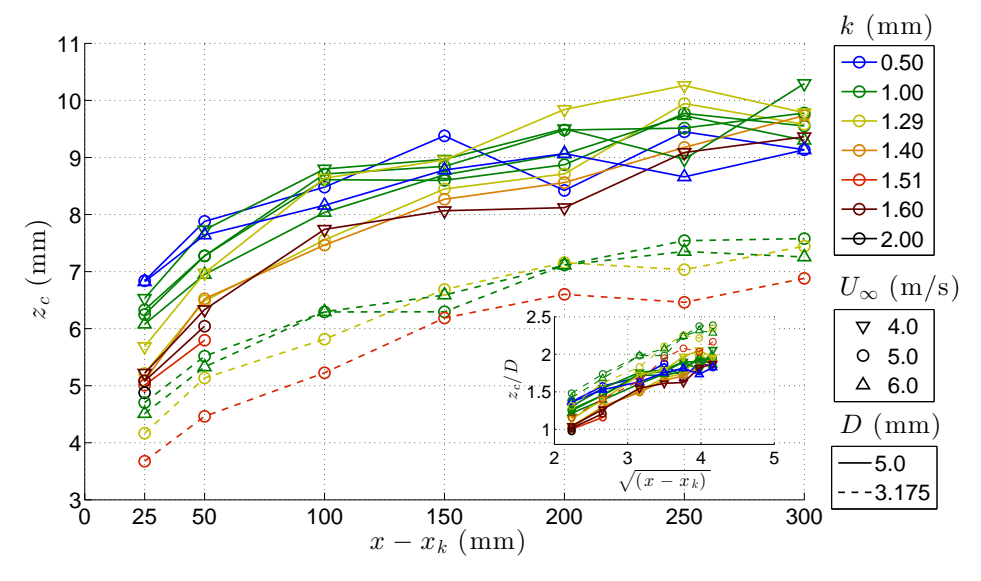


Figure 3.22: Streamwise evolution of z_c for various k, D, and U_{∞} combinations for an isolated roughness element; note, the transitional cases are removed because the z_c characteristic length scale is not appropriate for these cases given the fundamental change in the shape of the spanwise distribution of the disturbance velocity.

ing rate of z_c , for all cases, as expected, there is a monotonic spanwise growth of z_c throughout the streamwise measurement domain and the spreading rate decreases downstream. Finally, the inset of Figure 3.22 demonstrates that z_c , when scaled with D, follows an approximately $\sqrt{x-x_k}$ relationship; although this result requires additional investigation.

3.4.3 Disturbance Energy Density Results

With the development of definitions of wall-normal (η_c) and spanwise (z_c) characteristic length scales for the isolated roughness element induced disturbance, it is now possible to calculate the y-z plan-integrated disturbance energy density, e. Figure 3.23 provides the energy density streamwise evolution for the same cases considered in Figure 3.12.

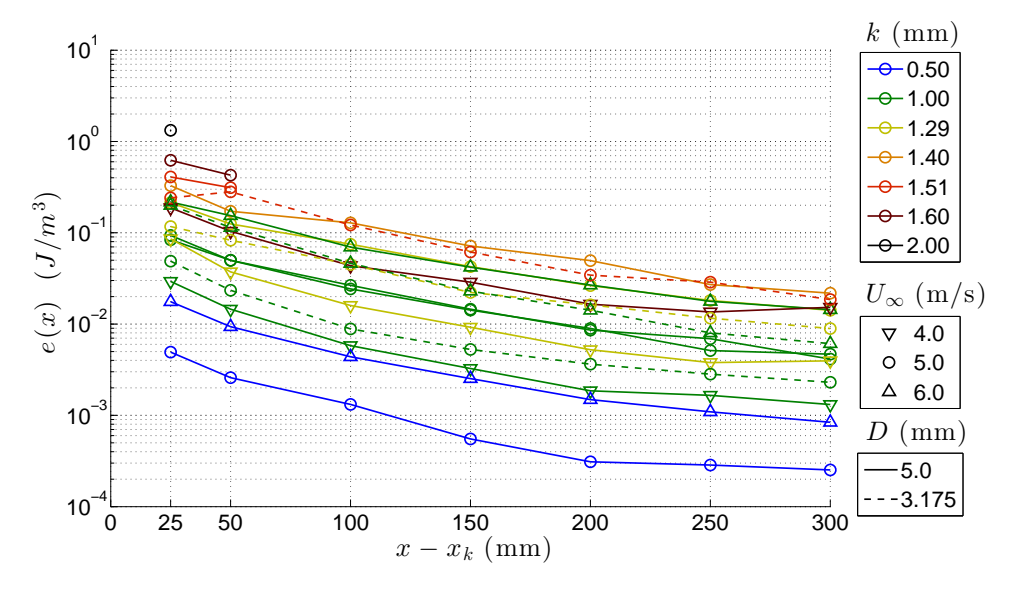


Figure 3.23: The disturbance energy density, e, for various k, U_{∞} , and D combinations for an isolated roughness element. See Table 2.1 for the complete parameter definitions for each case.

Despite similar trends in the streamwise evolution of the disturbance energy (Figure 3.12) and the disturbance energy density (Figure 3.23), there are distinct conclusion to be gained from each representation. By calculating the energy density, the *amplitude* of the

disturbance may be investigated as it develops downstream. It is clear that this amplitude decreases with increasing x for all non-transitioning cases. For the transitional cases, only the results upstream of the onset of instability are provided.

3.5 Disturbance Energy Density Scaling

In the preceding sections, the disturbance produced by an isolated roughness element has been characterized for a range of controllable parameters; namely, roughness element height, roughness element diameter, and freestream velocity. In addition to these results, it is advantageous to examine if the disturbance energy density evolution with x may be scaled using these parameters (i.e. if e(x) and x can be made non-dimensional such that a universal relationship is found between both non-dimensional quantities independent of the geometrical and flow parameters). The energy density provides an integral measurement of the disturbance amplitude and the scaling of this characteristic amplitude may lend insight into the critical parameters in bypass transition.

In previous studies (see, for example, [19], [30], [32], [51]),

$$Re_k = \frac{u_k k}{\nu},\tag{3.9}$$

has been employed to represent the disturbance level introduced by roughness element(s). Furthermore, White et al. [54] demonstrate good scaling of the individual spanwise Fourier modes of the disturbance energy in the domain near a roughness element array using Re_k^2 . In the study by Kurian et al. [32], the modal disturbance energies are demonstrated to collapse well over a larger range of streamwise locations using $Re_k^{2.3}$ for two roughness element heights, although this study used a non-zero pressure gradient swept-wing boundary layer.

It is advantageous however, to develop scaling in terms of *user-controllable* parameters, i.e. parameters that can be prescribed and controlled in a given experiment independent of each other. Toward this end,

$$Re_{k\infty} = \frac{U_{\infty}k}{\nu},$$
 (3.10)

is defined, based on the freestream velocity to generate a prescribable non-dimensional scaling parameter rather than using the boundary layer velocity at the height of the roughness element at the roughness element location, $u_k(x_k)$, which is a dependent rather than independent variable and is therefore less tractable than the independent U_{∞} parameter. The relationship between $Re_{k\infty}$ and Re_k follows directly from the relation between U_{∞} and u_k . In a Blasius boundary layer, these velocities are directly related through the wall shear stress [45], see Equation 2.1, which can be rearranged to provide the velocity gradient in the y range where the velocity of the boundary layer varies approximately linearly. The velocity at the roughness element height, for the undisturbed boundary layer,

$$u_k = k \left. \frac{\partial u}{\partial y} \right|_{y=0},\tag{3.11}$$

demonstrates that while k is an independent variable, the velocity gradient at the location of the roughness element height is a dependent variable, and hence is an unattractive choice for scaling. Thus, under the restriction that k is within the linear range of the velocity profile, the relationship between U_{∞} and u_k is given by:

$$u_k = k(0.332)U_{\infty} \frac{U_{\infty}}{\sqrt{x\nu}} \quad \text{where} \quad \frac{\partial u}{\partial y}\Big|_{y=k} = \frac{\partial u}{\partial y}\Big|_{y=0}.$$
 (3.12)

Finally, with simple manipulations, the relationship between the velocity at the roughness element height and the freestream velocity can be shown to be,

$$u_k = (0.332) U_\infty \frac{k}{\delta(x_k)},$$
 (3.13)

where $\delta(x_k)$ is the Blasius similarity length scale evaluated at the roughness element location.

In the current experiments, the boundary layer thickness at the roughness element location is $\delta_{0.99}(x_k) = 4.0$, 3.65, and 3.3 mm when $U_{\infty} = 4.0$, 5.0, and 6.0 m/s, respectively. If the linear range is assumed to be valid through $y/\delta_{0.99} \lesssim 0.35$, then the relation of Equation 3.13 is applicable for the cases where $k \leq 1.4$, 1.28, and 1.16 mm at $U_{\infty}=4.0$, 5.0, and 6.0 m/s, respectively. The error in a linear assumption for the Blasius profile, over the range $0 \le y/\delta_{0.99} \le 0.35$, is, on average, 0.30% with a maximum error of 1.21%; these error estimates were determined using a least-squares fit of a linear profile to the points following the Blasius solution over this range, with the Blasius profile point-resolution equal to that used in the experiments. For the cases investigated here, and listed in Table 2.1, the majority of the parameter combinations fall within this restriction (cases: 1-3, 8-11, 13-15, 17) with a few of the cases with a larger k value falling outside this range (cases: 4-7, 12, 16). Note that of these cases that fall outside of the linear region, not all cases demonstrate the same non-transitional/transitional state. It is worth noting that for the cases for which Equation 3.13 is valid, the scaling developed here can be converted to Re_k -based scaling using flow state parameters $(k, U_{\infty}, \text{ and } \delta(x_k))$ which are explicitly provided in Table 2.1. For the other cases, the relationship between $Re_{k\infty}$ and Re_k becomes non-linear and Equation 3.13 is no longer accurate to within the above defined linear approximation accuracy. Whether $Re_{k\infty}$ or Re_k is used to scale the disturbance energy, the parameters k, D, and U_{∞} will govern the disturbance energy density evolution with $(x-x_k)$. The scaling of the disturbance energy with each of these three parameters will be investigated individually, in order to learn from trends in the data and arrive at an appropriate *combined* scaling parameter that accounts for the effect of all three parameters together. Note that this investigation will only include streamwise positions where the flow has remained non-transitional.

In the work by White et al. [54] and Ergin and White [18] there was no scaling applied to the streamwise coordinate downstream of the roughness $(x-x_k)$. Fransson et al. [19] investigated the disturbance caused by a roughness element array and used a normalized streamwise length, X, coordinate for a non-zero pressure gradient boundary layer investigation, where $X = (2\pi)^2 C(\delta/\Delta z)^2$, and C was selected to align the fundamental mode (Δz) , and represents the spacing between roughness elements) at X=1. The use of the spanwise roughness element space is not possible in the current isolated roughness element investigation. Therefore, in the present investigations, after an extensive search, it was found that the best scaling (i.e. collapse of data from all cases examined) is achieved when the streamwise coordinate is non-dimensionalized by the viscous length scale, ν/U_{∞} , and scaled with the parameter k/D; this non-dimensional coordinate,

$$(x^* - x_k^*) = (x - x_k) \frac{U_\infty}{\nu} \frac{k}{D} = \frac{(x - x_k)}{D} Re_{k\infty} = \frac{k}{D} (Re_x - Re_{x_k}),$$
 (3.14)

is denote with *starred* labels. Figure 3.24 provides the energy density plotted versus this nondimensional streamwise coordinate and Equation 3.14 demonstrates that the combination of these parameters allows several interpretations, but the combined effect seems to provide the most successful streamwise scaling term.

With the streamwise coordinate normalized and scaled, investigations into the best energy

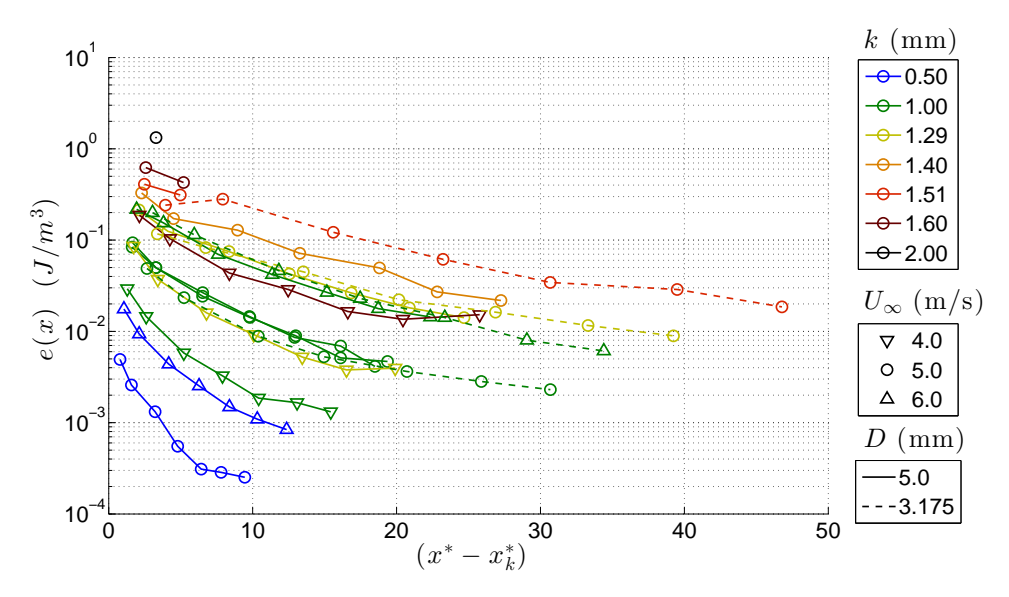


Figure 3.24: The disturbance energy density, e, versus the scaled streamwise coordinate $(x^* - x_k^*)$, for various k, U_{∞} , and D combinations for an isolated roughness element. See Table 2.1 for the complete parameter definitions for each case.

density scaling when k and U_{∞} are varied independently were conducted and the results are presented in Figures 3.25 and 3.26, respectively. In Figure 3.25, when the energy density is scaled with k^6 , the corresponding streamwise evolutions separate into three groupings based on U_{∞} . Similarly, in Figure 3.26, when the energy density is scaled with U_{∞}^6 , the energy density streamwise evolutions organize according to the seven k levels.

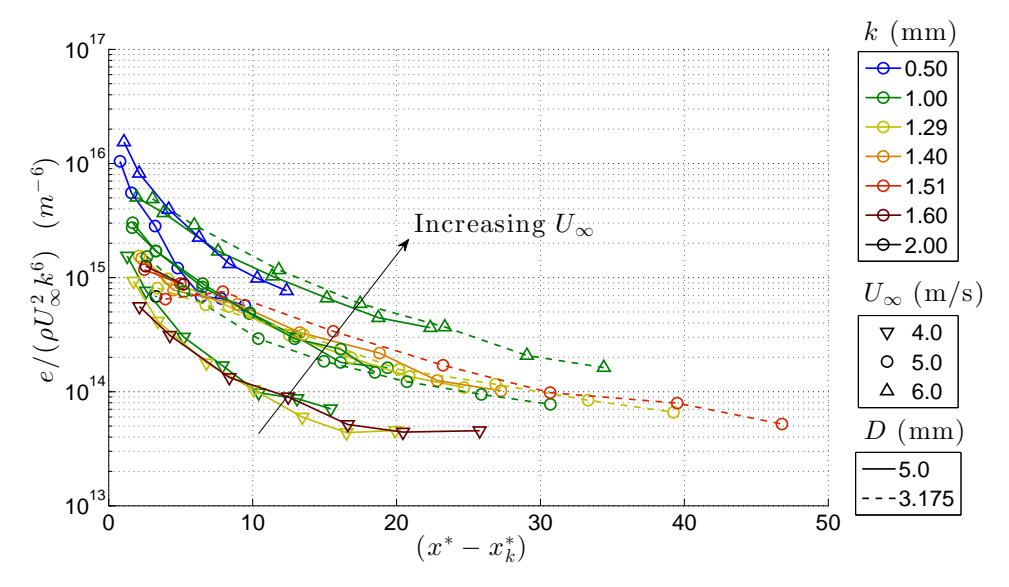


Figure 3.25: $e/(U_{\infty}^2 k^6)$ for various k, D, and U_{∞} combinations

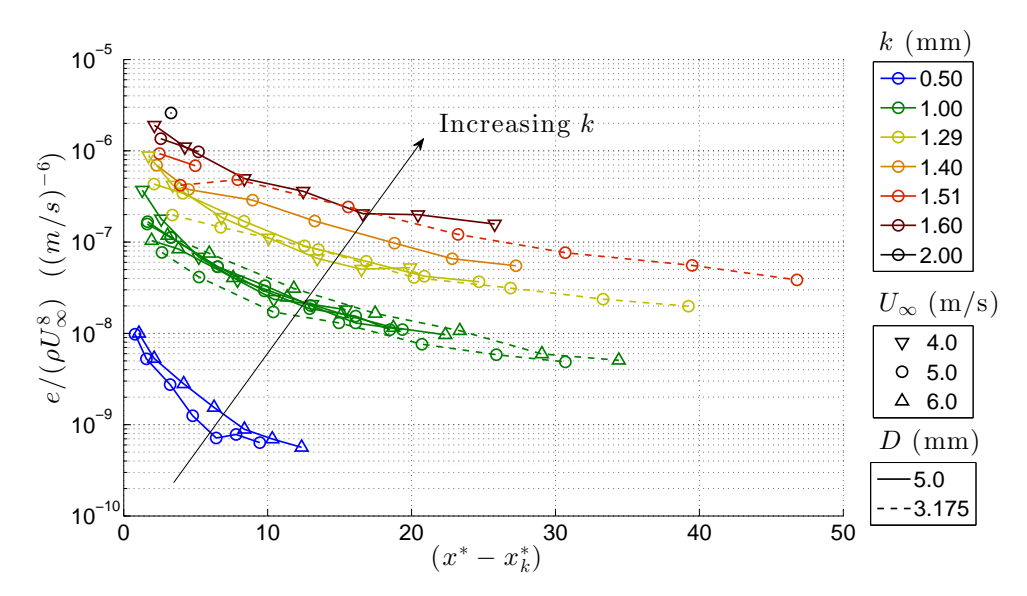


Figure 3.26: e/U_{∞}^{8} for various k, D, and U_{∞} combinations

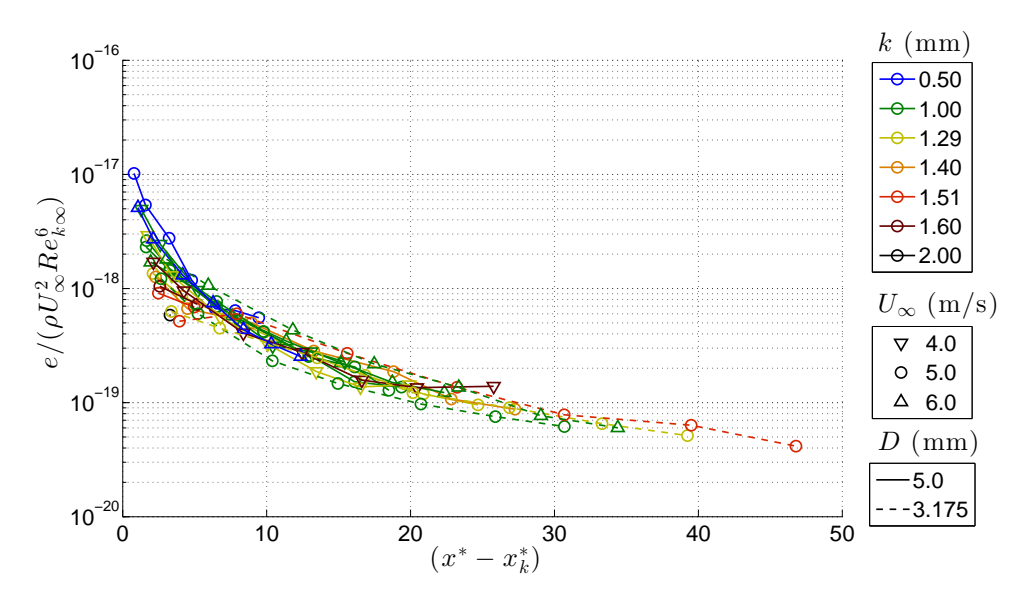


Figure 3.27: $e/(U_{\infty}^2 Re_{k\infty}^6)$ for various k, D, and U_{∞} combinations; semi log plot

Because both k and U_{∞} were found to scale the energy density when raised to the 6^{th} power, this suggests that an appropriate combined scale to account for variation of both parameters is $Re_{k\infty}^6$. Figure 3.27 demonstrates this scaling result on a semi-log plot, and Figure 3.28 provides the same results on a linear scale, with enlargement of the low-energy region and plot lines removed in order to more easily visualize the collapse of the data.

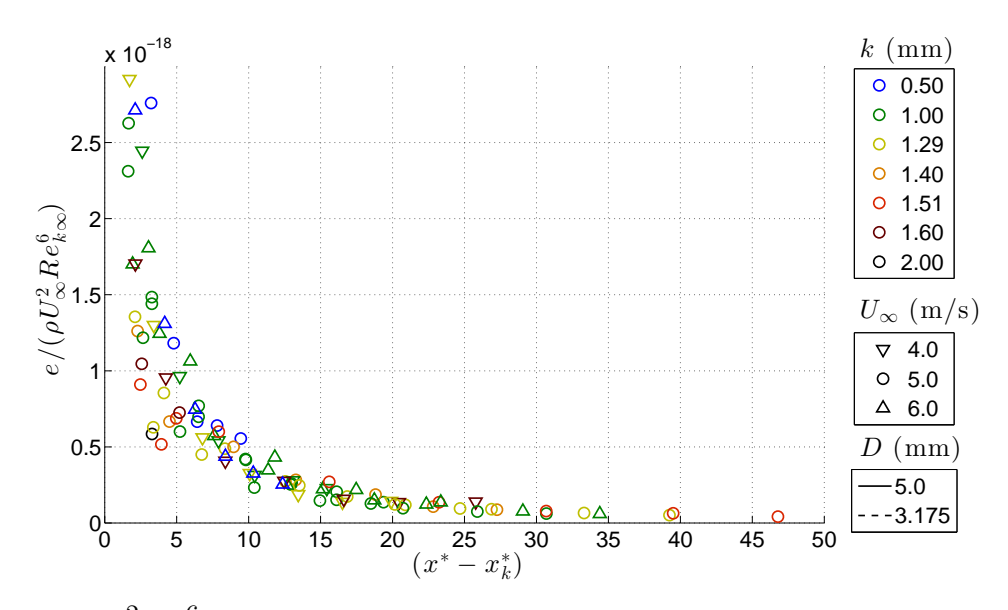


Figure 3.28: $e/(U_{\infty}^2 R e_{k\infty}^6)$ for various k, D, and U_{∞} combinations; linear plot, zoomed in, with no lines

The energy density data collapse well on a single curve with $Re_{k\infty}^6$; however, in the near roughness element region $(x^*-x_k^*) \leq 5$, the data do not collapse as well as in the downstream domain. Two possible causes are: first, the disturbance measurements in this most-upstream region may not be sufficiently resolved with the 1mm z-spacing of the hot wire measurements due to the large spanwise gradients of the disturbance. Furthermore, the 1mm hot wire sensor length may not achieve adequate spatial resolution in this high-spanwise-disturbance velocity gradient region; i.e. the disturbance measurement is inherently averaged over a 1mm spanwise region. Second, there may be wall-normal or spanwise velocity components that are non-negligible in this most-upstream measurement region which the hot wire either does not capture, or do not follow the same scaling argument. In the downstream region, $(x^*-x_k^*) \geq 5$, the data collapse well and the scaling argument presented is demonstrated to be valid over large range of streamwise locations for various k, D, and U_{∞} combinations.

Chapter 4

Unsteady Disturbance Results

The introduction of an unsteady disturbance by using a dynamically actuated roughness element requires careful determination of the roughness element motion parameters that are prescribed to introduce the targeted linearly-growing streak disturbance, without inducing complicated undesirable disturbances. Initial tests using an electromagnetic solenoid to move the roughness element resulted in unwanted disturbances during the roughness element motion, before the steady state disturbance was recovered. The use of the Squiggle® piezoelectric motor, as described in §2.3, allowed careful tuning of the roughness element motion without inducing unwanted (complicated) turbulent disturbances. This section examines the unsteady disturbance growth using the solenoid and Squiggle motor mechanisms and the disturbance growth in time and space is analyzed for the purpose of understanding the development of the disturbance and identifying the roughness element motion parameters that will introduce the desired streak disturbance; which is targeted for control (see Chapters 5 and 6).

4.1 Kinematics of the Unsteady Roughness Element

In order to evaluate the kinematics and resulting disturbance characteristics of a roughness element whose motion is controlled by an electromagnetic solenoid or piezoelectric (Squiggle) motor, a laser position sensor was used to measure the wall-normal height of the roughness element; sampled at 10 kHz. This position versus time information was then used to calculate the velocity and acceleration experienced by the roughness element under each actuation mechanism. The resolution of the laser sensor was within 2-5 μ m, as described in §2.3.

The roughness element actuation parameters of interest were the roughness element height, k, velocity, v_k , and acceleration, a_k . While the electromagnetic solenoid hardware allowed for only a mechanical stop to set the minimum and maximum roughness element deployment positions, the velocity and and acceleration could not be controlled, and hence they reached very high levels. The electromagnetic solenoid operates by generating an electromagnetic field to induce a motion in the ferrous plunger, which draws the plunger toward the electromagnet. Once the magnetic force on the plunger reaches a sufficient level, the plunger is drawn toward the coil. This results in a force acting on the plunger that increases as the plunger moves toward the coil and further into the electromagnetic field; this inherently unstable system results in a roughness element actuation (the roughness element is attached to the plunger) that accelerates until reaching a mechanical stop, which results in a very large velocity during actuation. Once the mechanical stop is reached, an extremely large deceleration is experienced as the plunger (and roughness element) transition from large to zero velocity in an extremely shot period of time. Figures 4.1a and 4.1b demonstrate the position, velocity, and acceleration characteristics for a solenoid driven roughness element deployed to a height of k=0.50 and k=1.29 mm; as measured by the laser position sensor. Note that only the upward roughness element motion is demonstrated here.

The solenoid-produced roughness element motion shows very large spikes in the magnitude of both the velocity and acceleration as the plunger reaches the mechanical stop at time \approx 0.005 s and time \approx 0.01 s, for k=0.5 and k=1.29 mm, respectively. The maximum v_k and a_k magnitude are noted on each figure for reference. Under these roughness element

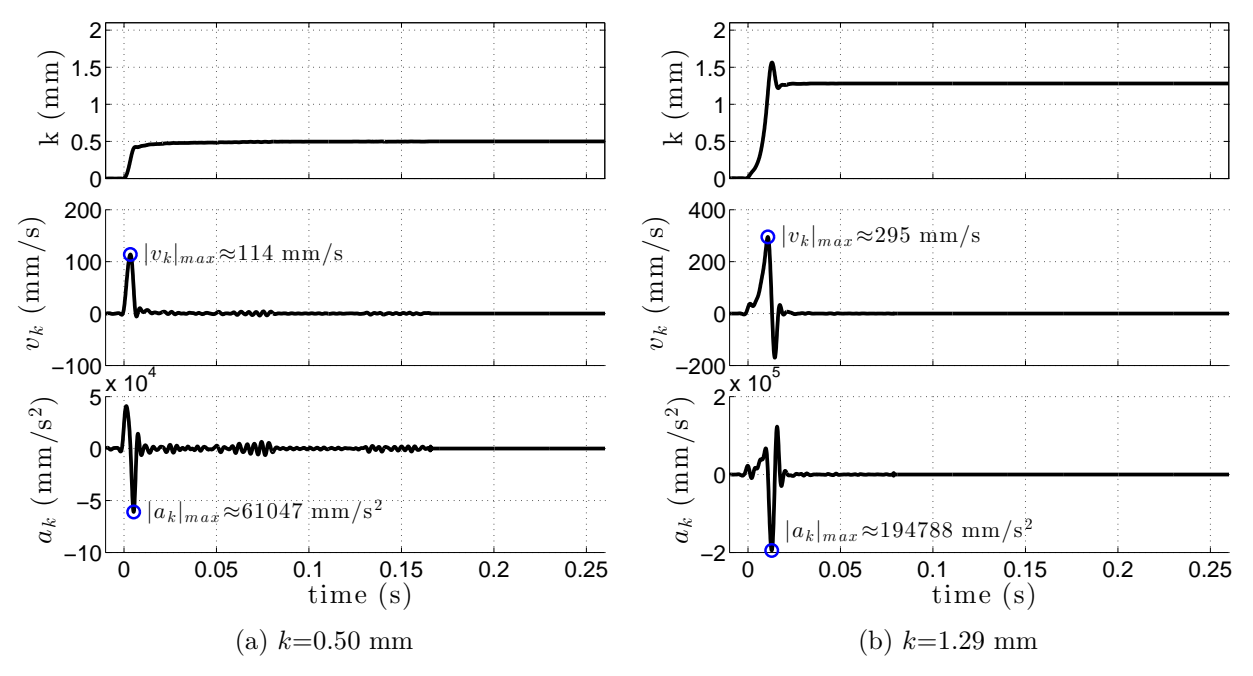


Figure 4.1: Roughness element actuation kinematics, during upward motion, experienced when using the electromagnetic solenoid with a fully deployed roughness element height of a) k=0.50 mm and b) k=1.29 mm.

actuation conditions, the resulting boundary layer disturbance grows and quickly exhibits turbulent signatures that move downstream, generating a turbulent wedge. After the roughness element is fully deployed and held stationary for some amount of time, the boundary layer disturbance relaxes to a non-turbulent, but disturbed, state. In §4.2, measurements of the spatio-temporal disturbance development as the roughness element is deployed under these conditions are presented and discussed.

The piezoelectric Squiggle motor allows for control of the position, velocity, and acceleration of the motion of a drive screw. The drive screw, which is controlled by a servo loop, is used to move a linear rail, which the roughness element is connected to, and thus there is no rotational motion transferred to the roughness element, see Figure 2.2. Many tests were carried out over a range of v_k and a_k using the Squiggle motor. The resulting motion parameters with $v_k = 7.5$ mm/s and $a_k = 1000$ mm/s², for two deployment heights, k=1.29

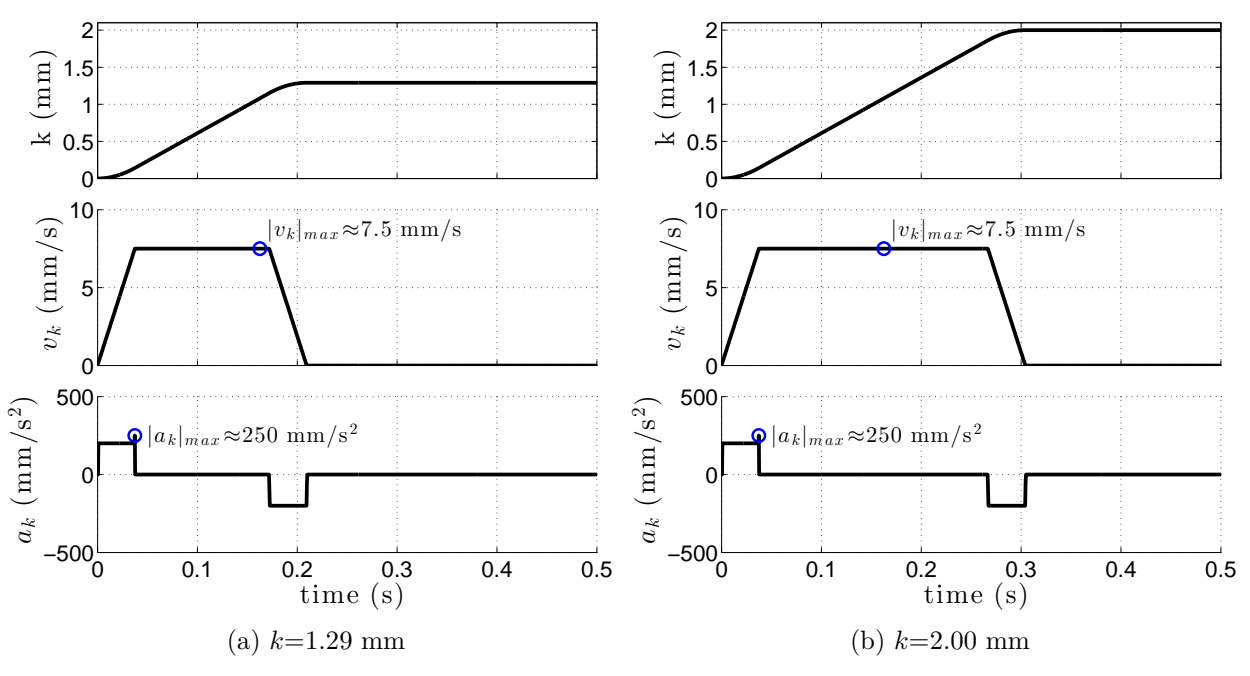


Figure 4.2: Roughness element actuation kinematics during upward motion, experienced when using the piezoelectric Squiggle motor, with a fully deployed roughness element height of a) k=1.29 mm and b) k=2.00 mm.

and k=2.00 mm, are provided in Figures 4.2a and 4.2b, respectively.

The motion of the Squiggle motor actuation provides a prescribed rise of the roughness element and, most importantly, does not exhibit large velocity and acceleration spikes at the start/stop times (time \approx 0/0.2 s and time \approx 0/0.3 s, for k=1.29 and k=2.00 mm, respectively). The objective of these tests was to determine the proper actuation parameters to quickly induce a streak disturbance into the boundary layer, but without nonlinear/undesirable disturbance effects/growth; in order to examine the ability to control this unsteady disturbance in real time. In order to quickly evaluate the presence of turbulence growth under various v_k and a_k combinations, a single downstream hot wire was positioned within the disturbance produced downstream of the roughness element. This hot wire was connected to an oscilloscope which allowed the real-time visualization of the non-turbulent/turbulent disturbance signatures as it convects past the hot wire. These signals were not recorded, and are thus not

provided here, but an estimate of the most appropriate v_k and a_k combination for operation was determined. In the following section, the spatio-temporal growth of the boundary layer disturbance induced by a roughness element actuated with the k, v_k , and a_k noted in Figures 4.1 and 4.2, are provided.

4.2 Unsteady Disturbance Evolution

In order to assess the spatio-temporal growth of the unsteady disturbance induced in the Blasius boundary layer by an isolated roughness element, hot wire data were collected which render the full temporal growth disturbance data at seven measurement planes. The steady-state contour results of §3.2.3 represent a subset of the full temporal disturbance growth results, which were collected for all results presented in §3.2.3. Rather than include all cases, the results for four specified cases (those discussed in §4.1) are presented in order to highlight differences and examine the dynamic response of the boundary layer to the unsteady disturbance. Two cases are presented for the solenoid actuation hardware, and two cases are presented for the Squiggle motor hardware. In Figures 4.3 to 4.6, each case is presented as the streamwise velocity disturbance develops over seven y-z planes, at five times of interest during the upward motion of the roughness element.

In Figure 4.3, as the roughness element moves upward, the disturbance grows in a coherent manner. The disturbances begin at the most upstream plane, and simply grow in strength, while retaining their overall spatial signature shape, as the roughness element is moved upwards. With increasing time, disturbance is convected downstream, and each measurement plane begins with a small disturbance which grows in amplitude until the steady state is reached at t_5 .

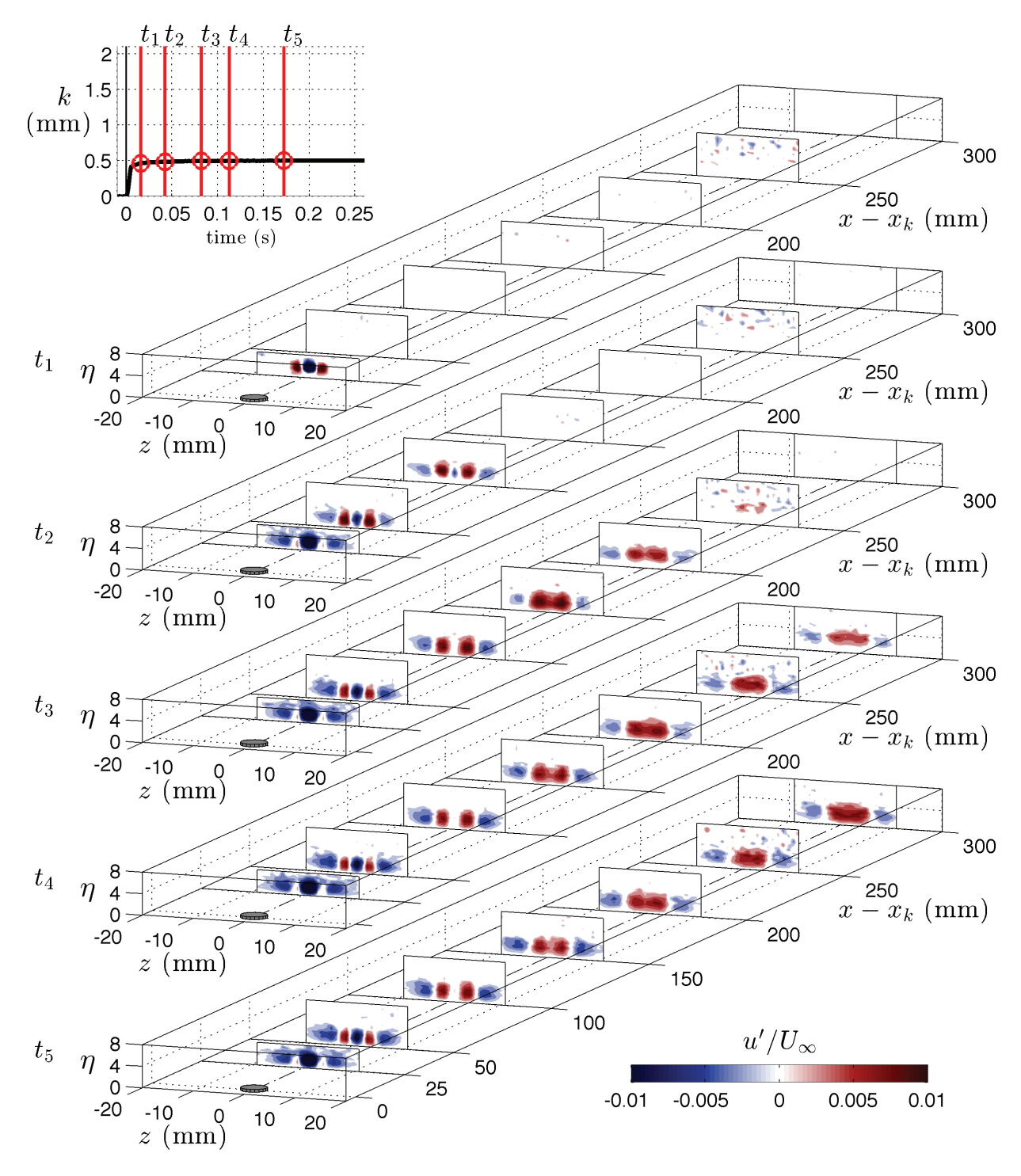


Figure 4.3: Unsteady streamwise velocity disturbance contours with a fully deployed roughness element height of k=0.50 mm, using a solenoid to actuate the roughness element. The roughness element height versus time is provided in the top-left plot; five time instants $(t_1$ - $t_5)$ corresponding to the disturbance contour results are labeled.

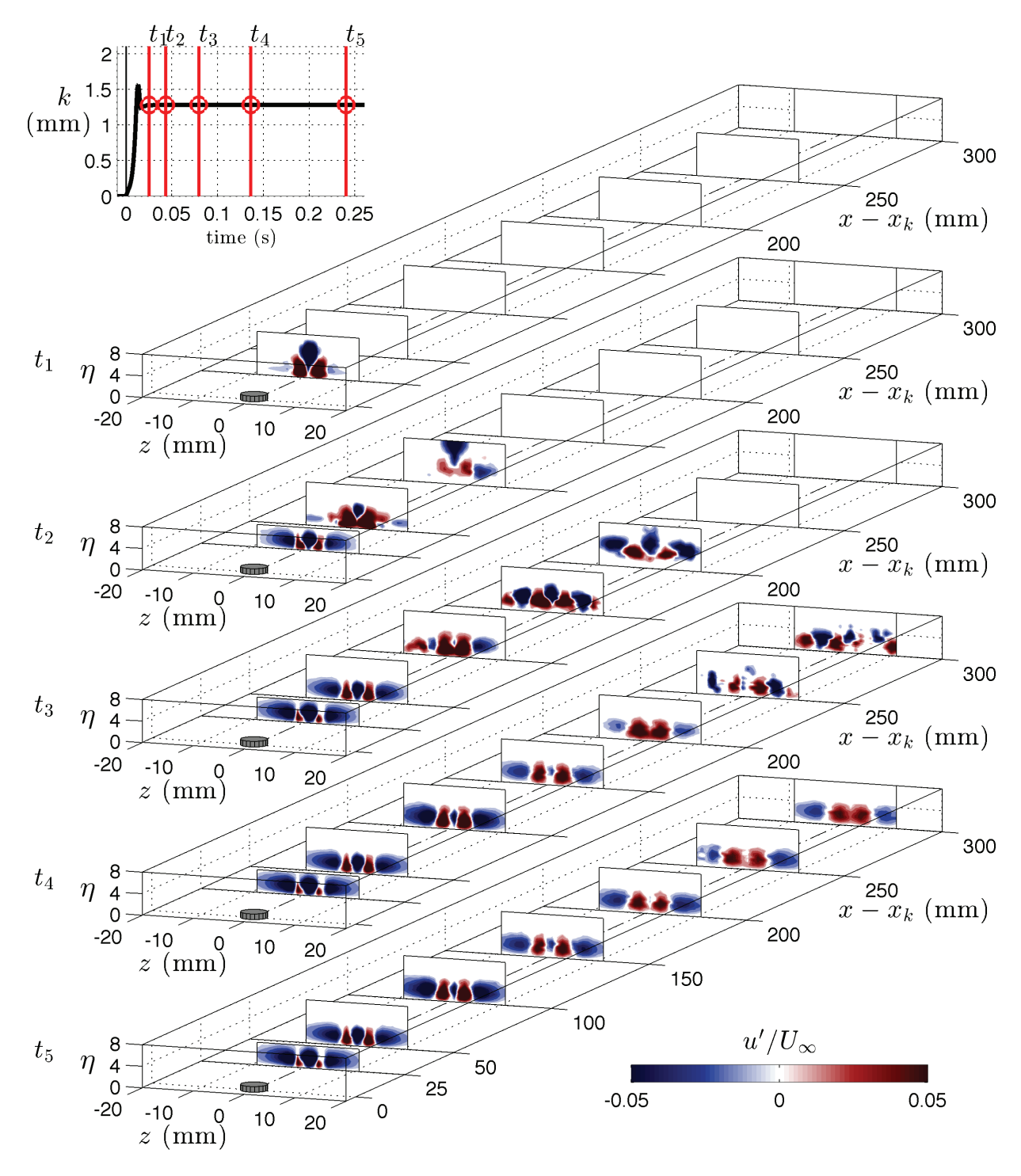


Figure 4.4: Unsteady streamwise velocity disturbance contours with a fully deployed roughness element height of k=1.29 mm, using a solenoid to actuate the roughness element. The roughness element height versus time is provided in the top-left plot; five time instants (t_1-t_5) corresponding to the disturbance contour results are labeled.

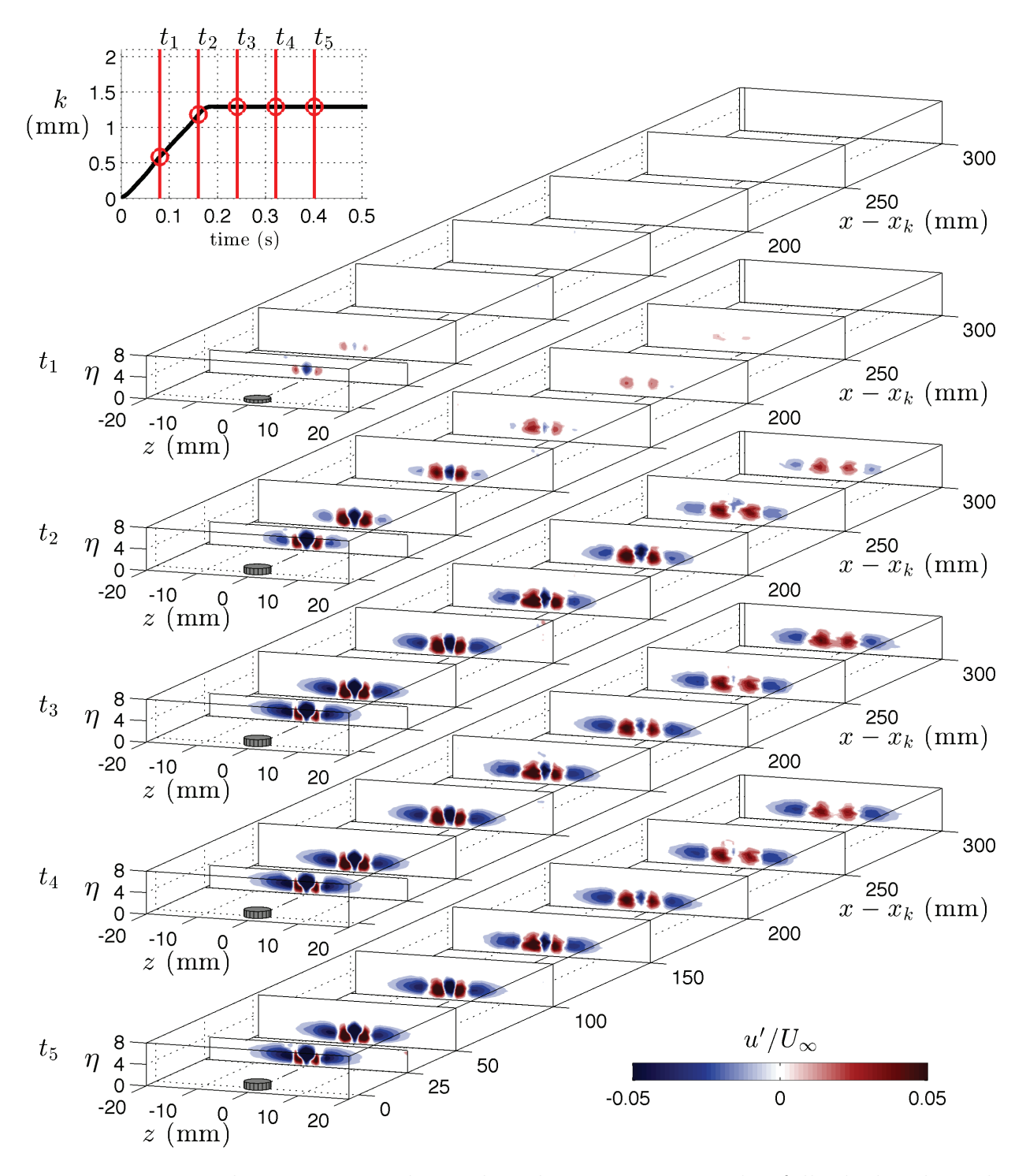


Figure 4.5: Unsteady streamwise velocity disturbance contours with a fully deployed roughness element height of k=1.29 mm, using the Squiggle motor to actuate the roughness element with prescribed motion parameters: $v_k = 7.5$ mm/s and $a_k = 1000$ mm/s². The roughness element height versus time is provided in the top-left plot; five time instants (t_1-t_5) corresponding to the disturbance contour results are labeled.

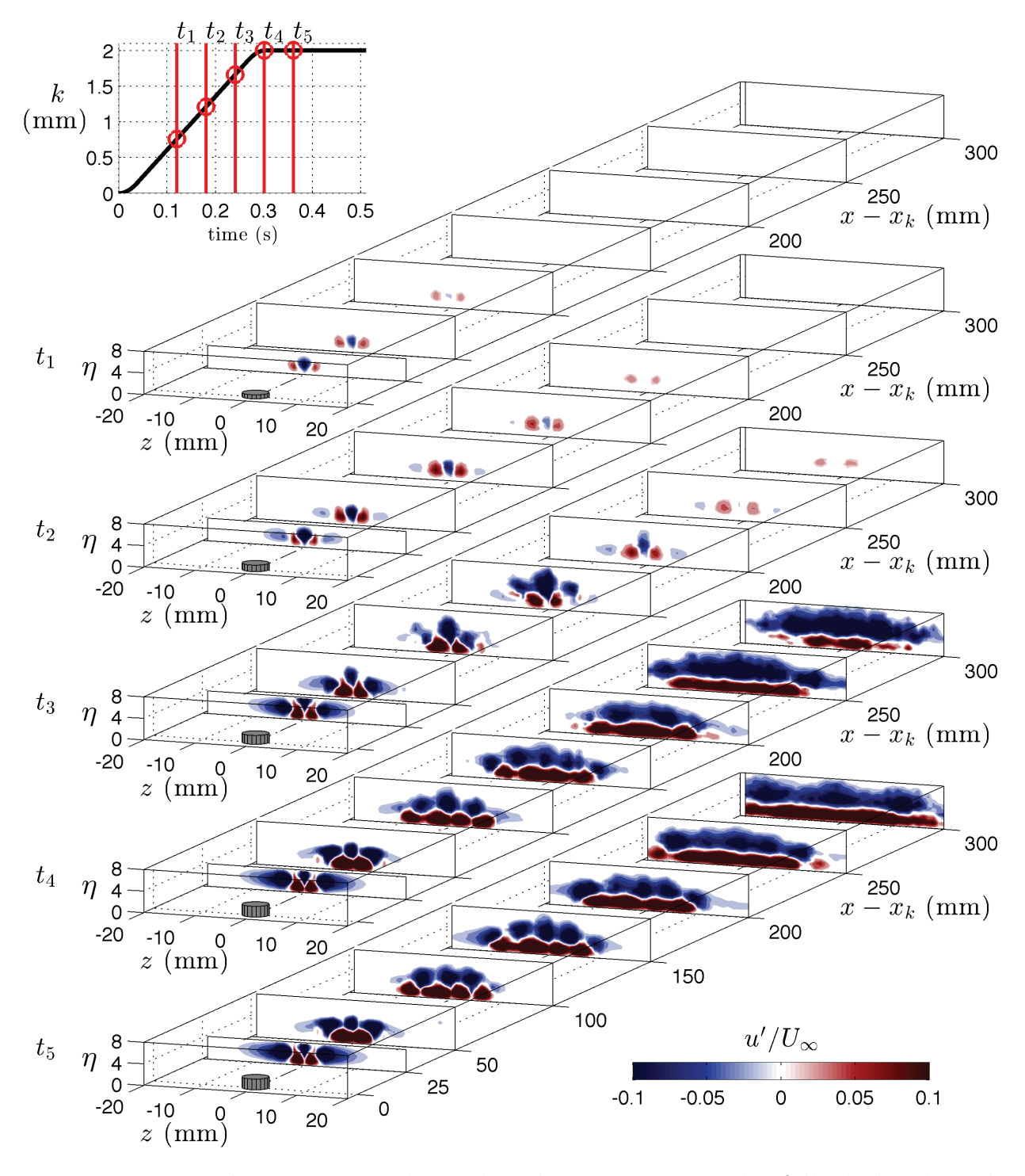


Figure 4.6: Unsteady streamwise velocity disturbance contours with a fully deployed roughness element height of k=2.00 mm, using the Squiggle motor to actuate the roughness element with prescribed motion parameters: $v_k = 7.5$ mm/s and $a_k = 1000$ mm/s². The roughness element height versus time is provided in the top-left plot; five time instants (t_1-t_5) corresponding to the disturbance contour results are labeled.

In Figure 4.4, the roughness element is also actuated with the solenoid, but to a higher roughness element height of k=1.29 mm; and the disturbance grows in a manner significantly different from Figure 4.3. At t_1 the disturbance has reached the $x-x_k=25$ mm plane, but indicates a strong negative disturbance away from the wall, with two very strong positive disturbances near the wall. This high-strength disturbance arrangement propagates downstream, and can be seen in subsequent y-z planes farther downstream as time progresses. However, at steady-state (t_5) , the arrangement and character of the disturbance is similar to the steady state result of Figure 4.3, albeit with a higher strength. The unusual disturbances that propagate downstream during the roughness element motion, when it is raised to a larger k will be problematic for the control efforts, and therefore, must be removed. The strength of the disturbance at steady state is dictated by the roughness element height, but there is a clear limit on k before unwanted dynamic disturbances are introduced into the boundary layer when using the solenoid to actuate the roughness element.

In Figure 4.5, the roughness element is actuated to k=1.29 mm, but using a slower velocity and acceleration ($v_k = 7.5$ mm/s and $a_k = 1000$). Similar to Figure 4.3, the disturbance is observed to develop by generating small, weak disturbances in each subsequent plane as time progresses, which grow in strength and maintain the same spatial distribution. The steady state result at t_5 demonstrates stronger disturbance than Figure 4.3, but without the complicated disturbance development of Figure 4.4.

Finally, in Figure 4.6, the same actuation parameters are used as in Figure 4.5, but the roughness element is raised to k=2.0 mm. The disturbance grows with complex motions until t_3 when the disturbance becomes complex (turbulent motions) and never recovers to a non turbulent disturbed state. This represents a k that is beyond the steady state coherent disturbance level, and is beyond the target for control.

The results of §3.2.3 were examined in detail for the maximum height without turbulent motions, when $v_k = 7.5$ mm/s and $a_k = 1000$, and the roughness element is able to be deployed to the same height as any of the steady-state, non-turbulent cases without inducing turbulent disturbances (i.e. a max height of k=1.4 mm; intermittent turbulent disturbances would be expected at k=1.51 mm).

Chapter 5

Control Model Development

Description of the control efforts is split into six sections to demonstrate the progression from the control model design and development to the results of the active steady and unsteady flow control. First, in §5.1, the concept behind the the control method is explained and the control model is outlined. Next, in §5.2, boundary layer response models are developed using Input/Output data over a range of discrete roughness element heights, §5.2.1, and plasma actuator voltages, §5.2.2. The resulting response models are then used to tune feedforward and feedback controller parameters in §5.3. The completed control model is discussed in §5.4. An investigation of the control results for a steady disturbance is provided in §6.1; and, finally, the unsteady disturbance control results are analyzed in detail in §6.2.

5.1 Control Model

The control model used in this study is intended to be sufficiently robust, while being simple, to allow real-time evaluation of sensor inputs and implementation of the controller output in order to cancel growing unsteady boundary-layer streaks. The effort presented here further simplifies the model by using only a single upstream¹ and a single downstream² shear sensor to provide input information to the model. Admittedly, the use of single-upstream and

¹ Upstream refers to the location of the shear sensor relative to the control model output location (i.e. forcing by the plasma actuator), see Figure 5.1.

 $^{^2}$ Downstream refers to the location of the shear sensor relative to the control model output location (i.e. forcing by the plasma actuator), see Figure 5.1.

single-downstream sensors will under-resolve the three-dimensional disturbances induced by the roughness element and plasma actuators; however, this arrangement satisfies the goal of developing a simple, low-cost, control system. Furthermore, the current study includes the exhaustive study of the physical characteristics of the roughness element induced disturbance, which greatly benefit the interpretation of the single sensor measurement. The result is a control model that is optimized at the location of the isolated sensors, but will provide a demonstration of the ability for such a simple control system to provide unsteady streak disturbance control. A feedforward-feedback control model approach is employed, and implemented using the setup described in Figure 2.5, and the controller parameters (gains, time delays, etc.) are determined through disturbance-input/shear-stress-output (herein simply referred to as Input/Output, or I/O) data collection. The I/O data are used to develop accurate zeroth- and first-order (i.e. simple) models that represent the boundary layer's dynamic response to prescribed unsteady forcing. The use of a feedforward controller, coupled with known boundary layer I/O dynamics to the disturbance and actuator input, should theoretically allow for immediate control of a disturbance to the target level (i.e. the undisturbed Blasius boundary layer shear stress level). However, inevitable approximations in modeling the boundary layer dynamics and deviations in flow conditions from those under which the models are obtained, lead to deterioration in the proportional-integral (PI) feedback controller to drive the disturbance level to zero at the location of the feedback sensor. Although a PI feedback control model alone (without feedforward control) could achieve a zero disturbance level, the speed of response of this mode of control is inherently limited by the convective time delay between the actuator and feedback sensor. Thus, feedback control alone may react too slow to control unsteady streak disturbances. For a detailed description of the construction of the near-wall shear stress sensors and their locations, see §2.6.2; additional details regarding the control hardware and operational details can be found in §2.6. Figure 5.1 provides the generalized control concept for this work. On the *top-side* of the 2D-plate, a demonstration of the boundary layer response to the roughness element and plasma actuator effects is used to arrive to a targeted downstream shear stress set point (i.e. the Blasius level for an undisturbed boundary layer). On the *bottom-side* of the 2D-plate, the control model concept is demonstrated with the feedforward and feedback information being drawing from the upstream and downstream shear stress sensors, respectively.

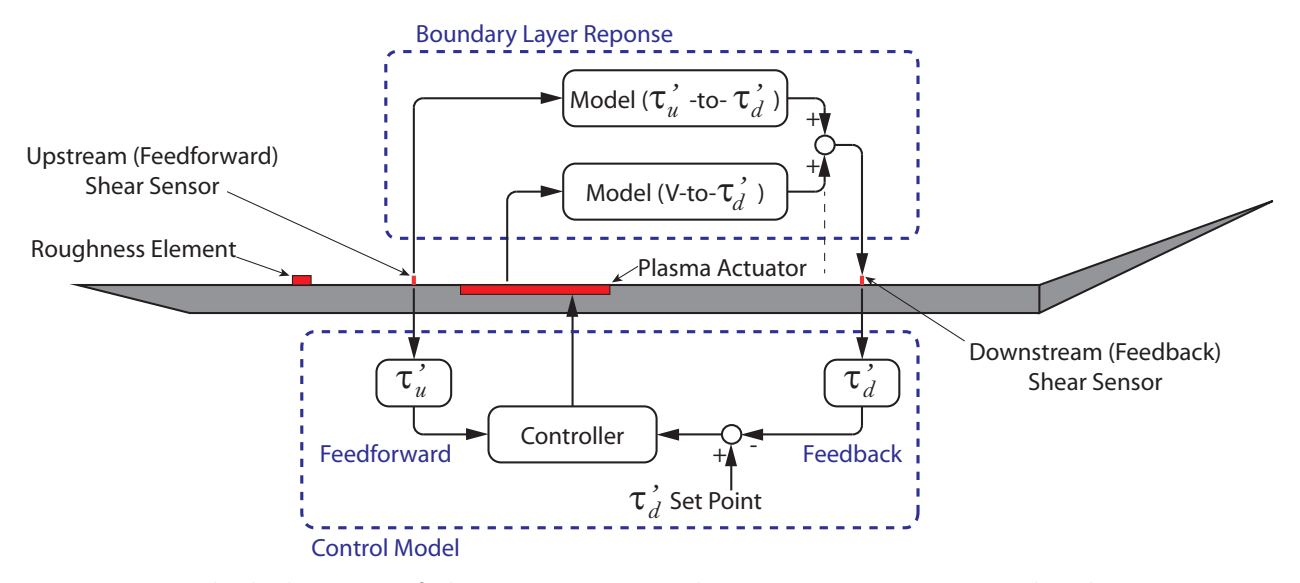


Figure 5.1: Block diagram of the primary control system components and a demonstration of the feedforward-feedback control model implementation of this study.

The block diagram of the feedforward-feedback controlled boundary layer is demonstrated in Figure 5.2. The input to the control model is acquired with the upstream³ and downstream shear stress sensors, τ'_u and τ'_d , respectively. The output of the control model is a voltage, which multiplies a high-frequency sine wave with unity amplitude, sent to the high-voltage amplifier that drives the plasma actuator. Finally, the control target (set point) is a zero

³Note that while the roughness element is used to induce a known shear stress disturbance in the boundary layer, the upstream shear stress sensor signal is taken as the input to the control model. This approach appropriately mimics a real-world implementation, where an upstream shear stress disturbance from an *unknown* source may be sensed.

downstream shear stress disturbance, relative to the Blasius level.

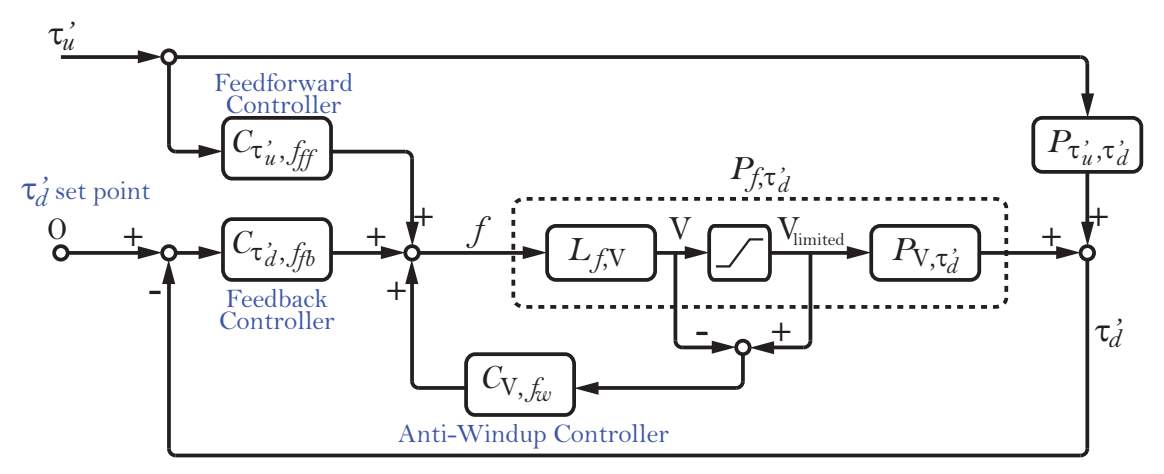


Figure 5.2: Block diagram of the feedforward-feedback control model form used in this study including the boundary layer response models and controllers.

Referring to Figure 5.2, the control model incorporates a zeroth-order boundary layer response (plant) model connecting the upstream shear stress disturbance to the downstream shear stress disturbance, $P_{\tau'_{l},\tau'_{d}}$, and a first-order model connecting the plasma actuator voltage to downstream disturbance shear stress, $P_{V,\tau'_{d}}$. In the implementation of the control model, it was necessary to include a mapping function, $L_{f,V}$, that converts the controller output, f, to a voltage that may be sent to the plasma actuator; this mapping function is discussed further in §5.3.2. The voltage sent to the plasma actuator is passed through a limiting block, which prevents the controller from sending a voltage that is outside the useable voltage range, which is discussed further in §5.2.2. The plasma actuator response model, $P_{V,\tau'_{d}}$, gives the boundary layer's natural response to plasma forcing in terms of a downstream shear stress disturbance value, and the container: $P_{f,\tau'_{d}}$, represents a linear transfer function relationship between the controller function, f, and the downstream shear stress disturbance, τ'_{d} .

The control model incorporates two controller transfer functions which provide the feed-

forward and feedback contributions. The feedforward component of the controller, $C_{\tau'_{u},f_{ff}}$, takes the measured upstream disturbance shear stress input and outputs a control contribution, f_{ff} . Similarly, the feedback component of the controller, $C_{\tau'_{d},f_{fb}}$, takes the measured downstream disturbance shear stress input and outputs a control contribution, f_{fb} . As further discussed in §5.3.2.1, a wind-up correction contribution to the controller output, with dynamics given by the transfer function: $C_{V,fw}$, is also used to prevent the feedback controller's integral error term from accumulating error (i.e. voltage input to the actuator) when the disturbance is outside the controllable range (i.e. the disturbance is too small or too large to be controlled within the minimum and maximum operating limits of the plasma actuator).

Note that the control target (set point) is noted as "0" in Figure 5.2. At this set point, the wall shear stress at the streamwise location of the feedback sensor corresponds to the Blasius level. In the control model implementation this target, the Blasius shear stress level, is actively adjusted to account for small freestream variations. This slight adjustment in the set point was made using a hot wire in the freestream of the wind tunnel, which provided real-time measurement of U_{∞} . In the laboratory environment, this correction was essentially negligible, but would provide a more appropriate Blasius target in a non-ideal setting.

The completed control model was implemented using MathWorks Simulink software and uploaded to the dSpace hardware. An example Simulink model is provided in Appendix A7.4 in Figure A.1; Figures A.2 - A.11 provide the sub-model Simulink blocks.

5.2 Boundary Layer Response Models

The development of simple boundary layer response models was the first step toward generating the control model by understanding and capturing the physical response of the boundary layer to prescribed forcing (from the roughness element or the plasma actuator). The control block diagram incorporates two boundary layer response plant models. The first relates the upstream disturbance shear stress (induced by the roughness element) to downstream shear stress, $P_{\tau'_u, \tau'_d}$, and is discussed in §5.2.1. The second relates the plasma actuator voltage to downstream disturbance shear stress, P_{V, τ'_d} , and is discussed in §5.2.2.

5.2.1 Roughness Element Response Model

The first boundary layer response model relates the upstream shear stress disturbance, τ'_u , to the downstream shear stress disturbance, τ'_d , through a plant model in the form of a transfer function. The prescribed boundary layer streak disturbance is physically introduced here by the roughness element; §3.2.3 and §4.2 allow for a comprehensive understanding of the physical relationship between the roughness element and streak disturbance, in both the steady and unsteady scenarios. This understanding allows the control efforts to use the roughness element as an instrument to induce the streak disturbance, but the control input to the feedforward controller to be defined as the resulting shear stress within the boundary layer (as opposed to the actual roughness element movement); this way of defining the control input is more physically relevant to real-world streak disturbance control, where streaks may occur from other mechanisms that can be tracked (e.g. freestream turbulence, random freestream velocity variation above an airfoil with rivets on the surface, etc.).

The plant model transfer function,

$$\frac{\mathcal{T}'_d(s)}{\mathcal{T}'_u(s)} = P_{\tau'_u, \tau'_d}(s) = K_\tau \ e^{-t_{d,\tau} s},\tag{5.1}$$

is implemented using a zeroth-order linear model with time delay (the appropriateness of this model will be clarified when discussing Figure 5.4). The model terms are given the (simplified) subscript τ to represent the input, τ'_u ; the output of the roughness element and plasma actuator boundary layer response models is a downstream shear stress disturbance, so the upstream variable is used to distinguish the nomenclatures for the two models. The model parameters include a gain, K_{τ} and time delay, $t_{d,\tau}$, which may each be independent of or dependent on the model input, τ'_u (corresponding to linear or non-linear input/output relation, respectively); it will be demonstrated, later in this section, that a constant value is sufficient for each parameter (i.e. each may be regarded as independent of the input over the range of interest).

Input/Output data were collected in order to determine the appropriate plant model parameters, this was conducted when deploying the roughness element from a flush-with-the-wall condition to a few discrete roughness element heights, which provided approximately step function input with different step size. The upward and downward motion of the roughness element was executed at the highest velocity/acceleration combination of the roughness element that would not initiate turbulent disturbances (which are outside the scope of the disturbances targeted for control). As described in §4.2, the following roughness element kinematic parameters allowed disturbance introduction, up to $k\approx 1.5$ mm, without persistent turbulent motions: $v_k = 7.5$ mm/s and $a_k = 1000$ mm/s². The roughness element motion is therefore the closest to a step function as possible (which is desirable for obtaining the first-order model response parameters) as the flow physics would allow. The data were

collected for a range extending from k=0.5 mm, where the disturbance is very small and nearly negligible, up to a maximum of k=1.5 mm, where the disturbance amplitude is just under that which will initiate intermittent turbulent bursts, in steps of 0.1 mm. The roughness element was deployed from flush with the wall, to the prescribed height, and was held at the fully up/down locations for approximately 1 second; therefore, one up/down cycle had a period of 2 seconds. Figure 5.3 demonstrates the motion of the roughness element along with the upstream and downstream shear stress over 60 seconds (corresponding to 30 cycles of motion) where, at full deployment, k=1.2 and the downstream sensor was placed at $x_{fb}=450$ mm. The shear stress sensors were placed such that a positive disturbance was measured, and Figure 5.3 clearly shows that as the roughness height is increased, the shear stress at both sensors increases as well.

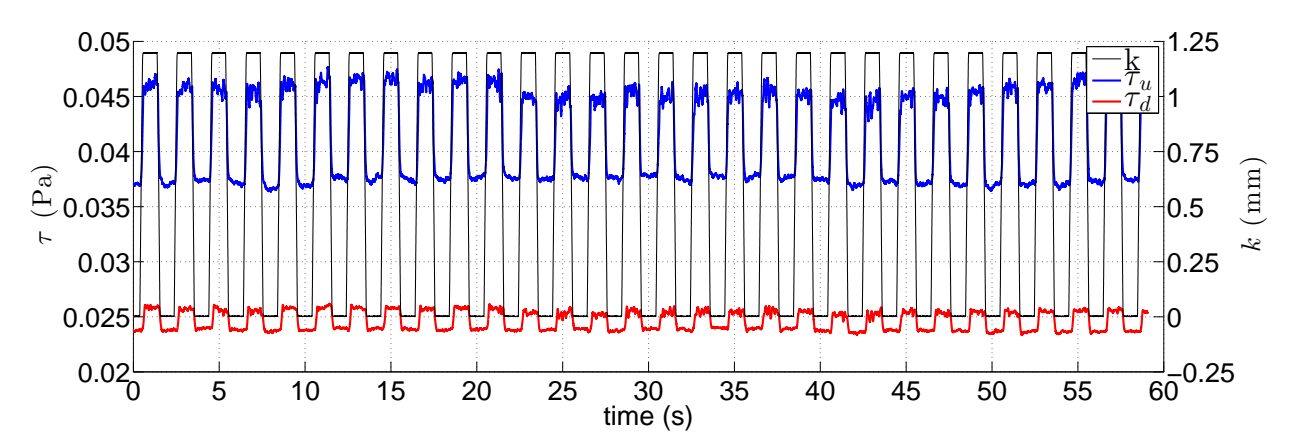


Figure 5.3: Example unsteady I/O data collected for determination of the boundary layer response model to roughness disturbance input. Sata shown are obtained for "sudden" deployment of the roughness element from k=0 to 1.2 mm with the feedback sensor located at x_{fb} - x_k =300 mm.

The variability of the upstream and downstream shear stress disturbance level from one roughness motion cycle to another was due to small spatial wandering of the streak disturbance in either the wall-normal or spanwise direction. It is clear from the wall-normal and spanwise disturbance profiles of , for example, Figure 3.18, that even small (say <1 mm)

spatial variations in the location of the streak disturbance will cause measurable changes in the measured shear stress disturbance at the sensor location.

After acquiring the multi-cycle I/O data for each discrete roughness element height, the results for each height were phase averaged to remove subtle cycle-to-cycle differences to reveal the average expected boundary layer shear stress disturbances over the range of controllable disturbance levels. Figure 5.4 provides the phase averaged result for the data provided in Figure 5.3 and the resulting gain, K_{τ} and time delay, $t_{d,\tau}$, are noted.

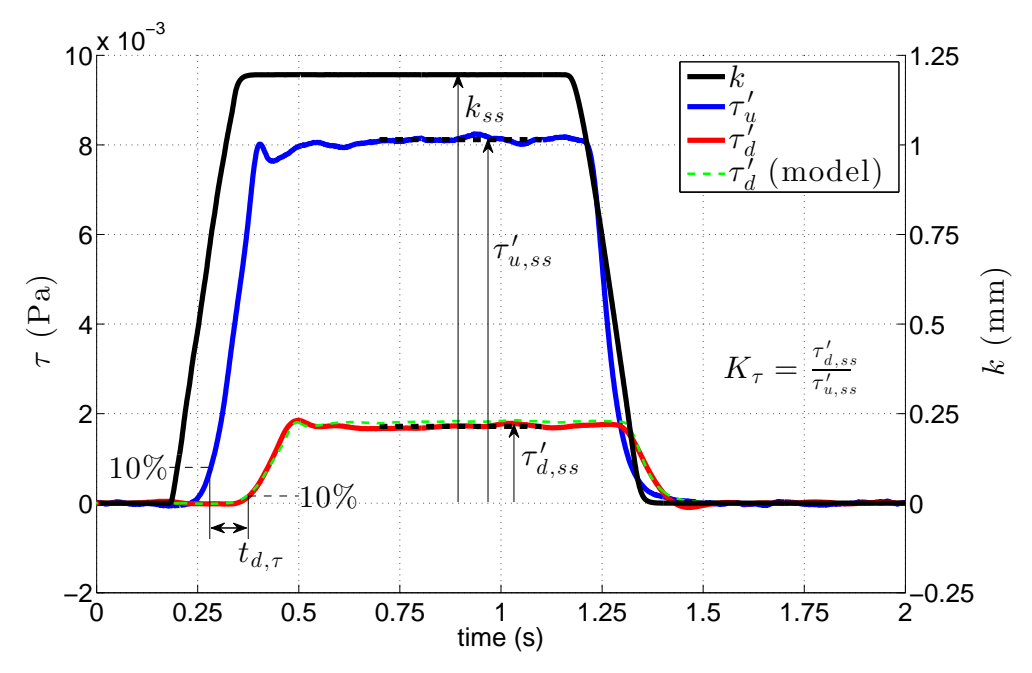


Figure 5.4: Example phase-averaged I/O data for the boundary layer response model parameter determination for k=1.2 mm with the feedback sensor located at x_{fb} - $x_k=300$ mm.

The gain, K_{τ} is calculated as the ratio of the downstream to upstream disturbance shear stress values at steady-state. The determination of the time delay, $t_{d,\tau}$, which is primarily representative of the convection time for the roughness element induced disturbance to travel from the upstream to the downstream shear stress sensor, is also demonstrated in Figure 5.4 where the sheer stress response start time at each sensor is taken when the disturbance reaches 10% of its steady-state value. The calculated convection velocity, based on the

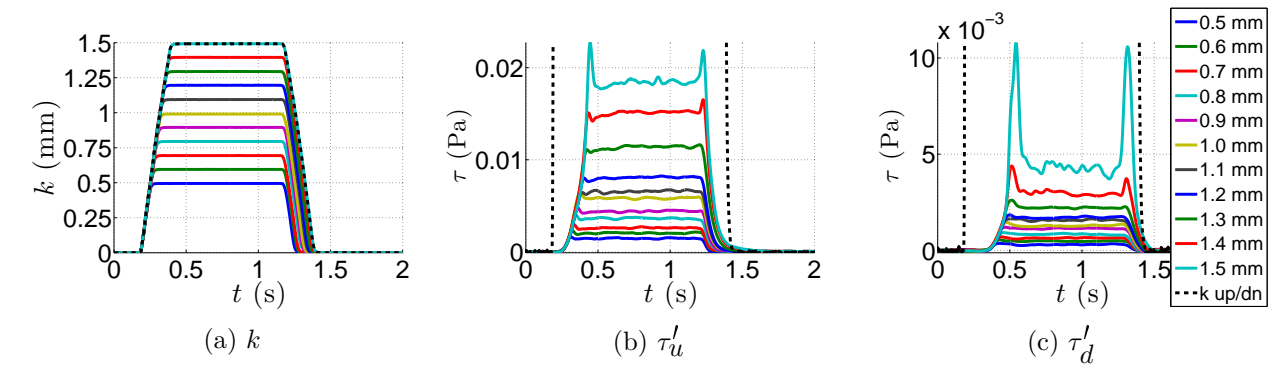


Figure 5.5: Phase averaged I/O data results for various k values with the feedback sensor at x_{fb} - x_k =300 mm. Provided are the a) roughness element motion, b) the upstream shear stress disturbance, and c) the downstream shear stress disturbance developments in time.

streamwise sensor positions and the undisturbed boundary layer velocity at each sensor (noted in Figure 2.10), was U_c =2.58 m/s (U_c/U_∞ =0.52). Figure 5.5 provides a comparison of the roughness element motion as well as the resulting upstream and downstream shear stress disturbance values at each discrete roughness element deployment height used in this study.

With I/O data collected at many discrete roughness element heights, it is possible to generate the necessary parameters for the response model transfer function provided in Equation 5.1 and compare the resulting parameters. Figure 5.6 demonstrates the various values of K_{τ} and $t_{d,\tau}$ determined at each discrete k. Due to the relative *insensitivity* of the gain and time delay to k (with an RMS relative to each mean of 0.0212 and 0.0037, or 9.4% and 4.1% of each mean, respectively), the mean value was used for each, which has the advantage of simplifying the controller model. Table 5.1 provides the boundary layer response parameters which were found for K_{τ} and $t_{d,\tau}$ at each of three downstream shear stress sensor streamwise placement locations.

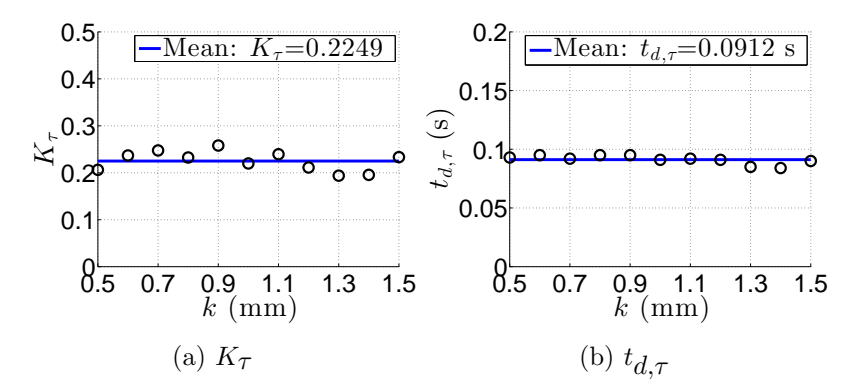


Figure 5.6: Plant model, $P_{\tau_u',\tau_d'}$, parameters for the a) gain and b) time delay with the feedback sensor at x_{fb} - x_k =300 mm.

x_{fb} - x_k	K_{τ}	$t_{d, au}$
(mm)		(s)
200	0.4433	0.0485
250	0.3122	0.0722
300	0.2249	0.0909
300(r)	0.2671	0.0898

Table 5.1: Parameters used in the upstream disturbance shear stress to downstream disturbance shear stress boundary layer response model, with the downstream (feedback) shear stress sensor positioned at various streamwise locations. Note that the model development process was repeated with an independent dataset at the x_{fb} - x_k =300 mm location, and these results are also provided, although they were never used for control experiments.

5.2.2 Plasma Actuator Model

The second boundary layer response model relates the plasma actuator voltage, V, to the resulting downstream shear stress disturbance, τ'_d , through a plant model transfer function.

The plant model transfer function,

$$\frac{\mathcal{T}'_d(s)}{\mathcal{V}(s)} = P_{V,\tau'_d}(s) = \frac{K_V e^{-t_{d,V}s}}{(t_{c,V} s + 1)},\tag{5.2}$$

which is approximated by a first-order model (this will be justified with I/O data, and shown in Figure 5.8) and the model terms are given the subscript V to represent the input

of the plant; the output of the boundary layer response model is a downstream shear stress disturbance. The model has three parameters: gain, K_V , time delay, $t_{d,V}$, and time constant, $t_{c,V}$, which may all be independent or dependent of the model input, V, for linear or non-linear transfer functions, respectively. It will be demonstrated, later in this section, that a constant value is sufficient for representing the time delay and time constant parameters (i.e. each may be regarded as independent of the input over the plasma actuator input voltage range of interest); however, the gain is dependent upon the input voltage.

For the plasma actuator, the test for acquiring the I/O data uses an input voltage that is effectively a step-function. The high-frequency 4 kHz plasma actuator input sine wave signal is prescribed with an amplitude (between approximately 1.6 and 2.6 V) using a function generator. This signal is multiplied by a unit step function with a hold time of 1 second at each on/off state; resulting in a 2 second on/off cycle period. The plasma actuator input signal is passed through a high-voltage amplifier (x1000) and sent to the positive electrode. The acquired boundary layer response data at each discrete input voltage value (sine wave amplitude multiplied by the unit step function) includes approximately 30 cycles. Figure 5.7 demonstrates the I/O data acquired with an input voltage of 2.4 kV, showing the input voltage amplitude, upstream shear stress (which is unaffected by the plasma actuator forcing), and the downstream shear stress. The downstream shear sensor, which is positioned to capture the positive disturbance induced by the roughness element, measures a negative shear stress disturbance from the plasma actuator. Therefore, as the voltage signal increases, the measured shear stress decreases.

I/O data similar to those shown in Figure 5.7 were acquired for different step sizes ranging from V=1.6 kV to 2.6 kV, in increments of 0.05 to 0.1 kV, depending on how the sensitivity of τ'_d to the forcing voltage changed with the voltage level. Many cycles of the downstream

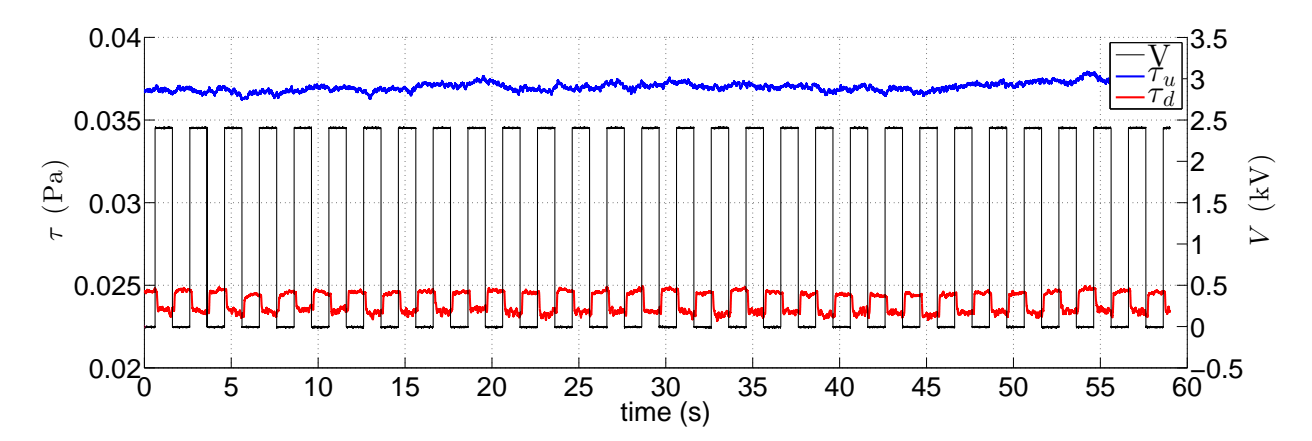


Figure 5.7: Example I/O data for determination of the boundary layer response model parameters for V=2.4 kV and the feedback sensor located at x_{fb} - x_k =300 mm.

shear stress response to the repeated step input were phase averaged in order to smooth small cycle-to-cycle differences. The results were then used to determine the plant model parameters, using methods similar to those used with the roughness element response data. Figure 5.8 provides the phase averaged results from Figure 5.7 where V=2.4 kV, and also shows how the model parameters are determined from the response data.

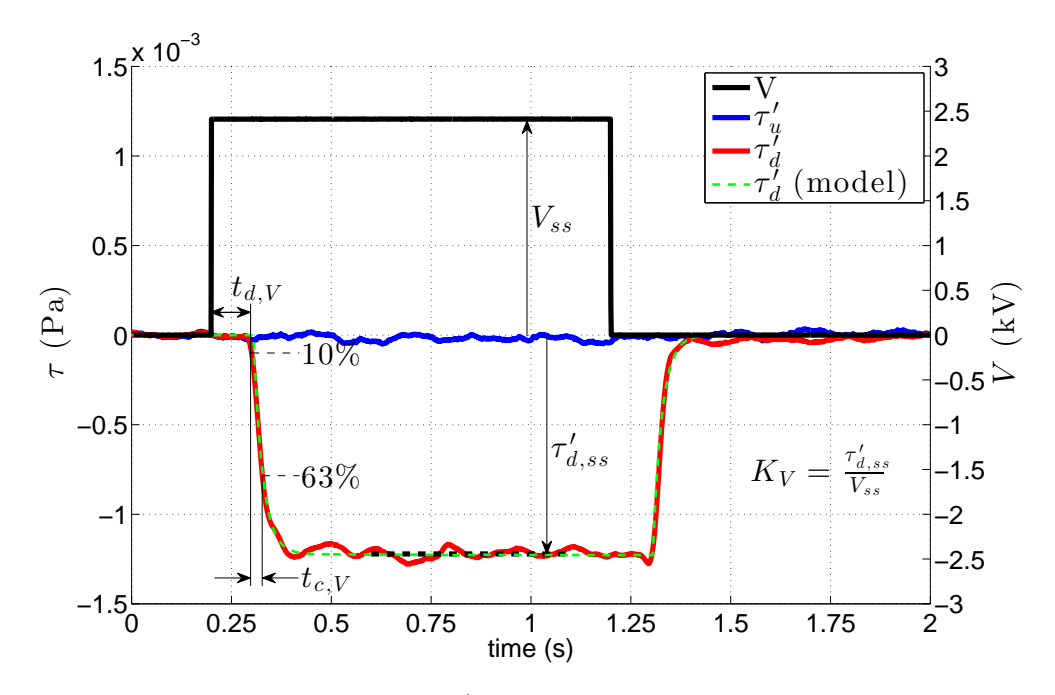


Figure 5.8: Example phase averaged I/O data for determination of the boundary layer response model parameters for a step change in input voltage from V=0 to 2.4 kV with the feedback sensor located at x_{fb} - x_k =300 mm.

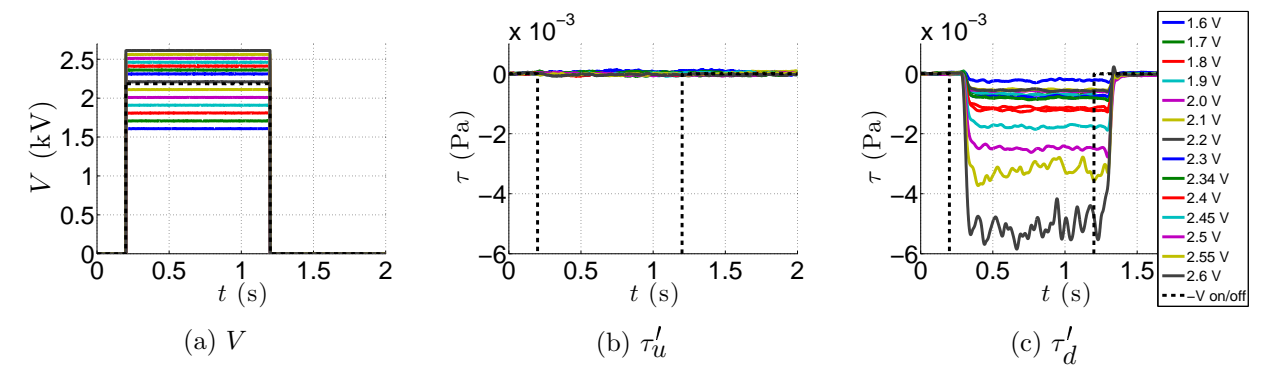


Figure 5.9: Phase averaged I/O data results for various values of the input voltage step size, V, with the feedback sensor at x_{fb} - x_k =300 mm. Provided are the a) voltage input, b) the upstream shear stress disturbance, and c) the downstream shear stress disturbance developments in time.

Note, that while the phase averaged result comparing the data (red) and the model (green) are almost identical in this example, the result for this voltage provided the best match; I/O data and model results for other voltage values do not match the model so perfectly at steady-state, although the agreements remain reasonably good. See Figure 5.12 (square symbols and magenta line) to further examine the agreement between the steady-state measured results and model result at each discrete voltage. It is important to recognize that any disagreement between the data and the fit line (linear least squares fit) do not represent I/O data problems, but is rather, error in the appropriateness of the simple, linear fit that was selected to be used for model simplicity.

The process of determining the phase-averaged results and resulting plant model parameters was repeats for all input voltages and the results are provided in Figure 5.9, which provides a comparison of the change in the disturbance shear stress with input voltage for different values of the input voltage step size. As expected, there is no appreciable upstream shear stress disturbance because the upstream shear stress sensor is located upstream of the plasma actuator.

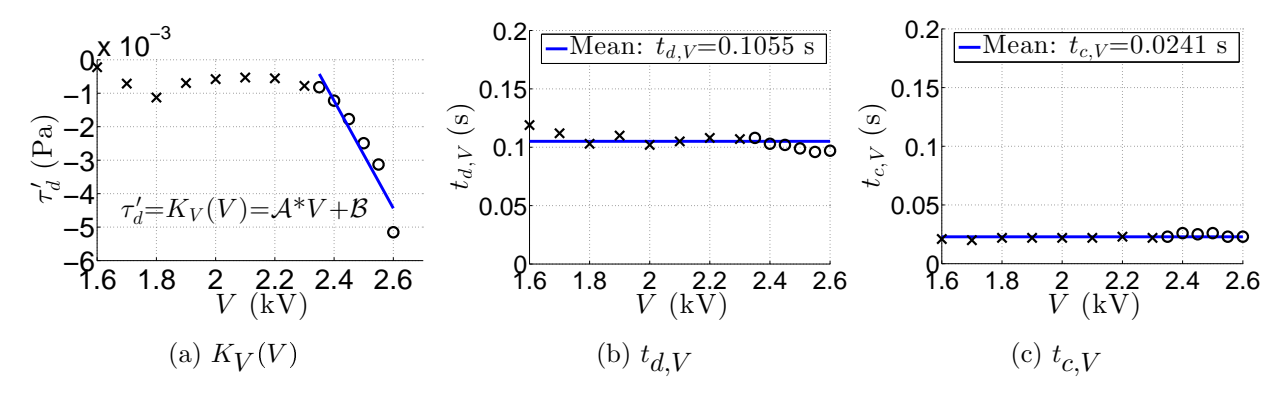


Figure 5.10: Parameters for the transfer function characterizing the dynamic response of the boundary layer to the plasma actuation: a) gain, b) time delay, and c) time constant with the feedback sensor at x_{fb} - x_k =300 mm. Note that the \circ -symbols represent the subset of useful voltages, while the \times -symbols represent non-useful plasma actuator voltages.

Figure 5.10a demonstrates the relationship between the plasma actuator voltage amplitude (step size) and the steady state downstream shear stress disturbance. As see from the figure, there is some range of plasma actuator voltage, larger than the plasma minimum turn-on voltage (V=1.6 kV), where the plasma induced downstream shear stress disturbance is independent of the plasma voltage, $1.6 \leq V \leq 2.35 \text{ kV}$. Therefore, the useful range of plasma actuator voltages was $2.35 \leq V \leq 2.6$, for this particular plasma actuator under the specific flow conditions of the experiments, where the downstream shear stress disturbance was monotonically dependent on voltage amplitude supplied to the plasma actuator. Plasma actuator voltage amplitudes larger than 2.6 kV provided a forcing level that induced turbulent disturbances into the boundary layer that were undesirable for the control objectives, and were thus also not useful. This range of useful voltages also dictates the range of controllable downstream shear stress disturbance levels. Over the range of interest, noted by the data points represented by the circles, a linear least-squares fit (shown by the blue line in Figure 5.10a),

$$\tau'_{d,ss} = K_V(V) = \mathcal{A} * V + \mathcal{B}, \tag{5.3}$$

represents the $t'_{d,ss}$ to V relation well (though not perfectly); where, \mathcal{A} and \mathcal{B} represent the linear-fit slope and offset, respectively.

Because the plasma actuator boundary layer response plant model (Equation 5.2) includes the gain, $K_V(V)$, which is a function of voltage, the development of a properly tuned controller was not straightforward and results in a nonlinear transfer function, P_{V,τ'_d} . In order to alleviate this complication and use the controller tuning guidelines presented by Skogestad [47], a mapping function was added to the control model,

$$L_{f,V} = V = (f - \mathcal{B})/\mathcal{A}, \tag{5.4}$$

that linearizes the transfer function, P_{f,τ'_d} (see Equation 5.5), connecting the controller output, f, to the downstream shear stress disturbance. Note that f is effectively a targeted downstream shear stress level to counteract that which is predicted from the upstream sensor information and sensed by the downstream sensor and has units of downstream shear stress; therefore, $L_{f,V}$ is the equivalent of $1/K_V$. The resulting plant,

$$P_{f,\tau'_d} = L_{f,V} P_{V,\tau'_d} = \frac{e^{-t_{d,V}s}}{(t_{c,V} s + 1)}, \tag{5.5}$$

has a constant gain of unity. Under this modification, the feedback controller design may be conducted using Skogestad's recommendations.

The determination of $t_{d,V}$ and $t_{c,V}$ is demonstrated in Figure 5.8. The time delay was defined as the average of the time difference between the plasma actuator voltage step to

x_{fb} - x_k (mm)	$t_{d,V}$ (s)	$t_{c,V}$ (s)	\mathcal{A}	\mathcal{B}
200	0.0595	0.0198	-0.0278	0.0664
250	0.0814	0.0196	-0.0152	0.0356
300	0.1055	0.0241	-0.0170	0.0389
300(r)	0.1051	0.0229	-0.0161	0.0373

Table 5.2: Parameters used in the plasma actuator voltage to downstream disturbance shear stress boundary layer response model, with the downstream (feedback) shear stress sensor positioned at various streamwise locations. Note that the model development process was repeated with an independent dataset at the x_{fb} - x_k =300 mm location, and these results are also provided, although they were never used for control experiments.

reach 2% of the max value, and the time at which the downstream shear stress reaches 10% of its steady state value. These percentage threshold values were selected at a safe level to ensure that each time stamp would be well established and above the noise level present on the measurement signal when boundary later is undisturbed (i.e. when the plasma was off). Note, due to the effectively step-function plasma input voltage signal, using nearly any threshold with the plasma voltage signal would result in the same time delay determination. The time constant was calculated as the time it takes for the downstream shear stress disturbance response to rise from 10% to 63% of the steady state disturbance level. Table 5.2 provides the boundary layer response parameters, $t_{d,V}$, $t_{c,V}$, \mathcal{A} , and \mathcal{B} for each of three downstream shear stress sensor streamwise placement locations.

5.3 Controller Design

With the development of plant models to convert upstream shear stress disturbances and plasma actuator voltages to downstream shear stress disturbances, the determined plant model parameters can be used to generate and tune appropriate controllers for the control model. In this section, the methods used to determine the forms for the feedforward, $C_{\tau'_u, f_{ff}}$,

and feedback, $C_{\tau'_d, f_{fb}}$, controllers and their parameters are presented and explained. The feedforward control model branch uses a proportional controller, while the feedback model branch uses a proportional-integral controller. The control theory used in developing the feedback controller model comes from Skogestad [47], wherein a discussion regarding PIDcontrollers developed for controlling first- and second-order plant models is presented and the tuning of the controller parameters is investigated. The choice of a feedforward-feedback control model is motivated by the complementary advantages of the two methods. i) The feedforward component should allow "predictive", and hence very fast, disturbance suppression, which in reality, however, will be imperfect due to the inevitable approximation of the I/O models, and their parameters. ii) The proportional-integral (PI) feedback component should allow the controller to drive the disturbance level to zero if given sufficient time, which corrects for any remainder feedforward controller errors due to the aforementioned I/O model approximations. The PI feedback controller could be used exclusively to achieve a zero-disturbance level, but would be limited in its ability to adjust sufficiently fast to an unsteady disturbance, as will be investigated in the control results section (§6.2).

The cascaded form of a PID controller,

$$\frac{F_{PID}(s)}{I_{PID(s)}} = K_P \left(\frac{t_I s + 1}{t_I s}\right) (t_D s + 1), \qquad (5.6)$$

where F(s) is the control output and I(s) is the controller input. The integral time parameter, t_I , and the derivative time parameter, t_D , offer the ability to tune the aggressiveness and stability of the controller; here, the derivative component will not be used, to maintain simplicity of the controllers. The specific means by which the parameters of the various controller transfer functions were determined/tuned for the feedforward, $C_{\tau'_U,f_{ff}}$, feedback

$\frac{x_{fb}-x_k}{\text{(mm)}}$	K_{ff}	K_{fb}	$t_{I,fb}$ (s)	K_t
200	0.4433	0.1664	0.0198	12.63
250	0.3122	0.1204	0.0196	12.75
300	0.2249	0.1141	0.0241	10.37
300(r)	0.2671	0.1088	0.0229	10.92

Table 5.3: Parameters used in the feedforward and anti-windup feedback controllers, with the downstream (feedback) shear stress sensor positioned at various streamwise locations. Note that the model development process was repeated with an independent dataset at the x_{fb} - x_k =300 mm location, and these results are also provided, although they were never used for control experiments.

 $C_{\tau'_d,f_{fb}}$, and feedback anti-wind-up, $C_{V,fw}$, are described in the following sections. Table 5.3 provides the controller parameters used in the control model for the feedforward and anti-windup feedback controllers. The methods and explanation of these results are presented in the following subsections.

5.3.1 Feedforward Controller

The feedforward controller, $C_{\tau'_{u},f_{ff}}$, utilized a simple gain relationship, to associate between the upstream shear stress disturbance and controller output,

$$\frac{F_{ff}(s)}{\mathcal{T}'_{u}(s)} = C_{\tau'_{u}, f_{ff}} = K_{ff}, \tag{5.7}$$

where the gain is determined from the roughness element boundary layer response I/O model, $P_{\tau'_{l},\tau'_{l}}$, of §5.2.1. This provides the necessary parameter(s), which in this case is simply a gain,

$$K_{ff} = -K_{\tau}. (5.8)$$

The use of a pure (negative) gain for the feedforward controller, is based on the boundary layer response model $P_{\tau'_u,\tau'_d}$, which is a zeroth-order model (i.e. a direct proportional relationship) with a time delay. Specifically, the appropriate feedforward control output requires that the resulting downstream shears stress when passed through the plasma actuator boundary layer response model P_{f,τ'_d} results in a disturbance of equal magnitude but opposite sign to that of the roughness element induced disturbance. Specifically, referring to Figure 5.2, perfect cancellation of the roughness element disturbance through feedforward control requires:

$$\mathcal{T}'_{u}(s)P_{\tau'_{u},\tau'_{d}}(s) = -\mathcal{T}'_{u}(s)C_{\tau'_{u},f_{ff}}(s)P_{f,\tau'_{d}}(s). \tag{5.9}$$

The equations for the boundary layer response transfer functions (Equations 5.1 and 5.5) are substituted into Equation 5.9,

$$K_{\tau} e^{-t_{d,\tau}s} = -C_{\tau'_{u},f_{ff}}(s) \frac{e^{-t_{d,V}s}}{(t_{c,V} s + 1)},$$
 (5.10)

and, by rearranging the terms, the resulting feedforward transfer function,

$$C_{\tau'_{u},f_{ff}}(s) = -K_{\tau} \left(t_{c,V} \ s+1 \right) e^{-(t_{d,\tau} - t_{d,V})s}. \tag{5.11}$$

The results of the I/O model development demonstrated that the time delays, $t_{d,\tau}$ and $t_{d,V}$, are approximately the same; therefore, the exponential term in Equation 5.11 is ignored. In addition, the time constant, $t_{c,V}$, is ignored in designing the controller in the interest of simplicity. Thus, the feedforward controller transfer function is simply,

$$C_{\tau_{u}^{\prime},f_{ff}} = -K_{\tau}. \tag{5.12}$$

Table 5.3 provides the resulting feedforward gain values for the model developed at each streamwise feedback sensor location.

5.3.2 Feedback Controller

The feedback controller is developed as a proportional-integral (PI) controller, which allows the control model to achieve a zero-error level, if given sufficient time to converge. The linearized plasma actuator plant model, P_{f,τ'_d} , parameters are used along with the tuning rules and recommendations presented by Skogestad [47] to determine the PI-controller parameters: K_{fb} and $t_{I,fb}$; in the feedback controller transfer function,

$$\frac{F_{fb}(s)}{\mathcal{T}'_{d}(s)} = C_{\tau'_{u}, f_{fb}} = K_{fb} \frac{t_{I, fb} \ s + 1}{t_{I, fb} \ s},\tag{5.13}$$

where $F_{fb}(s)$ is the feedback output, $\mathcal{T}'_d(s)$ is the downstream shear stress disturbance in the LaPlace domain, K_{fb} is the controller gain. The integral time constant is determined as:

$$t_{I,fb} = min\{t_{c,V}, 8t_{d,V}\},$$
 (5.14)

which is the lesser of the time constant and eight times the time delay of the boundary layer response model for the plasma actuation input (Equation 5.2). The time constant was always smaller than the time delay (see Table 5.2), and hence it was selected as the integrator time constant, for all streamwise locations of the feedback sensor.

For the feedback controller gain, it is necessary to calculate the appropriate gain value,

 K_{fb} , based on the unity gain, the time delay, $t_{d,V}$, and the time constant, $t_{c,V}$ of the linearized plant model (see Equation 5.5). According to the PID tuning rules outlined by Skogestad [47], the feedback controller gain,

$$K_{fb} = \frac{0.5}{k_{fb}} \frac{t_{c,V}}{t_{d,V}},\tag{5.15}$$

where k_{fb} =1, is determined for all streamwise locations of the feedback sensor. Figure 5.11 demonstrates the independence of K_{fb} of the applied plasma actuator voltage amplitude for the I/O data presented in Figure 5.10.

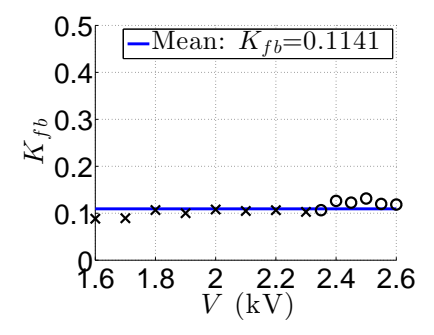


Figure 5.11: Feedback controller gain at various plasma actuator voltages, with the feedback sensor at x_{fb} - x_k =300 mm. The \circ -symbols represent the range of useful voltages, while the \times -symbols represent non-useful plasma actuator voltages. For the purposes of model development, all data points were used to determine the proper gain, because the time delay and time constant are independent of plasma voltage.

The final feedback gain and integral time values at each streamwise feedback sensor location are provided in Table 5.3. As expected, K_{fb} increases and $t_{I,fb}$ decreases as x_{fb} decreases because the feedback information is delivered faster (because of the shorter convective time over the shorter streamwise fetch) and thus the controller is allowed to respond more aggressively while maintaining a stable controller output.

5.3.2.1 Feedback Controller Windup Correction

Preliminary tests demonstrated the need for an additional control model component to account for integrator error accumulation when the shear stress disturbance level was outside of the controllable range. There is a minimum turn-on voltage (1.6 kV) for the plasma actuator, which results in a non-negligible level of negative downstream shear stress disturbance; therefore, any positive disturbances of a lesser intensity are uncontrollable. Furthermore, as demonstrated in Figure 5.10a, there is a minimum voltage (2.35 kV) where the output forcing is variable with voltage; therefore, using a voltage setting of <2.35 kV is equivalent to using 2.35 kV, and thus the lower voltages are useless. Additionally, there is a maximum level of plasma actuator voltage (2.6 kV) that is useful for control, higher voltages than this maximum will result in strong forcing that produces turbulent disturbances, which are not useful for the intended control. In either case, when the required plasma actuator voltage for control is too low or too high to achieve, or to be useful, the integral portion of the feedback controller should not be allowed to accumulate error; a process referred to as *Integrator* Wind-Up[5]. The control model diagram in Figure 5.2 demonstrates the implementation of the windup controller, C_{V,f_w} , and the parameters are developed in this section.

The windup correction was implemented in accordance with the recommendations presented by Astrom and Murray [5]. The anti-windup transfer function, C_{V,f_w} , takes the form:

$$\frac{F_w(s)}{(\mathcal{V}_{\text{limited}}(s) - \mathcal{V}(s))} = C_{V,f_w}(s) = \frac{K_t}{s},\tag{5.16}$$

where $F_w(s)$ is the controller output, $(\mathcal{V}_{\text{limited}}(s) - \mathcal{V}(s))$ represents the level of intogrator windup error that will be negated, and K_t is the controller tuning gain. Trial and error was

used to determine K_t , in order to achieve sufficient windup correction speed, while avoiding instability (overshoots/oscillations in the controller output). As presented by Astrom and Murray [5], the anti-windup takes the form of an integrator with a gain (i.e. K_t) that is tuned with the controller's integral time, $t_{I,fb}$, viz,

$$K_t = \frac{1}{k_t * t_{I,fb}}. (5.17)$$

Astrom and Murray [5] recommend that K_t be a fraction of $1/t_{I,fb}$, resulting in the form presented in Equation 5.17, where k_t is a selectable tuning value. The selection of k_t governs the stability and also the time response of the windup correction. If the resulting K_t is too large, then the windup reset can occur simply due to measurement noise; if too low, then windup may still occur. A value of k_t =4 was found to provide a stable and yet windup-correcting result for K_t .

5.4 Steady State Analysis of I/O Models

Figure 5.12 demonstrates the steady state boundary layer response to a range of roughness element heights and plasma actuator voltages. Note that the plasma actuator boundary layer response and corresponding model downstream shear stress values have been made negative in order to facilitate comparison with their counterparts for the roughness element. The data allow assessment of the expected control performance at steady state, but not during transients where the full dynamics as given by the boundary layer response transfer function, as provided in Equations 5.1 and 5.2, must be accounted for.

With the roughness element deployed to some height, the expected upstream and downstream shear stress disturbance may be seen with the blue or red lines, respectively. Multiplying the

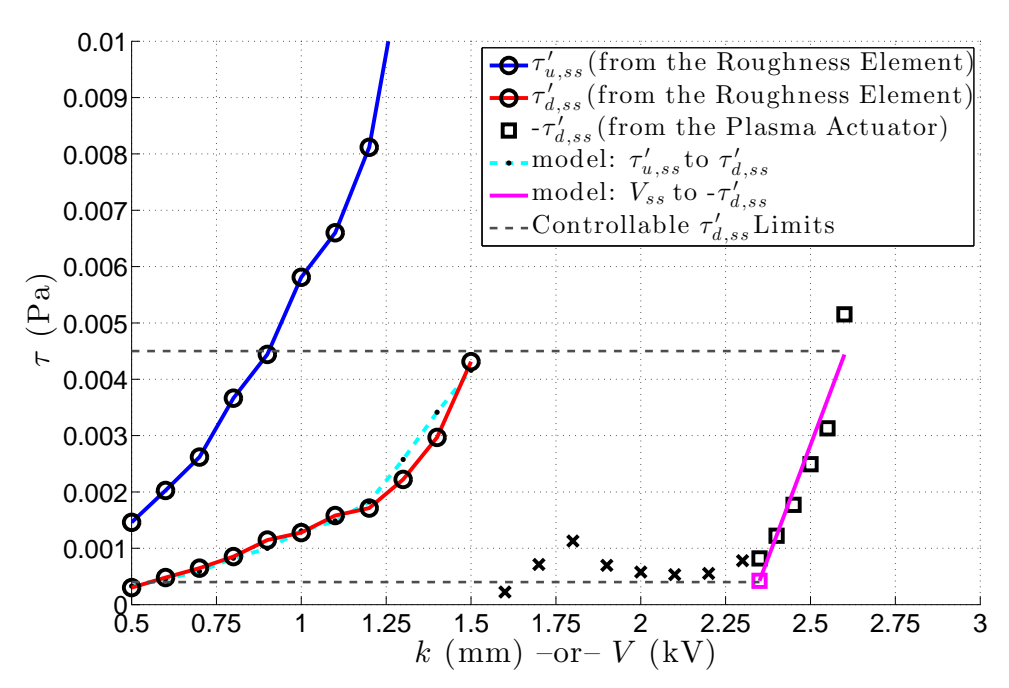


Figure 5.12: Upstream and downstream wall shear stress disturbance for different roughness element heights, and downstream wall shear stress disturbance for different plasma actuator voltage amplitudes with the feedback sensor at x_{fb} - x_k =300 mm (noted by symbols). The broken cyan line shows the steady state downstream shear stress disturbance predicted based on multiplying the upstream shear stress disturbance with K_{τ} (see Equation 5.1). The magenta line is a least-squares straight line fit to the square symbols (see Equation 5.3).

upstream shear stress disturbance by K_{τ} (which is equal to negative the gain used with the feedforward controller), the downstream shear stress is predicted by the cyan dashed line. This outcome is in good agreement with the actual measured downstream shear stress (red). Furthermore, the boundary layer response to plasma actuator forcing is demonstrated with the magenta line fitted to the useable voltage values (squares), and the resulting controllable downstream shear stress disturbances are those falling within the range of the magenta line. The expected input disturbance (cyan) may then be compared to the output control disturbance (magenta) to provide the appropriate match between roughness element height (upstream shear stress disturbance) and plasma actuator voltage. Figure 5.12 also shows that while the roughness element induced disturbance can be controlled to a low level, the disturbance at k=0.5 mm is just below the controllable shear stress lower limit. Toward the high end, the roughness induced shear stress is controllable up to the maximum height (before turbulence is induced) at k=1.5 mm, where the appropriate voltage for control is just less that V=2.6 kV. It is notable that while all of the discrete roughness element heights investigated in the I/O data collection, except k=0.5 mm, fall within the controllable range of the plasma actuator voltage, the unsteady roughness element actuation will pass through $0 \le k \le 0.5$ mm on each full up/down cycles. This will present an uncontrollable transient time before a sufficient roughness element height is achieved to lead to a controllable disturbance level which will be investigated further in the control results presented in §4.2.

After fully developing the control model with the appropriate plant and comptroller parameters, a Simulink model was developed, which was uploaded to the dSpace control/interface system to implement the control model. An example Simulink model is provided in Appendix 7.4 in Figure A.1; Figures A.2 - A.11 provide the sub-model Simulink blocks which are color-coded to match those within Figure A.1 and provide the calibration

values and controller model parameters.

Chapter 6

Control Experiment Results

A series of control experiments were carried out where the roughness element height, freestream velocity, control strategy, streamwise location of the feedback sensor, and steady state hold time were varied in order to evaluate the effectiveness of the developed control model under these different conditions. Table 6.1 presents the array of test conditions used for these tests. In §6.1 the control effectiveness with a steady state disturbance is investigated; while in §6.2, the ability of the control model to attenuate unsteady disturbances is evaluated in detail.

6.1 Steady Disturbance Control

In a precursor study to the current control efforts, an experimental control study was conducted whose targeted disturbance were steady-state and slowly-varying streak disturbances generated by an array of roughness elements. The details and results of that study are not contained herein, but were co-authored by Kyle Bade and published with Hanson *et al.* [26]. The current control efforts build upon those in [26], by targeting unsteady streak disturbances generated by an isolated roughness element, rather than the steady disturbances generated by an array of stationary roughness elements.

A series of control experiments were carried out where the roughness element height was varied from k=0 to a specified height, similar to the I/O data of Figures 5.3 and 5.7. Results were collected with and without active control, and all results featured a prolonged *hold*

Case	k_{min}	k_{max}	U_{∞}	Control Method	x_{fb} - x_k	t_h/f_k
(CC)	(mm)	(mm)	(m/s)	(feedforward or feedback)	(mm)	(s)/(Hz)
1	0	0.5	5	ff+fb	300	2.0/0.25
2	0	1.0	5	ff+fb	300	2.0/0.25
3	0	1.1	5	ff+fb	300	2.0/0.25
4	0	1.2	5	ff + fb	300	2.0/0.25
5	0	1.3	5	ff+fb	300	2.0/0.25
6	0	1.4	5	ff + fb	300	2.0/0.25
7	0	1.0	4	ff+fb	300	2.0/0.25
8 (2)	0	1.0	5	ff + fb	300	2.0/0.25
9	0	1.0	6	ff + fb	300	2.0/0.25
10	0	1.4	4	ff + fb	300	2.0/0.25
11 (6)	0	1.4	5	ff+fb	300	2.0/0.25
12	0	1.4	6	ff+fb	300	2.0/0.25
13 (alt)	0	1.0	6	ff+fb	300	2.0/0.25
14	0	1.0	5	ff	300	2.0/0.25
15	0	1.0	5	fb	300	2.0/0.25
16(2)	0	1.0	5	ff+fb	300	2.0/0.25
17	0	1.2	5	ff	300	2.0/0.25
18	0	1.2	5	fb	300	2.0/0.25
19 (4)	0	1.2	5	$ff{+}fb$	300	2.0/0.25
20	0	1.4	5	ff	300	2.0/0.25
21 (6)	0	1.4	5	fb	300	2.0/0.25
22	0	1.4	5	ff+fb	300	2.0/0.25
23	0	1.0	5	ff+fb	200	2.0/0.25
24 (2)	0	1.0	5	ff+fb	300	2.0/0.25
25	0	1.2	5	ff+fb	200	2.0/0.25
26 (4)	0	1.2	5	ff+fb	300	2.0/0.25
27	0	1.4	5	ff+fb	200	2.0/0.25
28 (6)	0	1.4	5	ff+fb	300	2.0/0.25
29	1.0	1.2	5	ff+fb	300	0.05/6.06
30	1.0	1.2	5	ff+fb	300	0.1/3.85
31	1.0	1.2	5	ff+fb	300	0.2/2.00
32	1.0	1.2	5	ff+fb	300	0.5/0.93
33	1.0	1.2	5	ff+fb	300	2.0/0.25
34	1.0	1.4	5	ff+fb	300	0.05/5.71
35	1.0	1.4	5	ff+fb	300	0.1/3.85
36	1.0	1.4	5	ff+fb	300	0.2/2.00
37	1.0	1.4	5	ff+fb	300	0.5/0.93
38	1.0	1.4	5	ff+fb	300	2.0/0.25

Table 6.1: Summary of test parameters for the control experiments. Subsets of experiments (separated by a line) investigate the effect of each parameter (highlighted in darker gray).

time, $t_h \approx 2.0$ s, at the fully retracted and fully deployed roughness element heights. This allowed for steady-state uncontrolled and controlled results to be obtained and analyzed at various k values. The next section, §6.2, will examine the unsteady control results, wherein the controller gains and integration time constant affect the effectiveness of the control model. This section will examine the results during the steady-state *hold* time, and provides a simplified set of data for analysis.

Figure 6.1 demonstrates the results of uncontrolled and controlled disturbances at the upstream and downstream shear stress sensors, under various stationary roughness element heights. The upstream sensor measures nominally the same disturbance shear stress, τ'_u , with and without control, thus the "controlled" upstream shear stress is omitted but was checked for agreement with the uncontrolled measurement. The downstream sensor, which captures the effectiveness of the control, demonstrates that the appropriate level of plasma voltage is supplied and the controlled-disturbance shear stress, $\tau'_{d,\mathcal{C}}$, is driven to zero at all roughness element heights. The ability of the control model to achieve a zero disturbance level at steady state is expected, given the PI feedback controller, however, the laboratory implementation and demonstration of this active control for an isolated streak is an original accomplishment.

In order to further evaluate the effectiveness of the control model, the freestream velocity was set to $U_{\infty}=4.0$, 5.0, and 6.0 m/s, with k=1.0 and 1.4 mm. Two of these freestream velocities correspond to off-design control conditions because the freestream velocity was always set to $U_{\infty}=5.0$ m/s during the I/O model development used for the controller design; the control results are presented in Figures 6.2a and 6.2b, for k=1.0 and 1.4 mm, respectively. Clearly, the disturbed downstream shear stress is driven to the Blasius level ($\tau'_{d,\mathcal{C}}\approx 0$) in all cases, except where $U_{\infty}=6.0$ m/s with k=1.4 mm. Under the latter conditions, the

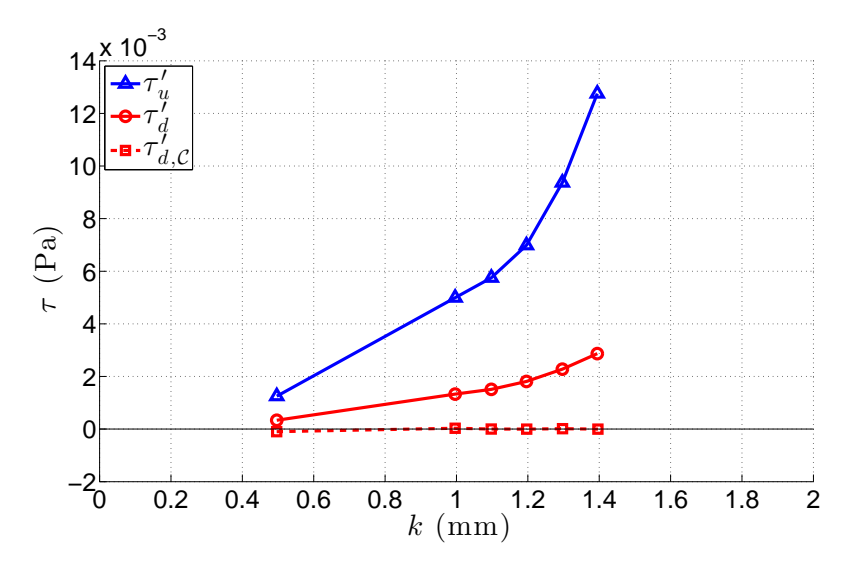


Figure 6.1: Steady-state control results for the upstream (blue) and downstream (red) shear stress sensors at various roughness element heights, k, with U_{∞} =5.0 m/s and the feedback sensor located at x- x_k =300 mm.

investigation of the streak disturbance characteristics in §3.2.3 clearly showed that under these conditions, a turbulent disturbance would be generated; therefore, the controller is not expected to successfully control this more complex disturbance. The presence of a turbulent disturbance is further confirmed by the greatly increased level of shear stress at both the upstream and downstream sensors.

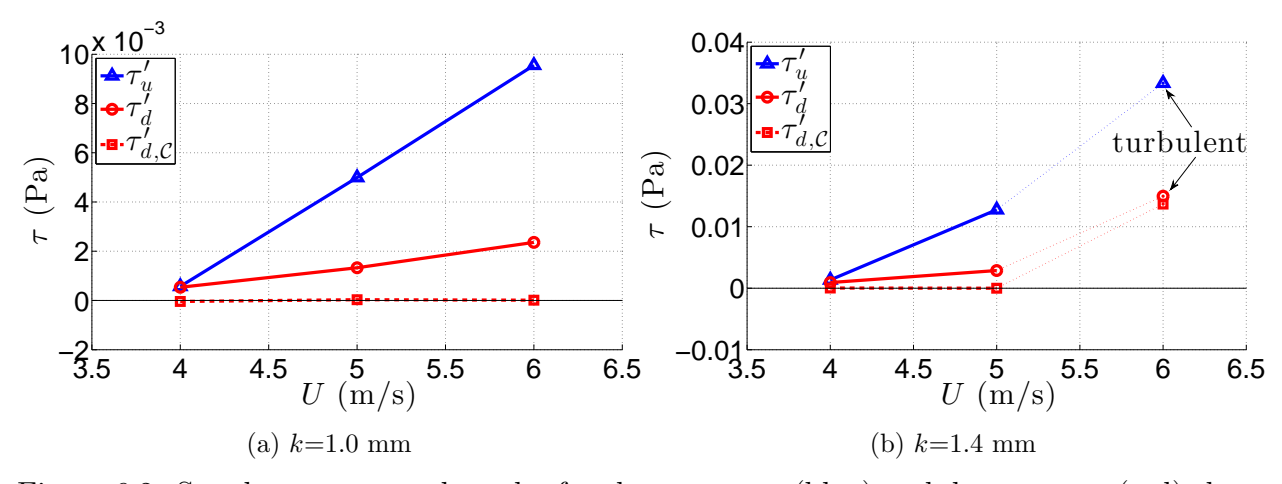


Figure 6.2: Steady-state control results for the upstream (blue) and downstream (red) shear stress sensors at various freestream velocities, U_{∞} , with the feedback sensor located at x- x_k =300 mm. The roughness element height is varied from k=0 to a) k=1.0 mm and b) k=1.4 mm.

For the results presented in Figures 6.2a and 6.2b, the Blasius 'target' shear stress was set based on the knowing that the freestream velocity is different from the design value of 5 m/s. If information regarding the different freestream velocity value is not used to adapt the control set point, the control model would attempt to achieve the U_{∞} =5.0 m/s based target shear stress, despite $\pm 20\%$ change in the freestream velocity. To adapt for changes in the control set point due to variation in the freestream velocity without user intervention, the input signal from the freestream sensor is used, in addition to the two shear stress sensors, must be used by the control model. The results at steady state once again demonstrate a zero shear stress disturbance; a consequence of the effectiveness of the freestream correction method as well as the feedback portion of the control model. These results are not provided here because they are identical to that of Figures 6.2a and 6.2b.

Finally, the feedback sensor was positioned at various downstream locations, relative to the plasma actuator, and the steady-state control results are provided in Figures 6.3a, 6.3a, and 6.3c for k=1.0, 1.2, and 1.4 mm, respectively. As expected, the upstream and downstream uncontrolled shear stress magnitude increases with roughness element height. Note that, consistent with expectation, the downstream disturbance magnitude shows a very small natural decrease with downstream location over the x_{fb} - x_k =200-300 mm range. Similarly, the upstream shear stress disturbance magnitudes, τ_u^I , show some variability, but this is simply a run-to-run variation; the upstream shear stress disturbance is nominally the same, regardless of x_{fb} . Clearly, the controlled shear stress demonstrates an essentially zero disturbance level in these steady-state results. Presumably, this fully controlled level is achieved faster with the downstream sensor located closer to the plasma actuator (faster feedback response), which will be investigated further in the analysis of the unsteady results (§6.2.4).

While the current control experiments were designed with simplicity in mind (i.e. a single

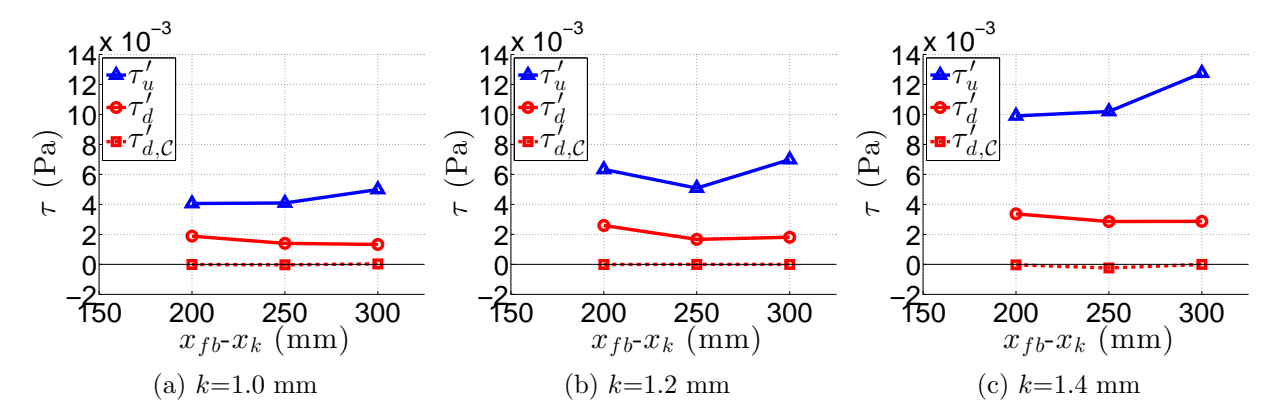


Figure 6.3: Steady-state control results for the upstream (blue) and downstream (red) shear stress sensors at various roughness element heights and downstream shear stress sensor locations, with U_{∞} =5.0 m/s.

roughness element, a signal upstream sensor, a single downstream sensor, and a freestream velocity sensor), it is the greater ambition of this work to control the entire three-dimensional roughness element induced streak disturbance. In order to assess the effectiveness of the control model over the entire downstream disturbance plane, full y-z planar data sets were acquired using the 3-axis traverse and 4-hot-wire setup used to acquire the planar disturbance contour results of §3.2.3 at $x-x_k=305$ mm, with the feedback sensor located at $x_{fb}-x_k=300$ mm. Figures 6.4a and 6.4b, provide contour planes of the steady-state upstream and downstream, respectively, disturbances induced by the roughness element deployed to k=1.2 mm. Figure 6.4c provides a contour plane of the steady-state disturbance at the downstream plane induced by the plasma actuator with V=2.4 kV. Note that while these contour results are presented to represent the planar disturbances at the sensor planes, the actual measurements were performed 5mm downstream of each sensor in order to avoid interaction with the nearby wall-shear sensor and hotwire(s). Also note that these contour planes are presented using the wall-normal coordinate, y, which is in mm, rather than the height η used in presenting the results in §3.2.3 and Chapter 4.

The upstream roughness-element-induced disturbance plane, Figure 6.4a, demonstrates

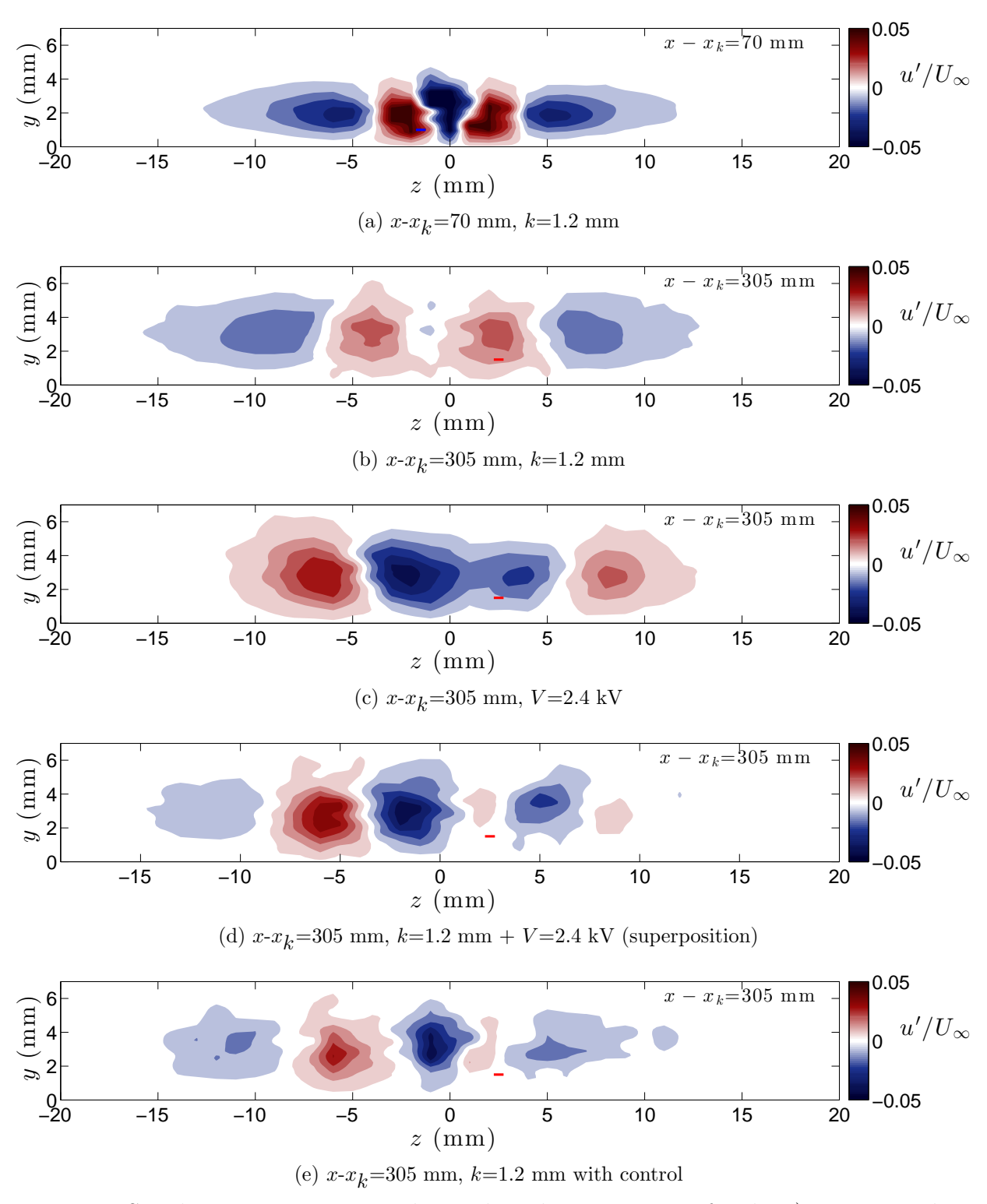


Figure 6.4: Steady-state streamwise velocity disturbance contours for the a) upstream plane with k=1.2 mm, b) downstream plane with k=1.2 mm, c) downstream plane with V=2.4 kV, d) downstream plane with a superposition of the V=2.4 kV disturbances, and e) downstream plane with control active with V=2.4 kV disturbances, and e) downstream plane with control active with V=2.4 kV disturbances,

the expected aspects of a negative wake-disturbance, approximately centered at z=0, with high, then low, disturbances to each side. The disturbance is symmetric and the upstream shear stress sensor is drawn using a solid blue line on the -z side, within the high-speed streak. In Figure 6.4b, at the downstream plane $(x-x_k=305 \text{ mm})$, the disturbance has grown in both the y and z directions, and has also experienced a spanwise shift of approximately 1 mm toward the negative z direction. The downstream sensor is shown on the +z side of the disturbance plane and within the high-speed disturbance. In Figure 6.4c, the downstream disturbance from the plasma actuator is provided, which is seen to be slightly shifted to the +z side. Also, the disturbance from the plasma actuator appears to be slightly stronger on the -z than the +z side. The shear stress sensor is located within a portion of the negative disturbance, and thus, the plasma actuator should be able to properly cancel the roughness element induced positive disturbance at this location. However, the spanwise shift and slightly asymmetric disturbance strength demonstrated in the plasma actuator disturbance will have consequences for properly cancelling the disturbance over the full downstream plane.

The appropriate plasma actuator voltage for cancelling the disturbance induced by the roughness element at k=1.2 mm should be $V\approx 2.43$ kV, according to the steady state I/O control model demonstrated in Figure 5.12. Therefore, the downstream disturbances generated by the roughness element and plasma actuator in Figures 6.4b and 6.4c are nearly matched for appropriate disturbance cancellation, at the downstream shear sensor location of (y, z)=(1.5, 2.5) mm. Figure 6.4d demonstrates the point-wise summation of the disturbances of Figures 6.4b and 6.4c, resulting in a superposition of the disturbances, which, according to linear theory¹, should produce the controlled downstream disturbance plane re-

¹provided that the disturbance level is sufficiently small that non-linear terms may be ignored in the

sult (with both roughness element and plasma actuator inputs being active simultaneously). In Figure 6.4e, the controlled disturbance for k=1.2 mm is provided, and demonstrates excellent agreement with the superposition result. The implication of the agreement between the superposition of the disturbances induced by the roughness element and the plasma actuator and that of the controlled result which represented the physical combination of the two disturbances in the actual flow environment, is that the disturbance grows linearly, which is desirable for the disturbance cancellation premise underlying the current control strategy.

The full y-z plane result of the controlled disturbance in Figure 6.4e shows that, at the location of the feedback sensor (red line), the disturbance is driven to zero. Unfortunately, this is not true for the entire disturbance plane. The mismatch of the spatial distribution and strength of the positive and negative disturbances in Figures 6.4b and 6.4c result in the imperfect planar disturbance cancellation. The agreement of the superposition and controlled-disturbance results, however, indicate that with proper matching of the roughness element and plasma actuator disturbance strength and spatial shape, complete cancellation of the roughness element disturbances would be expected. To elaborate on this, the plasma actuator disturbance plane is artificially shifted toward the negative z side, and the magnitude of the entire plasma actuator disturbances plane is multiplied by a gain. These modifications should be realizable in the wind tunnel given the validation of the superposition of the disturbances; an estimated control plane is provided in Figure 6.5, in which the plasma actuator disturbance plane is shifted by -1 mm in z and a gain of $0.52*u'/U_{\infty}$; this gain corresponds to an output voltage of approximately V=2.35 kV, which is smaller than the calculated optimal voltage of 2.43 kV for cancelling the disturbance when k=1.2mm (but this value was calculated for the sensor location, not the total planar disturbance

disturbance momentum equation

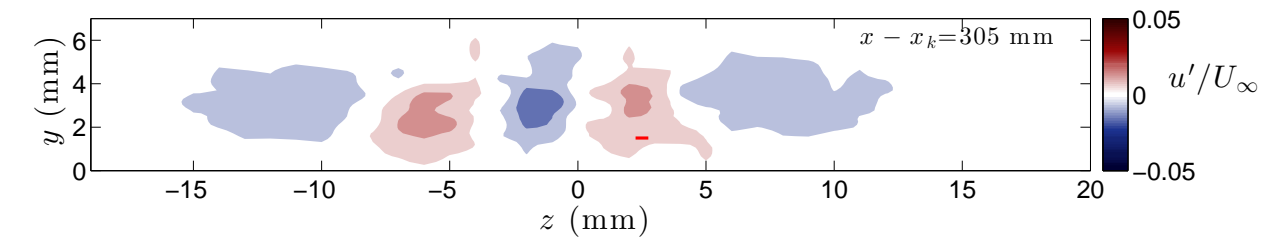


Figure 6.5: Steady-state streamwise velocity disturbance contours for the downstream plane with a superposition of the k=1.2 mm and V=2.4 kV disturbances with the plasma actuator plane shifted by -1 mm and multiplied by a gain of 0.52.

cancellation).

In order to further evaluate the effectiveness of the planar control, the disturbance energy was calculated, according to Equation 3.5. With control, the disturbance energy in the full plane is reduced by 40.1\% at steady-state, the majority of which is the noted disturbance cancellation in the +z half plane. In the latter half plane only, the disturbance energy is reduced by 66.2%. Considering the improper spatial matching of the disturbance, the success of this control is quite good. The modified superposition control plane provides a best case scenario using the current actuator geometry, and provides an energy reduction of 49.6%. Despite the qualitative similarities between the active control result and the superposed disturbances, the unmodified superposition plane actually increased the total disturbance energy by 50.6%, due to the strengthened disturbance magnitude regions in -z half plane caused by the spatial mismatch. In the +z half plane, the superposition result was reduced by 42.9%, and the estimated control (modified) superposition result reduced the disturbance energy by 60.4%. The control model result therefore achieved the best success, and the increase in the cancelled disturbance between the superposed and modified superposed results leads to the expectation that a shifted plasma actuator, to spatial match the roughness element induced disturbance in the entire y-z plane, would have greater success in cancelling the targeted disturbance in the entire plane. Further cancellation would be expected if plasma actuator geometry alterations could offer an even further improved spatial disturbance match with the roughness element induced disturbance (than can be achieved with a simple shift of the presently employed plasma actuator).

6.2 Unsteady Disturbance Control

A unique set of control experiments was carried out where an unsteady streak disturbance was induced by a dynamically actuated roughness element. This section investigates the ability of the control model to properly address these unsteady streaks and cancel/reduce their strength as characterized in the downstream plane. All results are presented as phase averaged data, based on the roughness element motion, using a minimum of 20 cycles; similar to the methods used in the Input/Output model data processing. In §6.2.1, the control effectiveness when moving the roughness element from k=0 to several discrete roughness element heights is examined. Next, in §6.2.2, the effect of the freestream velocity is investigated. In order to assess the effectiveness of the feedforward portion of the control model separately from that of the feedback portion, §6.2.3 provides the results of a series of control experiments with modified control models that include feedforward control only, feedback control only, and combined feedforward and feedback control (which is presented in all other sections). In §6.2.4, the feedback sensor is positioned at three different downstream locations in order to examine the control effectiveness and limitations with an altered convection time for the disturbance to reach the downstream measurement plane (i.e. an increased time delay in the plant models). As was explained in Chapter 5, a new control model was developed and used for each downstream sensor position. Finally, the ability of the control model to effectively control periodic disturbances with different frequencies but with a constant amplitude is investigated in §6.2.5; where the roughness element height oscillates between k=1.0 and 1.2 or 1.4 mm. The effective frequency of these disturbances is modified by altering the steady-state hold-time, t_h , of the roughness element. An investigation of the maximum controllable disturbance frequency is conducted, yielding various successful as well as unsuccessful results, both of which are instructive.

6.2.1 Effect of Roughness Element Height

The effect of roughness element height on the controller effectiveness is investigated in this section, or perhaps more appropriately, the ability of the controller to properly address a streak disturbance as it grows to various strengths before reaching steady state. The response of the boundary layer to various roughness element deployment heights was investigated in $\S 5.2.1$, and it was found that by altering k, the strength of the disturbance was increased as demonstrated in Figure 5.5. Therefore, an investigation of various roughness element heights is akin to an investigation of the ability of the controller to address streaks of various amplitudes.

Figure 6.6 demonstrates the roughness element motion from k=0 to many discrete fully deployed roughness element heights. The velocity and acceleration of the roughness element motion are held constant ($v_k=7.5 \text{ mm/s}$ and $a_k=1000 \text{ mm/s}^2$, as determined to be appropriate in §4.1). The gray bands in Figure 6.6 are used to mark the time periods of upward (darker gray) and downward (lighter gray) roughness element motion; these bands are provided for k=1.4 mm in Figure 6.6 and are provided for the appropriate k motion on all subsequent control results plots for reference². These step-up/step-down roughness element

²The use of gray bands to mark the roughness element's motion periods was chosen in order to simplify the information provided on each control result figure. The actual k(t) could have equivalently been used.

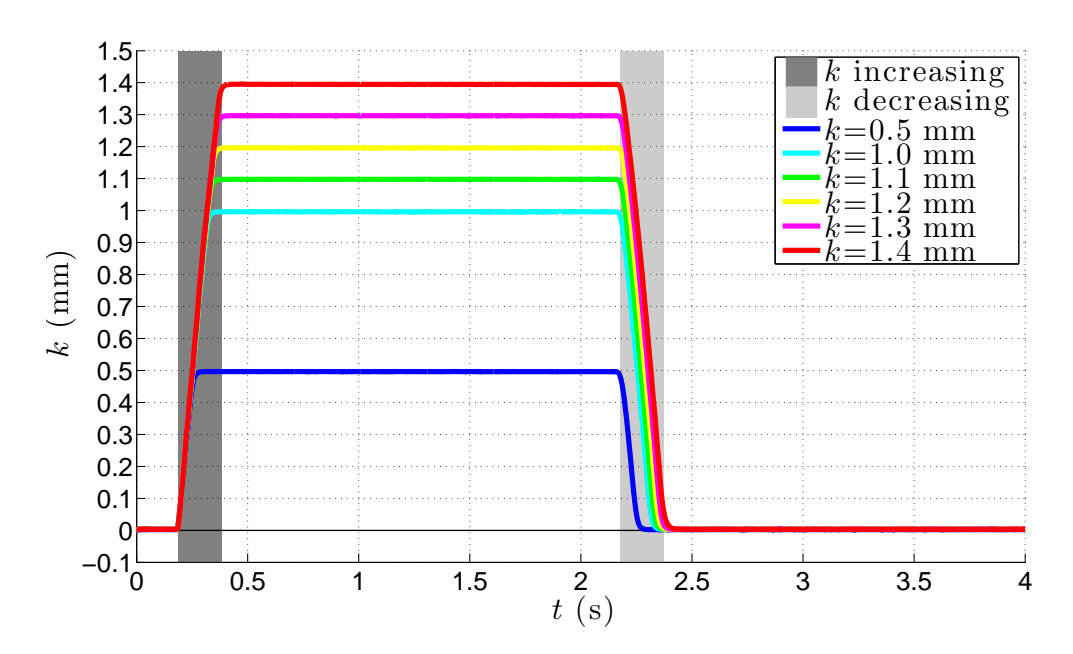


Figure 6.6: Dynamic (unsteady) roughness element motion from k=0 to various deployment heights, k. Note that the gray bands demonstrate time periods when the roughness element is in motion, either upward or downward, for k=1.4 mm, and are provided on all subsequent unsteady control results plots for the appropriate k.

motions, along with relatively long (≈ 2 s) periods of static roughness element height at the fully up and down positions, allow an assessment of the steady (examined in §6.1) controlled and uncontrolled disturbance results as well as the transient development of the unsteady disturbance during control, which is the focus of this section.

In Figure 6.7, the downstream shear stress, measured by the feedback sensor, is provided for the various roughness element deployments heights considered in Figure 6.6. Note that the uncontrolled shear stress measurement, $\tau'_d(t)$, is provided as a thin line, while the controlled downstream shear stress, $\tau'_{d,\mathcal{C}}(t)$, is a thicker line of the same color. As was seen in the steady-state disturbance control results of Figure 6.1, the controlled disturbance at each fully deployed roughness element height reaches a zero disturbance level (i.e. Blasius shear stress) after the initial transient effects subside $(1.1 \leq t \leq 2.2 \text{ s})$.

At the lowest roughness deployment height, k=0.50 mm (blue), the uncontrolled distur-

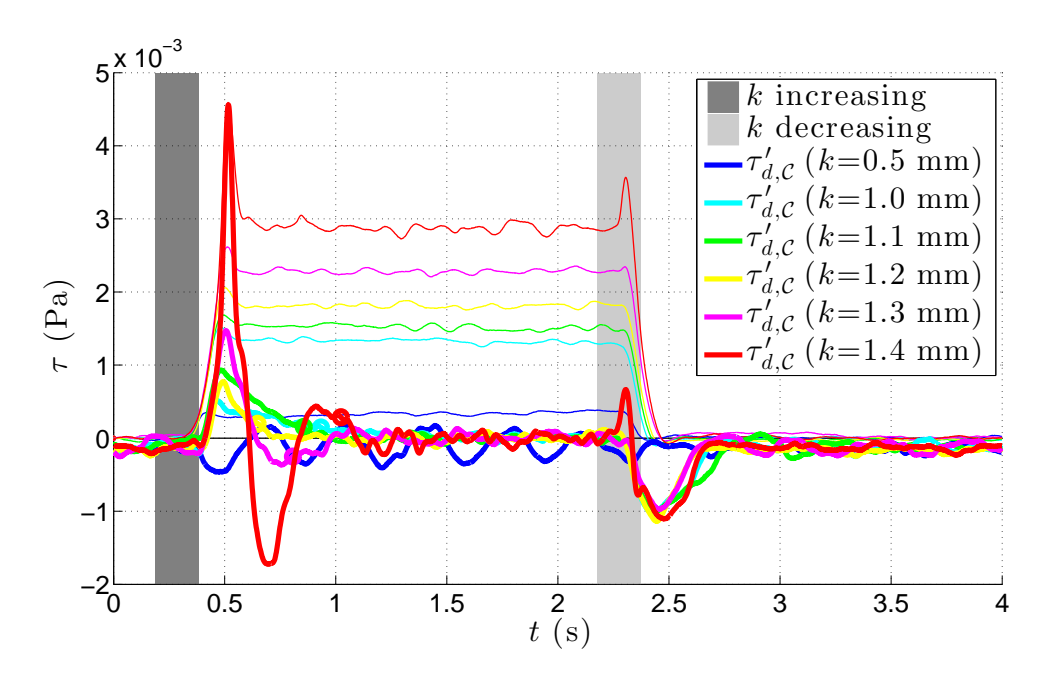


Figure 6.7: Unsteady control results for the downstream shear stress at various roughness element heights with the feedback sensor located at x_{fb} - x_k =300 mm and U_{∞} =5.0 m/s. The settling time for each signal is noted with a \circ -marker.

bance level is very near the *minimum controllable* shear stress level. As a result, when the disturbance fluctuates slightly at the location of the downstream shear sensor, the controller turns the plasma on and off. This results in an under and overly controlled disturbance, and a noisy phase averaged control result because the plasma is either off, resulting in a small uncontrolled disturbance; or on, resulting in overly strong forcing by the plasma actuator and a negative disturbance. At the larger roughness element heights, the disturbance level is well within the controllable shear stress range and the controller effectively drives the disturbance shear stress to zero (i.e. the Blasius level) after a period of time.

Focusing on the upward roughness element motion response in Figure 6.7 (this period of time is highlighted in Figure 6.8), it is possible to identify what appear to be over-damped and under-damped controlled disturbance responses, depending on the roughness element height. For k=1.0 and 1.1 mm (cyan and green) the response of the controlled disturbance

slowly reaches the zero-level without oscillations, which is indicative of a controller tuned for stability; although the tuning could likely be adjusted to offer a more aggressive error reduction and reach the zero level faster. For k=1.3 and 1.4 mm (magenta and red) the response of the controlled disturbance quickly reaches the zero-level, but overshoots (resulting in a negative disturbance) and oscillates, taking a large time to settle to the zero-disturbancelevel; this is indicative of an overly aggressive controller response and is only marginally stable in that the control objective is eventually achieved. Finally, for k=1.2 mm (yellow) the response of the controlled disturbance quickly reaches the zero-level and does not oscillate around the zero-disturbance-level; this is indicative of a properly and optimally tuned control system. The variability in the response of the controller to the unsteady disturbance induced by the roughness element at different heights shows that the PI-controller integration-error correction ranges from too aggressive (oscillatory) or too relaxed (long settling time) for all but the k=1.2 mm disturbance. All of the controlled disturbances intersect at approximately time=0.6 s, with the case with the largest k (red) reaching a zero-amplitude the fastest. However, the overly aggressive tuning results in an undershoot followed by the longest settling time (time to reach 10% of the steady state value and remain below this threshold).

Also clear in Figure 6.8, is that the controlled results all remain at a zero-disturbance level for approximately 0.1 s longer than the uncontrolled results, before undergoing a sharp increase in the shear stress disturbance around t=0.4 s. The sharp rise of the controlled disturbance approximately matches that of the uncontrolled disturbance for some time $(0.4 \le t \le 0.48$ s) after rising above zero. This time period is sufficient for all (except the (red) k=1.4 mm result) to reach the steady state disturbance and each controlled disturbance reaches only a fraction of the uncontrolled peak disturbance magnitude. The k=1.4 mm (red) result exhibits a similar response as the other k results, except that a very steep (fast) disturbance growth

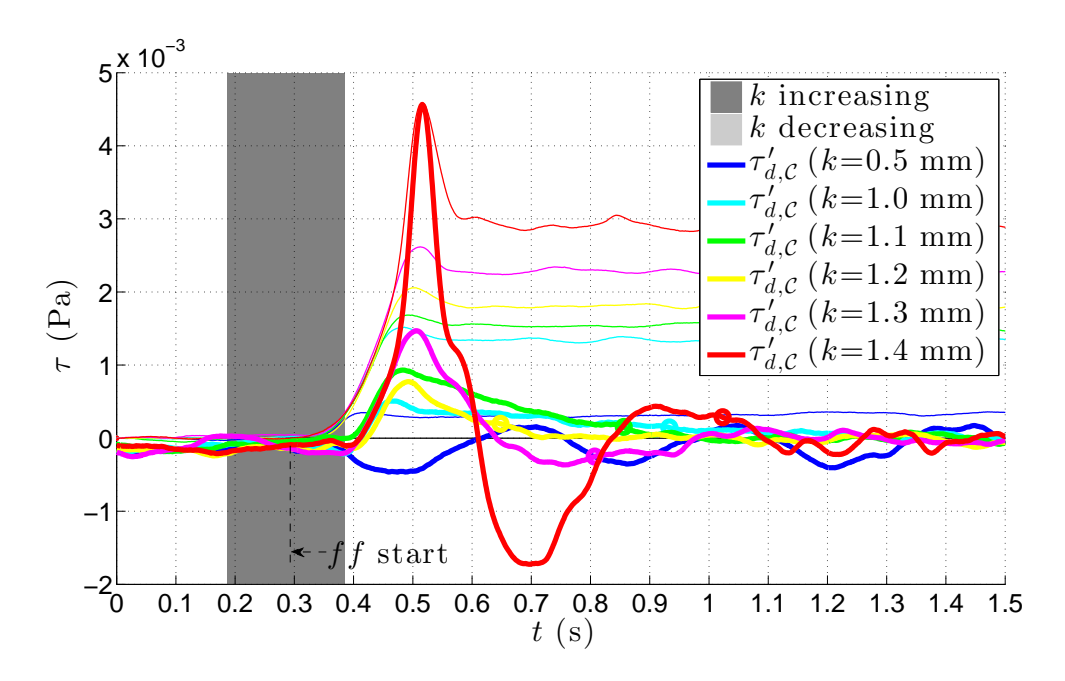


Figure 6.8: Unsteady control results for the downstream shear stress at various roughness element heights highlighting the transient effects during the upward motion of the roughness element; a zoomed in view of Figure 6.7. The settling time for each signal is noted with a o-marker.

is experienced from $0.48 \lesssim t \lesssim 0.52$ s, and the controlled disturbance reaches the uncontrolled peak disturbance magnitude. As noted in Figure 6.8, the feedforward (ff) controller output begins to take effect at t=0.293 s (which is before the uncontrolled disturbance reaches the downstream shear stress sensor and is thus purely feedforward control). Thus, as expected, the feedforward controller has an immediate effect in controlling the disturbance; however, the disturbance amplitude either grows to be larger than expected or faster than expected (based on the I/O data), resulting in the remaining disturbance level. Also noteworthy are that the peak disturbance for the uncontrolled and controlled disturbances occurs at the same point in time at each k.

The settling time, t_s , for each controlled disturbance to reach and maintain $\leq 10\%$ of the uncontrolled steady-state disturbance level is provided in Figure 6.9; note that the use of settling time here is not strictly typical in that the response is not to a perfect step input.

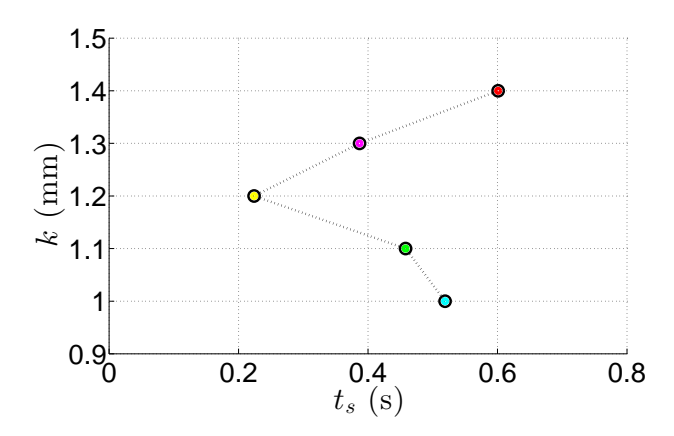


Figure 6.9: Settling time for the controlled disturbance to reach 10% of the uncontrolled steady-state disturbance level, for various roughness element heights, with the feedback sensor located at x_{fb} - x_k =300 mm and U_{∞} =5.0 m/s.

Note that the start-time for measuring the settling time for each signal is taken at the time at which the signal first exceeds 10% of the uncontrolled level. The settling time for k=0.5mm is not provided due to the very low disturbance amplitude, which resulted in the plasma actuator sporadically turning on/off and therefore no settling time is appropriate because a steady controlled state was not achieved. As previously discussed, the most optimally tuned response of k=1.2 mm provides the fastest settling time, while the other control response results, k=1.0/1.1 mm and k=1.3/1.4 mm, demonstrate that a longer time was required to achieve the steady-state controlled zero-disturbance amplitude. The non-optimal settling time for the various roughness element heights indicates that optimal tuning of the feedforward and feedback controllers were not used; however, the goal for these experiments was simplicity in the control model and real-world implementation, which was conducted successfully. Fortunately, the controller was sufficiently fast to control unsteady disturbances with a long hold time. In §6.2.5, the frequency of the unsteady disturbance fluctuation is investigated and the limitation of the controller to properly control a range of frequencies for the unsteady disturbances is further analyzed.

In order to better assess the control effectiveness within the boundary layer, y-z planar

disturbance measurements were acquired with and without control at the x_{fb} - x_k =305 mm plane. In order to collect these results, the downstream shear stress sensor was mounted below the flat plate, and passed through a very small hole in the wall. This allowed the four hot wires (attached to the overhead 3D transverse) to be used in acquiring the planar results, 5 mm downstream of the wall-mounted sensor location, in a similar fashion to the results of §3.2.3. The steady-state planar disturbance results of Figures 6.4b and 6.4e are expanded here to included the temporally developing disturbances. Figure 6.10 demonstrates the unsteady planar disturbance with k=1.2 mm with no control at $x-x_k=305$ mm; while Figure 6.11 provides the controlled flow result using the feedforward and feedback control model, at the same time instants relative to the upward motion of the roughness element as the uncontrolled results. Note that while the control results of Figures 6.7 and 6.8 are presented in terms of τ'_d , the results in Figures 6.10 and 6.11 are presented as the normalized velocity disturbance versus time, $u'(t)/U_{\infty}$. The maximum disturbance level at the downstream shear sensor location, in terms of the velocity disturbance, is seen to be $u'(t)/U_{\infty}\approx 1.2\%$, which is controlled to $u'(t)/U_{\infty}\approx 0.2\%$. The small remaining disturbance level at the sensor is likely due to the very long measurement time for these phase-averaged planar-disturbance results. The planar results were collected over approximately 8 hours of continuous control/acquisition, using the methods described in §2.4, and this allowed for a small drift in the shear sensor calibration. Note that all other control experiments were conducted with less than two hours between calibrations, and no calibration drift was found. The significance of the small calibration drift was exaggerated by the very small velocity disturbance level during the controlled disturbance measurement.

In Figure 6.10, the disturbance grows as was previously demonstrated in Figure 4.5, although at a slightly different final k, and shows the expected high-speed disturbances

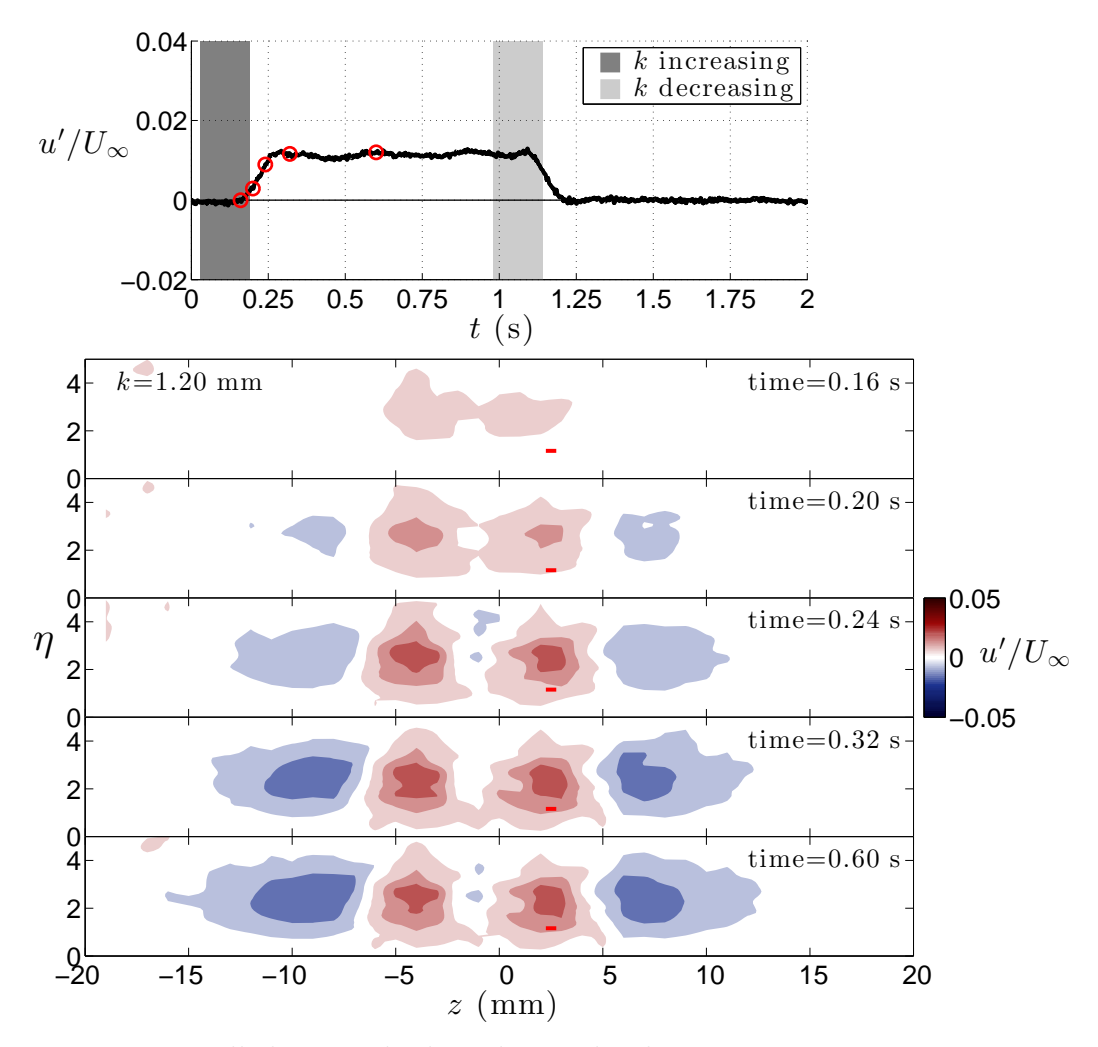


Figure 6.10: Uncontrolled unsteady disturbance development in time at x- x_k =305 mm, with a disturbance induced by a roughness element deployed from k=0 to 1.2 mm, with the feedback sensor located at x_{fb} - x_k =300 mm and drawn in the contours with a red line at (y, z)=(1.5, 2.5) mm. The top-plot provides the normalized velocity disturbance level versus time; five time instants are marked corresponding to the five disturbance contour results provided below.

shouldered by low-speed disturbances. These disturbances grow in time, without substantial change in their spatial distribution, until steady-state is achieved. In Figure 6.11 the controlled disturbance is seen to develop very differently in the left and right halves. As was discussed in the steady state results, the right-half plane has proper alignment of the (positive) roughness disturbance and (negative) plasma disturbance; however, the alignment is not optimal and the plasma actuator disturbance is stronger in the left-half plane. Clearly,

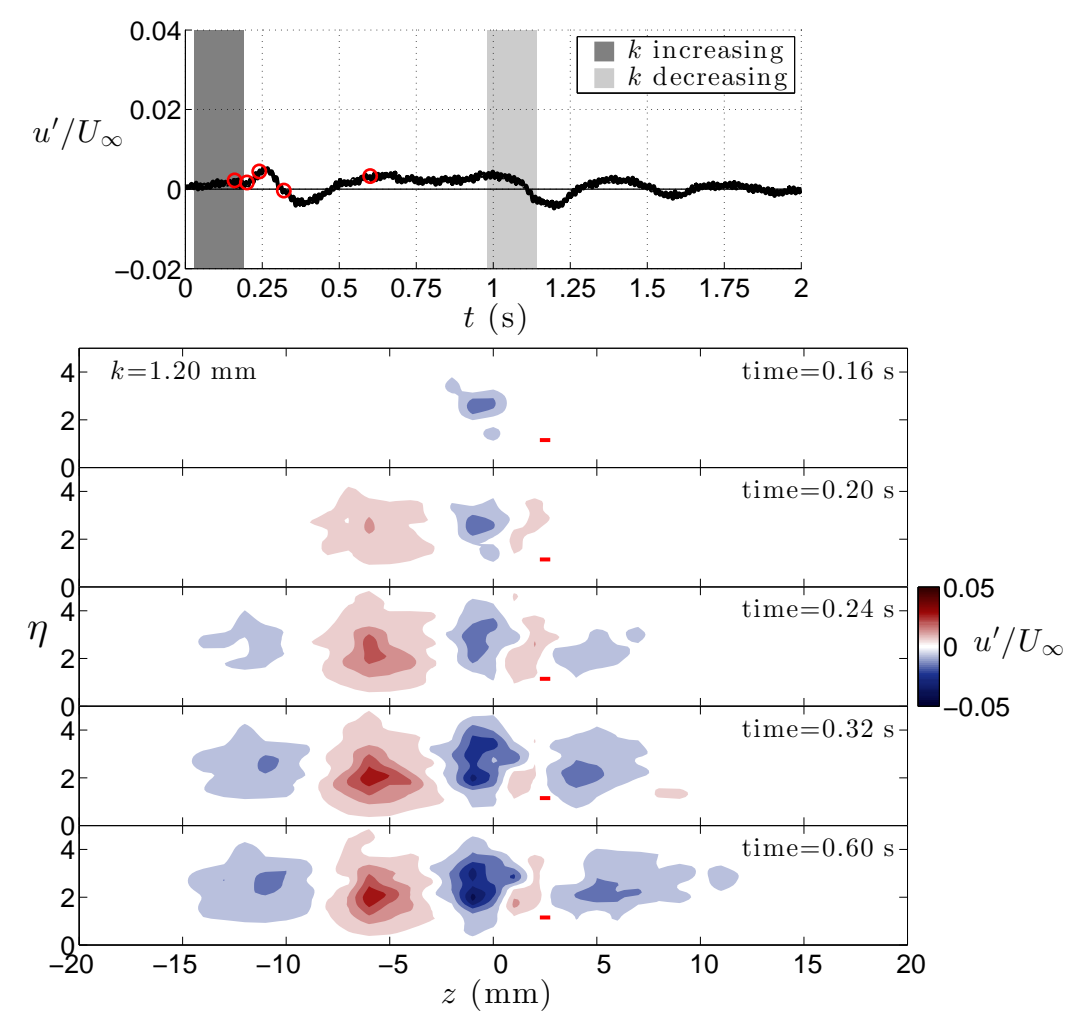


Figure 6.11: Controlled unsteady disturbance development in time at x- x_k =305 mm, with a disturbance induced by a roughness element deployed from k=0 to 1.2 mm, with the feedback sensor located at x_{fb} - x_k =300 mm and drawn in the contours with a red line at (y, z)=(1.5, 2.5) mm. The top-plot provides the normalized velocity disturbance level versus time; five time instants are marked corresponding to the five disturbance contour results provided below.

as the controlled disturbance grows, the controller is able to properly attenuate the disturbance at the shear sensor location. However, the disturbances in the left-hand plane are not properly addressed (due to the spatial mismatch) and these disturbances are not properly attenuated. The very good agreement between the steady-state superposition results (Figure 6.4d) and the actively controlled results (Figure 6.4e), allow the reasonable expectation that with proper spatial matching of the roughness element and plasma actuator disturbances,

the planar roughness element disturbance would be reduced/cancelled in both the left- and right-half planes.

The disturbance energy was calculated, according to Equation 3.5, to further evaluate the effectiveness of the planar-disturbance control quantitatively. These results are presented in Figure 6.12; where Figure 6.12a provides the total y-z energy, and Figure 6.12b represents the disturbance energy contained in the positive z-plane only. The disturbance energy in the full plane is reduced at all times when the boundary layer is disturbed, and by 40.1% at steady state. The majority of this cancellation is of the noted disturbance in the +z half plane, where the disturbance energy is reduced by 66.2%. Note that the disturbance energy development in time is presented with the contribution from background noise subtracted; this is accomplished by subtracting the mean disturbance energy level from the undisturbed portion (0 $\lesssim t \lesssim 0.1$ s), from the disturbance energy at all times ($E_{zero} \approx 5.0$ E-8 for the full plane, and $E_{zero} \approx 1.4$ E-8 in the +z half plane). Additionally, this results in an initial small negative disturbance energy from the controlled disturbance (from $0.15 \lesssim t \lesssim 0.24$ s), an effect of the feedforward controller activating immediately as a disturbance is detected at the upstream sensor and beginning plasma forcing ahead of the convecting disturbance. This was not noticed in the downstream shear stress disturbance results due to the very small magnitude of this effect; however, these planar disturbance energy results involve a summation of all disturbance effects in the downstream plane, and therefore this initial subtle disturbance reduction is captured.

6.2.2 Effect of Freestream Velocity

The control model was developed based on a freestream velocity of U_{∞} =5.0 m/s, which was used for all I/O model development data. In this section, the effectiveness of the controller

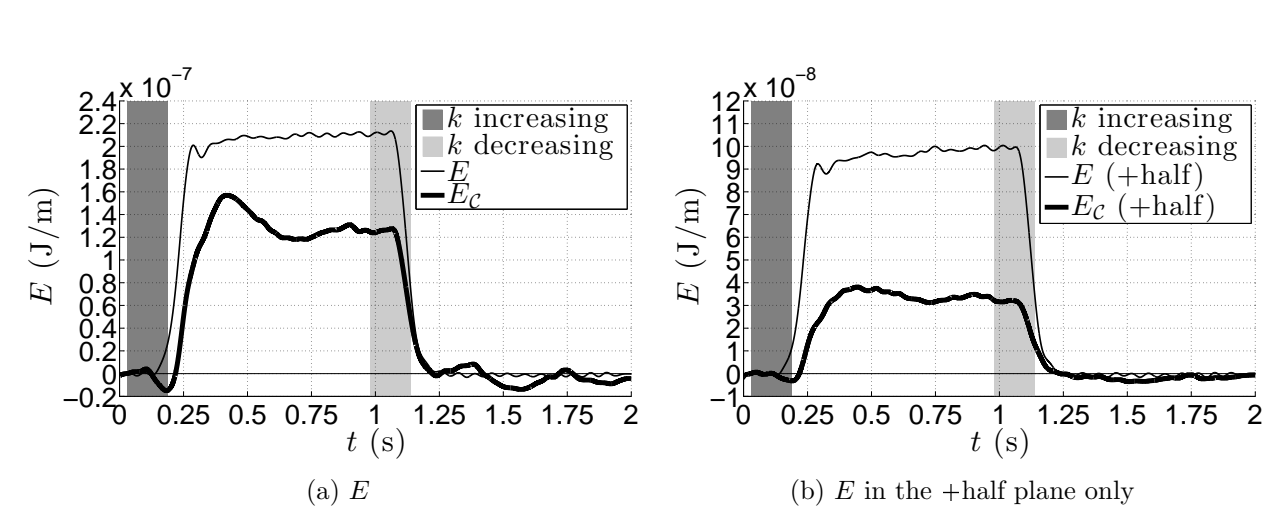


Figure 6.12: Energy contained in the y-z planar disturbance for the uncontrolled, E, and controlled, $E_{\mathcal{C}}$, unsteady disturbance as it develops in time at x- x_k =305 mm in a) the entire y-z plane and b) in the +z half plane only; with a disturbance induced by a roughness element deployed from k=0 to 1.2 mm, and the feedback sensor located at x_{fb} - x_k =300 mm.

to reduce the disturbance at off-design conditions is investigated with a $\pm 20\%$ change in the freestream velocity, to $U_{\infty}=4.0$ and 6.0 m/s, and the results are compared with the design velocity of 5.0 m/s. This investigation is similar to that of the changing roughness element height in that the disturbance strength will inherently change with freestream velocity (see §3.2.3); however, by altering the freestream velocity, the time delay characteristics of the boundary layer response will also change. In these experiments, the model will not be updated to have knowledge of these changes in the convective time delay; thus, the following control investigations are conducted outside of the scope of the model's I/O model data. For each investigated roughness element height (k=1.0 and 1.4 mm here), the shear stress disturbance magnitude at the upstream and downstream sensors is affected by the change in the freestream velocity. However, because the feedforward input to the control model is based on the shear stress disturbance amplitude at the upstream sensor (rather than the roughness element height), the controller should simply respond with a higher (or lower) control output according to the feedforward gain as if the roughness element were deployed

to a higher (or lower) height. The controller integral time constant, which is built into the feedback control system, is not adjusted to a faster (or slower) convection time delay to account for the disturbance reaching the downstream sensor faster (or slower) due to the change in freestream velocity.

In Figure 6.13, the uncontrolled and controlled responses at the downstream shear stress sensor are provided with k=0 to 1.0 mm. The controlled result for the design freestream velocity of U_{∞} =5.0 m/s (magenta) demonstrates the slowest response time to reach a zerodisturbance level. For the higher freestream velocity of U_{∞} =6.0 m/s (red), the faster convection time allows the feedback controller to more quickly integrate the controller error to reach the appropriate output control voltage to fully cancel the disturbance. For the lower freestream velocity of $U_{\infty}=4.0$ m/s (blue), the controller is effective in driving the disturbance to zero without much time delay. This is an unexpected result given that none of the various roughness element height results of Figure 6.7 were sufficiently controlled to a zerodisturbance level without feedback-controller contribution, and therefore the disturbance exhibited a sharp increase in level as the roughness element was raised with a slow control to zero. To explain this difference, the mechanism by which the plasma forces the flow must be further considered. As described in Hanson et al. [26], the slower freestream velocity (and resulting boundary layer velocity profile) causes fluid particles passing through the region of plasma actuator influence to exist within this forcing-region for a longer period of time. The result is a sustained forcing on the flow that is greater than with larger freestream velocities. Thus, the fully controlled lower freestream velocity (blue) result of Figure 6.13 is suspected to be due to a stronger imparted force (larger than the control model intends based on the I/O data at U_{∞} =5.0 m/s), which turns out to be a more successful forcing for complete control. This also explains the higher velocity result (red) which rises before the design result

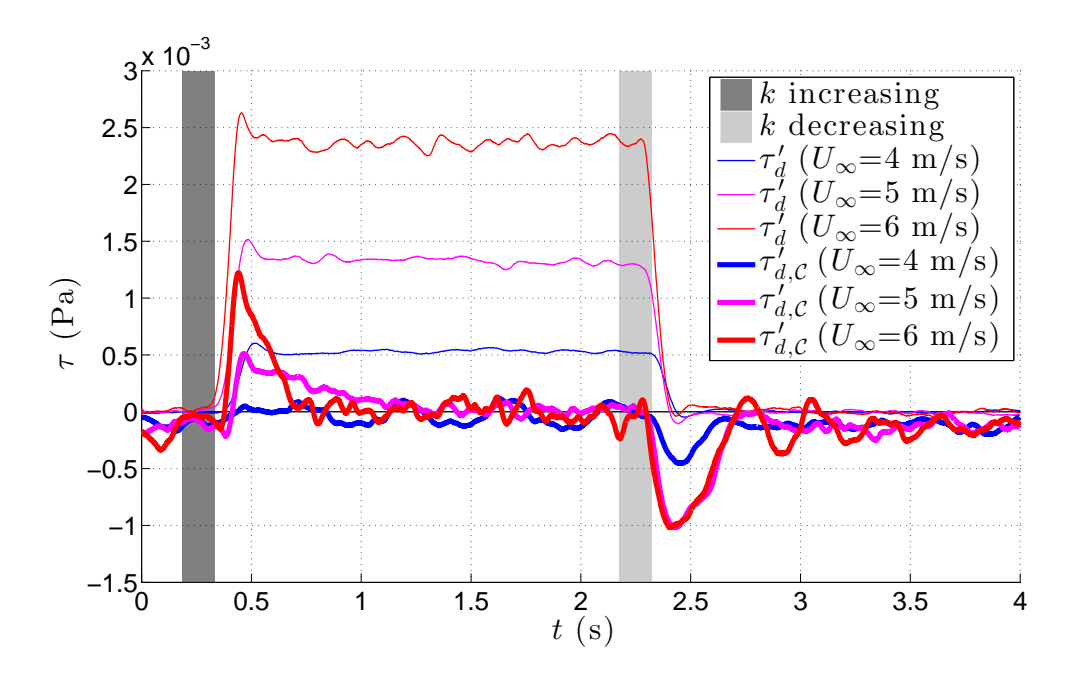


Figure 6.13: Unsteady control results for the downstream shear stress at various freestream velocities with the feedback sensor located at x_{fb} - x_k =300 mm and a fully deployed roughness element height of k=1.0 mm. The settling time for each signal is noted with a \circ -marker.

(magenta). It was found in Figure 6.8 that for all k, the rise in the controlled disturbance result after the upward motion of the roughness element occurred at nominally the same time delay from the start of the roughness motion; however, here, the red result rises sooner, an indication that the feedforward controller is less effective due to a short forcing action (due to the reduced time that the passing flow spends within the plasma actuator influence when $U_{\infty}=6.0 \text{ m/s}$). Note that this is further confirmed with the k=0 to 1.4 mm results in Figure 6.14.

In Figure 6.14 the uncontrolled and controlled response at the downstream shear stress sensor are provided with k=0 to 1.4 mm, with the most notable result being the presence of turbulent fluctuations at the larger freestream velocity (red). This is expected with k=1.4 mm and $U_{\infty}=6.0$ m/s, as the transition to a turbulent, albeit not equilibrium, boundary layer, was found to begin at a roughness element height of approximately k=1.51 and $U_{\infty}=5.0$ m/s

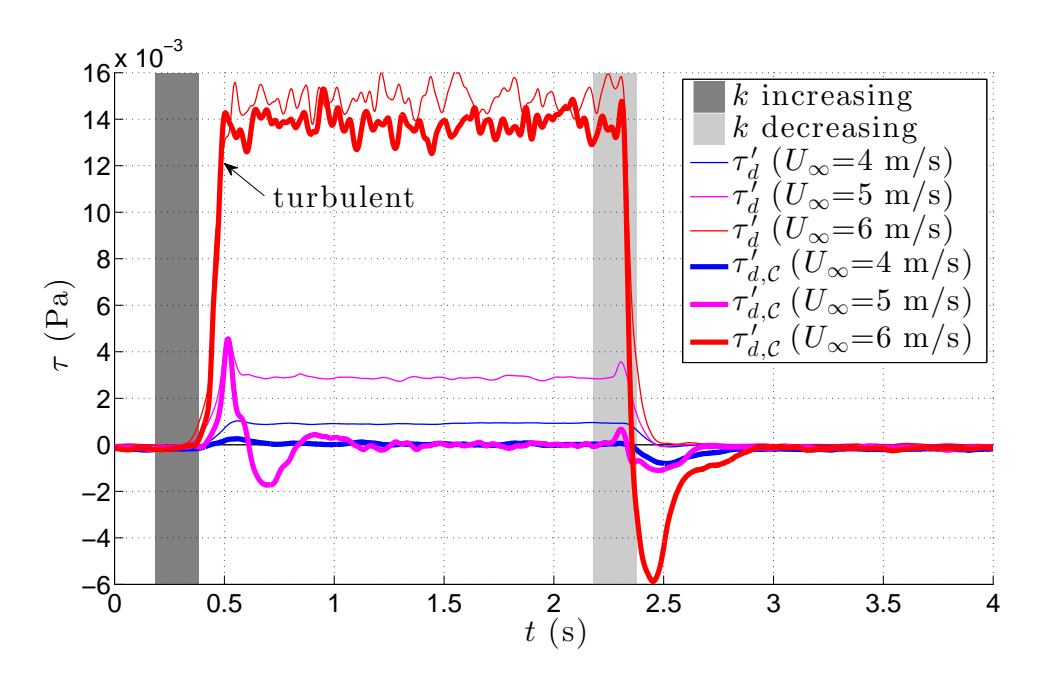


Figure 6.14: Unsteady control results for the downstream shear stress at various freestream velocities with the feedback sensor located at x_{fb} - x_k =300 mm and a fully deployed roughness element height of k=1.4 mm. The settling time for each signal is noted with a \circ -marker.

in §3.2.3, the 20% increase in freestream velocity is capable of increasing the disturbance amplitude sufficiently to cause transition to turbulence to happen at the lower roughness height of k=1.4 mm. As was seen in §6.2.1, the on-design disturbance with k=0 to 1.4 mm (magenta) is controlled, but with an over/undershoot control response demonstrating oscillations as the feedback controller integrates to the optimal plasma voltage level. The lower freestream velocity result (blue) demonstrates the fastest control to zero disturbance, likely due to the smaller disturbance amplitude and an effectively stronger feedforward controller due the stronger plasma forcing, as explained in the previous paragraph.

6.2.3 Feedforward vs. Feedback vs. Combined Control

In order to analyze the effectiveness of the feedforward and feedback controllers individually, each was operated with the other disabled as well as with both controller portions operational. The feedforward only controller should, in an ideal setting, perfectly cancel the disturbance using the developed I/O models. However, in the real world, the models are not perfect; for example, due to simplifications used in the models, accuracy in determining the model coefficients, variations due to freestream fluctuations, small sensor calibration drift, and possible spanwise and wall-normal wandering of the disturbances. In Figures 6.15, 6.16, and 6.17, the control results are provided with k=0 to 1.0, 1.2, and 1.4 mm, respectively. In each figure, the time at which the feedforward controller begins to provide an output voltage sufficient to initiate plasma formation is noted (as "ff start"), which is a function of the input from the upstream shear stress sensor (this signal is not shown but is recorded). Note that while the feedforward control begins before a notable downstream shear stress is measured at ≈ 0.3 s, the roughness element has already started moving upwards at ≈ 0.2 s and the disturbance has reached the upstream sensor at this time (at ≈ 0.3 s). As noted in §5.3.1 where the model is developed, the feedforward controller is a proportional gain model and therefore the model output will be in direct proportion to the upstream shear stress.

In Figure 6.15, the disturbance controlled using feedforward only (blue) demonstrates an immediate disturbance reduction resulting in the controlled disturbance never reaching the large amplitude of the uncontrolled response. However, the feedforward gain is not perfectly tuned and the controlled disturbance amplitude remains above zero (≈ 0.2 mPa, versus ≈ 1.2 mPa for the uncontrolled disturbance) during the steady-disturbance time period ($0.6 \lesssim t \lesssim 2.2$ s). The feedback only controlled disturbance (red) reaches a zero disturbance level, but the time required to do so is quite large; furthermore, the initial disturbance level nearly reaches the full uncontrolled level which could initiate transition with a sufficient k or disturbance amplitude. The combined feedforward and feedback control (magenta), shows that the controlled disturbance is reduced immediately and over all times, reaching a zero

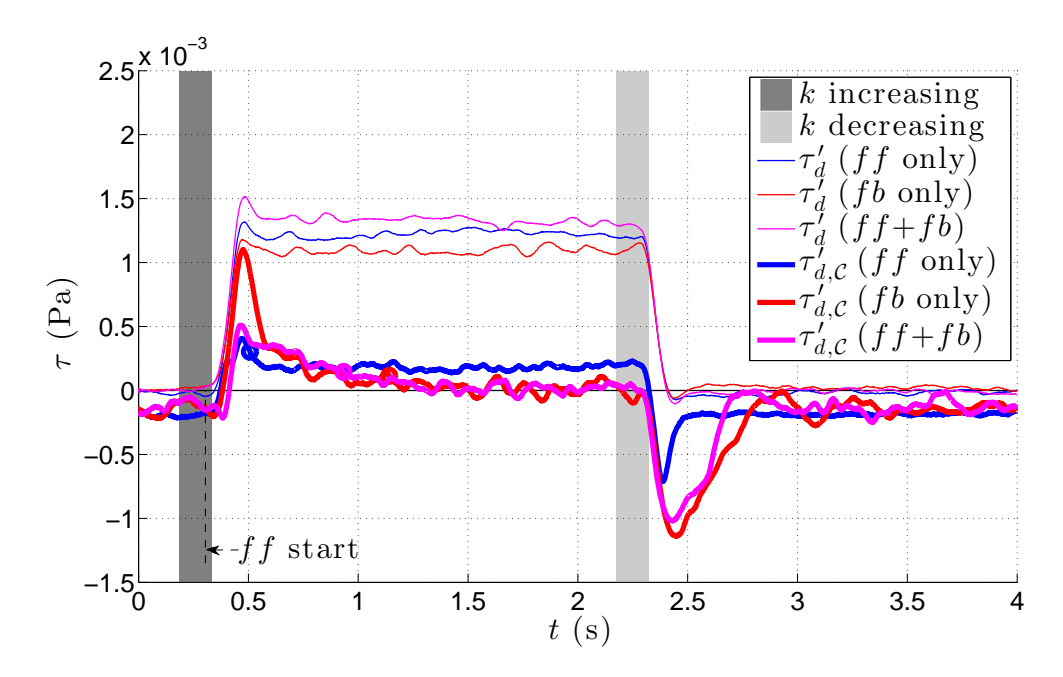


Figure 6.15: Unsteady control results for the downstream shear stress under feedforward-only control (ff), feedback-only control (fb), and feedforward+feedback control (ff+fb); with the feedback sensor located at x_{fb} - x_k =300 mm and a roughness element height of k=1.0 mm. The settling time for each signal is noted with a \circ -marker.

disturbance level faster than the purely feedback control result (red). The benefit of the feedforward control is clearly the fast reduction of the disturbance level, which is significant in this case where there in an initial large disturbance overshoot, while the feedback control allows the controller output to be iteratively modified to achieve a zero disturbance level.

The response with k=1.2 mm, in Figure 6.16, demonstrates many of the same characteristics as that with k=1.0 mm, however there are a few notable details. First, with the feedforward only response (blue), the undisturbed shear stress is notably lower than zero. It was originally thought hat this was caused by a small reduction in the freestream velocity, however, the magnitude was too large (and no other controlled result shows this type of undisturbed-boundary-layer reduction). It was determined, by examining the controller output voltages, that the controller was not fully turning the plasma off when the roughness element was withdrawn for this control case. Therefore, the plasma was sporadically

providing a low level forcing even when the boundary layer was undisturbed, resulting in a negative disturbance. This issue stems back to the use of a single sensor to detect the disturbance amplitude from a three dimensional boundary layer disturbance; the single sensor is susceptible to acting incorrectly if the disturbance is not positioned as expected, this problem would not exist if the entire disturbance field was known to the controller. Fortunately, the proper undisturbed level is known (the Blasius level, or a zero disturbance), and therefore the controlled disturbance portion of the result is still valid and instructive. This issue of forcing during the undisturbed portion of the controlled result is also seen in the feedback only and combined results of Figure 6.16 and the feedforward result of Figure 6.15; although, in these cases, the effect is much less. Note that the disturbed but controlled potion of the feedforward-only results (blue) in Figures 6.15 - 6.17 demonstrate a proportionate level of remaining disturbance which increases with roughness element height, regardless of the undisturbed magnitude; this indicates that the feedback controller is acting as expected during the disturbed time, regardless of the control output when there is no disturbance.

Demonstrated in Figure 6.16 is the ability of the feedforward plus feedback controller to outperform i) the feedforward controller in terms of the final controlled disturbance amplitude and ii) the feedback controller in the time taken to reach the fully controlled level. With the combined controller, the disturbance is immediately reduced by the feedforward contribution; then, the feedback controller only needs to provide a small modification to the control level. In contrast, without the feedforward control, the feedback controller takes longer to integrate the error to resolve the appropriate output voltage to achieve a fully reduced disturbance level. Also, the rise of the feedback-only result (red) clearly occurs in sync with the uncontrolled results; indicating that the feedforward controller is indeed responsible for this initial limiting of the disturbance "overshoot" seen in the feedforward-capable results

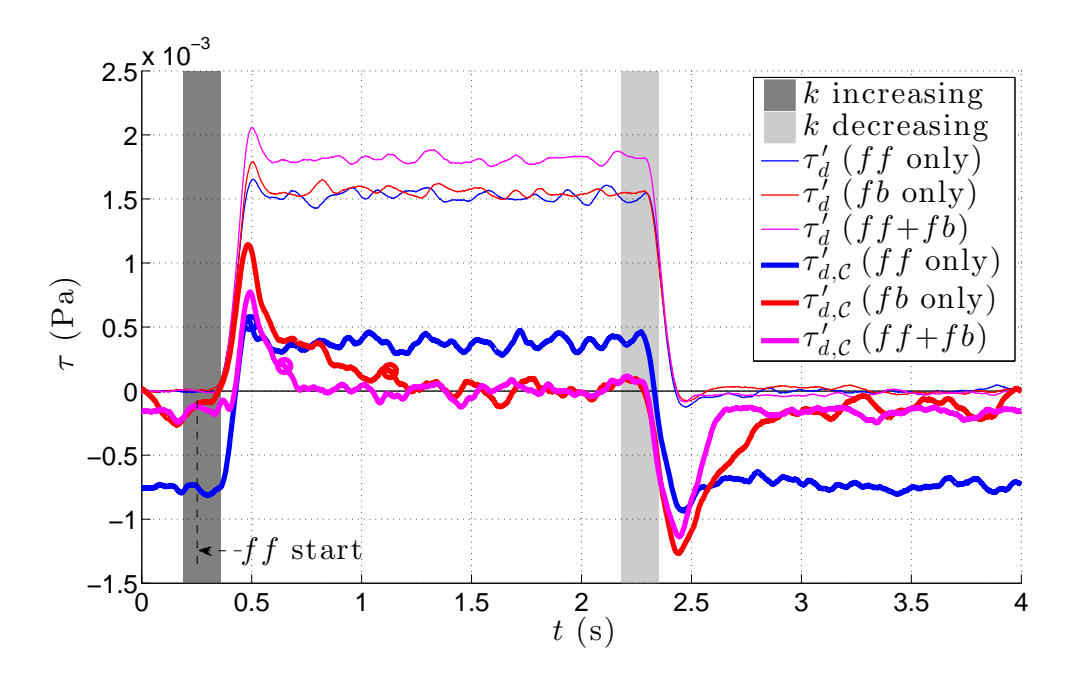


Figure 6.16: Unsteady control results for the downstream shear stress under feedforward-only control (ff), feedback-only control (fb), and feedforward+feedback control (ff+fb); with the feedback sensor located at x_{fb} - x_k =300 mm and a roughness element height of k=1.2 mm. The settling time for each signal is noted with a \circ -marker.

(blue, magenta).

In Figure 6.17, the maximum roughness element height is increased to k=1.4 mm; this results in an overshoot of the disturbance amplitude as the roughness element moves upward, before the disturbance amplitude reaches the steady-state level. As was seen with the k=0 to 1.0 and 1.2 mm results, the feedforward-only (blue) response shows a reduced, but still positive, disturbance amplitude with control. However, unlike the lower roughness element height results, the feedforward plus feedback (magenta) result exhibits an oscillatory response resulting in a prolonged settling time. The feedback only (red) results only exhibit a very small overshoot and as a result, reaches a zero-disturbance level the fastest. This difference is due to the strong positive overshoot disturbance that occurs with the upward roughness element motion, in the prescence of the feedforward controller output voltage. Because the disturbance remains very strong even with feedforward control, the feedback controller

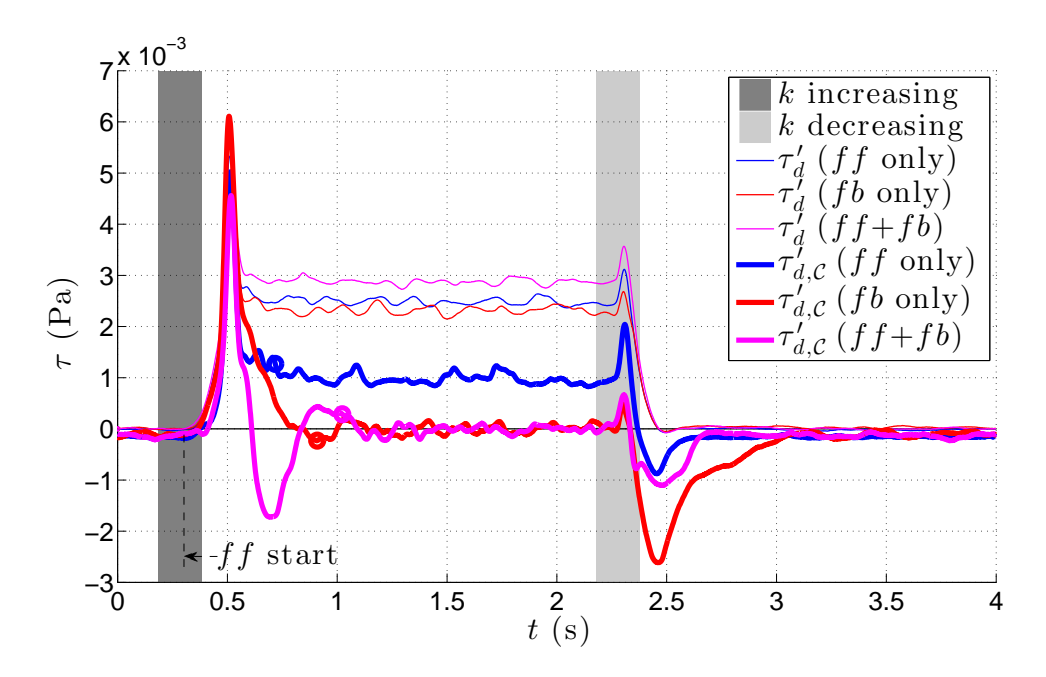


Figure 6.17: Unsteady control results for the downstream shear stress under feedforward-only control (ff), feedback-only control (fb), and feedforward+feedback control (ff+fb); with the feedback sensor located at x_{fb} - x_k =300 mm and a roughness element height of k=1.4 mm. The settling time for each signal is noted with a \circ -marker.

reaches a very large voltage contribution, resulting in a negative disturbance that persists after the spike in positive disturbance quickly relaxes to the steady-state level; the large positive spike in disturbance lasts for ≤ 0.1 s. This spike causes the feedforward and feedback controllers to request a larger plasm actuator voltage, which results in a negative disturbance when the positive disturbance spike quickly drops to the steady state level. The feedback controller's slow response causes the larger voltage level to persist, longer than it should, resulting in the negative disturbance. The problem is compounded by additionally (larger) feedforward voltage, resulting in oscillatory behavior. Thus, the large positive disturbance (but not turbulent) spike causes the feedback-only controller to outperform the combined feedforward/feedback controller, by not reacting as aggressively to the large, brief spike in disturbance amplitude.

The settling time results for the feedforward-only, feedback-only, and combined feedfor-

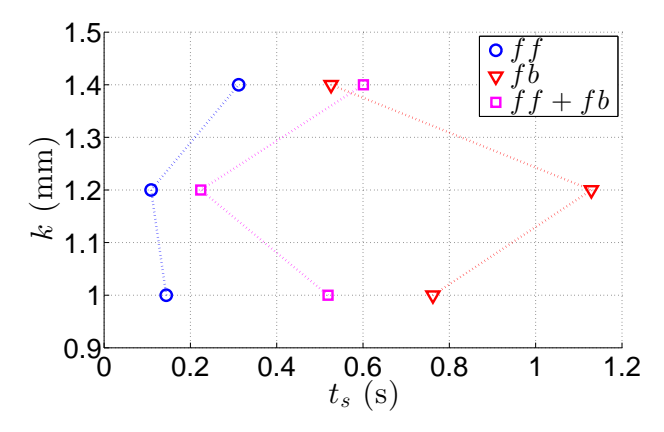


Figure 6.18: Settling time for the controlled disturbance to reach 10% of the uncontrolled steady-state disturbance level, for various roughness element heights, under purely feedforward control (ff), purely feedback control (fb), and combined control (ff+fb).

ward+feedback control efforts, with k=0 to 1.0, 1.2, and 1.4 mm, are provided in Figure 6.18. Note that the settling time reference points are also included as a \circ -marker on Figures 6.15 - 6.17. The feedforward control arrives to the steady-state controlled result the fastest in all cases, however, this does not lead to zero-disturbance. As was observed, the combined control provides the fastest performance for k=0 to 1.0 and 1.2 mm, but the feedback-only result outperforms the combined control when k=0 to 1.4 mm due to the large brief positive disturbance spike. Note that the dotted lines in Figure 6.18 are provided to demonstrate the shift in the best-case performance, and do not represent the expected trend between points.

6.2.4 Effect of the Streamwise Location of the Feedback Sensor

The results presented in the previous sections allow the investigation of the controlled flow response to various disturbance amplitudes, freestream velocities, and controller methods. The location of the sensors, as explained in detail in §2.6.2, is such that each sensor is placed within a high-speed streak as near as possible to the peak disturbance level, while remaining within the linear region of the undisturbed boundary layer. This was done to maximize the disturbance signal amplitude while maintaining the ability to calibrate each sensor based

on the Blasius solution for shear stress. A sensor placement optimization investigation may yield an alternative optimal position, but was not within the scope of the present work. However, in an effort to assess some aspects of the streamwise sensor placement, a set of control experiments was performed with the downstream shear stress sensor positioned at various locations: x_{fb} - x_k =200, 250, and 300 mm; which was made possible by the use of one of the four 3D-traverse mounted hotwires as the feedback sensor. Note that the wallnormal and spanwise position of the sensor was not changed; the spatial distribution of the disturbance does not change significantly over this targeted streamwise domain (see, for example, Figure 3.8b-d). With the feedback sensor located at each of the three streamwise locations, a new control model was developed by collecting new I/O data, according to the methods described in §5.1 (the resulting model and controller parameters are listed in Tables 5.1, 5.2, and 5.3). As in the previous investigations, these experiments were carried out with a dynamically actuated roughness element deployed from k=0 to various heights: k=1.0, 1.2, and 1.4 mm. Note that the results at the mid-range streamwise location, x_{fb} - x_k = 250 mm, are omitted because they provide no additional information and the trends with varying streamwise location of the shear sensor are most clear with the furthest upstream and downstream sensor results only.

In Figure 6.19 the controlled flow results are provided with k=0 to 1.0 mm. Inspecting the most upstream feedback (blue) and most downstream feedback (red) sensor location results, it is clear that with the shorter convective time delay of the more upstream feedback sensor position, the feedback controller is able to integrate the control-error to achieve a zero-disturbance much faster than with the more downstream sensor. The more upstream sensor receives feedback information much faster and is therefore able to resolve the optimal controller output voltage in a much shorter time. Furthermore, the feedback gain, K_{fb} for

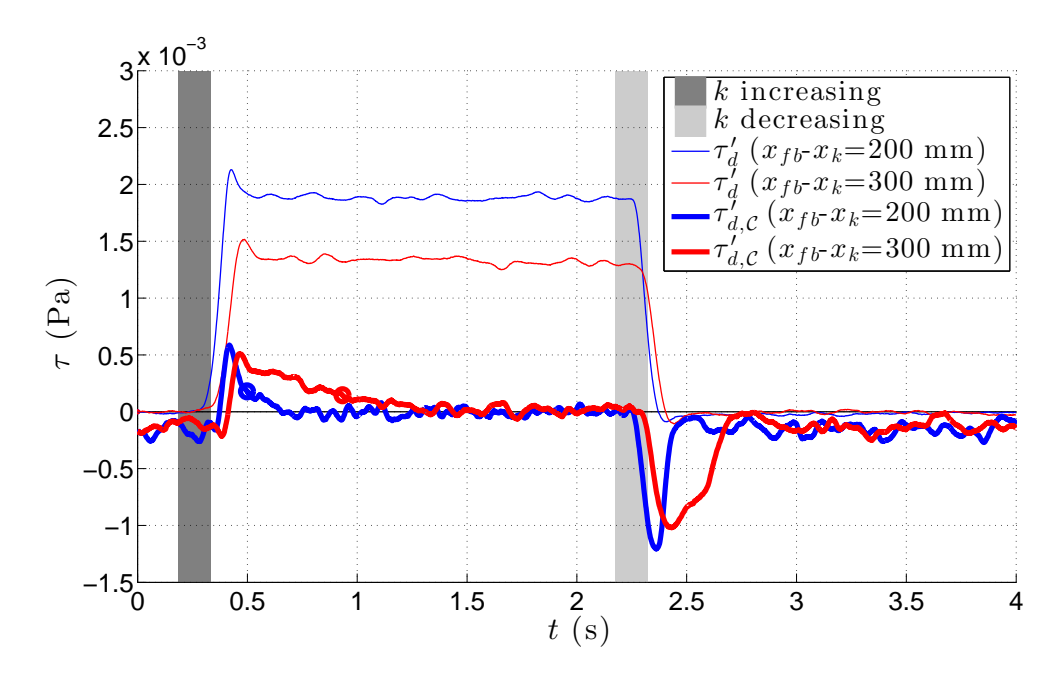


Figure 6.19: Unsteady control results for the downstream shear stress with the feedback sensor at multiple downstream locations with a fully deployed roughness element height of k=1.0 mm. The settling time for each signal is noted with a \circ -marker.

the more upstream sensor location, was larger, resulting in a more aggressive but still stable controller. The results with the feedback sensor at the most downstream position take longer to recover a zero-disturbance level; this is true for both the upward- and downward-motion of roughness element induced unsteady disturbance.

In Figure 6.20, where k=1.2 mm, a similar controlled disturbance response is seen as that in Figure 6.19, where the control results using the upstream feedback sensor (blue) recover a zero-disturbance level faster than the more downstream feedback sensor (red). The control results with the sensor at both locations recover a zero-disturbance level faster with k=1.2 mm than for k=1.0 mm, despite a greater induced disturbance amplitude when k=1.2 mm. This is consistent with the results in §6.2.1, which found that the controller was tuned most appropriately to quickly attenuate the disturbance generated when k=1.2 mm; thus, the integral controller tuning causes the feedback controller to respond more aggressively,

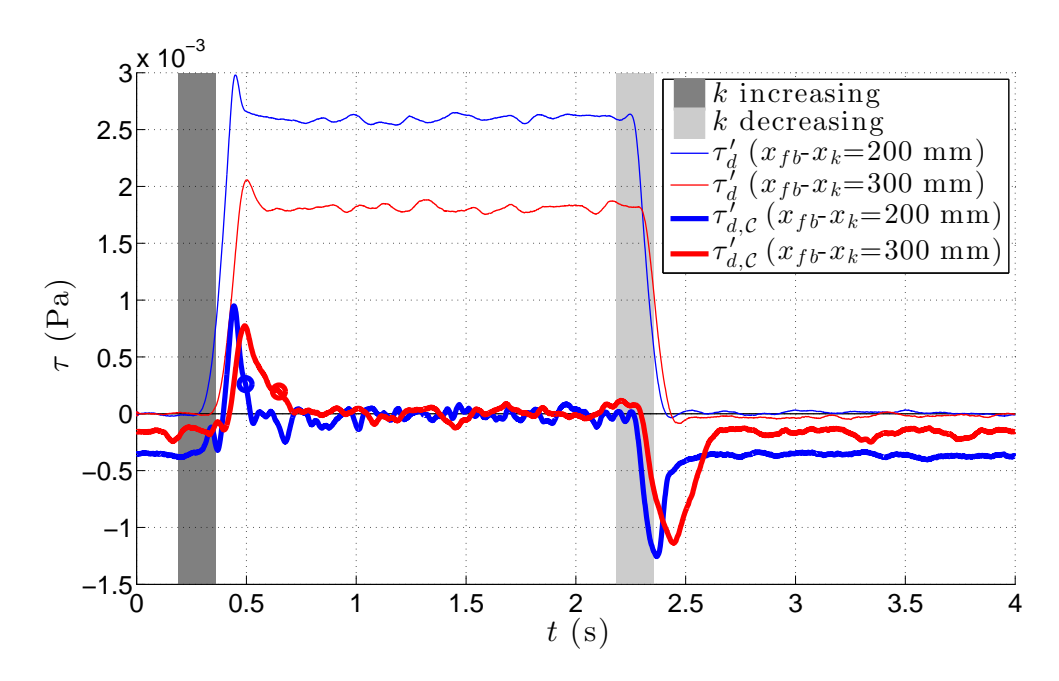


Figure 6.20: Unsteady control results for the downstream shear stress with the feedback sensor at multiple downstream locations with a fully deployed roughness element height of k=1.2 mm. The settling time for each signal is noted with a \circ -marker.

resulting in a faster disturbance attenuation than for the k=1.0 mm result.

In Figure 6.21, as was seen in Figure 6.17 where k=1.4 mm as well, an overshoot of the control voltage is observed (a negative disturbance following the large positive spike induced by the roughness traveling upwards) with the feedback sensor located at both downstream locations. The integral controller is not able to respond to this sharp change in disturbance amplitude sufficiently fast, and the result is a negative disturbance, induced by the plasma actuator, which eventually relaxes to the appropriate voltage to just cancel the roughness element induced disturbance. The positive spike disturbance is able to reach nearly the same amplitude as the uncontrolled result, which demonstrates a limitation of the control model because, at this high-disturbance level, transition may occur with slightly larger initial disturbance amplitudes. Again, the upstream sensor recovers to the zero-disturbance level much faster than the downstream sensor; however, the negative-amplitude due to over-

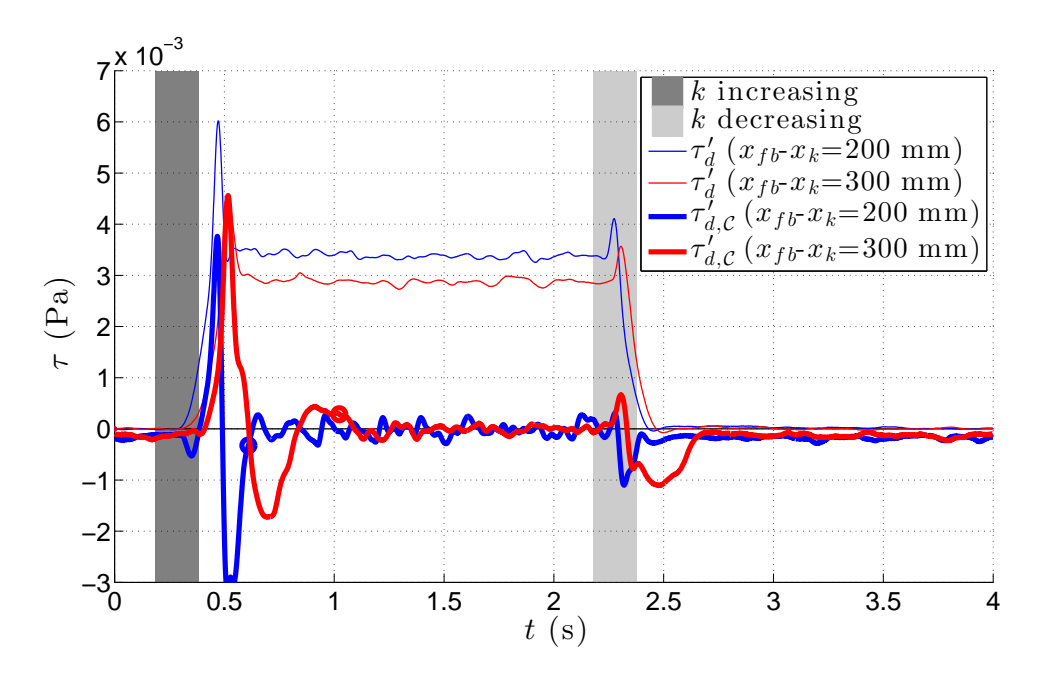


Figure 6.21: Unsteady control results for the downstream shear stress with the feedback sensor at multiple downstream locations with a fully deployed roughness element height of k=1.4 mm. The settling time for each signal is noted with a \circ -marker.

forcing by the plasma actuator is much stronger with the upstream located feedback sensor, resulting in a negative disturbance that is near as strong as the positive disturbance. This is clearly a drawback to the upstream feedback sensor location which may result in transition caused by the plasma actuator (although no transition is detected here).

An assessment of the settling time from Figures 6.19 - 6.21 is provided in Figure 6.22, which demonstrates the shortened settling time for the k=0 to 1.2 results relative to the k=0 to 1.0 mm results. The effect of the control output oscillations for the k=0 to 1.4 mm results are also shown, which results in the longest settling time. For all k, the x_{fb} - x_k =200 mm results reach the fully-controlled zero-disturbance level faster than the x_{fb} - x_k =300 mm, demonstrating that positioning the downstream sensor closer to the actuator benefits the system response time and would ultimately allow control of faster disturbance fluctuations. In §6.2.5, disturbances of various fluctuating frequencies are investigated, which allows the

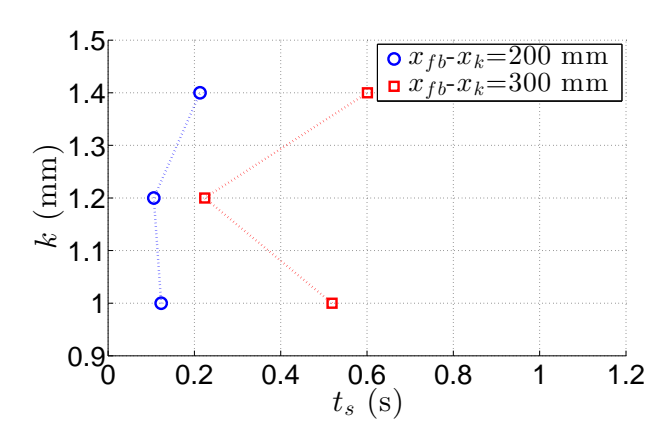


Figure 6.22: Settling time for the controlled disturbance to reach 10% of the uncontrolled steady-state disturbance level, for various roughness element heights, with the feedback sensor located at x_{fb} - x_k =200, 250, and 300 mm.

unsteady disturbance limitation to be further identified.

6.2.5 Effect of the Unsteady Disturbance Frequency

In order to assess the frequency response of the control model, the motion parameters of the roughness element were modified from that used in all previous control experiment sections; namely, t_h =2.0 s, v_k =7.5 mm/s, and a_k =1000 mm/s². Here, these parameters were adjusted to provide a range of roughness element motion frequencies, while changing the roughness element height between k=1.0 to 1.2 mm (or k=1.0 to 1.4 mm). Thus, with this roughness element motion profile, a disturbance is always present, but the strength of the disturbance is modulated at different frequencies by changing the hold times at the low and high k values. In Figure 6.23a, the roughness element motion is demonstrated with various hold times, t_h at k=1.0 and k=1.2 mm. The case where t_h =2 s represents the same parameters used for all control result presented this far, except that the minimum roughness element height is now k=1.0 mm, rather than k=0. The target of the current experiments was to test the effectiveness of the control model as the frequency of the unsteady streak disturbances increases. This is demonstrated in Figure 6.23b, where each roughness element motion is

divided by the period of motion, T_k , resulting in a normalized time scale and an associated frequency of oscillation,

$$f_k = 1/T_k, (6.1)$$

rather than a hold time. Thus, by prescribing various t_h , v_k , and a_k values for the roughness element's motion, a range of frequencies, f_k , were achieved. Ideally, it is desirable to have pre sinusoidal roughness element motion to directly obtain the frequency response of the control system,. However, the control software of the Squiggle motor (see §2.3 for details) did not provide an easy provision to accomplish this. Therefore, the sinusoidal motion was approximated with a trapezoidal profile (which approaches the sinusoidal form as the hold time is decreased; see Figures 6.23 and 6.24), while remaining within the velocity and acceleration limits found to avoid the introduction of spurious disturbance (see Chapter 4). In addition, results for the present experiments were also obtained for different values of v_k and a_k (over the range: $3.0 \le v_k \le 15.0$ mm/s and $100 \le a_k \le 10000$ mm/s²), and there was no noteworthy difference in the control results; therefore these results are not discussed here.

Theoretically, the included control results are initiated over a range of steady-state hold times, t_h , are converted to frequency equivalents using: $f_{t_h}=1/(2t_h)$. However, the actual frequencies (as noted, for example, in the legend of Figure 6.23b) follow the calculation based on Equation 6.1 which uses the entire cycle time, which includes the time during the roughness element motion; resulting in frequencies slightly smaller than those predicted by: $f_{t_h}=1/(2t_h)$.

In addition to the investigations with the roughness element actuated between k=1.0 and 1.2 mm, an equivalent set of control results were collected with the roughness element

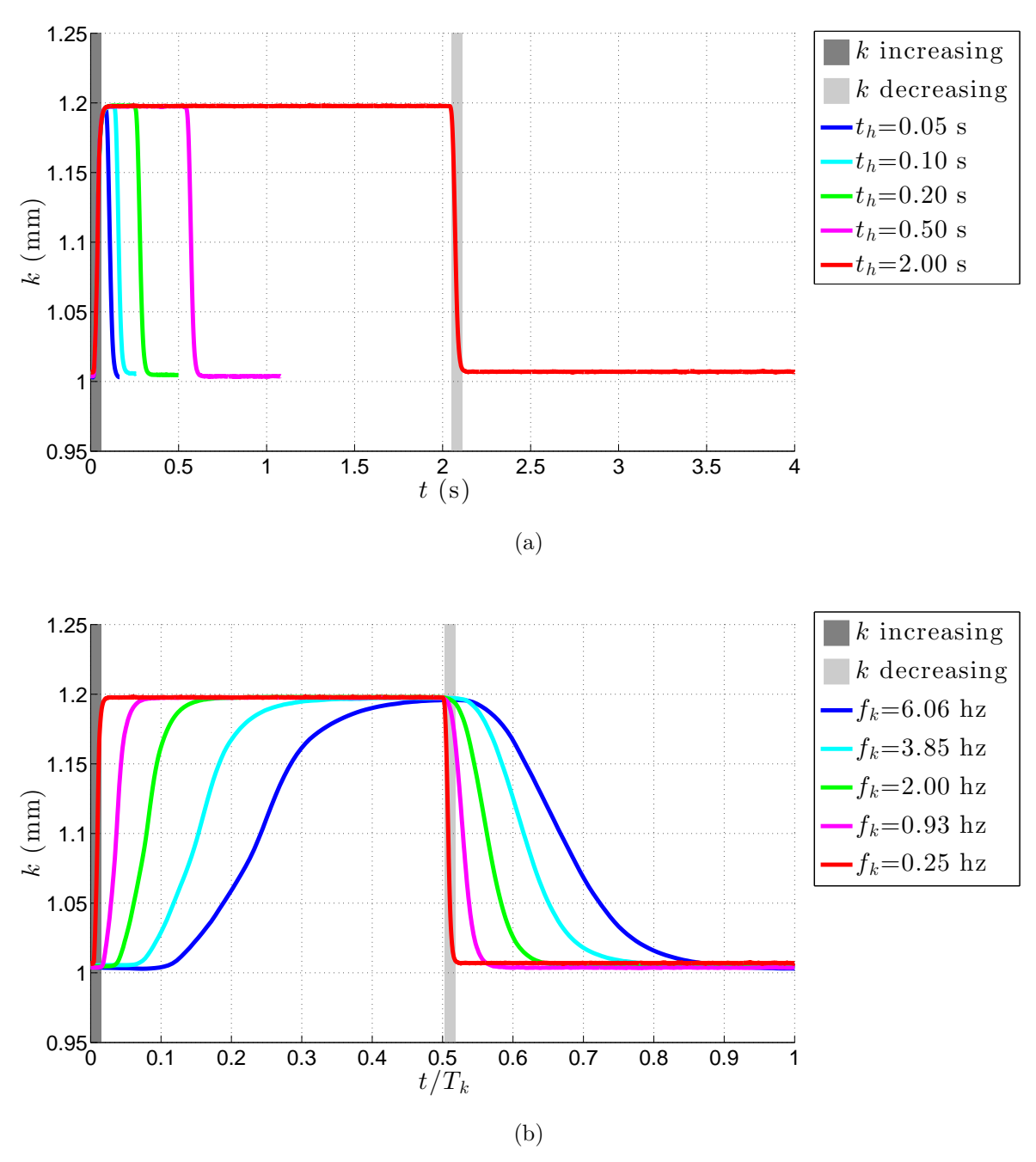


Figure 6.23: Unsteady roughness element motion from k=1.0 to 1.2 mm with a) various steady-state hold times, t_h , resulting in b) a range of equivalent unsteady disturbance frequencies, $f_k=1/T_k$. Note that the gray bands demonstrate time periods when the roughness element is moving either up or down, with $t_h=2.0$ s ($f_k=0.25$ Hz), and are provided on all subsequent unsteady control results plots, for the applicable t_h or f_k .

traveling between k=1.0 and 1.4 mm. These experiments resulted in the same set of unsteady disturbance frequencies, but with larger disturbance amplitudes. Figures 6.24a and 6.24b demonstrate the roughness element motion versus time, and cycle-period-normalized time, respectively.

For these unsteady control results the disturbance is always present (i.e. $k \ge 1.0$ mm at all times); therefore, when the uncontrolled and controlled disturbances are presented as the disturbance relative to the Blasius shear stress (i.e. k=0), the uncontrolled results are always above the zero-level. Also, for the control results, the control is active at all times and attempts to force the disturbance level to the Blasius level (zero disturbance) at all times. The results of Figures 6.25 and 6.26 are presented, synchronized to the roughness element upward-motion, for various t_h values; note that at the higher frequencies, the resulting downstream disturbance is not always at the same phase³ The result is that disturbance measurements that are phase-synced to the roughness element motion but produced with smaller t_h (blue and cyan), or larger f_k , may not be phase-synced for the measured the resulting downstream disturbance.

In Figure 6.25 the unsteady control results are provided on non-normalized time-scale. This representation of the results more easily allows for a visual assessment of the limitation with a smaller hold time, t_h . For the longest hold time result, 2 seconds (red), the uncontrolled disturbance (thin line) is able to develop to a steady state at k=1.0 and 1.2 mm, which are both well above the zero-disturbance (Blasius) level. These steady-state disturbance levels are in good agreement with the steady-state results of Figure 6.7 at the same k.

³For a long steady state hold time result, the disturbance growth(rise) times line-up because the roughness element is raised, and held for a long time so the downstream sensor measures the disturbance created by that roughness element motion; however, by increasing the actuation frequency, the measured downstream disturbance may correspond to a previous roughness element motion whose disturbance has convected downstream. Therefore a high-frequency disturbance could be at any point in its phase when it reaches the downstream sensor.

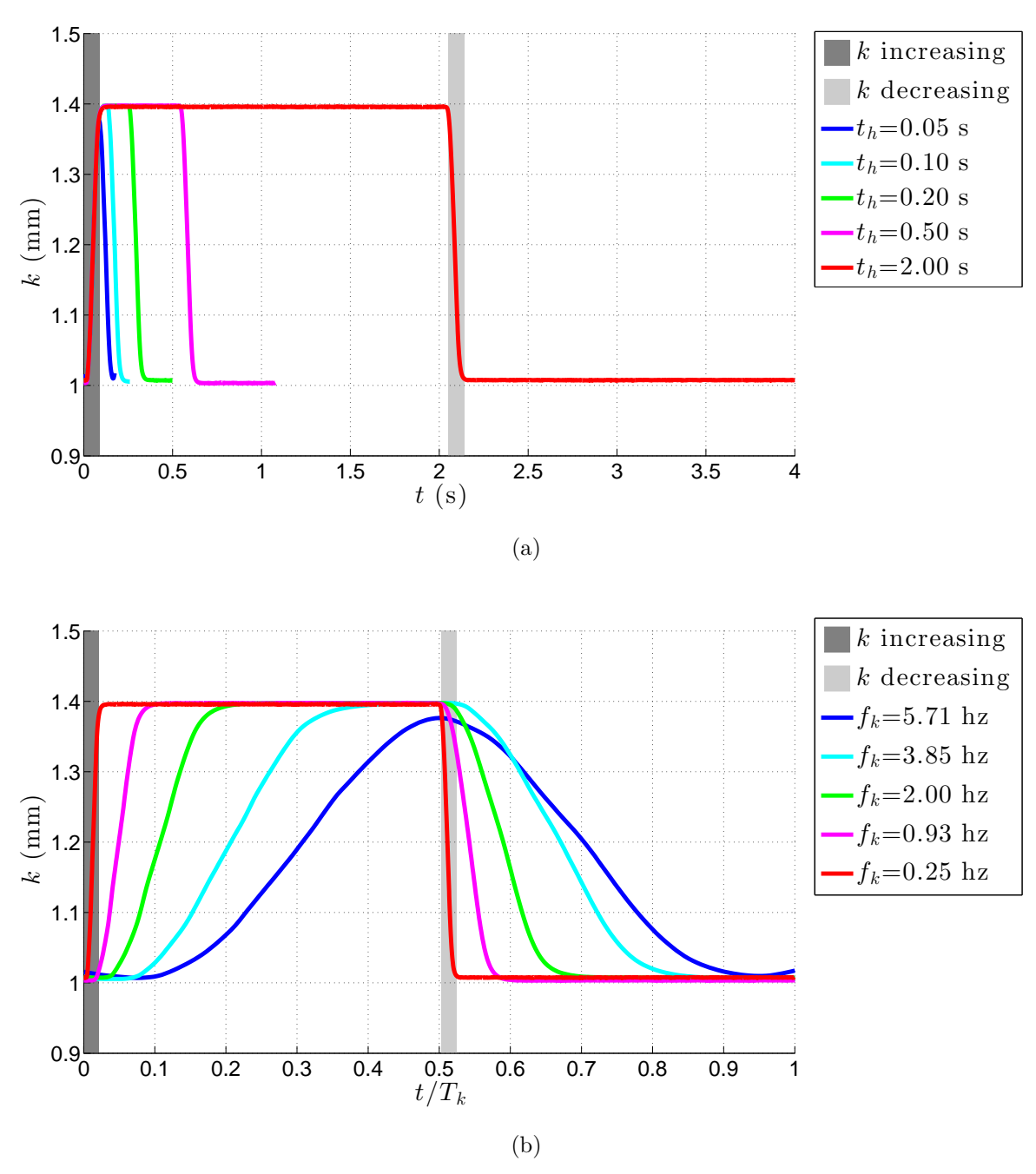


Figure 6.24: Unsteady roughness element motion from k=1.0 to 1.4 mm with a) various steady-state hold times, t_h , resulting in b) a range of equivalent unsteady disturbance frequencies, f_k . Note that the gray bands demonstrate time periods when the roughness element is moving either up or down, with $t_h=2.0$ s ($f_k=0.25$ Hz), and are provided on all subsequent unsteady control results plots, for the applicable t_h or f_k .

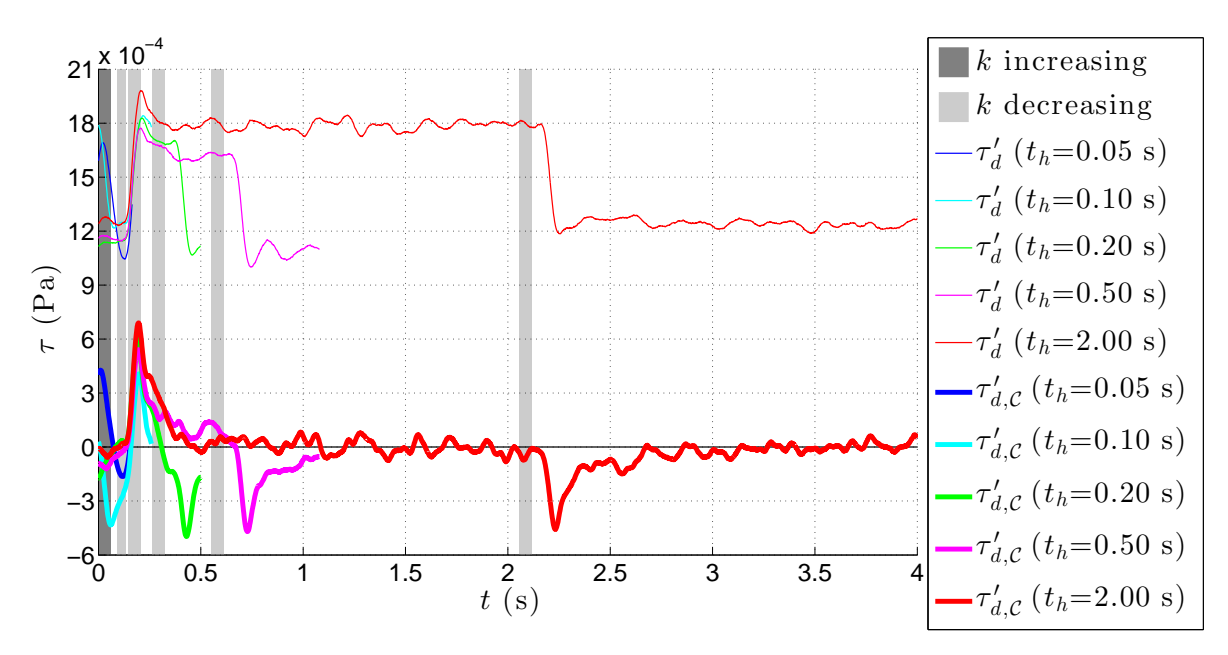


Figure 6.25: Control results with the unsteady roughness element motion from k=1.0 to 1.2 mm with various steady-state hold times, t_h . The uncontrolled results are represented with thin lines, while the controlled disturbance are represented with thicker lines of the same color.

As t_h is decreased, the steady state disturbance level is established for less time; for $t_h < 0.2$ s (blue and cyan), no discernible steady state disturbance is observed, although the range of disturbance magnitude stays within the limits of the min/max disturbance levels seen with the longer hold time results. The controlled disturbances (thick lines) all reach, or fluctuate around, the zero disturbance level. While the controller is unable to completely attenuate the quickly varying disturbance, the reduction of the entire disturbance level would be expected to accomplish the underlying goal of preventing the disturbances from reaching an amplitude which would initiate transition. These results are further investigated, based on f_k , in Figure 6.27.

Figure 6.26 provides the control results for the larger maximum roughness element height, k=1.0 to 1.4 mm. The results are similar to that of Figure 6.25, however, the very large overshoot of the disturbance when the roughness element moves upward is present even with

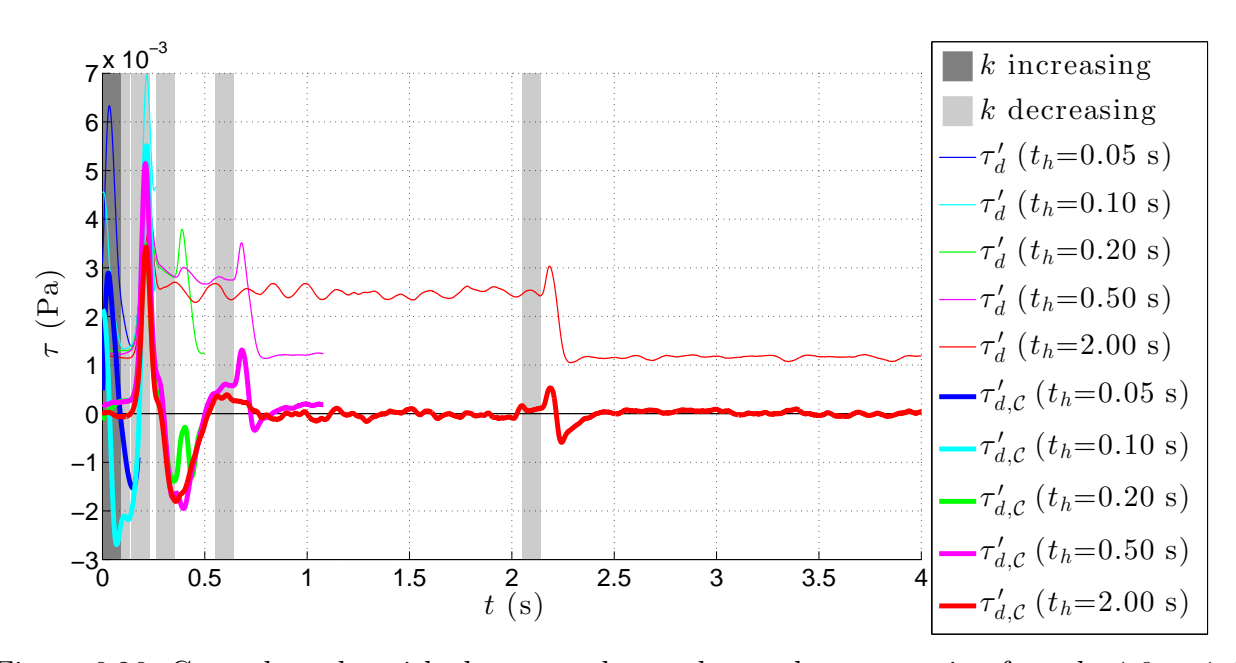


Figure 6.26: Control results with the unsteady roughness element motion from k=1.0 to 1.4 mm with various steady-state hold times, t_h . The uncontrolled results are represented with thin lines, while the controlled disturbance are represented with thicker lines of the same color.

control, albeit at a somewhat reduced level. Examining the t_h =2.0 s result (red), it can be seen that the sharp positive disturbance rise occurs over approximately 0.05 seconds. This rise time is actually less than the convection time delay for a disturbance to move from the upstream shear stress sensor to the downstream sensor ($t_{d,\tau}\approx0.9$ s, according to Table 5.1). Therefore, the feedforward controller should be able to partly attenuate this abrupt disturbance (as it does, shifting the entire disturbance toward the zero-line), but the feedback controller will have no opportunity to control this disturbance, which is why the large positive spike in the disturbance magnitude occurs. Aside from the very high initial disturbance spike, the controller does shift all the disturbances toward zero (the Blasius level) and reaches a steady zero-disturbance for the longer hold-time results, $t_h \geqslant 0.5$ s.

Next, in Figures 6.27 and 6.28, the unsteady disturbances of Figures 6.25 and 6.26, respectively, are normalized by their associated fluctuation periods (T_k) and presented individually,

to examine the frequency response limitations of the disturbance control. In Figure 6.27, a steady state controlled disturbance is achieved in Figures 6.27i and 6.27g, only. The results of Figure 6.27e, where f_k =2.00 Hz, appear to achieve a steady state with the uncontrolled result, and the controlled state just reaches a zero disturbance before the disturbance changes (decreases); and the fluctuations of Figures 6.27c and 6.27a, where $f_k \geqslant 3.85$ Hz, clearly never reach a steady uncontrolled or controlled state. Thus, the limit for unsteady disturbance control is $f_k \lesssim 2.00$ Hz (or $t_h \approx 0.2$ s). The results of Figure 6.28 demonstrate nearly identical limitations on the successful control based on the frequency of the disturbance variation (i.e. f_k =2.00 Hz seems to be the limitation for reaching a steady zero-disturbance with control).

A Fast Fourier Transform (FFT) of each uncontrolled and controlled disturbance signal was performed to analyze the disturbance energy contained at the fundamental frequency of each unsteady disturbance (i.e. at the roughness element oscillation frequency); note that the mean of each signal was subtract in order to avoid a strong DC component at f_k =0. The FFT results are presented to the right of each signal plot in Figures 6.27 and 6.28 and demonstrate that the cycle frequency, f_k , was the strongest component. Note, that the maximum ordinate level is $4*10^{-4}$ Pa in Figure 6.27, and an order of magnitude higher, $4*10^{-3}$ Pa, in Figure 6.28.

The primary difference in the controlled disturbance results of Figures 6.27 and 6.28 appears to be in the level of maximum remaining disturbance with control. While all of the control results shift the mean disturbance level from above zero to be at, or very close to zero, the controlled disturbances of Figure 6.28 have a positive spike maximum disturbance very near the uncontrolled maximum. In contrast, the results of 6.27 show that the mean and maximum disturbance levels are reduced at all f_k . To facilitate this analysis, maximum (MAX), mean, and root mean squared (RMS) values are calculated for the uncontrolled and

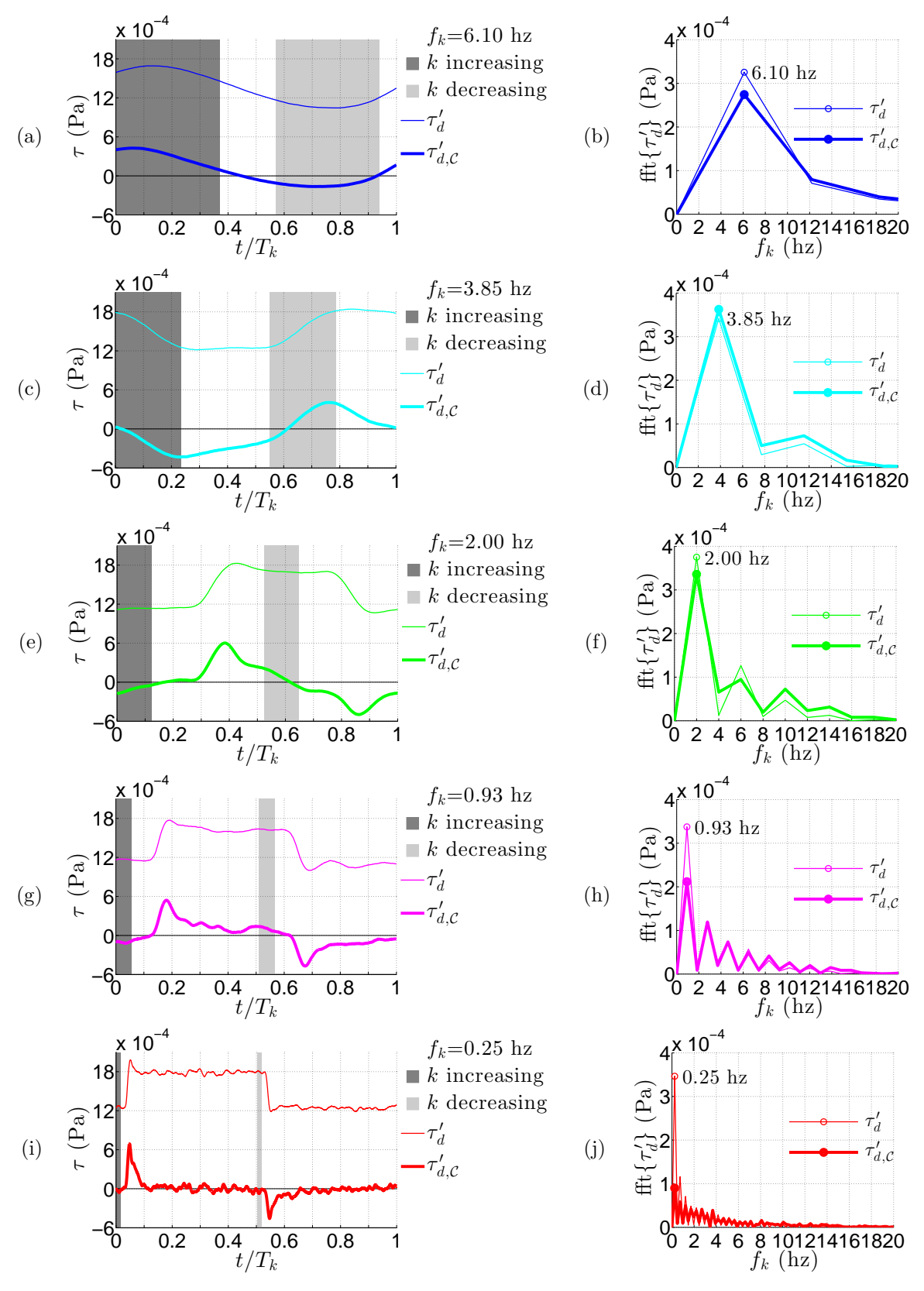


Figure 6.27: Unsteady roughness element motion from k=1.0 to 1.2 mm with various frequencies, f_k : phase-average uncontrolled and controlled signals (left) and the corresponding FFT (right).

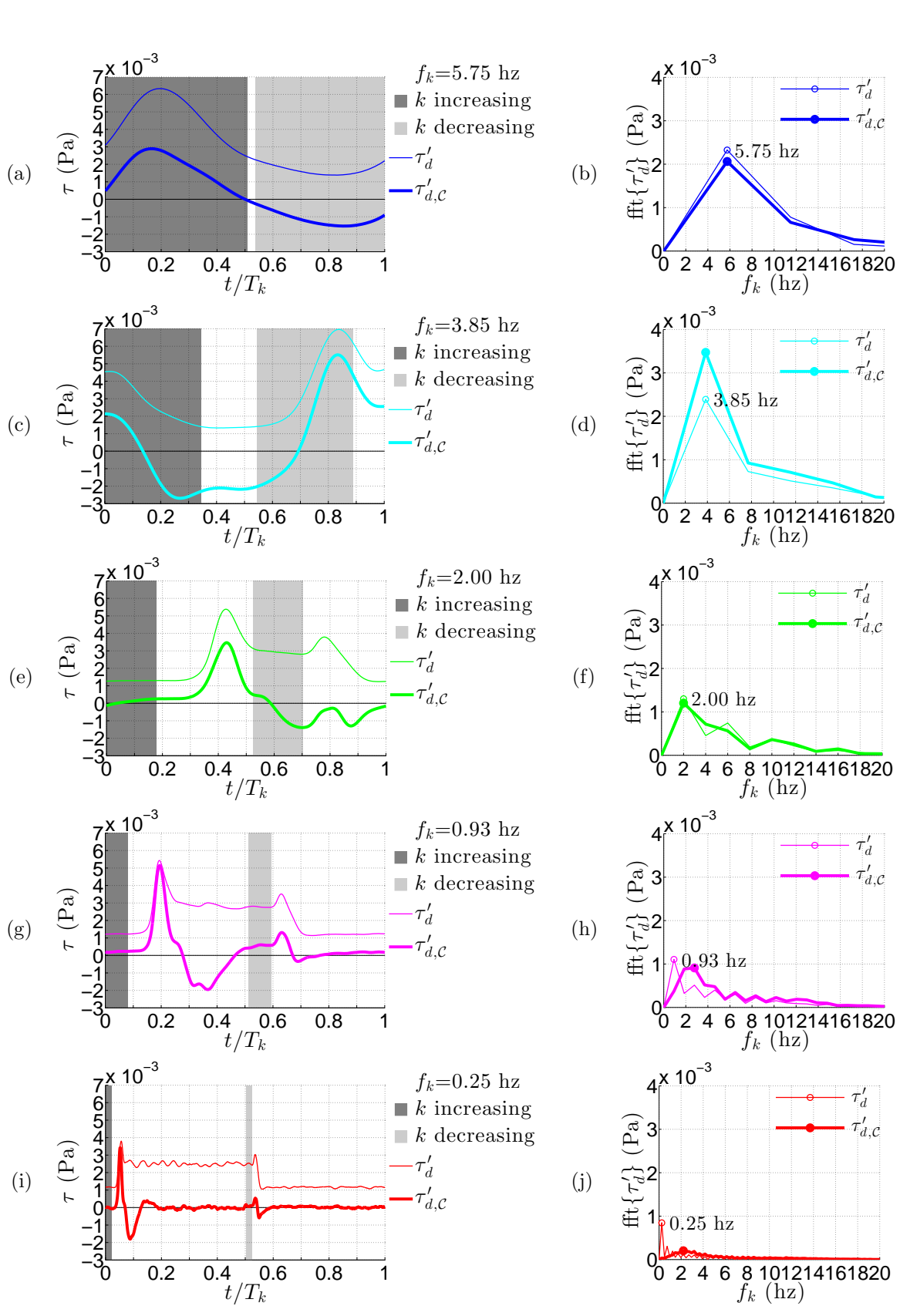


Figure 6.28: Unsteady roughness element motion from k=1.0 to 1.4 mm with various frequencies, f_k : phase-average uncontrolled and controlled signals (left) and the corresponding FFT (right).

controlled disturbance traces shown in Figures 6.27 and 6.28, and the outcome is presented in Figure 6.29. The maximum disturbance experiences a significant reduction with control for k modulation between 1.0 and 1.2 mm (Figure 6.29a); and k modulation between k=1.0 and 1.4 mm (Figure 6.29b) show that the maximum disturbance is not reduced for the lower frequencies and reduced by a limited amount at larger frequencies. By reducing the maximum disturbance magnitude, the likelihood of the the streak disturbance to experience transition is reduced. As demonstrated in Figures 6.29c and 6.29d, the mean disturbance is driven to nearly zero at all investigated frequencies.

The results of Figures 6.29e and 6.29f show the RMS of the controlled and uncontrolled disturbance as functions of frequency. For the low roughness element oscillation amplitude (k)change from 1.0 to 1.2 mm), the control reduces the RMS the most at the lowest frequencies but this reduction diminishes with increasing frequency. This effect may be seen more clearly on a magnitude frequency-response plot, depicting the ratio of the controlled and uncontrolled peak FFT values of the downstream shear versus frequency; see Figure 6.30a. Using this plot, one may identify a *cut-off* frequency below which, the control reduces the shear stress fluctuations by more than 3dB (approximately 71% of the uncontrolled disturbance FFT peak). This frequency is found to be approximately 1.3 Hz. Similarly, for the larger roughness element motion oscillations amplitude (k change from 1.0 to 1.4 mm), Figure 6.30b provides the ratio of the controlled to uncontrolled disturbance peak FFT values. The 3dB (0.71 on plot) frequency cutoff appears occur at a lower frequency, but additional data should be collected to verify these results, which appear more sporadic (specifically, the data point at f_k =0.93 Hz). Regardless, the controllable limitation is approximately $f_k \lesssim 1.3$ Hz in each case.

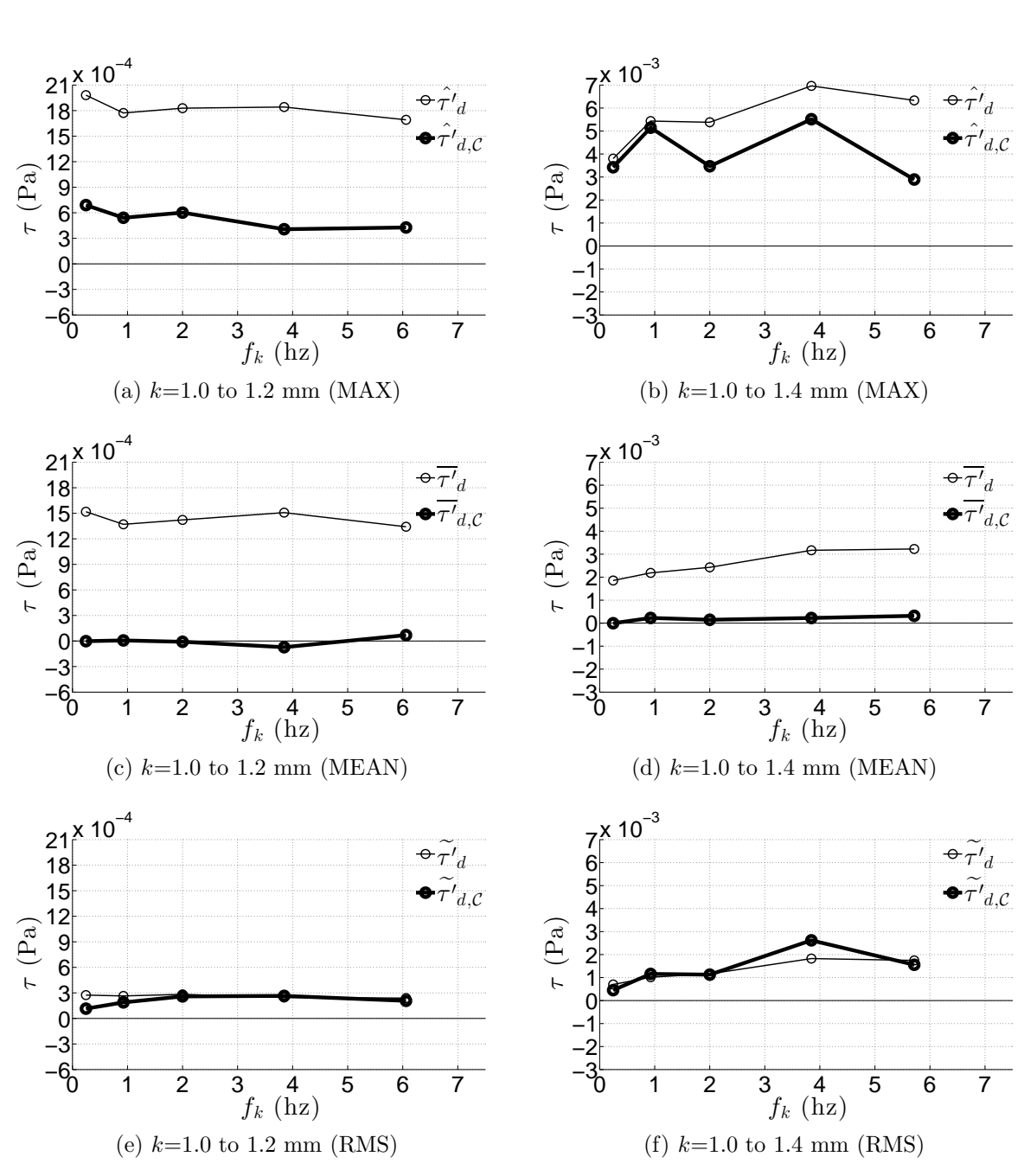


Figure 6.29: Maximum, Mean, and RMS of the uncontrolled and controlled disturbance periods at various roughness-disturabnce frequencies for a,c,e) k=1.0 to 1.2 mm and b,d,f) k=1.0 to 1.4 mm. The maximum of the disturbance signal is noted with a hat, $\hat{\tau'}_d$, the mean is noted with an overbar, $\overline{\tau'}_d$, and the RMS is noted with a tilde, $\hat{\tau'}_d$.

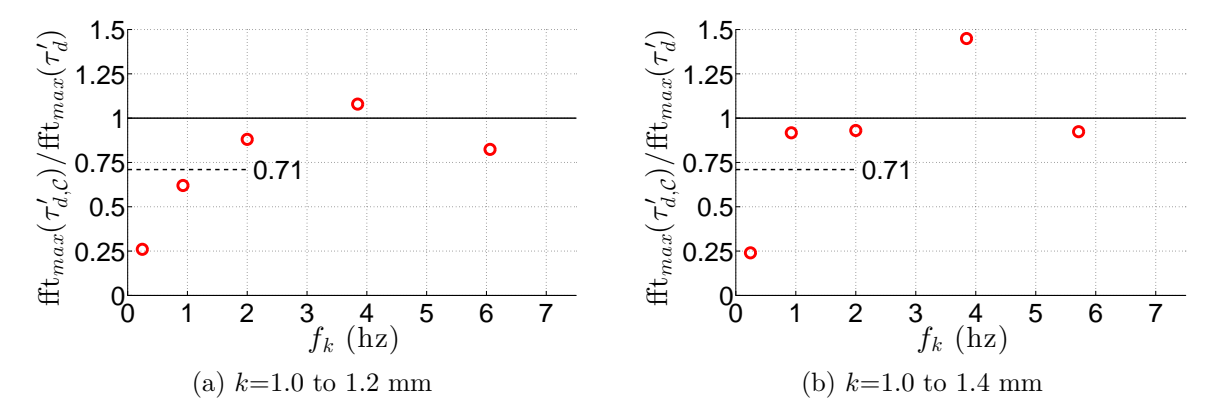


Figure 6.30: The ratio of the controlled to the uncontrolled disturbance peak FFT values at various roughness element disturbance frequencies for a) k=1.0 to 1.2 mm and b) k=1.0 to 1.4 mm.

Chapter 7

Conclusions

7.1 Physical Aspects of the Roughness Element Induced Disturbance

The steady-state disturbance induced into a Blasius boundary layer by an isolated cylindrical roughness element deployed at the wall is studied in detail. Hot wire measurements provide high spatial resolution measurements in the wall-normal direction, providing *primarily* streamwise velocity measurements of the undisturbed and disturbed flow state over a large domain downstream of the roughness element. The basic flow is established and verified as Blasius by examining the boundary layer thickness growth as well as the boundary layer shape factor over the domain of interest. Flow visualization results compliment the hot wire measurements and provide insight into the non-transitional, intermittent, and continuously transitional flow character.

A dynamic roughness element is used to introduce a disturbance into the boundary layer. The use of an actuated roughness element allows for hot wire measurements of the undisturbed and disturbed flow states to be collected at the exact same location in the boundary layer. This method provides flow disturbance measurements without error due to wall-find inaccuracies, although could result in very small wall-normal shifts of the disturbance location. It is better for wall-find errors to manifest in wall-normal location error of the flow

disturbance, than to manifest in disturbance intensity error, as may be experienced with other methods.

Flow visualization results demonstrate non-transitional, intermittently transitional, and continuously transitional boundary layer flow conditions at various roughness element heights, k, with constant D=5.0 mm and $U_{\infty}=5.0$ m/s. It is found that under these conditions, intermittent turbulent spots occur at $k\approx1.51$ mm, resulting in $Re_{k\infty}=499$ or $Re_k=340$. This is in good agreement with the critical Reynolds number analysis, by Tani [48] and von-Doenhoff and Braslow [51], where $Re_{k,cr}=372$. Thus, intermittent transition is first observed just below this critical Reynolds number; while continuous transition is found at k=1.6 mm ($Re_k=382$), where $Re_{k,cr}=380$. Meanwhile, no transition is observed at k=1.4 mm where $Re_k=276$, well below the critical Reynolds number at this condition of $Re_{k,cr}=360$. Finally, in the flow visualization results where continuous transition was observed, the turbulent wedge was found to grow at a half-angle of 2-8° depending on the local Re_x , and in good agreement with the results of Gad-el-Hak et al. [20] and Asai et al. [3].

Hot wire results provide detailed measurements of the disturbance within the boundary layer over large range of roughness and flow parameters. Contours of the streamwise velocity of the disturbance generated by a range of roughness element heights demonstrate the gradual increase in disturbance intensity with increasing k, D, or U_{∞} . At sufficiently a large (k, D, U_{∞}) combination, the onset of transition is encountered and a re-arrangement of the disturbance is observed. Prior to transition, a spanwise varying arrangement of positive and negative streak disturbances is present in the boundary layer. After transition, these disturbances are seen to be arranged in the wall-normal direction with positive disturbance levels near the wall and negative disturbance levels away from the wall. This change in arrangement is shown to correspond to the difference in laminar and turbulent flow conditions, with

each having the undisturbed, laminar profile subtracted to arrive at the disturbance profile. The spanwise extent of the isolated roughness element disturbance is found to be dependent on the disturbance intensity, and for a non-transitional disturbed flow over the investigated streamwise domain extends approximately $4 \lesssim z/D \lesssim 6$ in total spanwise size. The spanwise extent of disturbed fluid for a transitional disturbance grows with streamwise location and this growth rate (half-angle) is discussed in the flow visualization conclusions.

The streamwise development of the total planar disturbance energy is found from the y-z planar disturbance results for many parameter combinations, as detailed in Table 2.1. The disturbance energy is calculated as an integral in y and z for the isolated element because the induced disturbances cover a finite span. This differs from roughness element array investigations where periodic roughness element arrays produce flow disturbances over an indefinite span and thus a spanwise RMS is utilized and integrated in the wall-normal direction. The results show that the total y-z planar disturbance energy increases with increasing k, D, and U_{∞} . Furthermore, the total energy is shown to decay monotonically with increasing streamwise location. The energy contribution from the three distinct disturbance regions is investigated, namely, the low-speed wake, high-speed vortex-induced, and lowspeed vortex-induced regions. It is observed that growth of the disturbance energy in the high-speed vortex-induced disturbance region correlates well with the onset of transition when this region spans a sufficiently large streamwise extent, while the negative disturbances either show steady decay, or only negligible growth. The amplification of only the positive vortex-induced disturbance is a significant observation which will be investigated in more detail in the future.

The disturbance energy density is defined employing wall-normal (η_c) and spanwise (z_c) characteristic length scales. The wall normal characteristic length scale is taken as the

location of peak disturbance magnitude, which for non-transitional cases approaches a wall-normal distance of $\eta_c \approx 2.2$ at downstream locations, and agrees well with literature on streak disturbances induced with freestream turbulence. Upstream locations demonstrate a reduced η_c distance that follows closely with the disturbance initiation location, namely, k. The intermittent or continuously transitional cases demonstrate a double-peaked spanwise-summed disturbance profile with a reduce maximum peak distance from the wall, corresponding to the increased near-wall velocity gradient of the turbulent boundary layer (i.e. the positive disturbance). The spanwise length scale is characterized by the wall-normal summed disturbance with the distance between zero-crossings (slope-sign dependent) providing a measure of the spanwise spacing of the vortex-pair centers generated by the roughness element. The disturbance energy density provides a quantitative representation of the amplitude of the induced disturbance, accounting for the potential for disturbance spanwise spreading without amplitude changes. The results demonstrate a steady decrease as the disturbance convects downstream for all cases except those which undergo transition.

A scaling factor for the streamwise evolution of the energy density is developed using the independently controllable parameters: k, D, and U_{∞} . The streamwise coordinate is normalized as $(x^* - x_k^*) = (x - x_k) \frac{U_{\infty}}{\nu} \frac{k}{D}$ and the appropriate relationship between this parameter and k and U_{∞} is investigated independently. It is found that both parameters scale the normalized energy density to the 6^{th} power and this leads to the implementation of $Re_{k\infty}^6$ to collapse the normalized disturbance energy density. Very good collapse of the data at all streamwise locations is observed, except those closest to the roughness element where strong non-streamwise velocity components may be non-negligible and thus the flow physics will be different from the further downstream flow field. This non-collapse of the data near the roughness element may also be explained by insufficient spanwise spatial resolution of

the hot-wire measurements due to the sharp spanwise gradient of the streamwise velocity disturbances.

An investigation was conducted into the roughness element motion parameters (velocity, v_k , and acceleration, a_k) which allowed the introduction of unsteady streak disturbances, without complex undesirable/complex disturbances using the isolated roughness element. It was found that if an electromagnetic solenoid is used, it produced a sudden and fast motion, resulting in complex boundary layer disturbances that propagated downstream when the roughness element was raised over k=0.5 mm. It was desirable to raise the roughness element higher than k=0.5 mm in order to generate streak disturbances over a relatively wide range of steady state magnitude. By using a servo-loop controlled piezoelectric Squiggle[®] motor, the actuation parameters could be prescribed. It was found that setting the parameters: $v_k=7.5$ mm/s and $a_k=1000$ mm/s², it was possible to produce desirable disturbances using roughness element heights up to nearly $k \leq 1.4$ mm.

7.2 Control of the Roughness Element Induced Disturbance

The unique control study presented here proved both effective and instructive for future control efforts. The control strategy is presented with the goal of providing real-time control of a roughness element induced streak disturbance using plasma actuators. A feedforward+feedback control model is developed using Input/Output (I/O) data to capture the boundary layer response to different levels of roughness element height and plasma actuator voltage. To develop these models, the roughness element is deployed to a range of heights, from k=0, using the actuation parameters determined to not induce non-linear disturbance

 $(v_k = 7.5 \text{ mm/s and } a_k = 100 \text{ mm/s}^2)$, approximating a step-function disturbance input. The corresponding downstream shear stress output is recoded and used to develop I/O models for the boundary layer response to roughness element disturbance. Similar I/O data are acquired for the plasma actuator, when stepping the drive voltage from V=0 to a range of voltages. The I/O boundary layer response is determined to be captured well using a firstorder model. The effect of the plasma actuator forcing on the boundary layer demonstrates a minimum and maximum useable voltage range for the control efforts. The minimum voltage is dictated by the induced disturbance, which begins to increase in magnitude, monotonically, after some minimum voltage; which was found to be $V=2.35~\mathrm{kV}$ for the current plasma actuator and flow conditions. Notably, this is higher than the minimum plasma formation voltage, V=1.6 kV, where a minimum forcing is generated; the effective disturbance within $1.6 \le V \le 2.35$ kV showed no change in the disturbance magnitude and is therefore useless for the control work. The maximum voltage before boundary layer transition occurred was found to be V=2.6 kV; thus, the useful voltage range for control purposes was $2.35 \le V \le 2.6$ kV. Over this useable range of voltages, the I/O boundary layer response is captured well using a first-order model; however, unlike with the roughness element, the model gain is dependent on the input voltage. The gain dependence is accounted for by using a mapping function, which maintains a linear first-order model in representing the plasma actuator response, simplifying the feedback controller development.

The feedforward controller is a simple proportional controller. Using the boundary layer model parameters (gain, time delay, time constant), the tuning rules provided by Skogestad [47] for first- and second-order models, are used to create a cascaded Proportional-Integral (PI) controller for the feedback. The feedback controller is further outfitted with anti-windup correction, for when the disturbance level is uncontrollable (i.e. the controller requested

plasma actuator voltage is above or below the useable voltage range), resulting in an effective feedforward/feedback control model.

It is found that the control model is able to control the disturbance level to the Blasius level at steady state, for all conditions that did not produce a turbulent disturbance (which was outside of the intended control). It is demonstrated that a superposition of the roughness element induced disturbance and the plasma actuator disturbance results in a disturbance magnitude and spatial distribution very similar to that measured when both types of disturbances are active simultaneously during the control; this confirms these disturbances grow linearly and, therefore, with proper matching of the spatial distribution of the roughness and actuator induced disturbances, a full planar cancellation of the roughness element induced disturbance by the plasma actuator is expected.

The effect of roughness element height on the control results is investigated, and it is shown that at all fully deployed k values, the controller is able to control the disturbance to a zero level. The exception is for the lowest roughness element height, k=0.5 mm, where the disturbance strength is below the controllable minimum disturbance level. It is determined that the control model tuning worked the best for the k=1.2 mm roughness element height, which follows the fact that k=1.2 mm falls near the middle of the tuning k values collected. The I/O model development data used to determine the controller tuning parameters represented an average of the values obtained for all k values in order to create simple controllers, likely resulting in the tuning having an best-case construction for control of the k=1.2 mm disturbance. Larger and smaller k values result in slow but stable control, or overly aggressive and less stable (decaying oscillations) control results. The feedforward portion of the controller is shown to be effective, but insufficient (due to gross simplification in the controller design) to completely control each disturbance, but the feedback control is

able to integrate the control error to achieve a zero disturbance level. Planar maps of the unsteady disturbance velocity were acquired for the uncontrolled and controlled result and demonstrate that the disturbance at the sensor is driven to zero, but elsewhere in the plane the disturbance remnant persists even with control; it has been established in §6.1 that this can be corrected with proper matching of the spatial distribution of the disturbance produced by the roughness element and plasma actuator. The disturbance energy in the full plane was reduced by 40.1%, and in the positive half plane (where the alignment and shape of the roughness element and plasma actuator disturbances matched the best) by 66.2%.

By altering the freestream velocity, it is found that the controller is able to achieve a zero disturbance amplitude despite the $\pm 20\%$ change in freestream velocity, which was outside the range of I/O model development data range, leading to deviation in the disturbance strength as well as the convective time delay from what is observed at the "design" freestream velocity. At lower velocity, the control led to a zero disturbance level without a notable contribution from the feedback controller, using primarily the feedforward controller. This is due to the greater forcing imparted by the plasma actuator with a reduced disturbance convection velocity. This dependence of forcing effectiveness on freestream velocity, which was first reported in Hanson et~al.~[26], also results in a reduced effectiveness of the feedforward controller when the freestream velocity is increased.

The relative effectiveness of the feedforward and feedback controller, and the advantages of the combined feedforward with feedback control are investigated. The feedforward control is shown to be faster than the feedback control, but insufficient to achieve a zero disturbance due to inaccuracies in the model parameters and the simplistic design of the controller. The feedback control is able to achieve a zero disturbance, but a longer time is required to do so. The combined feedforward and feedback control reaches the zero disturbance

level faster than the feedback only control result; demonstrating that the combined control strategy provides a compromise between fast control with limited accuracy (due to model inaccuracies/approximations in the feedforward controller) and slow control with a very accurate final result (feedback control). One case is observed, however, where the feedback-only control outperformed the combined feedforward and feedback control. Further analysis is required to understand the conditions that lead to this behavior.

Positioning the feedback sensor closer to the control model output (plasma actuator) location provides a faster and more effective control result, by reducing the convective time delay.

The frequency response of the controller to achieve the Blasius control target is found to be $f_k \lesssim 1.3$ Hz; disturbances that fluctuate faster than this do not reach the set point level. However, the mean disturbance level was attenuated to the Blasius level for all tested frequencies, $0.25 \leqslant f_k \leqslant 6.10$ Hz, when the roughness element motion was from k=1.0 to 1.2 mm and when k=1.0 to 1.4 mm. Control of disturbance frequencies much higher than 1.3 Hz should be possible with more accurate feedforward control models and/or faster feedback response, by placing the feedback sensor closer to the actuator, to reduce the convective time delay of the control loop.

7.3 Comments for Future Physics Experiments

The many experiments carried out using flow visualization and hotwire measurements in the pursuit of the results in this dissertation have produced unique and expansive information regarding the governing physics and characteristics of the disturbance generated by an isolated roughness element in a Blasius boundary layer. Unfortunately, not all aspects of the

induced disturbances could be investigated within the scope of this dissertation; below is a list of recommendations for future investigations and analysis.

A proper scaling investigation should be conducted on the energy contained within the positive disturbance. This is a very promising idea that could lead to a useful practical criterion that may be employed to predict when transition occurs given the roughness element geometry.

A scaling argument for E would be interesting because it would not require additional determination of the wall-normal, y_c , and spanwise, z_c , length scales and may be more readily applicable in subsequent studies.

7.4 Comments for Future Control Experiments

The many experiments and analyses that have been conducted in pursuit of this dissertation have guided this research along the way, additionally, there were aspects of the control experiments that were identified as target areas for improvement, but could not be addressed in the current work due to time limitation. These recommended areas for improvement in future control experiments are briefly presented here for documentation and reference.

The plasma actuator length plays a major role in the available forcing which is useable to control disturbances and should be carefully considered in order to optimize the available forcing to attenuate a targeted range of boundary layer disturbance. The streamwise length of the plasma formation region dictates the minimum and maximum available flow forcing. Using a shorter plasma region provides a smaller forcing to the boundary layer (at the minimum plasma formation voltage), because the flow spends less time within the forcing domain as it convects downstream; however, in order to achieve larger forcing, the voltage

must be increased to levels that may initiate transition before reaching the required forcing strength to counteract the target disturbance. Conversely, a long plasma formation region will have an inherently larger forcing at the minimum voltage level, which will limit the ability of the actuator to address small disturbances. Together, the length of the plasma actuator and drive signal will provide a range of available forcing, and it is critical to properly select the actuator geometry to make available the proper level of forcing. An alternative method for altering the forcing level of the plasma actuator is to set a constant voltage amplitude to operate the plasma, and by changing the duty cycle of the high frequency drive signal, the output forcing should be adjustable. This will still require a careful selected actuator geometry to make the range of proper forcing attainable.

A critical aspect of the control efforts developed here was the placement of the small set of controller input sensors (two in this case, one upstream and one downstream of the plasma actuator). With the use of more sensors, a better picture of the disturbance field may be acquired and used to generate the best controller output. Aside from simply using more sensors, which is a real option but to a limited extent, a true optimization of the sensor location(s) should be conducted. The current work includes a very large host of spatio-temporal data, downstream of the roughness element, that may be mined for confirmation of, or determination of, the optimal location to place controller sensors. This objective could not be addressed due to time limitation.

On a related topic, the streamwise placement of the plasma actuator was a critical aspect of the control effectiveness that was not within the scope of this work. It was found, near the end of these control efforts that, for $k \ge 1.51$ mm, transition occurred upstream of the plasma actuator and the control model never had an opportunity to modulate the streak disturbances before secondary instabilities resulted in turbulence. By moving the plasma

actuators upstream, closer to the disturbance initiation location (the roughness element location here), it would presumably be possible to reduce the streak disturbance strength (in a transiting arrangement) before transition and thus prevent the downstream turbulent wedge. The current efforts demonstrate that this is expected to be possible.

The control models developed in this work, and associated controller parameters, cover a range of parameter space (disturbance level, feedback sensor location, etc.). By collecting I/O data over a very larger parameter space, it may be possible to develop scaling rules for the appropriate controller parameters. A Simulink simulation model was developed during this work, and may provide the framework to conduct this investigation.

The control efforts were carried out with what was determined to be reasonably robust models, however, by investigating a range of controller parameters it may be found that modifications of these parameters (the integral controller gain or time delay, for example) realizes a more successful control effort. These parameters should be investigated and optimized. This may be done through a simulated experiment to explore the parameter space without the real-world complications of the wind tunnel environment. A Simulink simulation model was developed during this work, and may provide the framework to conduct this investigation.

The current work used a plasma actuator that was carefully constructed and positioned such that the best possibly isolated roughness element induced streak disturbance attenuation could be achieved. After conducting the control experiments, it was determined that the spanwise position of the plasma actuator centerline was slightly offset from the roughness element induced disturbance centerline. Furthermore, it was found that the spanwise distribution of the disturbance generated by the plasma actuator was less that than produced by the isolated roughness element. By increasing the positive electrode spacing, and shift-

ing the actuator in the spanwise direction, it should be possible to attenuate the targeted planar disturbance throughout the entire y-z plane. This recommendation follows the near perfect attenuation of the disturbance at the downstream sensor location, and the very good agreement between planar results of the controlled disturbance and that of the superposed disturbances. With proper spatial matching of the disturbances, full cancellation should be possible.

Considerations were not taken to properly address the streak disturbance generated during the downward motion of the roughness element. This disturbance does experience slightly different time delays (for example) which would result in an alternative I/O model and control model, as noted as the end of §6.2.1. The goal of the present work is to control streak disturbances, and the roughness element is simply used as a tool to induce the disturbances in a prescribed manner into the boundary layer; therefore, different optimal control parameters existing when the streak is grown (upward roughness element motion) or decaying (downward roughness element motion) are not ideal and this should be considered in future control studies. It is possible, as was done here, that the downward motion difference could be ignored because the real objective is to induce streaks of various amplitudes. But the change in time delay sue to the location of ht stop of the roughness element when the height is changed is likely not negligible when addressing persistently unsteady disturbances.

APPENDIX

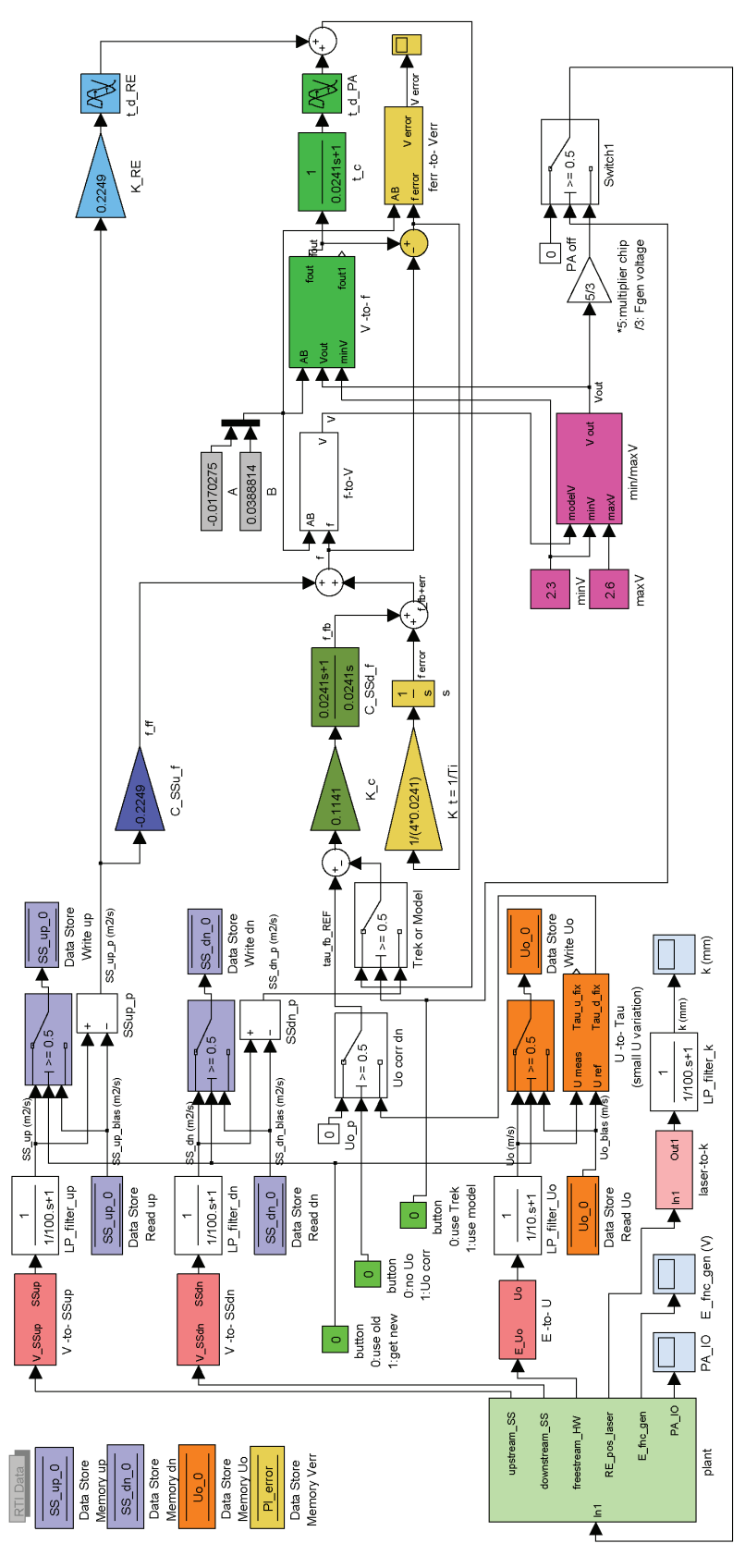


Figure A.1: An example Simulink control model used in this study (note: all sub-blocks are provided below).

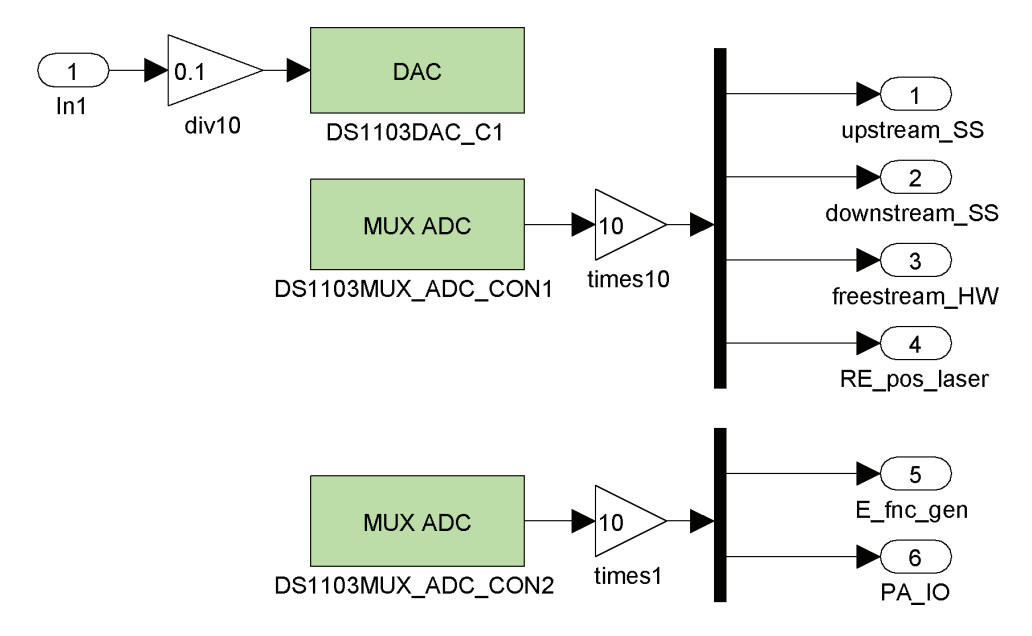


Figure A.2: Submodel: DSpace A/D (Input) and D/A (output) blocks to provide the input and output model voltage signals.

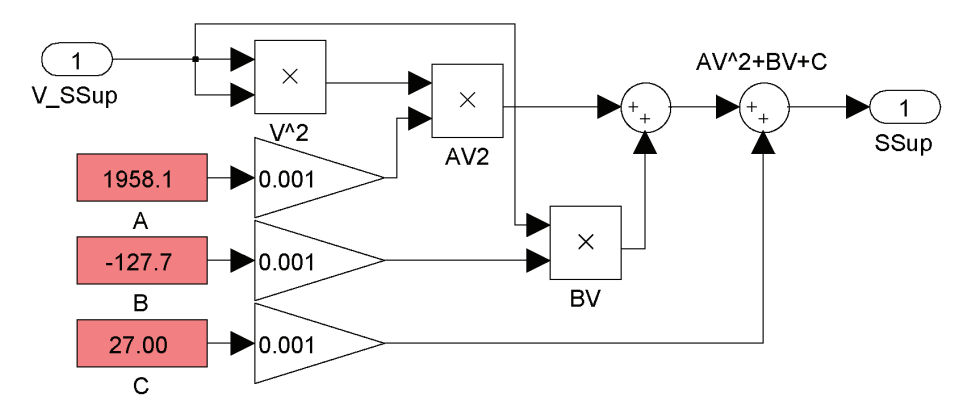


Figure A.3: Submodel: Upstream shear stress sensor calibration, voltage to streamwise shear stress.

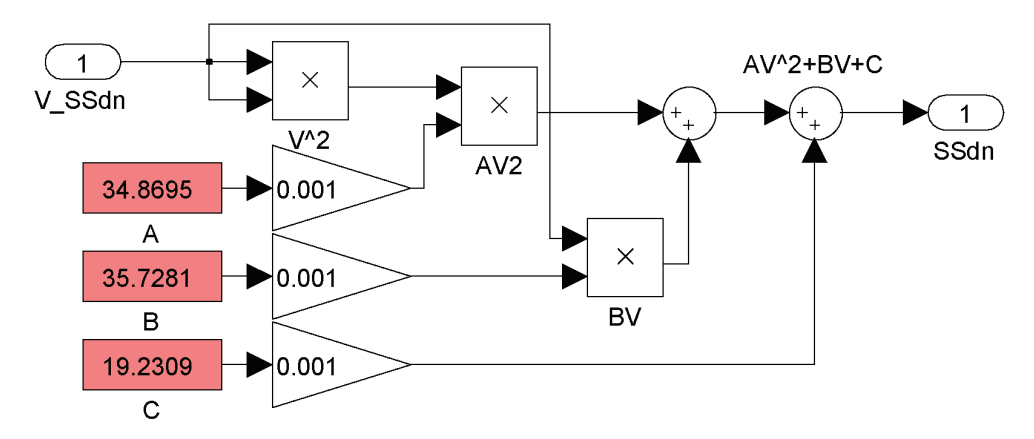


Figure A.4: Submodel: Downstream shear stress sensor calibration, voltage to streamwise shear stress.

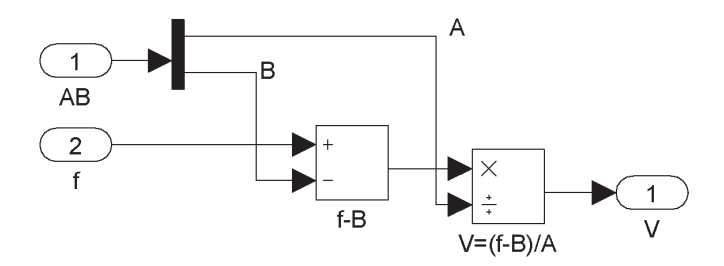


Figure A.5: Submodel: Conversion of the controller output, f, to voltage

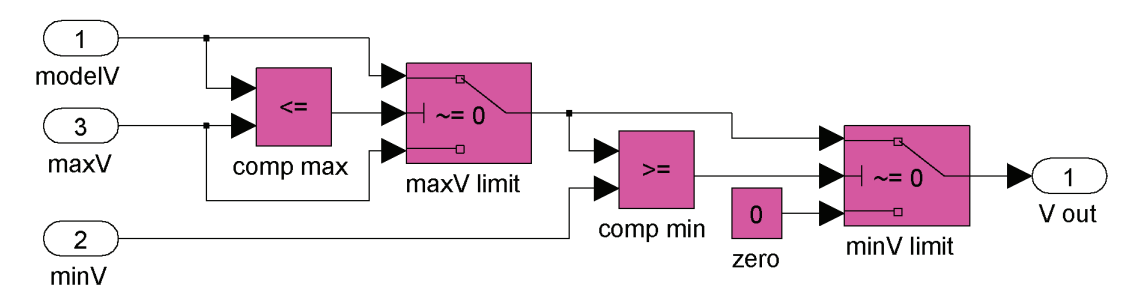


Figure A.6: Submodel: Limiting block to prevent plasma actuator voltage outside the useable range.

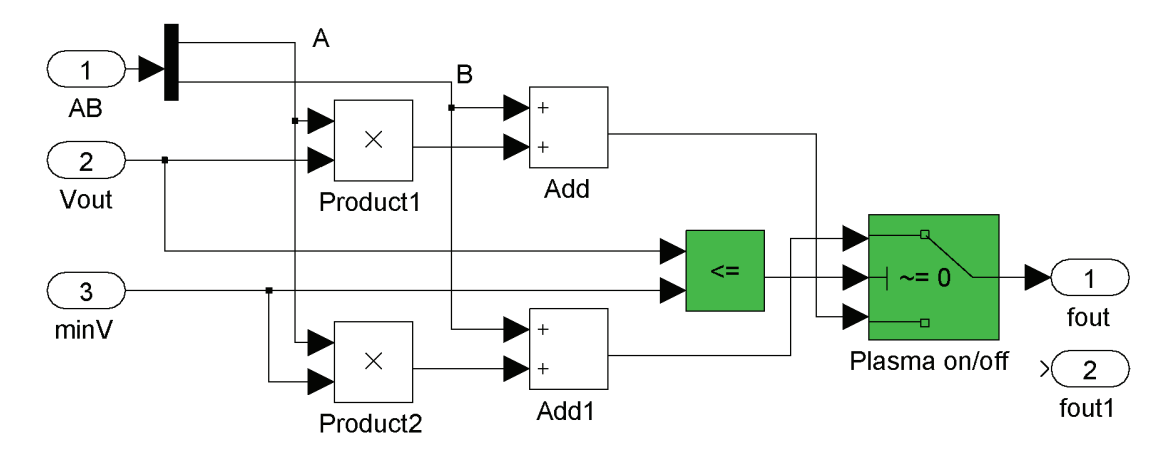


Figure A.7: Submodel: Conversion of the limited plasma actuator voltage to downstream shear stress.

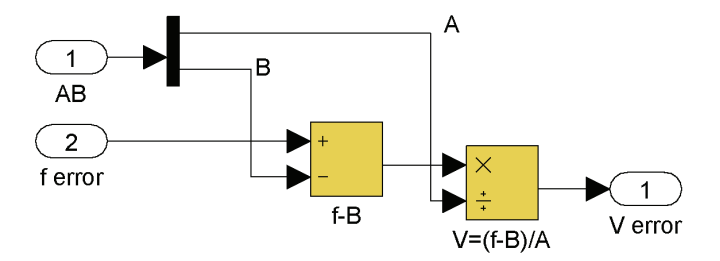


Figure A.8: Submodel: Conversion of the integral controller output error to a voltage error for monitoring purposes.

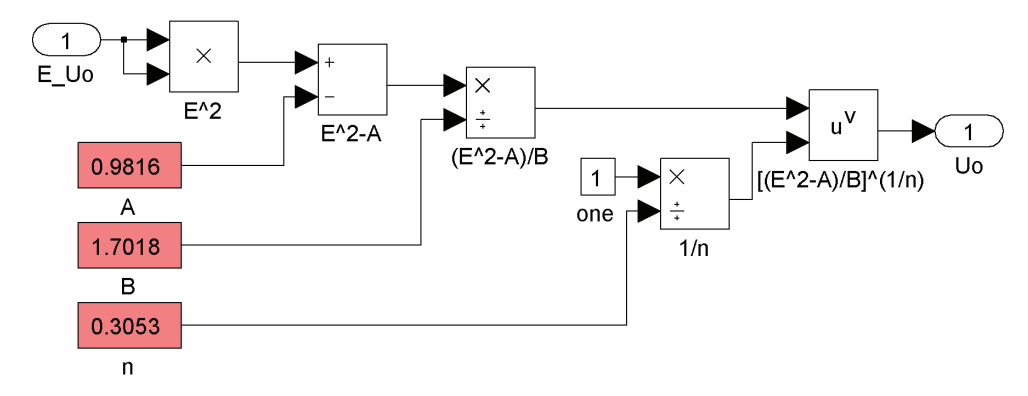


Figure A.9: Submodel: Freestream velocity hot wire calibration: voltage to streamwise velocity.

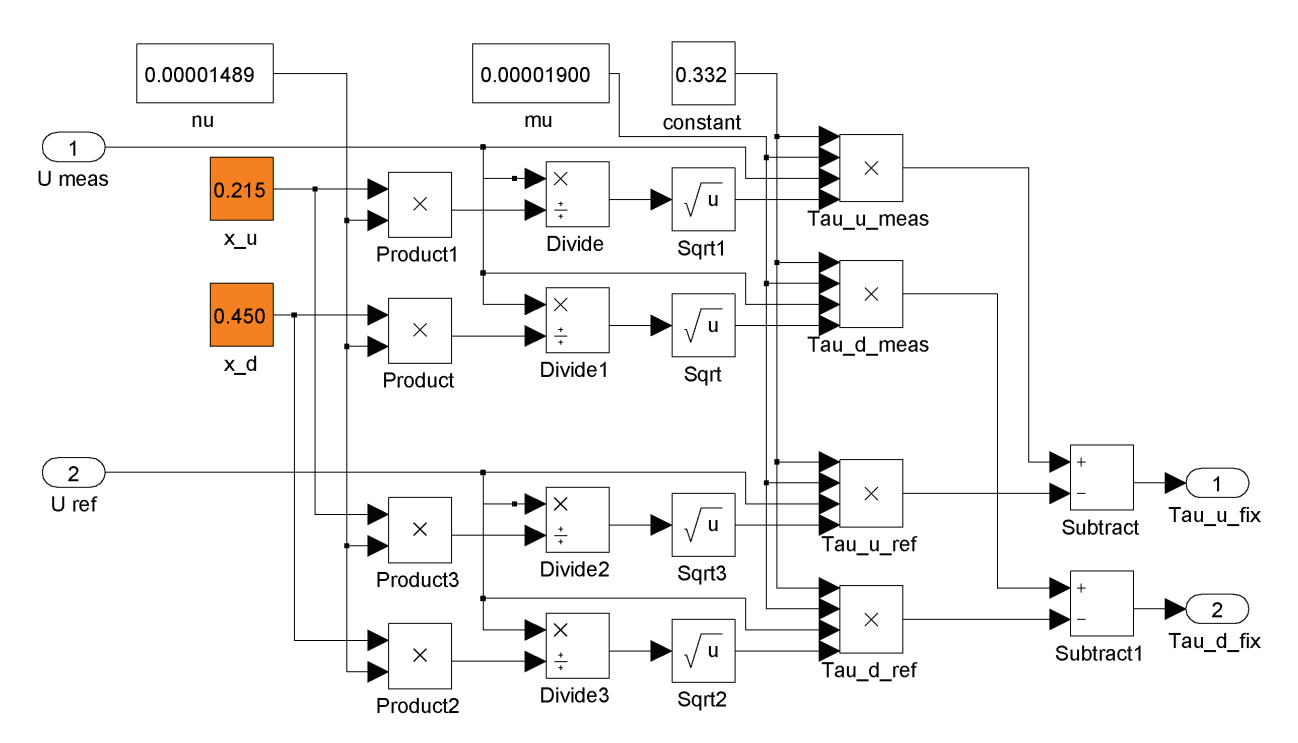


Figure A.10: Submodel: Blasius shear stress correction, based on the streamwise location of the shear stress sensors and the difference between the measured freestream velocity during the I/O data collection, and measured freestream velocity at the time of the active control.

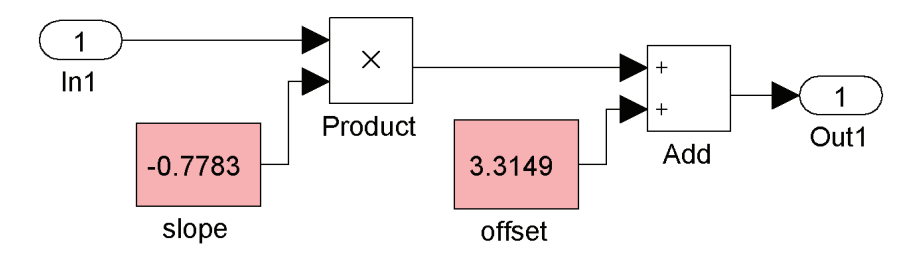


Figure A.11: Submodel: Laser sensor calibration, voltage to roughness element height, k.

BIBLIOGRAPHY

BIBLIOGRAPHY

- [1] M. Acarlar, C. Smith, A Study of Hairpin Vortices in a Laminar Boundary Layer. Part 1. Hairpin Vortices Generated by a Hemisphere Protuberance, Journal of Fluid Mechanics, vol. 175, pp. 1-41, 1987.
- [2] P. Andersson, L. Brandt, A. Bottaro, D. Henningson, On the Breakdown of Boundary Layer Streaks, Journal of Fluid Mechanics, vol. 455, pp. 289-314, 2002.
- [3] M. Asai, K. Sawada, M. Nishioka, Development of Turbulent Patch in a Subcritical Boundary-Layer Transition, Fluid Dynamics Research, vol. 18, pp. 151-164, 1996.
- [4] M. Asai, M. Minagawa, M. Nishioka, *The Instability and Breakdown of a Near-Wall Low-Speed Streak*, Journal of Fluid Mechanics, vol. 455, pp. 289-314, 2002.
- [5] K. Astrom, R. Murray, Feedback Systems, Princeton University Press, ch. 10.4, pp. 306-308, 2010.
- [6] A. Bakchinov, G. Grek, B. G. B. Klingmann, V. V. Kozlov, Transition experiments in a boundary layer with Embedded Streamwise Vortices, Physics of Fluids, vol. 7, issue 4, pp. 820-832, 1995.
- [7] B. Belson, O Semeraro, C. Rowley, D. Henningson, Feedback control of Instabilities in the Two-Dimensional Blasius Boundary Layer: The Role of Sensors and Actuators, Physics of Fluids, vol. 25, pp. 1-17, 2013.
- [8] F. Bertolotti, Response of the Blasius Boundary Layer to Free-Stream Vorticity, Physics of Fluids, vol. 9, issue 8, pp. 2286-2299, 1997.
- [9] A. V. Boiko, K. J. A. Westin, B. G. B. Klingmann, V. V. Kozlov, Experiments in a Boundary Layer Sujected to Free Stream Turbulence. Part 2. The Role of TS-Waves in the Transition Process, Journal of Fluid Mechanics, vol. 281, pp. 219, 1994.
- [10] A. V. Boiko, Receptivity of a Flat Plate Boundary Layer to a Free Stream Axial Vortex, European Journal of Mechanics - B/Fluids, vol. 21, issue 3, pp. 325-340, 2002.

- [11] L. Brandt, C. Cossu, J. Chomaz, P. Huerre, D. Henningson *On the Convectively Unstable Nature of Optimal Streaks in Boundary Layers*, Journal of Fluid Mechanics, vol. 485, pp. 221-242, 2003.
- [12] L. Brandt, Numerical Studies of the Instability and Breakdown of a Boundary-Layer Low-Speed Streak, European Journal of Mechanics - B/Fluids, vol. 26, issue 1, pp. 64-82, 2007.
- [13] K. Butler, B. Farrell, Optimal Perturbations and Streak Spacing in Wall-Bounded Turbulent Shear Flow, Physics of Fluids A, vol. 5, issue 3, pp. 1637-1650, 1993.
- [14] L. Cattafesta, M. Sheplak, *Actautors for Active Flow Control*, Annual Review of Fluid Mechanics, vol. 43, issue 1, pp. 247-272, 2011.
- [15] C. Corke, M. L. Post, and D. M. Orlov, Single dielectric barrier discharge plasma enhanced aerodynamics: physics, modeling and applications, Exp. in Fluids, vol. 46, pp. 1-26, 2009.
- [16] C. Cossu, L. Brandt, Stabilization of Tollmien-Schlichting Waves by Finite Amplitude Optimal Streaks in the Blasius Boundary Layer, Physics of Fluids, vol. 14, issue 8, pp. L57-L60, 2002.
- [17] P. G. Drazin, W. H. Reid, Hydrodynamic Stability, Cambridge University Press, 1981.
- [18] F. Ergin, E. White, Unsteady and Transitional Flows Behind Roughness Elements, AIAA Journal, vol. 44, issue 11, pp. 2504-2514, 2006.
- [19] J. Fransson, L. Brandt, A. Talamelli, C. Cossu, Experimental and Theoretical Investigation of the Nonmodal Growth of Steady Steaks in a Flat Plate Boundary Layer, Physics of Fluids, vol. 16, issue 10, pp. 3527-3528, 2004.
- [20] M. Gad-el-Hak, R. Blackwelder, J. Riley, On the Growth of Turbulent Regions in Laminar Boundary Layers, Journal of Fluid Mechanics, vol. 110, pp. 73-95 (8 plates), 1981.
- [21] M. Gaster, C. Grosch, T. Jackson, *The Velocity Field Created by a Shallow Bump in a Boundary Layer*, Physics of Fluids, vol. 6, issue 9, pp. 3079-3085, 1994.
- [22] A. Haidari, C. Smith, *The Generation and Regeneration of Single Hairpin Vortices*, Journal of Fluid Mechanics, vol. 277, pp. 135-162, 1994.

- [23] R. Hanson, P. Lavoie, A. Naguib, J. Morrison, *Transient Growth Instability Cancellation by a Plasma Actuator Array*, Experiments in Fluids, vol. 49, issue 6, pp. 1339-1348, 2010.
- [24] R. Hanson, P. Lavoie, K. Bade, A. Naguib, Steady-State Closed-Loop Control of Bypass Boundary Layer Transition Using Plasma Actuators, 50th AIAA Aerospace Sciences Meeting, Nashville, TN, January 9-12, 2012.
- [25] R. Hanson, Control of Transient Growth Induced Transition in a Zero-Pressure Gradient Boundary Layer Using Plasma Actuators, PhD Thesis, University of Toronto, Institute for Aerospace Studies, 2013.
- [26] R. Hanson, K. Bade, B. Belson, A. Naguib, P. Lavoie, C. Rowley, Feedback Control of Slowly-Varying Transient Growth by an Array of Plasma Actuators, Physics of Fluids, vol. 26, issue 2, 2014.
- [27] S. Jacobson, W. Reynolds, Active Control of Streamwise Vorticies and Streaks in Boundary Layers, Journal of Fluid Mechanics, vol. 360, issue 1, pp. 179-211, 1998.
- [28] T. Jukes, K. Choi, Dielectric-Barrier-Discharge Vortex Generators: Characterisation and Optimisation for Flow Separation Control, Experiments in Fluids, vol. 52, pp. 329-345, 2012.
- [29] T. Jukes, K. Choi, On the Formation of Streamwise Vortices by Plasma Vortex Generators, Journal of Fluid Mechanics, vol. 733, pp. 370-393, 2013.
- [30] P. Klebanoff, W. Cleveland, K. Tidstrom, On the Evolution of a Turbulent Boundary Layer Induced by a Three-Dimensional Roughness Element, Journal of Fluid Mechanics, vol. 237, issue 1, pp. 101-187, 1992.
- [31] J. Kendall, Experimental Study of Disturbances Produced in a Pre-Transitional Laminar Boundary Layer by Weak Freestream Turbulence, AIAA conference paper, pp. 1-10, 1985.
- [32] T. Kurian, J. Fransson, P. Alfredsson, Boundary Layer receptivity to Free-Stream Turbulence and Surface Roughness Over a Swept Flat Plate, Physics of Fluids, vol. 23, issue 3, pp. 1-13, 2011.
- [33] M. Landhal, A Note on an Algebraic Instability of Inviscid Parallel Shear Flows, Journal of Fluid Mechanics, vol. 98, issue 2, pp. 243-251, 1980.
- [34] P. Lavoie, A. Naguib, J. Morrison, Transient Growth Induced by Surface Roughness in a Blasius Boundary Layer in Proceedings of ICTAM, Adelaide, Australia, 2008.

- [35] G. Lemonis, T. Dracos, A New Calibration and Data Reduction Method for Turbulence Measurement by Multihotwire Probes, Experiments in Fluids, vol. 18, pp. 319-328, 1995.
- [36] F. Lundell, Reactive Control of Transition Induced by Free-Stream Turbulence: An Experimental Demonstration, Journal of Fluid Mechanics, vol. 585, pp. 1-41, 2007.
- [37] F. Lundell, A. Monokrouses, L. Brandt, Feedback Control of Boundary Layer Bypass Transition: Experimental and Numerical Progress, AIAA paper No. 2009-612, 2009.
- [38] A. Mandal, L. Venkatakrishnan, J. Dey, A Study on Boundary-Layer Transition Induced by Free-Stream Turbulence, Journal of Fluid Mechanics, vol. 660, pp. 114-146, 2010.
- [39] M. Matsubara, P. Alfredsson, Disturbance Growth in Boundary Layers Subjected to Free-Stream Turbulence, Journal of Fluid Mechanics, vol. 430, issue 1, pp. 149-168, 2001.
- [40] A. Naguib, J. Marrison, T. Zaki, On the Relationship Between the Wall-Shear-Stress and Transient-Growth Disturbances in a Laminar Boundary Layer, Physics of Fluids, vol. 22, issue 5, pp. 1-13, 2010.
- [41] R. Pattenden, S. Turnock, X. Zhang, Measurements of the flow over a low-aspect-ratio cylinder mounted on a ground plane, Experiments in Fluids, vol. 39, issue 1, pp. 10-21, 2005.
- [42] E. Reshotko, *Transient Growth: A Factor in Bypass Transition*, Physics of Fluids, vol. 13, issue 5, pp. 1067-1075, 2001.
- [43] D. Rizzetta, M. Visbal, Direct Numerical Simulations of Flow Past an Array of Distributed Roughness Elements, AIAA Journal, vol. 45, issue 8, pp. 1967-1976, 2007.
- [44] W. Saric, Boundary-Layer Stability and Transition in Wall-Bounded Flows in Springer Handbook of Experimental Fluid Mechanics, (edited by C. Tropea, A. L. Yarin, J. F. Foss), Springer, ch. 12.3, pp. 886-896, 2007.
- [45] H. Schlichting, K. Gersten, Bounday-Layer Theory, Springer, ch. 6.5, pp. 156-164, 2000.
- [46] G. B. Schubauer, P. S. Klebanoff, Contributions on the Mechanics of Boundary-Layer Transition, NACA Report 1289, pp. 853-864, 1956.
- [47] S. Skogestad, Simple analytic rules for model reduction and PID controller tuning, Modeling, Identification and Control, vol. 25, no. 2, pp. 85-120, 2004.

- [48] I. Tani, Boundary Layer Transition, Annual Review of Fluid Mechanics, vol. 1, p. 169-196 1969.
- [49] N. Vaughan, T. Zaki, Stability of Zero-Pressure-Gradient Boundary Layer Distorted by Unsteady Klebanoff Streaks, Journal of Fluid Mechanics, vol. 681, pp. 116-153, 2011.
- [50] M. Visbal, The Laminar Horseshoe Vortex System Formed at a Cylinder/Plate Juncture, AIAA Conference, pp. 1-16, June 1991.
- [51] A. E. von Doenhoff, A. L. Braslow, *The Effect of Distributed Surface Roughness on Laminar Flow*, Boundary Layer and Flow Control: Its Principals and application, pp. 657-681, 1961.
- [52] E. White, Transient Growth of Stationary Disturbances in a Flat Plate Boundary Layer, Physics of Fluids, vol. 14, issue 12, pp. 4429-4439, 2002.
- [53] E. White, F. Ergin, *Using Laminar-Flow Velocity Profiles to Locate the Wall Behind Roughness Elements*, Experiments in Fluids, vol. 36, issue 5, pp. 805-812, 2004.
- [54] E. White, J. Rice, F. Ergin, Receptivity of Stationary Transient Disturbances to Surface Roughness, Physics of Fluids, vol. 17, issue 6, pp. 1-12, 2005.
- [55] T. Zaki, P. Durbin, Mode Interaction and the Bypass Route to Transition, Journal of Fluid Mechanics, vol. 531, issue 1, pp. 85-111, 2005.
- [56] T. Zaki, From Streaks to Spots and in to Turbulence: Exploring the Dynamics of Boundary Layer Transiton, Flow, Turbulence, and Combustion, vol. 91, issue 3, pp. 451-473, 2013.